Structural and biochemical studies of orthomyxovirus nucleoproteins as targets of the antiviral Mx proteins

Dissertation zur Erlangung des akademischen Grades des
Doktors der Naturwissenschaften (Dr. rer. nat.)

eingereicht im Fachbereich Biologie, Chemie, Pharmazie der
Freien Universität Berlin

vorgelegt von

M. Sc. Alexej Dick

aus Jekaterinowka (Primorsky Krai, Russland)

Berlin, 2016

Die vorliegende Arbeit wurde von September 2011 bis März 2016 am Max-Delbrück-Centrum für Molekulare Medizin unter der Anleitung von Prof. Dr. Oliver Daumke angefertigt.

1. Gutachter: Prof. Dr. Udo Heinemann
2. Gutachter: Prof. Dr. Oliver Daumke

Disputation am: 24/06/2016

CONTENTS

1 Introduction 1
1.1 RNA viruses 1
1.2 Negative-strand RNA viruses (NSV) 2
1.3 The *Orthomyxoviridae* family 3
1.3.1 The influenza virus (IFV) 4
1.3.1.1 Historical introduction 5
1.3.1.2 The architecture of the influenza virus 5
1.3.1.3 Influenza virus replication cycle 7
1.3.2 Thogoto- and Dhori virus 10
1.4 Structural overview of sNSV nucleoproteins (NPs) 11
1.5 Innate immune response against viruses 15
1.6 Mx proteins in innate immune system 18
1.6.1 Historical introduction of MxA 18
1.6.2 Structural overview of Mx proteins 20
1.6.2.1 The GTPase domain 21
1.6.2.2 Functional role of G domain dimerization 22
1.6.2.3 Oligomerization via the stalk 25
1.6.3 Antiviral mechanism of MxA and MxB 26
1.7 Scope of this work 30
2 Materials and Methods 32
2.1 Materials 32
2.1.1 Instruments 32
2.1.2 Chemicals 32
2.1.3 Enzymes 32
2.1.4 Kits 32
2.1.5 Crystallization screens and tools 33
2.1.6 Microorganisms 33
2.1.7 Vectors 34
2.1.8 cDNA clones 34
2.1.9 Media and antibiotics 34
2.1.10 Buffers 35
2.2 Molecular biology methods 36

2.2.1 Polymerase chain reaction 36
2.2.2 Restriction digest 37
2.2.3 Agarose gel electrophoresis 37
2.2.4 Purification of separated DNA 37
2.2.5 Ligation 37
2.2.6 Competent *E. coli* cells 37
2.2.7 Transformation 37
2.2.8 Bacterial storage 38
2.2.9 Site directed mutagenesis 38
2.2.10 Constructs and point mutants used in this study 39
2.2.11 Isolation of plasmid DNA 40
2.2.12 DNA sequencing 40
2.2.13 Sequence alignment 40
2.3 Biochemical methods 40
2.3.1 Sodium dodecyl sulfate polyacrylamide gel electrophoresis (SDS-PAGE) 40
2.3.2 Viral NP over-expression and solubility test 40
2.3.3 Large scale protein over-expression and purification 41
2.3.4 Expression of selenomethionine (SeMet) incorporated protein 41
2.3.5 Protein concentration determination 42
2.3.6 Protein storage 42
2.3.7 Circular dichroism spectroscopy (CD) 43
2.3.8 Nucleotide detection via reverse-phase HPLC 43
2.3.9 Nucleotide binding assay 44
2.3.10 RNA/DNA binding assay 44
2.3.11 Nucleotide hydrolysis assay 45
2.3.12 Analytical gel filtration 45
2.3.13 Right angle light scattering (RALS) 46
2.3.14 Analytical ultracentrifugation (AUC) 46
2.3.15 Electron microscopy (EM) 47
2.3.16 Oligomerization assay 47
2.3.17 Homology modeling 47
2.3.18 Other assays and techniques 48
2.4 Crystallographic and computational methods 48
2.4.1 Crystallization 48

2.4.2 Cryo-protection 49
2.4.3 Data collection 49
2.4.4 Protein structure solution 49
2.4.4.1 Protein structure solution for the THOV NP 53
2.4.5 Atomic model building and data refinement 53
2.4.6 Structure analysis and figure preparation 54
3 Results 56
3.1 Nucleotide binding for G domain dimerization, GTPase activation and antiviral activity of MxA 56
3.1.1 Expression of G domain mutants 56
3.1.2 The GTPase mechanism of MxA 57
3.1.3 A single intact catalytic center is sufficient for nucleotide hydrolysis 63
3.1.4 Nucleotide binding and hydrolysis are required for the antiviral function of MxA 64
3.1.5 Role of nucleotide binding and hydrolysis in formation of cytoplasmic MxA assemblies 67
3.1.6 G255E and V268M are natural genetic variations in the putative G interface 70
3.2 Biochemical characterization of the human MxB GTPase 72
3.2.1 Expression of a soluble MxB construct 72
3.2.2 The oligomerization state of MxB 73
3.2.3 Concentration-dependent GTP hydrolysis of MxB 74
3.2.4 MxA stimulates the GTPase activity of MxB 75
3.3 Biochemical and structural characterization of the THOV and DHOV NP 76
3.3.1 Protein over-expression and solubility tests 76
3.3.2 Large scale NP expression and purification 78
3.3.3 Salt and protein concentration optimization 79
3.3.4 Folding status of the THOV NP 80
3.3.5 RNA and DNA binding 81
3.3.6 Oligomeric state of the NPs 87
3.3.7 The isolated MxA loop L4 does not bind THOV NP *in vitro* 88
3.4 Structure of the THOV NP 91
3.4.1 Crystallization 91
3.4.2 Structure determination of the THOV NP$^{\Delta 188\text{-}196}$ 93
3.4.3 Structural analysis of the THOV NP$^{\Delta 188\text{-}196}$ structure 98

3.4.4 Structural comparison with negative-sense single-stranded RNA viruses (NSRVs) 102
3.4.5 Functional analysis of the THOV NP$^{\Delta 188\text{-}196}$ structure 104
3.4.5.1 Single-stranded RNA/DNA binding 104
3.4.5.2 Oligomerization 105
3.4.5.3 Electron microscopy (EM) analysis of THOV/DHOV-RNPs 107
4 Discussion 111
4.1 G domain dimerization of MxA and its role for the antiviral activity 111
4.2 MxA as a regulator of the MxB GTPase 114
4.3 Structural comparison of the THOV NP within the *Orthomyxoviridae* family 117
4.4 THOV NP sensitivity towards the antiviral MxA GTPase 119
4.5 Oligomeric model of the THOV-RNP 122
Appendix A – Instruments 125
Appendix B – Chemicals 126
Appendix C – Dynamin superfamily alignment 127
Appendix D - *Orthomyxoviridae* nucleoprotein alignment 132
Appendix E – Abbreviations 136
Bibliography 139
Abstract 150
Zusammenfassung 151
Publications 153
Acknowledgement 154
Erklärung 155

LIST OF FIGURES

Figure 1: Unrooted phylogenetic tree of the known NSVs. 3
Figure 2: Phylogenetic relationships within the family *Orthomyxoviridae*. 4
Figure 3: Schematic model of IFAV particle. 6
Figure 4: The IFAV replication cycle. 8
Figure 5: Phylogenetic tree of the genus THOV within the *Orthomyxoviridae* family. 10
Figure 6: Structural comparison of sNSV NPs. 12
Figure 7: Gating mechanism of sNSV NP-RNA binding coupled to RNP assembly. 13
Figure 8: Negatively stained electron micrographs of NSVs nucleocapsids/RNPs. 14
Figure 9: Molecular architecture of IFAV RNPs. 15
Figure 10: Pathogenic RNA and DNA detection in mammalian cells. 17
Figure 11: Phylogenetic tree of Mx proteins. 19
Figure 12: Structure of human Mx GTPases. 20
Figure 13: Dimerization-dependent GTPase activation of MxA and dynamin. 23
Figure 14: G domain dimerization of dynamin related GTPases and the SRP receptor. 24
Figure 15: Oligomerization interfaces of MxA. 26
Figure 16: Antiviral activity sites of Mx proteins during different viral infections. 28
Figure 17: Expression and purification of hsMxA^{M527D}. 57
Figure 18: G domain architecture of MxA. 58
Figure 19: Nucleotide binding analysis. 59
Figure 20: Analytical gel filtration analysis. 60
Figure 21: Protein concentration-dependent GTPase/XTPase activity of MxA mutants. 61
Figure 22: Analysis of the GTPase activity. 63
Figure 23: G domain mutants interact with the viral NP. 65
Figure 24: A functional GTPase is crucial for antiviral activity. 66
Figure 25: Intracellular distribution of MxA G domain mutants. 67
Figure 26: Co-localization study of MxA G domain mutants with Syntaxin 17. 68
Figure 27: Complex formation of MxA with the LACV nucleoprotein (N). 69
Figure 28: Effects of MxA polymorphisms in the G interface. 71
Figure 29: Expression and purification of hsMxB$^{\Delta N85+\Delta L4}$. 73
Figure 30: Right angle light scattering analysis of MxB $^{\Delta N85/\Delta L4}$ 74
Figure 31: GTPase activity of MxB compared to MxA. 75
Figure 32: Analysis of the GTPase activity of MxA and MxB. 76
Figure 33: Expression and solubility test of IFAV and THOV NPs. 77

Figure 34: Expression and purification of the wt THOV NP. 78
Figure 35: Expression and purification of the wt DHOV NP. 79
Figure 36: Salt and protein concentration optimization for THOV and DHOV NP. 80
Figure 37: CD-spectra of the wt THOV NP and wt IFAV H1N1 NP. 81
Figure 38: Wt THOV NP bound to polyU-molecules of different length. 82
Figure 39: Thermodynamic parameters for the wt THOV NP bound to different polyU oligos. .. 83
Figure 40: RNA binding assays for THOV and DHOV NP. 84
Figure 41: Integrated ITC graphs for the wt THOV bound to viral UTRs. 85
Figure 42: Thermodynamic parameters for the wt THOV NP bound to viral UTRs. 86
Figure 43: Oligomeric state of the wt THOV and wt DHOV NP in solution. 87
Figure 44: Trimeric form of wt THOV NP bound to a pU24mer ssRNA. 88
Figure 45: Loop L4-peptide-1 binding analysis. 89
Figure 46: Loop L4-peptide-2 and-3 binding analysis. 90
Figure 47: Examples of THOV NP crystals. 91
Figure 48: Examples of wt DHOV NP crystals. 92
Figure 49: Anomalous difference map of the THOV $NP^{\Delta 188\text{-}196}$. 96
Figure 50: Initial 2Fo-Fc, Fo-Fc and anomalous difference map of THOV $NP^{\Delta 188\text{-}196}$ crystal. 96
Figure 51: Three-fold symmetry of the THOV $NP^{\Delta 188\text{-}196}$ within the crystal lattice 97
Figure 52: Ramachandran plot of the THOV $NP^{\Delta 188\text{-}196}$ structure 97
Figure 53: THOV $NP^{\Delta 188\text{-}196}$ monomer. 98
Figure 54: Structure and domain architecture of the THOV $NP^{\Delta 188\text{-}196}$. 99
Figure 55: The crystallographic trimer of THOV $NP^{\Delta 188\text{-}196}$. 100
Figure 56: Electrostatic surface potential of THOV $NP^{\Delta 188\text{-}196}$. 101
Figure 57: Structural comparison of orthomyxovirus NPs. 102
Figure 58: Structural comparison of NSRV NPs. 103
Figure 59: Binding to ssRNA/ssDNA of internal and N-terminal deletion constructs. 104
Figure 60: Analytical gel filtration analysis. 106
Figure 61: NP visualization on ssRNA by electron microscopy. 108
Figure 62: Electron microscopy of wt DHOV NP at different NP:nucleic acid ratios. 109
Figure 63: Role of nucleotide in the antiviral activity of human MxA. 114
Figure 64: Surface conservation plot of THOV $NP^{\Delta 188\text{-}196}$. 118
Figure 65: Surface B-factor plot of THOV $NP^{\Delta 188\text{-}196}$. 119
Figure 66: Amino acid cluster mediating MxA resistance. 121
Figure 67: Model of the THOV-RNP. 122
Figure 68: Model of the THOV-miniRNP. 124

LIST OF TABLES

Table 1: Antiviral profile and localization of human and mouse Mx proteins..... 27
Table 2: Detailed list of all constructs used in this work. 39
Table 3: Summary of the biochemical and antiviral activity of the studied mutants. 60
Table 4: RNA/DNA sequences and binding parameters for the wt THOV NP. 86
Table 5: Peptides used in this study for ITC experiments. 89
Table 6: Crystallizable deletion constructs of the THOV and DHOV NP. 93
Table 7: Data collection statistics of native and SeMet THOV NP$\Delta^{188\text{-}196}$ crystals. 94
Table 8: Refinement statistics for the THOV NP$\Delta^{188\text{-}196}$. 95
Table 9: Binding characteristics of the deletion mutants of THOV and DHOV NP. 105
Table 10: Amino acids responsible for MxA resistance. 120

1 Introduction

1.1 RNA viruses

Viruses are the smallest self-replicating entities on earth (reviewed in (1)). The Russian biologist Dmitry Ivanovsky reported in 1892 for the first time that extracts from infected tobacco leaves were still infectious after passing through a filter which was small enough to retain bacteria (reviewed in (1)). He worked on the now known tobacco mosaic virus (TMV). Several years later in 1898, the Dutch biologist Martinus Beijerinck repeated these experiments and discovered that the filtrate could only multiply in dividing cells. He called the infectious particle *contagium vivum fluidum* (soluble living germ) and invented the first time the term 'virus'. Since this discovery at the end of the 19th century, our understanding of viruses has developed dramatically (reviewed in (1,2)).

Viruses have shaped the history of their hosts. All known living organisms have viral parasites and viruses cause a number of severe diseases in eukaryotes. For example, in humans, they are responsible for the common cold or serious influenza outbreaks, chickenpox, herpes, polio, Ebola, and the acquired immune deficiency syndrome (AIDS). Also some types of cancer are linked to viruses, such as to the Epstein-bar virus (EBV) or the human papilloma virus (HPV) (reviewed in (1)).

Since viruses have no own metabolism, they hijack subcellular machineries of invaded cells to replicate and produce viral particles in an infective form (virions) to disseminate their genes. Viruses are encapsulated by a protein shell (non-enveloped, such as adeno virus) and sometimes by an additional host cell-derived lipid membrane (enveloped, such as influenza virus). They come in two flavors, those that have a genome of DNA and those with an RNA coding genome. Both nucleic acids can be used by different viruses in double-stranded or single-stranded manner. Further classification of RNA viruses according to the sense or polarity of their RNA into negative-sense (-) and positive-sense (+), or ambisense RNA viruses is possible. The RNA of positive-sense viral RNA is similar to messenger RNA (mRNA) and can therefore be immediately translated by the host cell. In contrast, negative-sense viral RNA is complementary to mRNA and must be converted to positive-sense RNA by an RNA polymerase before translation (3). Therefore, the purified RNA of a negative sense virus is not infectious by itself, because it has to be converted to a positive sense RNA for replication by a viral reverse

transcriptase. Viruses with an ambisense genome carry both nucleic acid strands encoding for proteins (reviewed in (1)).

This doctoral thesis deals with single-stranded (-) RNA viruses of the orthomyxovirus family such as the Thogoto (THOV) and Dhori (DHOV) virus. Therefore, a short overview of the negative-strand RNA viruses is given in the following chapter.

1.2 Negative-strand RNA viruses (NSV)

NSV are a group of viruses that comprise a broad spectrum of human pathogens including, influenza, Ebola, mumps, measles and hantaviruses. Besides humans, they can also infect vertebrates, arthropods and plants. Virus families with an RNA genome that infect vertebrates outnumber those with DNA genomes by about two to one, and among viruses infecting plants, this number is even higher. This displays the evolutionary success of RNA usage as genetic material. However, the high error rates of RNA transcription limits the genome size to about 30 kb or less (reviewed in (1)).

NSVs are divided into two groups: NSVs with a segmented (s) or non-segmented (ns) genome (Figure 1). The order Mononegavirales (insinuating to the monopartite and single-stranded genomes) comprise families of nsNSVs which contain a single genomic segment with 5-10 genes sequentially arranged. This order contains four families, which are *Bornaviridae* (e.g. borna disease virus (BDV)), *Filoviridae* (e.g. ebola virus), *Paramyxoviridae* (e.g. measles virus, mumps virus) and *Rhabdoviridae* (e.g. rabies virus, vesicular stomatitis virus (VSV)) (reviewed in (4)). Segmented NSVs (sNSVs) contain two or more segments. They are grouped in the order Multinegavirales which contains three families; *Arenaviridae* (e.g. lassa virus), *Bunyaviridae* (e.g. hanta virus, rift-valley fever virus) and *Orthomyxoviridae* (reviewed in (4)). The next chapter will introduce the members of the orthomyxovirus family in more detail.

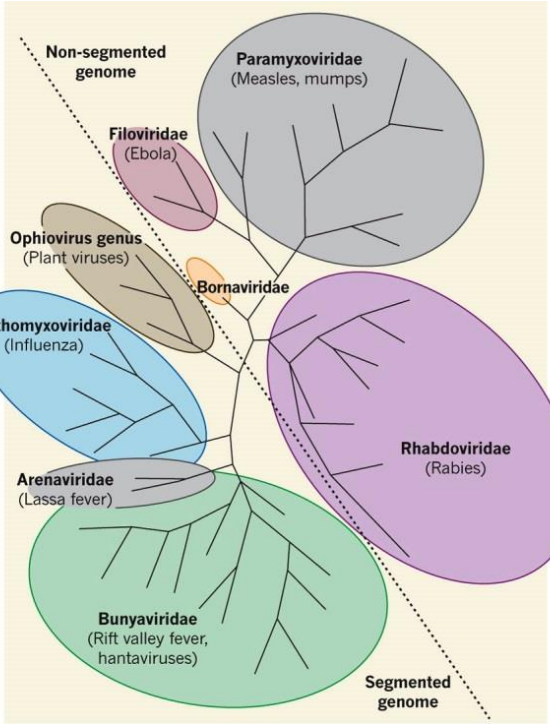

Figure 1: Unrooted phylogenetic tree of the known NSVs.

Representative human pathogens/diseases (except for the genus ophiovirus) in each of the families are indicated in parentheses. Ophioviruses represent a genus rather than a family. The diagonal dashed line separates non-segmented from the segmented NSVs. Arenaviruses have two genomic segments, bunyaviruses have three, ophioviruses three or four (depending on the virus) and orthomyxoviruses six to eight. Figure was adopted from (5).

1.3 The *Orthomyxoviridae* family

Orthomyxoviruses (*orthos*, Greek for 'straight'; *myxa*, Greek for 'mucus') are enveloped viruses. The members of the *Orthomyxoviridae* family are negative-sense, single-stranded, and segmented RNA viruses (sNSV). Segmentation of their genome allows a remarkable evolutionary advantage of these viruses, such as high genetic flexibility and adaptability to new host species due to 'mixing' events between different subtypes and mutants by a mechanism called reassortment. The reassortment process is sometimes occurring when two similar viruses infect the same cell. The combination of genetic material can lead to a novel virus with new fatal properties for the host and cause epidemics or even worldwide pandemics (6).

The *Orthomyxoviridae* family comprises seven genera or types (6): the influenza virus A, B and C (IFAV, IFBV and IFCV), the Thogoto virus (THOV), the Johnston atoll virus, the Quaranfil virus, and the Infectious Salmon Anemia (ISA) virus (Figure 2) (6). The THOV genus contains 6 distinct viruses or species: the Dhori virus (DHOV) and its subtype Batken virus

(BKNV), as well as the species Araguari virus, Aransas Bay virus (ABV), Bourbon virus (BOUV), Jos virus (JOSV) and Upolu virus (UPOV) (6). The genus ISA virus, with the species ISAV, is very distinct from influenza viruses A, B, and C.

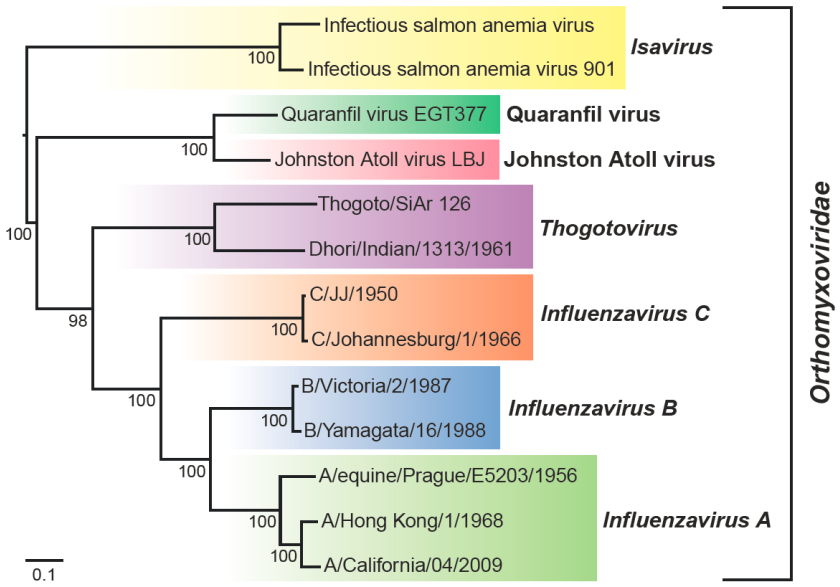

Figure 2: Phylogenetic relationships within the family *Orthomyxoviridae*.

The phylogeny is based on the sequence alignment of the PB1 domain of the polymerase. The tree was mid-point rooted and bootstrap values (1000 replicates) are indicated on the branches. Figure adopted from (6).

The first three genera contain viruses that cause influenza in vertebrates, including avian species, humans, and other mammals. ISA viruses infect salmon, and Thogoto viruses are arboviruses and infect vertebrates and invertebrates, such as ticks and mosquitoes (6).

The THOV and DHOV are structurally and genetically very close related to the best studied member of the orthomyxovirus family, the influenza virus. The next three chapters give an overview on the architecture and replication cycle of the influenza virus.

1.3.1 The influenza virus (IFV)

1.3.1.1 Historical introduction

The influenza virus represents a global threat to humanity, and seasonal influenza epidemics are responsible for thousands of deaths annually (7). The influenza virus is the most common cause for human respiratory infections in humans. They cause high morbidity and mortality, especially in the elderly, infants and people with chronic disease. Outbreaks have occurred at least since the Middle Age or even since ancient times (8). Influenza causes approximately 200,000 hospitalizations and 36,000 deaths in a typical endemic season in the United States (US) (9). Beside the annual winter outbreaks, pandemic IFAVs occasionally emerge. There have been approximately 14 pandemic IFAV outbreaks since 1510. In the past 120 years, there were pandemics in 1889, 1918 (Spanish flu), 1957 (Asian flu), 1968 (Hong Kong flu), 1977 (Russian flu), and 2009 (Swine flu) (8). The worst pandemic in 1918, the Spanish flu, lead to 675,000 deaths in the US and up to 50 million worldwide (10). The following pandemics in 1957 and 1968 caused approximately 70,000 and 34,000 deaths in the US, respectively (9). Most recently, the swine flu (pH1N1) in 2009 caused approximately 270,000 hospitalizations, and 13,000 deaths in the US (11).

1.3.1.2 The architecture of the influenza virus

Viruses are sophisticated macromolecular assemblies. They are very efficient in using a limited number of proteins to fulfill their life-cycle within the infected host cell. Viruses carry the entire molecular machinery necessary for the efficient packaging of viral genomes, the escape from an infected cell, the survival and transfer to a new host cell (adaptation), and the attachment, invasion/penetration, and initiation of a new replication cycle.

Influenza viruses are enveloped viruses, with a host cell-derived lipid membrane. In addition to IFAV, there are two other types of influenza viruses, namely the influenza B (IFBV) and C (IFCV) virus. IFAV and IFBV are more similar to each other than to IFCV, and only IFAV poses a significant risk of zoonotic infections, host switch, and the ability for pandemic outbreaks (reviewed in (1)). IFAV genomic RNA is segmented into eight segments, which encode at least 10 open reading frames (ORFs) (Figure 3): Hemagglutinin (HA), Neuraminidase (NA), Nucleoprotein (NP), Matrix protein 1 (M1), Matrix protein (M2), the Non-structural proteins 1 and 2 (NS1, NS2, also known as nuclear export protein, or NEP), and the

heterotrimeric polymerase complex composed of three proteins, the polymerase acidic protein (PA), the polymerase basic protein 1 (PB1), and the polymerase basic protein 2 (PB2) (12).

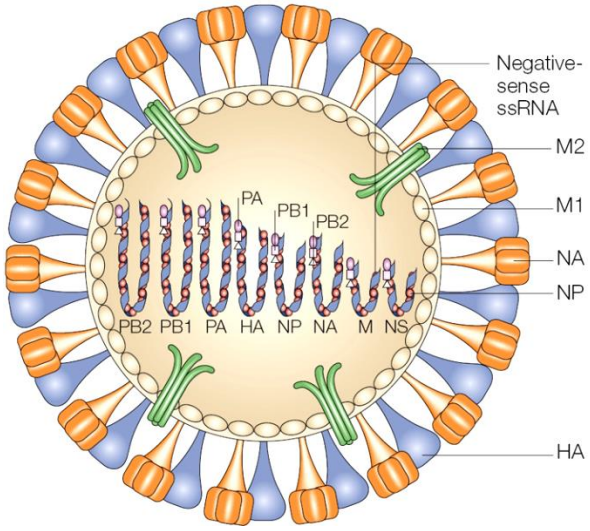

Figure 3: Schematic model of IFAV particle.

Two surface glycoproteins, hemagglutinin (HA) and neuraminidase (NA), and the M2 ion-channel protein are embedded in the viral envelope, which is derived from the host plasma membrane. The ribonucleoprotein complex comprises a viral RNA segment associated with the nucleoprotein (NP) and three polymerase proteins (PA, PB1 and PB2). The matrix (M1) protein is associated with both ribonucleoprotein and the viral envelope. A small amount of non-structural protein 2 is also present, but its location within the virion is unknown. Figure adapted from (13).

The HA protein is a type I glycosylated integral membrane protein (e.g. the C-terminus is positioned towards the cytosol) and functions as a viral receptor-binding and a membrane fusion protein. HA recognizes sialic acids (SA), and in particular the most common SA N-acetyl neuraminic acid, displayed on epithelial host cell glycoproteins. IFAVs adapted to birds have an HA receptor-binding specificity for α2-3-linked SA, while HAs from IFAVs adapted to humans have higher specificity for α2-6-linked SA (9). For initiation of virus infection, HA binds sialic acid receptors on the surface of the host cell, leading to virus internalization by endocytosis. The endosomal acidic pH leads to a conformational change in HA, which causes fusion of the viral membrane with the endosome and release of the vRNPs into the cytoplasm (9).

NA is a type II integral membrane glycoprotein (e.g. the N-terminus is positioned towards the cytosol). Its sialidase enzymatic activity cleaves host cell SA allowing release of newly produced virions, and SA on viral glycoproteins to prevent aggregation of nascent viral particles (9). There are 18 HA (H1-18) and 11 NA (N1-11) subtypes which are used as antigenic differentiation markers for the classification of IFAV (14). HA and NA are major antigenic

targets of the humoral immune response to IAV. Furthermore, important antiviral drugs like oseltamivir and zanamivir target the NA protein.

The main function of the NP is to encapsulate the virus genome into the RNPs for RNA transcription, replication and packaging, and it is also involved in the trafficking of the RNPs between the cytoplasm and the nucleus (15). The regulation of the movement of the parental virion and of the export of newly assembled viral RNPs from the host cell nucleus is performed by the M1 protein, which forms a coat inside the viral envelope (16). The M1 protein also keeps the vRNPs attached to the inner layer of the virus. Furthermore, M1 interacts with cytoplasmic domains of the surface glycoproteins. The M2 protein is a proton channel integral to the viral envelope and mediates the acidification of the viral interior, thereby facilitating the dissociation of M1 from the viral NP, which is a crucial step for the unpacking of the viral genome (17). M2 is the target of the adamantane class of antiviral drugs (9). NS1 regulates the transport of viral mRNA and other polyadenosine (polyA) containing mRNA from the nucleus and likely suppresses the interferon response after virus infection (18,19). The NS2 protein is responsible for the nuclear export of viral RNPs (vRNPs) (20). For replication and transcription of viral RNA in the host cell nucleus, a heterotrimeric polymerase complex composed of PA, PB1 and PB2 is formed with the assistance of viral NPs. The heterotrimeric polymerase is bound to a short hairpin structure at the 3' and 5' untranslated regions (UTRs) of each RNA segment. PB1 is a RNA-dependent RNA polymerase (RdRp). PB2 functions in mRNA synthesis by binding host mRNA caps. These 7-methylguanylate caps (m^7G) are of great importance for stability and maturation of mRNA in eukaryotes. PA is necessary for a functional polymerase complex, including endonucleolytic cleavage of host RNAs (9). The polymerase complex lacks a proofreading activity resulting in a high gene mutation rate, which is a crucial evolutionary advantage of the influenza virus (21).

The next chapter provides a more detailed description of the function of the here mentioned viral proteins in the influenza virus life-cycle.

1.3.1.3 Influenza virus replication cycle

To ensure the survival of a virus, they have to transport the viral genome from an infected to an uninfected host cell. To express, replicate and spread the viral genome, viruses have evolved a variety of strategies during evolution dependent on their host range.

The influenza virus replication cycle, as depicted in Figure 4, starts with binding to cellular sialic acid receptors by the HA protein and subsequent membrane fusion (Figure 4a) in endosomal vesicles.

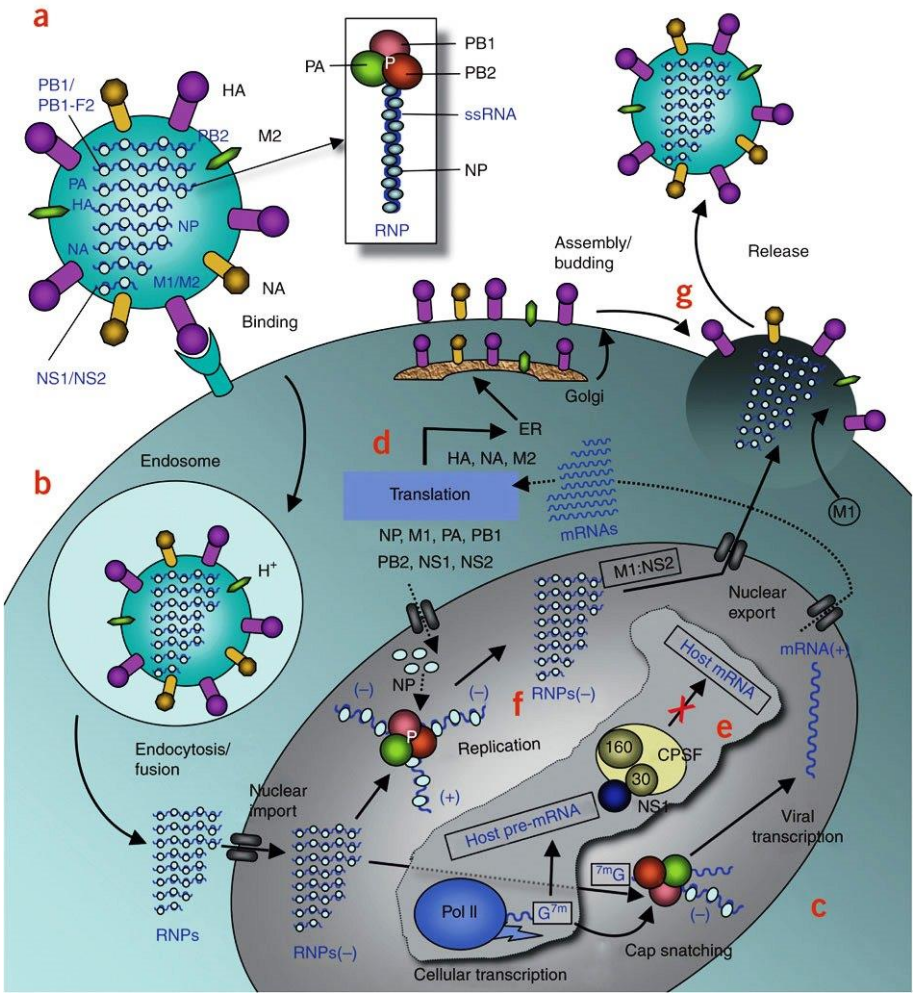

Figure 4: The IFAV replication cycle.

All the components participating in the IFAV life cycle are described in the text above. CPSF-Cleavage and polyadenylation specificity factor. Figure adapted from (22).

The three viral proteins PA, PB1 and PB2, together with viral NPs, form the vRNPs. Low endosomal pH triggers conformational rearrangements of HA and therefore the fusion with the endosomal membrane. The M2 protein additionally facilitates the influx of protons (H^+) into the virus and triggers dissociation of the M1 protein from the vRNPs (Figure 4b) (22). The vRNPs are released into the cytoplasm and transported into the nucleus initiated by the nuclear localization signals (NLS) on the NPs (23). In the nucleus, the viral mRNA synthesis is initiated by cleaved 5′-capped RNA fragments from host pre-mRNAs. The PB2 subunit of the polymerase binds to 5'-capped host pre-mRNA (24), and the endonuclease domain of PA cleaves the pre-mRNA 10-13 nucleotides downstream of the cap (25) (Figure 4c). The cleaved 3' end of the capped RNA segment is used for viral mRNA transcription (26). This 'cap snatching' occurs on nascent pre-mRNAs. After the viral mRNA is transported into the cytoplasm for translation of HA, NA and M2, these proteins are processed in the endoplasmic reticulum (ER) and glycosylated in the Golgi apparatus, and subsequently transported to the cell membrane (22) (Figure 4d). As a viral defense against the host cell, the NS1 protein suppresses the production of host mRNA (including interferon-β mRNAs) by inhibiting the 3'-end processing of host pre-mRNAs (27) (Figure 4e). Viral mRNA does not need to be 3'-end processed by the host cell machinery, in contrast to host pre-mRNA. Consequently, the viral mRNA (vRNA) is transported into the cytoplasm, while the host mRNA export and translation is inhibited (22). In addition to the capped RNA-primed mRNA synthesis, the viral polymerase also replicates the (unprimed) vRNA in the following steps: 1. (-)vRNA, 2. (+)copy(c)RNA, 3. (-)vRNA. For both replication steps, the NPs are necessary and are present on the vRNA and cRNA (28) (Figure 4f). The M2-NS2 complex mediates the export of vRNPs into the cytoplasm via a NS2-CRM1 (Exportin-1) interaction (20). The cellular vRNPs are incorporated into new viruses and bud off after reaching the cell membrane. The HA and NA proteins of the newly produced viruses carry terminal sialic acids. The NA cleaves theses moieties and release the virus from the cell surface (22) (Figure 4g). The newly generated virus particles are now ready to infect new host cells.

The Thogoto and Dhori virus are also members of the orthomyxovirus family and were subject of this doctoral thesis. They are introduced in more detail in the following chapter.

1.3.2 Thogoto- and Dhori virus

Like influenza A, B and C, Thogoto (THO) and Dhori (DHO) viruses belong to the family of *Orthomyxoviridae* (see also 1.3). DHOV is a member of the genus THOV (Figure 5). Both THOV and DHOV infect humans and livestock in Europe, Asia, and Africa. They represent a group of arboviruses, tick-borne viruses (transmitted by arthropod vectors) and show similar morphologic and genetic architecture compared to influenza. Both were first isolated in the 1960ies, THOV in the Thogoto forest near Nairobi, Kenya (29), and DHOV from *Hyalomma dromedarii* ticks, collected from camels in Dhori, Gujarat State, India (30).

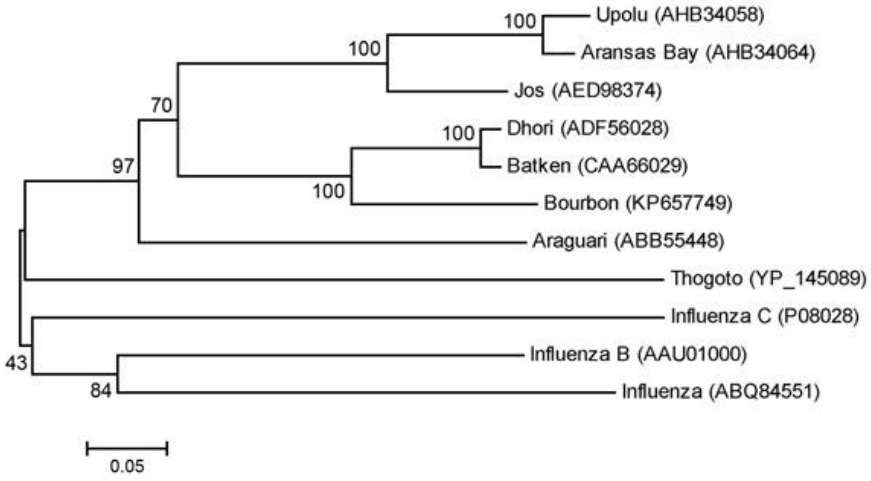

Figure 5: Phylogenetic tree of the genus THOV within the *Orthomyxoviridae* family.

A neighbor-joining method was applied with 2,000 bootstrap replicates for grouping analysis. Values at nodes are bootstrap values. GenBank accession numbers are in brackets. Scale bars indicate number of amino acid substitutions per site. Analysis was performed on the basis of the viral NP. Figure was adapted from (31).

THOV infection cause febrile illness and abortions in sheep. Humans infected with THOV show symptoms with involvement of the central nervous system such as meningitis and neuromyelitis optica. A laboratory accident in the 1980ies showed that DHOV can infect humans via the aerosol rout causing febrile illness and encephalitis (32). DHOV is highly pathogenic in mice and has been used as a model system for the influenza virus (33)

The genome of THOV has 6 segments of single-stranded, negative sense RNA, while that of DHOV comprises 7 segments. Both NPs are of similar size of around 52 kDa. RNA sequencing indicate that the ends of the RNAs are complementary, just as in influenza (34). Furthermore, the sequence of the heterotrimeric polymerase segments (PA, PB1 and PB2), and of the NP

segment of THOV and DHOV are similar to influenza as well (35). In contrary, the only glycoprotein of THOV and DHOV is unrelated to influenza but has sequence similarity to the baculovirus glycoprotein gp64, indicating an adaptation to the arthropod host (36).

In 2014, a new member was identified in the THOV genus, the bourbon virus, isolated from a man from Bourbon County, Kansas, USA, who became ill after being bitten by ticks, and subsequently died (31). It is the first known THOV to be associated with human disease in the United States and shows the importance of *Orthomyxoviridae* research.

The next chapter provides a structural overview of the previously mentioned NPs, from segmented negative-strand RNA viruses (sNSVs), which are essential for transcription and replication of the virus.

1.4 Structural overview of sNSV nucleoproteins (NPs)

Most viruses have RNA genomes that are replicated and transcribed into mRNA by a viral encoded RdRp. The RdRp catalyzes the replication of RNA from an RNA template. In contrast to the DNA-dependent RNA polymerase which catalyzes the transcription of RNA from a DNA template (reviewed in (1)). A prominent feature of (-)RNA genomes is that they are never free of proteins, e.g. they are always decorated with multiple copies of a nucleoprotein (NP) forming together with the polymerase the ribonucleoprotein particles (RNPs) (reviewed in (4)). The viral NPs are remarkable multifunctional in nature. Besides encapsulating RNA into RNPs for transcription and replication of the virus, they are able to discriminate between the viral RNA (vRNA) and viral mRNA or cellular RNA, to protect the viral genome from degradation and to avoid dsRNA formation. Interaction with viral or cellular proteins at the cytoplasmic surface of the plasma membrane promotes further packaging of these RNPs into infectious progeny virions (37).

Structural information regarding RNA-free NP and NP-RNA complexes of nsNSVs was obtained during the last years, including the families *Rhabdoviridae*, *Paramyxoviridae* and *Bornaviridae* (38-41). The RNA-bound NP structures of VSV and rabies virus provided first insights how RNA encapsulation is performed for nsNSRVs. Structural information has now also been extended to sNSVs from the families *Arenaviridae*, *Bunyaviridae* and *Orthomyxoviridae* (42-47). However, for the *Orthomyxoviridae* family, no RNA-bound NP

structures are available yet. Structural models of NPs can promote a functional understanding of these families. Hence, a brief structural overview of NPs from sNSVs is given in this chapter.

In the last few years, additional sNSV NP structures have become available (Figure 6). In contrast to nsNSV NPs, which all have a similar fold (4), sNSV NPs are structurally more diverse. Furthermore, three NP structures are now available from the *Orthomyxoviridae* family, including influenza A (44,45), B (46) and infectious salmon anaemia virus (47).

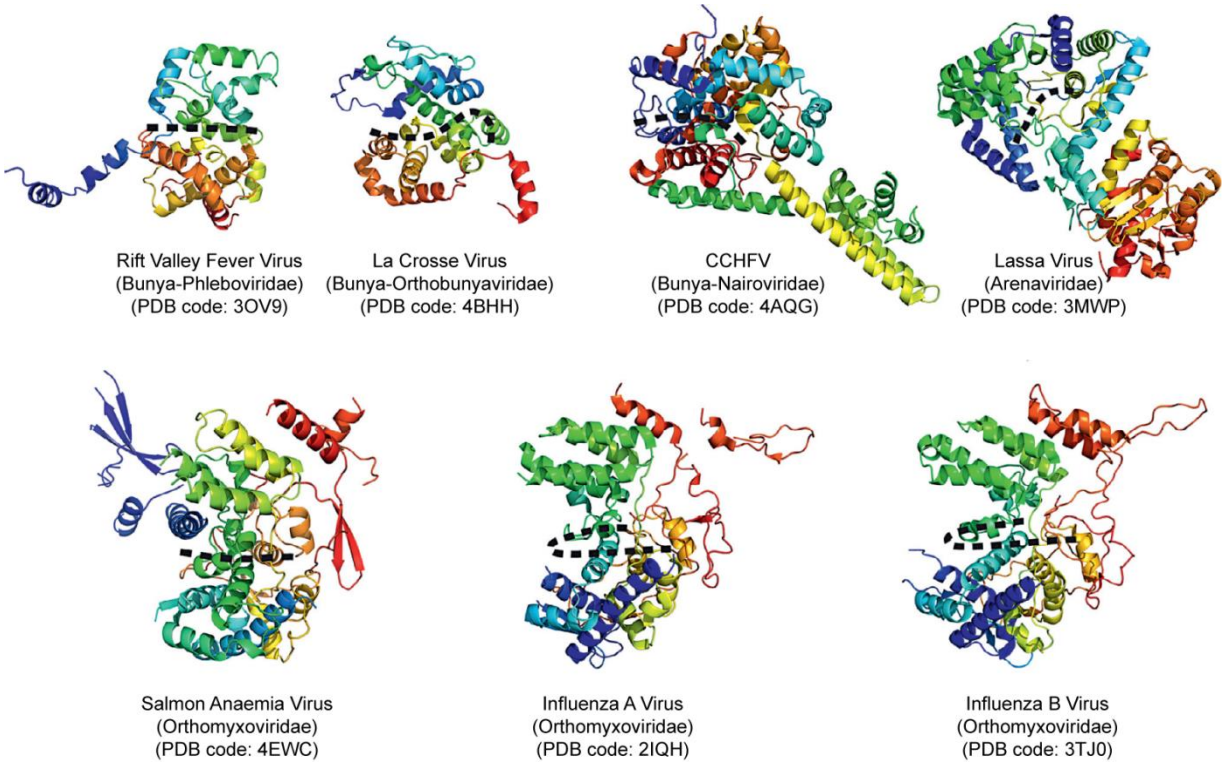

Figure 6: Structural comparison of sNSV NPs.

Crystal structures of sNSV NPs shown in cartoon representation. The polypeptide chain is colored according to the rainbow from the N- (blue) to the C-terminus (red). The black dotted line indicates the RNA-binding groove. Please note that the Lassa virus NP has an additional C-terminal domain with exoribonuclease activity involved in immune suppression (48). The N-terminus of influenza B and the infectious salmon anaemia virus NP is not involved in RNA binding (46,47). CCHF - crimean-congo hemorrhagic fever virus. Figure was adopted from (49).

The overall structure of these proteins is mainly α-helical and globular, containing a positively charged RNA-binding groove (indicated by the dashed lines in Figure 6) between an upper and lower lobe. All NPs have further extensions such as C-terminal and/or N-terminal arms (phlebovirus, orthobunyavirus), an internal/C-terminal tail loop (orthomyxoviruses), mobile

subdomains (CCHFV) or entire domains (Lassa virus), whose conformational flexibility regulates RNA binding and therefore RNP formation/assembly (49).

Crystal structures are available for monomers (IFAV NP, R416A (50), oligomers (RVFV, (51)) or oligomers in complex with RNA. Surprisingly, in the monomeric form, the RNA-binding groove is often filled by parts of the C-terminal tail loop (IFAV NP, R416A, Figure 7A) or by an N-terminal extension (RVFV) (Figure 7B). For Lassa virus, the RNA-binding groove is occupied by internal residues in the apo form; upon RNA binding, this auto-inhibited state is opened up, ready for assembly into RNPs (Figure 7C). In the auto-inhibited state, the NPs have a low RNA-binding affinity. In infected cells, the transition into the active, extended state of the RNP is probably facilitated by RNA binding (cooperativity) and/or polymerase interaction (49). Small RNAs can trigger NP oligomerization. However, NPs are also able to oligomerize without RNA since the apo forms of IFAV NPs crystallized as trimers (44,45), of IFBV NP as tetramer (46) and of ISAV NP as a dimer (47). A functional role of these small oligomers *in vivo* is still under debate.

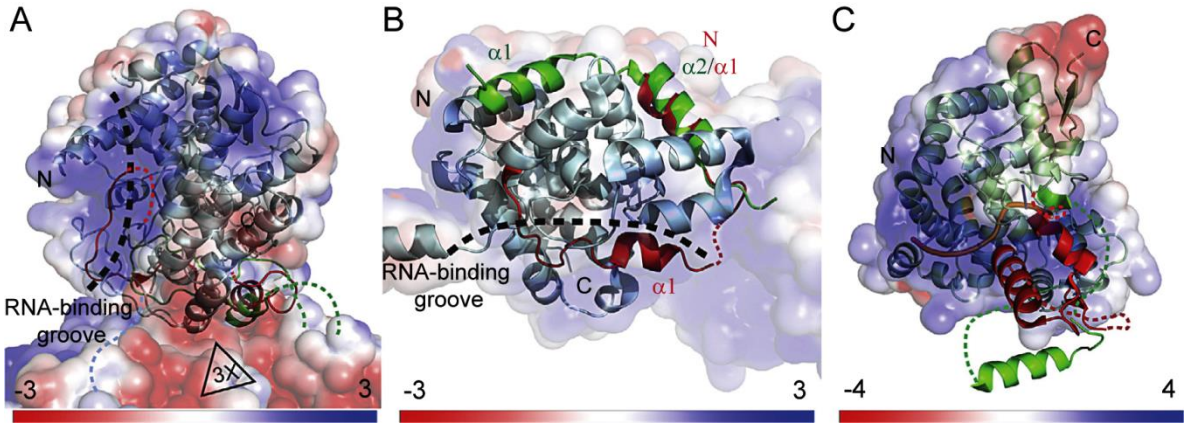

Figure 7: Gating mechanism of sNSV NP-RNA binding coupled to RNP assembly.

(A) Orthomyxoviruses: The monomeric (PDB code: 3ZDP) H1N1 NP structure is shown in cyan (cartoon representation), and the trimeric (PDB code: 2IQH) structure was superimposed and is shown in surface representation (indicated by 3X). In the trimeric structure, the C-terminal tail loop (green dashed line, residues 394-429) is protruding into the neighboring protomer, whereas in the monomer, parts of the tail loop is blocking the RNA-binding groove (red dashed line). (B) Bunyaviruses (phlebovirus): Same representation like in (A). In the hexameric structure (PDB code: 30V9), the N-terminal arm (in green) binds above the RNA-binding site. However, in the monomeric structure the N-terminal arm blocks the RNA-binding groove with helix α1 (in red). (C) Arenaviruses: Same representation like in A and B. The complete Lassa virus NP in the apo form (PDB code: 3T5Q) shows an internal region (in red, residues 115-163) occupying the RNA-binding groove. Upon binding to RNA (PDB code: 3T5Q, in cartoon), these residues open up (in green, residues 115-163) allowing the NP further to assemble into RNPs. The electrostatic surface is indicated by its scale values in k_BT at the bottom for each panel, and the putative RNA-binding groove is indicated by the dashed line. The figure was modified from (49)

The nucleocapsids (Ns) of the Mononegavirales (nsNSVs) order are long, flexible and helical oligomeric structures, whereas RNPs of sNSVs mainly form irregular, flexible, supercoiled structures (Figure 8). Recent crystal structures showed that the arms/tail of the N proteins of nsNSVs, which mediate oligomerization, are less flexible compared to the hinges in the arms of NPs of sNSVs. Structural differences between nsNSV and sNSV NP assemblies can thus be explained in large part by the flexibility of the terminal arms that mediates their oligomerization (reviewed in (4)).

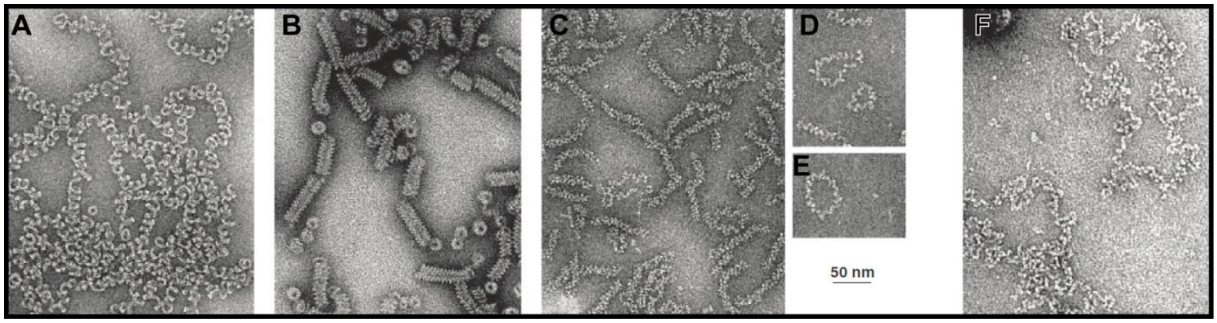

Figure 8: Negatively stained electron micrographs of NSVs nucleocapsids/RNPs.

Nucleocapsids and RNPs isolated from rabies virus (A), measles virus (B), influenza (C, D, E) and rift valley fever virus (F). The measles nucleocapsids (B) were produced recombinantly. C is prepared at 150 mM NaCl, whereas D and E was prepared at 15 mM NaCl. All images have the same magnification shown under E. Figure was modified from (4).

Recently, native and recombinant RNPs of Influenza virus were visualized using cryo-EM (52,53). The ~20 Å resolution structure of recombinant Influenza virus RNPs from Moeller et al. (Figure 9A) established a double-helical model with two antiparallel strands leading away and to the polymerase, which is located at one end of the RNP. A loop-region is located at the other end. The double-helical stem region has 4.9 NPs per turn and a rise of 32.6 Å between two neighboring NPs (Figure 9A). In contrast, Arranz et al. visualized native RNPs at 18 Å resolution with a rise step per monomer of 28.4 Å and a rotation angle of -57° to -64°, forming helical RNPs with approximately 12 NPs per turn (Figure 9B). However, in both RNPs, the NPs are arranged in a twisted and antiparallel fashion. It should be noted that Arranz et al. proposed a left-handed helix where the body domain of NP mainly facilitates the inter-protomer interaction, while Moeller et al. proposed a right-handed helix where the head domain of NP is likely to stabilize the RNP via inter-NP contacts.

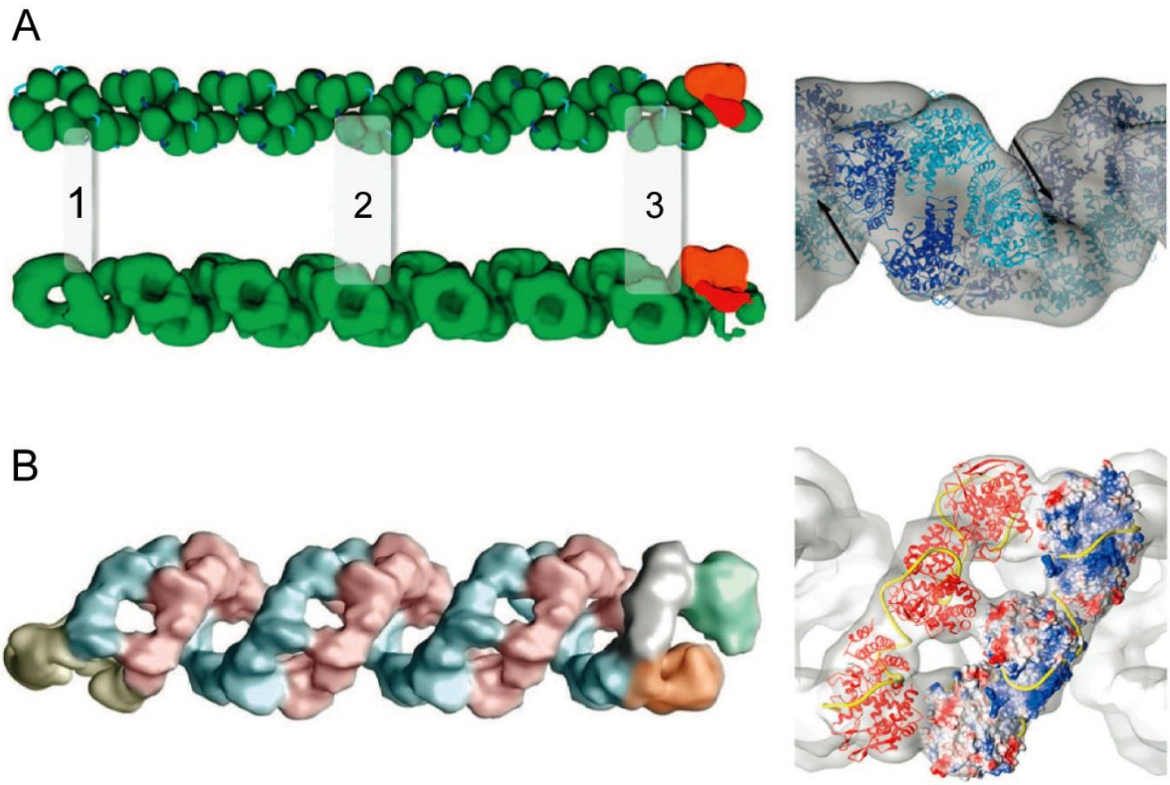

Figure 9: Molecular architecture of IFAV RNPs.

(A) Cryo-EM reconstruction of recombinant RNP (53). The heterotrimeric polymerase (PA, PB1, PB2) is shown in red, NPs in green and RNA in blue. The NP protomer is fitted into the EM map on the right panel. The NP strands are antiparallel, as indicated by the arrows. 1. Looped-end, 2. Central filament region, 3. RNA-polymerase end. (B) Cryo-EM reconstruction of a native RNP (52). The heterotrimeric polymerase (PA, PB1, PB2) is shown in orange and green, and is located at the right end. The two opposite-running NP–RNA strands are colored in blue and pink, respectively. The NP and RNA (yellow) are fitted into the EM map on the right panel. The NP strands are antiparallel as indicated by the arrows (upper right image). Figure was modified from (52) and (53).

1.5 Innate immune response against viruses

The recognition of pathogenic/viral patterns in mammalian cells is a prerequisite for a rapid and effective defense response. These pathogenic associated molecular patterns (PAMPSs) include single-stranded and double stranded viral nucleic acids. Host specific pattern-recognition receptors (PRRs) detect these PAMPs in the cytoplasm and within endosomes (54,55). Five classes are now known to play a role in detecting these components: 1. A family of transmembrane proteins named Toll-like receptors (TLRs, specially TLR3, TLR7, TLR8 and TLR9), 2. Retinoic acid-inducible gene I (RIG-I)-like receptors (RLRs, such as melanoma differentiation-associated gene 5 (MDA5) and retinoic acid-inducible gene I (RIG-I)), 3. Nucleotide-binding and oligomerization leucine-rich proteins (NLRs), 4. Absent in melanoma

2 (AIM2-) like receptors and 5. DNA sensors (DNA-dependent activator of IRFs (DAI), IFNγ-inducible protein 16 (IFI16), DEAH box protein 9 (DHX9), DHX36, DDX41, and cGAS-STING (Cyclic GMP-AMP synthase-Stimulator of IFN genes) (56,57). Interestingly, different RNA viruses are recognized by different RLRs. RIG-I for example is responsible for detecting *Paramyxoviridae*, *Orthomyxoviridae*, *Rhabdoviridae*, and some *Flaviviridae* family members. MDA5 however, recognizes *Picornaviridae* family members. The West Nile virus and Reovirus are detected by both RIG-I and MDA5 (58).

Binding of these PRRs to PAMPs activates a downstream cascade, triggers the expression of virus-response genes and pro-inflammatory cytokines (like type I interferons (IFNs), IL1β, IL18) and restricts viral replication (Figure 10). The IFNα/β receptor (IFNAR), a heterodimer composed of IFNAR1 and IFNAR2, activates the type I IFN signaling (59). Upon type I IFN binding to IFNAR, signal transduction via the Janus kinase (JAK) and signal transducer and activator of transcription (STAT) proteins takes place, resulting in nuclear translocation of the transcription factor complex IFN-stimulated gene factor 3 (ISGF3; composed of IFN-regulatory factor 9 (IRF9) and phosphorylated STAT1 and STAT2). As a consequence, hundreds of IFN-stimulated genes (ISGs) are activated (60,61). Among these genes are the protein kinase R, the 2'5'-oligoadenylate synthase, IFN-induced proteins with tetratricopeptide repeats (IFIT), IFN-induced transmembrane (IFITM) proteins (55), Immunity-related GTPases (IRGs, also known as p47 GTPases) (56), guanylate binding proteins (GBPs) (56), SAM domain and HD domain-containing protein 1 (SAMHD1) (62) or antiviral Mx proteins. The expressed proteins restrict the invaders at different stages including entry into host cells, protein translation, replication, assembly of new virus particles and spread. Investigating the antiviral mechanism of the IFN-induced Mx proteins was part of the present work, therefore a more detailed description of these proteins is given in the next chapters.

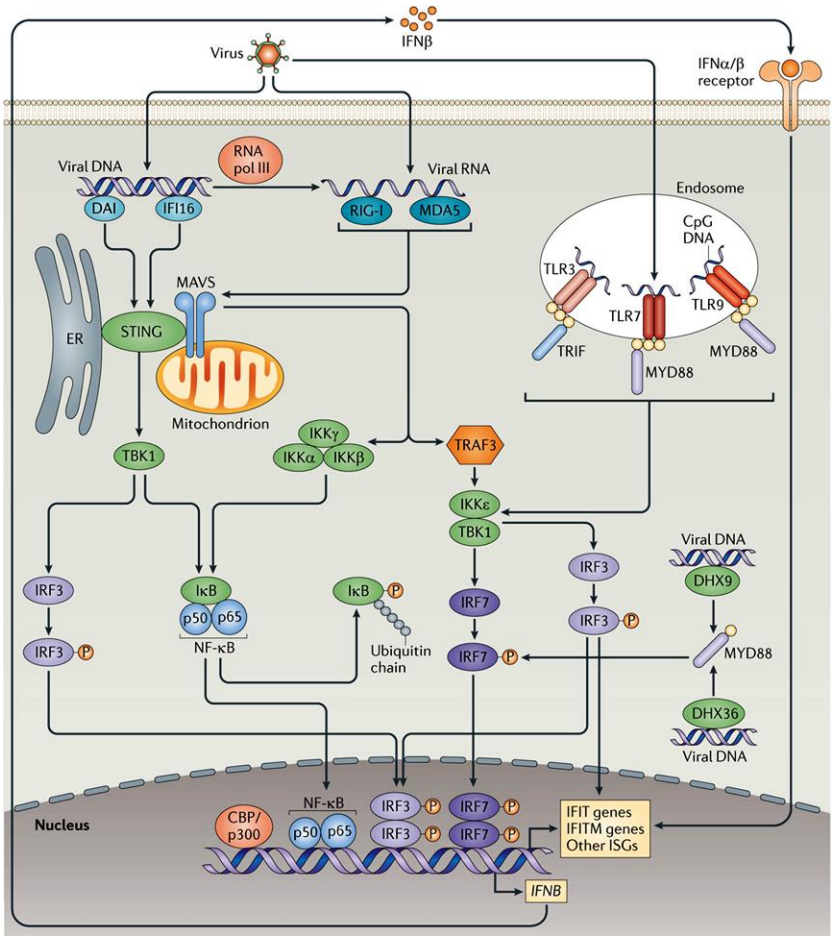

Figure 10: Pathogenic RNA and DNA detection in mammalian cells.

DNA is found in the cytoplasm and in endosomes during viral or bacterial infection or after the phagocytosis of dead cells. Upon viral infection, cytosolic DNA sensors, such as DNA-dependent activator of IRFs (DAI), IFNγ-inducible protein 16 (IFI16), DEAH box protein 9 (DHX9) and DHX36 recognize viral DNA such as CpG-A and CpG-B DNA in the cytosol and trigger the MYD88- and IRF7-dependent response. DNA binding by cGAS, DAI or IFI16 results in stimulator of IFN genes (STING)-dependent activation of IRF3 and NF-κB. The RNA polymerase III transcribes this DNA to generate short RNAs containing a 5′-ppp motif, which are ligands for RIG-I. Additionally, endosomal receptors such as the Toll-like receptors (TLRs), including TLR3, TLR7 and TLR9 (recognize CpG DNA) detect viral DNA within the endosomal membrane. Viral RNA is recognized by cytosolic RIG-I-like receptors (RLRs), such as melanoma differentiation-associated gene 5 (MDA5, recognizes long dsRNA) and retinoic acid-inducible gene I (RIG-I). The interaction of RLRs with mitochondrial antiviral signaling protein (MAVS) recruits the TANK-binding kinase 1 (TBK1) and IκB kinase-ε (IKKε), or the IKKγ (also named NEMO), IKKα and IKKβ, which results in the activation of IFN-regulatory factor 3 (IRF3) and nuclear translocation of nuclear factor-κB (NF-κB). The adaptor proteins TRIF and MYD88 interact with TLRs at endosomal membranes, leading to the activation of IRF3 or IRF7. Activated IRF3, IRF7 and NF-κB bind to the interferon-β (IFNB) promoter inducing transcription. The secreted IFNβ binds to the IFNα/β receptor leading to paracrine type I IFN signaling, which induces hundreds of IFN-stimulated genes (ISGs). Phosphorylated IRF3 can independently transcribe IFIT and IFITM genes without IFN signaling. IκB, NF-κB inhibitor. Figure was adapted from (56).

1.6 Mx proteins in innate immune system

1.6.1 Historical introduction of MxA

Mx proteins are key mediators of the IFN-induced innate antiviral response in vertebrates (63). In 1962, Jean Lindenmann discovered that the inbred mouse strain A2G is resistant to influenza virus doses that are lethal to other inbred strains (64). After this initial observation, he later showed that this innate resistance in A2G mice was linked to only one single dominant locus. He named it the myxovirus resistance (Mx)-gene, due to the resistance of the mice to orthomyxoviruses (64). This gene was expressed in a variety of cells ranging from macrophages to hepatocytes (64). Later it was shown that Mx-mediated virus-resistance was induced by type I (α/β) and type III (λ) interferons (IFNs) (65). After virus infection, the murine Mx1 protein is rapidly expressed in the nuclei of cells where virus replication occurs and blocks viral spread (66). Soon, it was revealed that Mx1 was the first member of a small gene family present in all vertebrate species (Figure 11) (67).

In the late 1980s, a second murine Mx protein was identified and named Mx2 (68). Mx2 is localized in the cytoplasm and has no antiviral activity against influenza virus (69). The human Mx-genes are named Mx1 and Mx2 which code for MxA and MxB protein, respectively. Recently, it was shown that the human MxB protein restricts (IFN-α-mediated) the human immunodeficiency virus type-I (HIV-1) and other primate lentiviruses but not orthomyxoviruses (70-72).

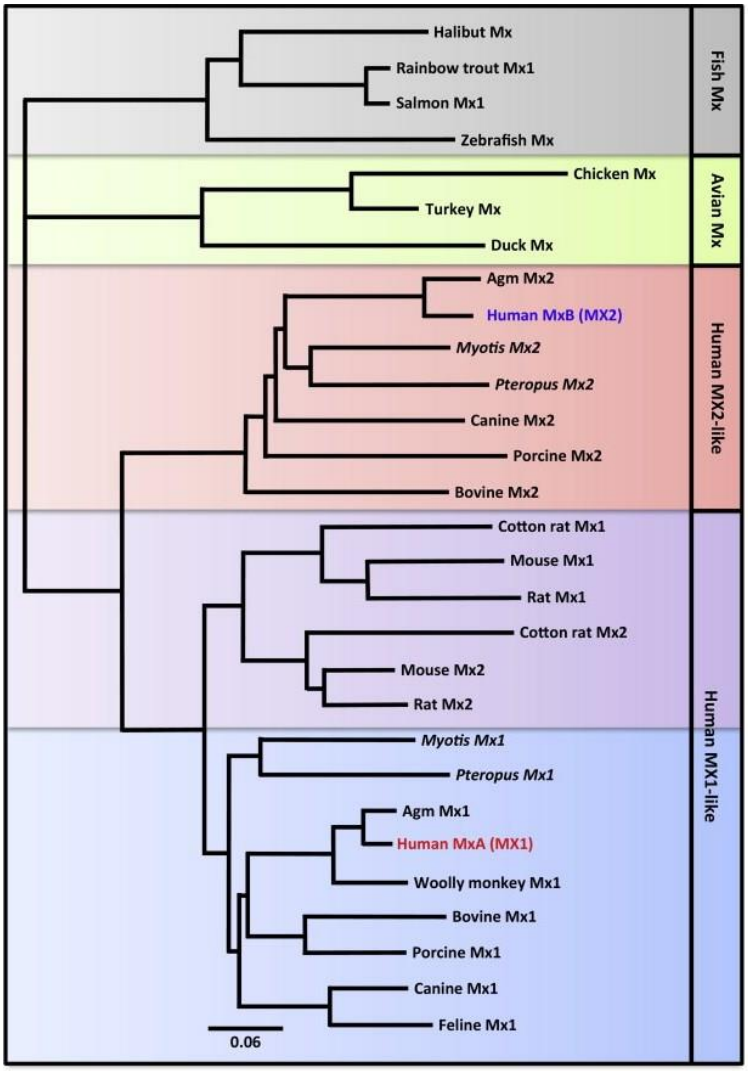

Figure 11: Phylogenetic tree of Mx proteins.

Currently known vertebrate Mx proteins can be classified into five subgroups according to sequence similarities: Scale bar represents genetic distance (amino acid substitutions per site). The following sequences were used for the alignment: African green monkey (agm) Mx1 (73), agm Mx2 (KJ650325), bovine Mx1 (P79135), bovine Mx2 (AF355147), canine Mx1 (AAF44684), canine Mx2 (AF239824), chicken Mx (Q90597), cotton rat Mx1 (DQ218274), cotton rat Mx2 (DQ218273), duck Mx (P33238), equine Mx1 (Q28379), equine Mx2 (XP_001491517), feline Mx1 (XM_006935878), halibut Mx (AAF66055), human MxA (A33481), human MxB (M30818), mouse Mx1 (NP_034976), mouse Mx2 (NP_038634), *Myotis davidii* Mx1 (XM_006754325), *Myotis* Mx2 (XM_006754324), porcine Mx1 (P27594), porcine Mx2 (AB258432), *Pteropus alecto* Mx1 (XM_006916729), *Pteropus* Mx2 (XM_006916730), rainbow trout Mx1 (AAA87839), rat Mx1 (NP_775119), rat Mx2 (NP_599177), salmon Mx (NP_001117165), turkey Mx (EF575607, partial sequence), woolly monkey Mx1 (JX297236), and zebrafish Mx (AF533769). Figure was adopted from (74).

1.6.2 Structural overview of Mx proteins

Mx proteins are large GTPases and sequence alignment indicates they belong to the dynamin superfamily, a class of mechano-chemical enzymes which are responsible for nucleotide-dependent membrane remodelling (63). Human MxA assembles into tetramers, shows low affinity binding to guanine nucleotides, concentration-dependent oligomerization and assembly-stimulated GTPase activation comparable to dynamins (75,76). Mx proteins are composed of an N-terminal GTPase (G) domain, a middle domain (MD), and a C-terminal GTPase effector domain (GED) but they are lacking the pleckstrin homology (PH) and prolin-rich domain present in dynamin (63) (Figure 12).

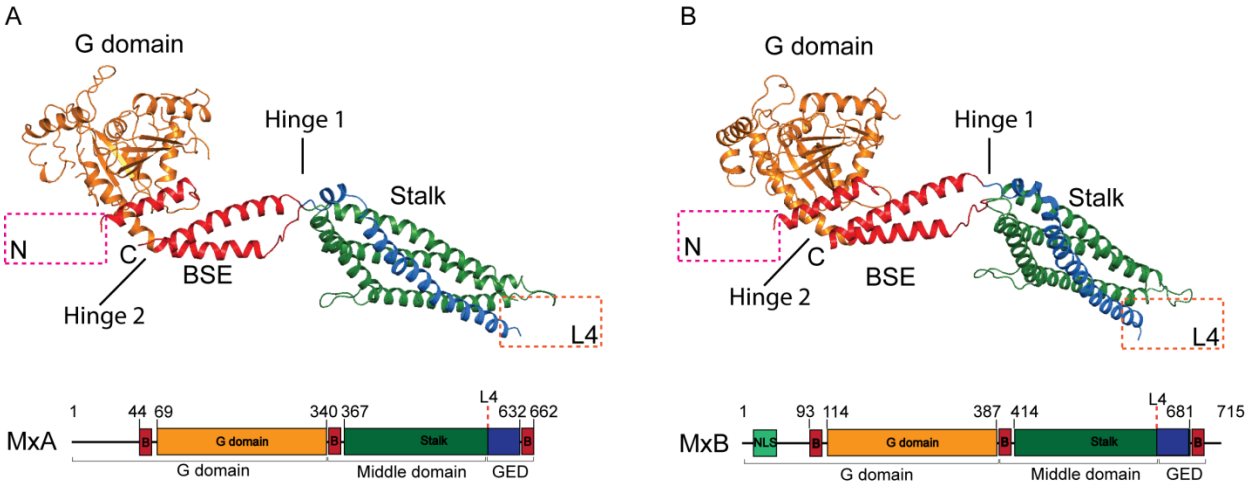

Figure 12: Structure of human Mx GTPases.

Structure-based domain and ribbon-type representation of MxA (A, PDB code: 3SZR) and MxB (B, PDB code: 4WHJ) monomers. The N- and C-termini are labelled. The unresolved loop L4 in the stalk is indicated by an orange box, and the flexible N-terminus indicated by a purple box. BSE: Bundle signalling element.

The crystal structure of nucleotide-free MxA shows an extended three-domain architecture (75,76). The globular G domain at one end of the molecule consists of six β-sheets surrounded by α-helices. The G domain is connected to the stalk built as a four-helix bundle (consisting of MD and GED). The connection between G domain and stalk is mediated by a bundle signalling element (BSE) which forms an extended structure in the center of the MxA molecule. It is composed of three helices, which are derived from widely dispersed sequence regions of MxA, and thus serves as an ideal sensor of transmitting the conformational changes from GTP binding and hydrolysis to the stalk (77). Hinge 1 and 2 at the flanking ends of the BSE provide

flexibility, and conformational freedom. Beside the stalk, which is the central oligomerization interface, the BSE plays also a crucial role in stabilizing oligomer formation (stalk-BSE interface) (75,76). The 40 amino acid long loop L4 (amino acid 533-572), located at the tip of the molecule (Figure 12A, indicated by the orange dashed box) comparable to the location of the PH domain of dynamin, binds negatively charged liposomes and mediates viral target recognition (73,78,79). Human MxB shares 63% sequence identity with MxA. Recently, also the crystal structure of human MxB was solved (Figure 12B) and shows a very similar overall fold except of the N-terminal flexible extension (Figure 12), indicated by the purple dashed box), comprising the NLS of MxB (80,81).

1.6.2.1 The GTPase domain

The GTPase (G) domain of the dynamin superfamily members including Mx proteins is the catalytic heart, generating the power required to perform its biological function. The G domain is the most conserved domain among dynamin homologs, and MxA shares 40% sequence identity to other dynamin superfamily members (82). Dynamin-related GTPases are characterized by low nucleotide affinities, and a low basal GTPase activity (63). For example the GTPase activity was experimentally determined to be around 1-5 min^{-1} for dynamin, MxA and hGBP1 at 37°C (75,83,84). Therefore, these proteins do not require any nucleotide exchange factors like small GTPases of the Ras superfamily. Comparable to Ras-like GTPases, large G proteins comprises five motifs in the GTPase domain (G1-G5) for nucleotide binding (85). The G1 motif or P-loop (phosphate-binding loop, consensus: GxxxxGKS/T) in close proximity to the β-phosphate of the bound nucleotide stabilize a crucial Mg^{2+} with the serine/threonine residue, important for GTP hydrolysis. A threonine from G2 together with an aspartate from G3 (consensus: DxxG) participates in Mg^{2+} coordination and additionally contacts the γ-phosphate. GTP and GDP are differentially coordinated in G2 and G3, leading to nucleotide-induced conformational changes in the surrounding regions. They are accordingly named switch I and switch II, respectively. A guanine base specific aspartate is found in the N/TKxD consensus of the G4 motif. Finally, the G5 motif interacts via several contacts with the guanine base and/or ribose.

1.6.2.2 Functional role of G domain dimerization

In contrast to small G proteins which regulate cellular signaling events, for example the Ras superfamily, large G proteins such as dynamin superfamily members are involved in cellular trafficking of vesicles, remodeling of cellular membranes or participate in antiviral defense mechanisms in a mechano-chemical fashion (reviewed in (86)).

Most G proteins display an intrinsically slow GTPase rate, which can be greatly stimulated by interaction with so called GTPase activating proteins (GAPs), like it is the case for small G proteins. In the context of the hetero-dimeric complexes together with the G protein, GAPs provide residues to stabilize regions within the catalytic center of small G proteins including flexible loops (switch regions) or the nucleotide itself (reviewed in (86)).

In contrast, large G proteins carry all elements that are required for GTPase activation and stabilization of active site residues internally in the G domain (87). Accordingly, large G proteins are known to activate themselves by homo-dimerization of their G domains. Activation of the GTP hydrolysis is achieved by stabilizing the flexible switch regions containing residues crucial for catalysis (Figure 13). As a consequence, the GTPase activity is greatly enhanced (87). Head-to-head homo-dimerization in dynamin, dynamin-1-like protein (DNM1L) and MxA G domains is mediated by a highly conserved interface across the nucleotide-binding site, the so-called G interface (77,88,89) (Figure 13).

Subsequently, GTP hydrolysis triggers a large scale conformational movement of the adjacent BSE domain, as shown for dynamin and MxA (77,88), that may act as a power stroke required for the cellular function of dynamin and MxA.

The understanding of the molecular basis for G domain dimerization and the functional consequences have been studied for a variety of GTPase in the last years, and some of them are briefly introduced in the following.

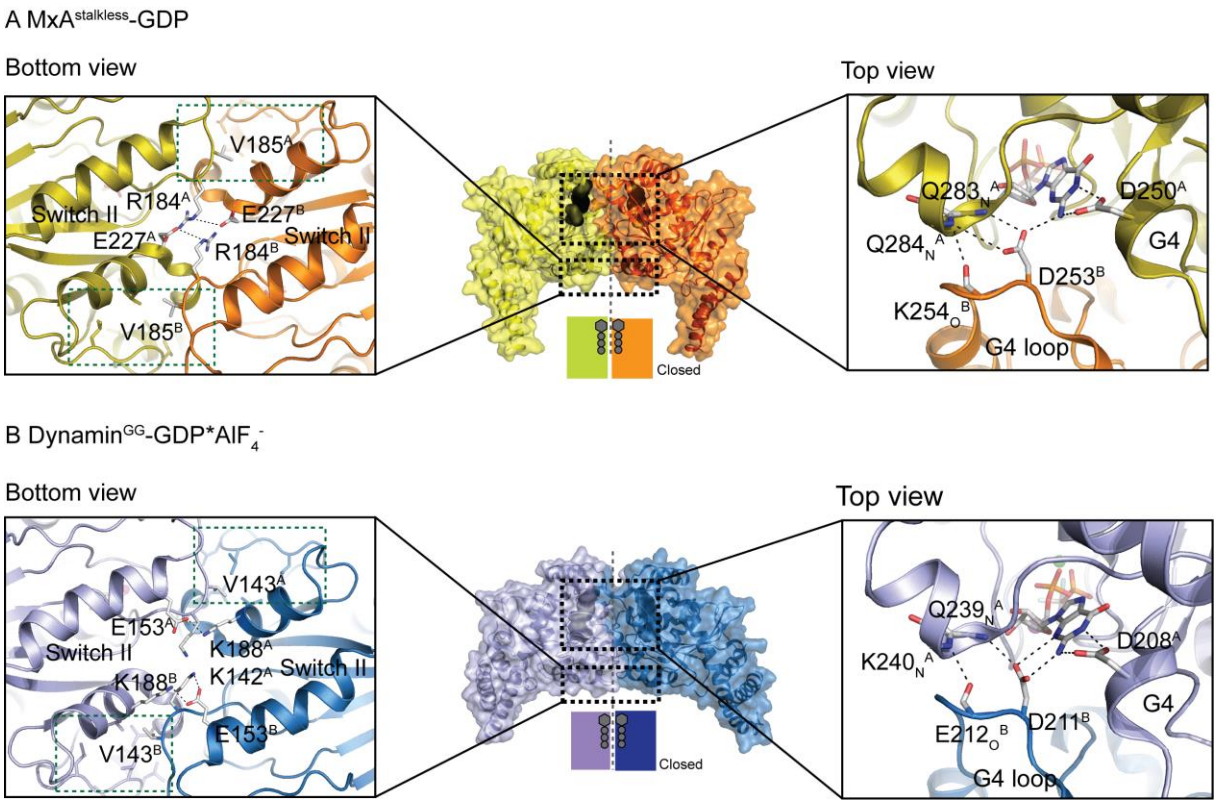

Figure 13: Dimerization-dependent GTPase activation of MxA and dynamin.

(A) GDP-bound homo-dimeric structure of a stalkless MxA construct (77) (PDB code: 4P4T) and the stabilizing G interface contacts viewed from the top and bottom. (B) GDP-AlF_4^--bound homo-dimeric structure of a G domain minimal BSE construct of dynamin 1 (88) (PDB code: 2X2F) and the stabilizing G interface contacts in the same views as (A). The additional subscript (O or N) represent the interaction of a main chain carbonyl or nitrogen, and the superscript signifies the respective G domain protomers. Dashed lines indicate hydrogen-bonds.

For the antiviral MxA protein, for example, the observed assembly and tubulation of lipids (78) led to a model where MxA forms rings around viral target structures (90). In this model, the G domains dimerize across adjacent rings, thereby mediating inter-ring contacts via the G interface (75,76). However, the visualization of these structures is experimentally challenging and has not been achieved to date. Similarly, the G domains in dynamin are thought to dimerize across helical turns formed around lipid tubes (88). Dynamin was shown to have a stalk-mediated assembly on the neck of clathrin-coated vesicles (91). The assembled GTP-bound G domains dimerize across adjacent helical turns and the power stroke during GTP hydrolysis may result in a sliding mechanism of the adjacent filaments, leading to constriction of the membrane template (92).

The dynamin G domain, fused to a truncated version of the BSE (GTPase-GED (GG) fusion) was crystallized in the presence of the GTP hydrolysis transition state mimic GDP-AlF_4^- (88) (Figure 13B). The structure revealed the catalytic machinery of both basal and assembly-stimulated GTPase activities of dynamin 1. Extensive interactions across the dimer interface

were found to stabilize the artificial GG dimer, including dual coordination of the guanine base in *cis* and in *trans* by the G4 loop (residues 205–216) which contains the conserved G4 element (^{205}TKLD^{208}). The G4 element imparts nucleotide specificity via Asp208 interactions with the guanine base in *cis*, and upon dimerization Asp211 from the adjacent monomer form additional hydrogen bonds with the guanine base in *trans*. Furthermore, additional *cis*- and *trans*-stabilizing loops are used for stabilization of the GG dimer. In contrast to small G proteins, dynamin 1 contains a Na^+ to neutralize the negative charge arising between the β- and γ-phosphate oxygen during catalysis. A similar head-to head dimerization mode was also observed for septin GTPases (93) and septin-related GTPases, such as immunity-associated proteins (GIMAPs) (94).

Similarly to dynamin, a truncated LG domain (Large GTPase domain) construct of the IFN-induced antiviral guanylate-binding protein-1 (hGBP-1) crystallized in the presence of GDP-AlF_3 in a head-to-head fashion (Figure 14A) (84).

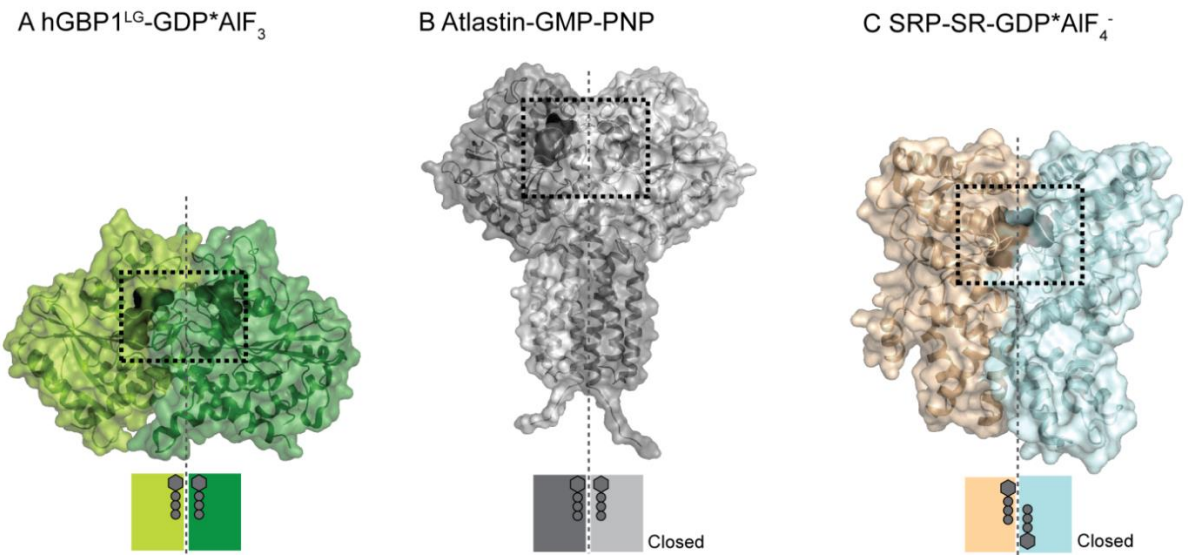

Figure 14: G domain dimerization of dynamin related GTPases and the SRP receptor.

(A) The GDP-AlF_3-bound LG domain dimer of hGBP1 (84) (PDB code: 2B92). (B) Structure of atlastin bound to GMP-PNP (95) (PDB code: 4IDP). (C) The GDP-AlF_4^--bound dimeric structure of the SRP-SR GTPases Ffh and FtsY (96) (PDB code: 2CNW). Note that the SRP-SR structure dimerizes in a head-to-tail fashion.

The resulting G interface involves the P-loop, the two switch regions which are stabilized in the dimer, and other loop regions, including the G4-loop contacting the guanine base in *trans*.

Atlastins are GTPases involved in the fusion of ER tubules in higher eukaryotes and which are closely related to the GBPs, tethering of opposing ER tubules may be facilitated by G domain dimerization as well (97,98). An atlastin 1 construct, including the G domain and the three helix bundle, showed a similar head-to-head dimerization via the G interface when bound to GMPPNP (95) (Figure 14B). Both G domains provide an 'arginine finger' (Arg48 in hGBP 1 and Arg77 in atlastin 1) from the P-loop into the active site to neutralize the negative charge occurring at the β- and γ-phosphate oxygen in the transition state.
Besides the above introduced head-to-head association of the G domain, also the signal recognition particle (SRP) GTPase dimerizes via the SRP receptor (SR) GTPase during cotranslational targeting of proteins to the membrane (96,99) (Figure 14C). Here, two members of this protein family dimerize in a head-to-tail style, leading to activation of their GTPase machineries. The bacterial homologs Ffh and FtsY face each other with their nucleotides bound in an antiparallel orientation within the G domains. Using mutants with nucleotide specificity altered from GTP to xanthosine 5'-triphosphate (XTP), Egea and colleagues proved that G domain dimerization is an essential step in activating the entire GTPase machinery (96,99).

In addition to the GTPase-derived energy generation within the G domain, the formation of high-order assemblies is a crucial step in performing antiviral function of the human MxA protein (75,76). Beside the main oligomerization interface within the stalk, a second interface between stalk and BSE plays a central role in oligomer formation. The next chapter gives a brief description of these two interfaces.

1.6.2.3 Oligomerization via the stalk

In the crystal structures of the full-length MxA (76) as well as in the isolated stalk (75), each monomer is assembled in a criss-cross pattern with three distinct interaction sites (Figure 15). Within this arrangement, all G domains are located on one side of the oligomer, whereas the putative membrane or virus binding sites loop L4 is located on the opposite side. The symmetric interface 2 in the centre of the stalks is responsible for MxA dimerization mainly by hydrophobic interactions (Figure 15A), whereas interface 1 and interface 3 (including loop L2) mediate contacts between MxA dimers during the formation of tetramers and higher oligomers.

In addition to these central interfaces within the stalk, the BSE interacts with the stalk of an adjacent parallel MxA monomer via a number of polar interactions (Figure 15B). Mutations within the stalk-BSE interface result in increased GTPase activity, and interfere with the antiviral activity, indicating a role of controlling the GTPase activity and antiviral function of MxA (76).

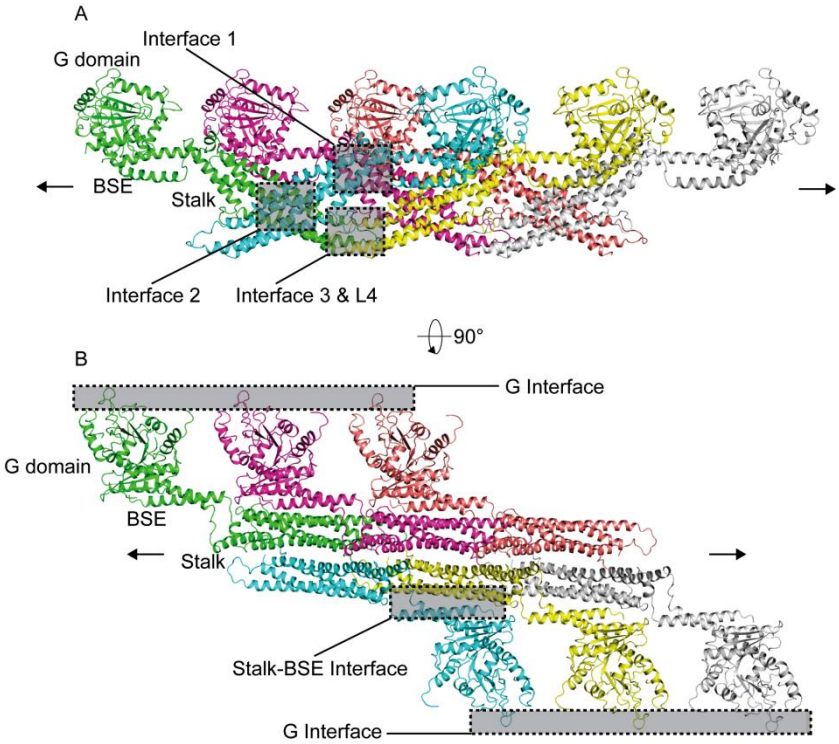

Figure 15: Oligomerization interfaces of MxA.

(A) Side view of an MxA filament represented by six monomers. The oligomerization interfaces are highlighted in grey boxes (B) Putative G domain-G domain dimerization sites (G interfaces) and intermolecular interactions between stalk and the BSE of two parallel monomers are highlighted in grey boxes.

1.6.3 Antiviral mechanism of MxA and MxB

Upon expression, different Mx proteins associate at distinct intracellular sites, and their antiviral function is influenced to some extent by their localization (Table 1) (74). It was shown that cytoplasmic Mx proteins transiently associate with intracellular membranes, e.g. with coat protein I (COPI)-positive membranes of the smooth endoplasmic reticulum (sER)/Golgi-intermediate compartment (100,101). A lysine-rich stretch in loop L4 of MxA was shown to contact negatively-charged lipids, leading to oligomerization and liposomes tubulation (78).

Membrane binding of Mx proteins may be an important feature for inhibiting viruses that replicate on membrane sites, such as bunyaviruses, positive-strand RNA viruses, the African swine fever virus (double-stranded DNA virus, ASFV), and poxviruses (102-104). Membrane binding could also stabilize intracellular Mx pools after IFN induction, and protect them from degradation (105). It may also have general functions, such as intracellular protein transport and sorting, as shown for MxB's involvement in regulating nucleocytoplasmic transport and cell-cycle progression (106). However, the physiological role of membrane binding is still not fully clear to date.

Mx protein	Localization	Virus	Virus family	Reference
Human MxA	Cytoplasm	THOV, IFAV	*Orthomyxoviridae*	(107-110)
		LACV, RVFV, Hantaan virus	*Bunyaviridae*	(111,112)
		Puumala virus, Tula virus,		(113,114)
		Dugbe virus, Crimean-Congo hemorrhagic fever virus		(114,115)
		VSV	*Rhabdoviridae*	(110,116)
		Measles virus,	*Paramyxoviridae*	(117)
		Human parainfluenza virus		(118)
		Coxsackievirus B	*Picornaviridae*	(119)
		SFV	*Togaviridae*	(120)
		Reovirus	*Reoviridae*	(121)
		HBV	*Hepadnaviridae*	(122,123)
		ASFV	*Asfarviridae*	(103)
		Monkey pox virus	*Poxviridae*	(102)
Human MxB (78 kDa)	Nuclear pore	HIV-1	*Retroviridae*	(70-72)
Human MxB (76 kDa)	Cytoplasm	-	-	
Mouse Mx1	Nucleus	THOV, DHOV, IFAV, BKNV	*Orthomyxoviridae*	(67,124-127)
Mouse Mx2	Cytoplasm	VSV	*Rhabdoviridae*	(128,129)
		Hantaan virus	*Bunyaviridae*	(128)

Table 1: Antiviral profile and localization of human and mouse Mx proteins.

SFV: Semliki forest virus, ASFV: African swine fever virus. Table was modified from (74).

Mx proteins have a broad antiviral activity as shown in Table 1, and they block viruses at different steps in their life cycle (Figure 16). The antiviral activity of mouse and human

Mx1/MxA strongly depends on (1) GTP binding and hydrolysis, (2) an intact bundle signaling element (BSE), and (3) oligomerization via the stalk (75,76,130,131). In contrast, inhibition of the hepatitis B virus by human MxA does not require GTPase activity (122). Comparison of simian MxA orthologs revealed that the loop L4 was subject to strong positive selection during primate evolution, in addition to 'hot spots' at the flexible N-terminus (73). The C-terminal part of the loop L4 was shown to be a major antiviral specificity determinant; in particular Phe561 differentially determined antiviral activity against orthomyxoviruses: Swapping loop L4 between Mx proteins demonstrated its central role for antiviral activity (73,79).

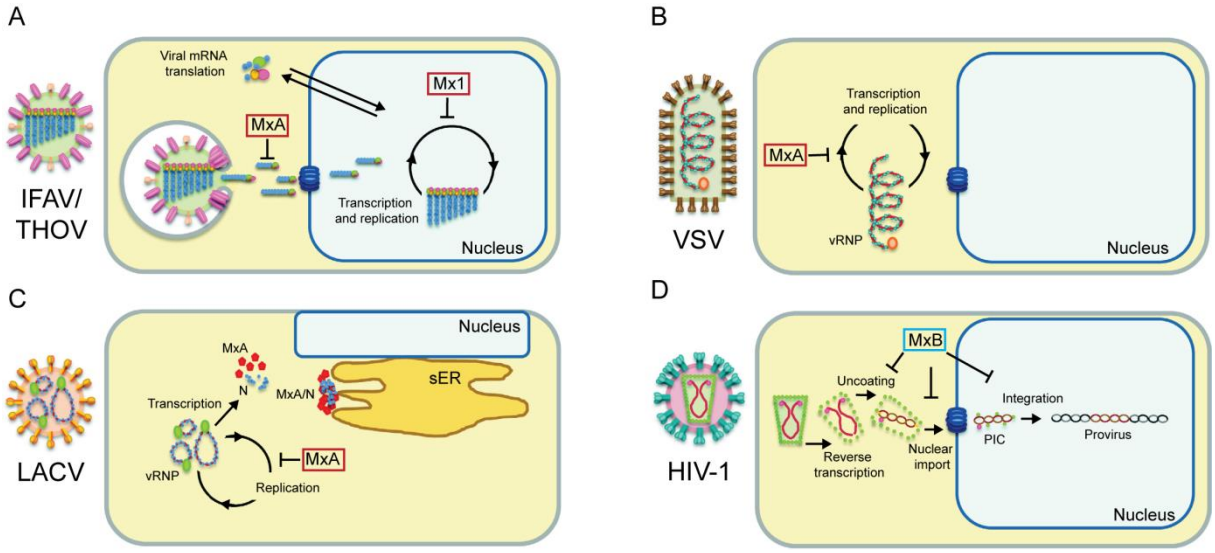

Figure 16: Antiviral activity sites of Mx proteins during different viral infections.

(A) Incoming vRNPs are blocked by the human MxA protein in the cytoplasm. Secondary transcription and replication of IFAV genomes are inhibited by interfering with synthesis and/or nuclear import of newly synthesized viral components. In contrast, mouse Mx1 acts in the nucleus and inhibits primary transcription. (B) VSV replicates in the cytoplasm where MxA inhibits primary transcription of incoming viral nucleocapsids. (C) In LACV (bunyaviruses, three RNA segments), early viral transcription leads to the synthesis of N. MxA sequesters N into perinuclear complexes, thereby blocking replication of the viral genome by the polymerase. (D) For HIV-1, the RNA genome on nucleocapsids is reverse-transcribed in the cytoplasm. The resulting pre-integration complex (PIC) is then transported into the nucleus, where the proviral DNA integrates into the host genome. MxB does not block reverse transcription but prevents uncoating, nuclear uptake and/or stability, or the integrase activity of the PIC, thus preventing chromosomal integration of proviral DNA. sER, smooth endoplasmatic reticulum. Figure was modified from (74).

In contrast, only the long 78 kDa isoform (+NLS) containing the flexible N-terminus of MxB was demonstrated to restrict HIV-1, but not the isoform lacking the NLS or loop L4 deletion mutants (70-72,132-134). Amino acids 37-44 downstream of the NLS, and in particular amino acid 37 was found to be a major specificity determinant (134). The short 76 kDa isoform lacking

the HIV-1 targeting sequence has not yet been shown to be antiviral active, but it is capable of forming hetero-oligomers with the long 78 kDa isoform, which may indicate a regulatory function (135). Transferring the N-terminal extension of MxB onto the human MxA or mouse Mx1 resulted in an Mx protein active against HIV-1 (133).

The viral target structures of MxA are still poorly investigated. The nucleocapsids of the THOV are known to be a target of the human MxA protein (108). The association might be cooperatively facilitated by assembled vRNPs (108,125,136). The polymerase subunit of IFAV PB2, which is associated with NPs, may serve as an additional target (125).

However, these results do not exclude the presence of other unknown cellular factors. Additional cellular host factors were shown to be crucial for binding of MxA to measles virus, IFAV, and Semliki Forest virus (SFV) (109,117,120,137). Also MxB may perform its antiviral activity by interacting with host cyclophilin A and proteins involved in the nucleocytoplasmic transport (71).

Host adaptation (viral mutations) of viral strains can provide hints which viral structures are targeted by Mx proteins. Human influenza strains are less sensitive to MxA inhibition than avian strains, and the sensitivity determinant was shown to be the NP (138,139). In particular, a few surface-exposed residues on the body domain of the NP have been demonstrated to be responsible for this MxA-resistance (140). Grafting these human residues to avian IFAV NP increased MxA-resistance and additionally weakened general replication fitness, indicating that crucial functional sites are targeted by MxA (140).

A model was proposed, where MxA oligomerize around vRNPs, resulting in ring formation and activation of GTPase activity by G domain association of adjacent rings (75-77,141,142). Conformational changes caused by GTP hydrolysis could lead to mislocalization of the vRNPs into aggregates (104), disruption of functional properties (125), or inhibition of nuclear import (109). In analogy, MxB might bind the capsid (core) of HIV-1 (132). However, GTP binding or hydrolysis by MxB seems not to be crucial to perform its antiviral activity against HIV (70-72,133).

1.7 Scope of this work

Myxovirus resistance (Mx) GTPases are induced by interferons and inhibit multiple viruses including influenza, Thogoto virus (THOV), and the human immunodeficiency viruses. They have the characteristic domain architecture of dynamin-related proteins with an amino-terminal GTPase (G) domain, a bundle signaling element (BSE), and a carboxy-terminal stalk responsible for self-assembly and effector functions. Human MxA is localized in the cytoplasm and is partly associated with membranes of the smooth endoplasmic reticulum (ER). It shows a protein concentration-dependent increase in GTPase activity, indicating regulation of GTP hydrolysis via G domain dimerization. However, the exact mechanism of GTP hydrolysis and the function of GTP binding and hydrolysis for the antiviral activity have not been characterized so far. **To clarify the role of GTP binding and the importance of the G domain interface for the catalytic and antiviral function of MxA**, I performed a thorough biochemical characterization in the first part of this doctoral thesis. Based on a structure-based mutagenesis, residues crucial for nucleotide-binding and dimerization were analyzed. The closely related human MxB protein is a potent restriction factor for HIV-1 and other lentiviruses, in addition to its already known involvement in regulating nucleocytoplasmic transport and cell-cycle progression. However, the role of GTP binding and hydrolysis in restricting HIV-1 is still under debate. Consequently, I **analyzed the GTPase activity of MxB in absence and presence of MxA to deduce possible differences to MxA.** A biochemical characterization of MxB might shed more light on their differential antiviral spectrum.

The tick-born transmitted THOV NP was identified as a target of the MxA GTPase. In viral particles, the NP is encapsulating the viral RNA and together with the viral polymerase they form the viral ribonucleoparticles (vRNPs), which are essential for transcription and replication of the virus. The second part of this thesis focuses on a basic biochemical characterization of the THOV and DHOV NP to understand the mechanism of RNA binding and oligomerization. To better understand the structural features of orthomyxovirus RNP formation, I **solved the atomic structure of the THOV NP**.

Finally, the atomic model of the THOV NP helps to identify putative interaction sites with the human MxA protein, and provides a structural model for other ortomyxoviruses, including influenza viruses.

2 Materials and Methods

2.1 Materials

2.1.1 Instruments

All instruments used during the present study are listed in Appendix A.

2.1.2 Chemicals

Chemicals from the following companies have been used: Fluka (Neu-Ulm, Germany), Roth (Karlsruhe, Germany), Calbiochem (Darmstadt, Germany), Merck (Darmstadt, Germany), Jena Bioscience (Jena, Germany), Qiagen (Hilden, Germany), Amersham (Piscataway, USA), Riedel-de-Haen (Seelze, Germany), Roche (Mannheim, Germany), Sigma-Aldrich (Steinheim, Germany), and Avanti (Alabaster, USA). A detailed list of all chemicals can be found in Appendix B.

2.1.3 Enzymes

DNAase I	Roche (Mannheim, Germany)
DpnI	New England Biolabs (Frankfurt am Main, Germany)
Pfu DNA polymerase	Stratagene (La Jolla, USA)
T4 DNA ligase	New England Biolabs (Schwalbach, Germany)
PreScission™ protease	GE Healthcare (München, Germany)
Restriction enzymes	New England Biolabs (Schwalbach, Germany)

2.1.4 Kits

NuPAGE© SDS Sample Buffer (4x)	Invitrogen (Karlsruhe, Germany)
NuPAGE© MOPS SDS Buffer Kit	Invitrogen (Karlsruhe, Germany)
NuPAGE© Novex 4-12% Bis-Tris	Invitrogen (Karlsruhe, Germany)

QIAprep™ Spin Miniprep Kit	Qiagen (Hilden, Germany)
QIAquick Gel Extraction Kit	Qiagen (Hilden, Germany)
GeneAmp© dNTPs	Roche Molecular Systems (Branchburg, USA)
Quick Start™ Bradford Protein Assay	Bio-Rad (München, Germany)
Quik Change® SDM Kit	Stratagene (La Jolla, USA)
Mark12™ unstained standard	Invitrogen (Karslruhe, Germany)
Unstained standard	Fermentas (St. Leon-Rot, Germany)
2-Log DNA ladder	NEB (Frankfurt am Main, Germany)
JBS Magic Triangle Phasing Kit	JBS (Jena, Germany)

2.1.5 Crystallization screens and tools

Crystallization screens and other consumables such as 24-well and 96-well plates, glass cover slides or micro bridges were used from Hampton Research (Aliso Viejo, the USA), Jena Bioscience (Jena) and Qiagen (Hilden).

The Classics Suite	Qiagen (Hilden, Germany)
The Classics Lite Suite	Qiagen (Hilden, Germany)
PACT Suite	Qiagen (Hilden, Germany)
ComPAS Suite	Qiagen (Hilden, Germany)
The JSCG+ Suite	Qiagen (Hilden, Germany)
The PEG I+II Suites	Qiagen (Hilden, Germany)
MPD Suite	Qiagen (Hilden, Germany)
The ProComplex Suite	Qiagen (Hilden, Germany)
JBScreen Plus HTS	Jena Bioscience (Jena, Germany)
Additive Screen™	Hampton Research (Aliso Viejo, USA)

2.1.6 Microorganisms

E.coli TG1	*K12, supE, hsdΔ5, thi, Δ(lac-proAB), F'[traD36, proAB+, lacq, lacZΔM15]* (Promega, Mannheim, Germany)
E.coli BL21 (DE3) Rosetta	*F^- ompT hsdsSB (rB^- mB^-) gal dcm (DE3) pRARE*

	(CmR) pRARE containing the tRNA genes argU, argW, ilex, glyT, leuW, proL, metT, thrT, tyrU and thrU (Novagen, Darmstadt, Germany)

2.1.7 Vectors

pSKB-LNB	pET28a + N-terminal PreScission^{TM} cleavage site, Kan^{R}, (O. Daumke, MDC Berlin)
pGEX-6P1	Amp^{R}, (GE Healthcare, Piscataway, USA)

2.1.8 cDNA clones

The cDNA for human (*Homo sapiens*) MxA and MxB was derived from ImaGenes Berlin, Germany.
The cDNA for the THOV-, DHOV-NP as well as H5N1-, H1N1 (1918)-, H1N1 (2009)-NP was derived from Prof. Dr. Georg Kochs, Institute of Virology, Universitätsklinikum, Freiburg.

2.1.9 Media and antibiotics

Luria-Bertani (LB)	10 g/L Bactotryptone, 10 g/L NaCl, 5 mM NaOH, 5 g/L yeast extract
Terrific Broth (TB)	12 g/L Bacto Tryptone, 24 g/L Bacto-yeast-extract, 4 g/L glycerol, 17 mM KH_2PO_4, 72 mM K_2HPO_4
M9 minimal medium	5.7 g/L Na_2HPO_4, 1.5 g/L KH_2PO_4, 1 g/L NH_4Cl, 0.5 g/L NaCl
Ampicillin sodium salt	1000x stock was 50 mg/mL in H_20, Roth (Karlsruhe)
Chloramphenicol	1000x stock was 34 mg/mL in EtOH, Roth (Karlsruhe)
Kanamycinsulfate	1000x stock was 10 mg/mL in H_2O for liquid cultures and 50 mg/mL in H_2O for plates, Roth (Karlsruhe)

2.1.10 Buffers

5x *Pfu* buffer	
New England Biolabs (Frankfurt am Main)	300 mM NaCl, 10 mM Tris-HCl pH 7.4, 0.1 mM EDTA, 1 mM DTT, 500 µg/mL BSA, 50 % glycerol
TSS buffer	85% LB-Medium, 10% PEG 3350, 5% DMSO, 50 mM $MgCl_2$, pH 6.5
10x TBE buffer stock (1L)	108 g Tris.base, 55 g boric acid, 9.3 g Na_2EDTA pH 8.0
Resuspension buffer (Lysis buffer)	50 mM HEPES pH 7.5, 400 mM NaCl, 250 µM Pefabloc, 1µg/mL DNAseI, 5 mM $MgCl_2$, 30 mM Imidazole, 2.5 mM β-Mercaptoethanol
Equilibration buffer	20 mM HEPES pH 7.5, 400 mM NaCl, 5 mM $MgCl_2$, 30 mM Imidazole, 2.5 mM β-Mercaptoethanol
Wash buffer 1	20 mM HEPES pH 7.5, 800 mM NaCl, 5 mM $MgCl_2$, 30 mM Imidazole, 2.5 mM β-Mercaptoethanol, 10 mM KCl, 1 mM ATP
Wash buffer 2	20 mM HEPES pH 7.5, 400 mM NaCl, 5 mM $MgCl_2$, 80 mM Imidazole, 2.5 mM β-Mercaptoethanol

Elution buffer	20 mM HEPES pH 7.5, 400 mM NaCl, 5 mM $MgCl_2$, 300 mM Imidazole, 2.5 mM β-Mercaptoethanol
Gel filtration buffer	20 mM HEPES pH 7.5, 150 mM (150 mM, 300 mM or 500 mM) NaCl, 2 mM $MgCl_2$, 2 mM DTT
Oligomerization Assay buffer	20 mM HEPES (pH 7.5), 150 mM NaCl, 2 mM $MgCl_2$
HPLC running buffer	10 mM TBAB, 100 mM potassium phosphate pH 6.5, 7.5 % (v/v) acetonitrile
GTPase buffer	50 mM HEPES pH 7.5, 150 mM NaCl, 5 mM $MgCl_2$, 5 mM KCl
ITC buffer	50 mM HEPES pH 7.5, 150 mM NaCl, 5 mM $MgCl_2$, 5 mM KCl
CD spectroscopy buffer	150 mM NaF, 10 mM Na_2HPO_4 pH 7.4
EM buffer	20 mM HEPES pH 7.5, 150 mM NaCl

2.2 Molecular biology methods

2.2.1 Polymerase chain reaction

The amplification of DNA fragments was conducted using the *Pfu* polymerase according to standard procedures (143).

2.2.2 Restriction digest

DNA was digested by using restriction enzymes according to the manufacture's protocol (New England Biolabs, Frankfurt am Main, Germany).

2.2.3 Agarose gel electrophoresis

1 % (w/v) agarose gels were prepared and electrophoretic experiments performed according to standard protocols (143) using 1x TBE buffer and 0.3 µg/mL ethidium bromide.

2.2.4 Purification of separated DNA

DNA was cut out from the agarose gel and purified using the QIAquick Gel Extraction Kit, (Qiagen, Hilden, Germany) according to the manufacturer's protocol.

2.2.5 Ligation

Insert and plasmid were spectrometrically quantified at λ = 260 nm. 10 ng of vector was ligated with a six fold molar excess of insert overnight at 4°C using T4 ligase (New England Biolabs, Schwalbach, Germany) following the manufacturer's protocol.

2.2.6 Competent *E. coli* cells

Competent cells were prepared according to (144). 1 L LB-Medium was inoculated with 10 mL preculture and grown at 37°C until an OD_{600} of 0.4. Bacteria were incubated on ice for 20 min, pelleted for 5 min at 1,200 g at 4°C and resuspended in 100 mL ice-cold sterile TSS buffer, flash frozen and stored at -80°C.

2.2.7 Transformation

Bacteria were transformed using the heat shock method according to the standard protocol (143). After insertion of the desired cDNA into the vector, *E. coli* TG1 was transformed with the ligation batch. Vectors were amplified and isolated. Finally, the expression-optimized

bacteria strain *E. coli* BL21 (DE3) Rosetta has been transformed with the isolated plasmids carrying the insert of interest.

2.2.8 Bacterial storage

Overnight cultures grown in selective (Rosetta: Kanamycin and Chloramphenicol; TG1: Kanamycin) LB-medium at 37°C were mixed 2:1 (v/v) with 50 % glycerol and bacteria stocks were stored at -80°C.

2.2.9 Site directed mutagenesis

Site-directed mutagenesis was carried out using cloned *Pfu* DNA polymerase (Stratagene, La Jolla, USA) according to the protocol described by (143). Reactions were carried out with and without DMSO.
Modifications are:

ddH_2O	20/ (15) µl
(DMSO)	(5 µl)
5x *Pfu* buffer	10 µl
dNTP's (2mM each)	5 µl
desired Primer (10 pmol/µl)	á 5 µl
desired plasmid (MiniPrep DNA)	4 µl
Pfu polymerase (2.5 U/µl)	1 µl

Temperature program used for point mutations: 5'' 95°C [1'' 95°C, 1'' corresponding primer-annealing temp. 56°C, 4'' 72°C] x 31, 10'' 72°C.
Temperature program used for deletion constructs 1'' 95 °C [1'' 95°C, 1'' corresponding primer-annealing temp. 58°C, 4'' 72°C] x 29, 10'' 72°C.

Selection of point mutants was carried out via *DpnI* digestion.

2.2.10 Constructs and point mutants used in this study

Protein	Mutation	Vector	Remark
hsMxA	M527D	pSKB-LNB	
hsMxA	M527D+K83A	pSKB-LNB	
hsMxA	M527D+T103A	pSKB-LNB	
hsMxA	M527D+V185Y	pSKB-LNB	
hsMxA	M527D+D250N	pSKB-LNB	
hsMxA	M527D+D253N	pSKB-LNB	
hsMxA	M527D+D250N+D253N	pSKB-LNB	
hsMxA	M527D+G255E	pSKB-LNB	
hsMxA	M527D+V268M	pSKB-LNB	
hsMxB	M574D	pSKB-LNB	
hsMxB	ΔN85+M574D	pSKB-LNB	
hsMxB	ΔN85+ΔL4+M574D	pSKB-LNB	
hsMxB	ΔN85+ΔL4	pSKB-LNB	
hsMxB	ΔN85+ΔL4+T151A	pSKB-LNB	
IFAV H5N1 NP	Wild type	pSKB-LNB	
IFAV H1N1 1918 NP	Wild type	pSKB-LNB	
IFAV H1N1 2009 NP	Wild type	pSKB-LNB	
THOV NP	Wild type	pSKB-LNB	
IFAV H5N1 NP	Wild type	pGEX-6P1	Insoluble
IFAV H1N1 1918 NP	Wild type	pGEX-6P1	Insoluble
IFAV H1N1 2009 NP	Wild type	pGEX-6P1	Insoluble
THOV NP	Wild type	pGEX-6P1	Insoluble
THOV NP	Wild type	pSKB-LNB	
THOV NP	Δ7	pSKB-LNB	
THOV NP	Δ14	pSKB-LNB	
THOV NP	Δ22	pSKB-LNB	
THOV NP	Δ67-79	pSKB-LNB	Insoluble
THOV NP	Δ188-196	pSKB-LNB	
THOV NP	Δ188-196+Δ378-387+EE415-416AA	pSKB-LNB	
THOV NP	EE415-416AA	pSKB-LNB	
DHOV NP	Wild type	pSKB-LNB	
DHOV NP	Δ28	pSKB-LNB	
DHOV NP	Δ76-86	pSKB-LNB	Insoluble
DHOV NP	Δ194-200	pSKB-LNB	
DHOV NP	Δ28+Δ194-200	pSKB-LNB	
DHOV NP	EFEE420-224AAAA	pSKB-LNB	

Table 2: Detailed list of all constructs used in this work.

Construct description: e.g. Δ7, the first 7 amino acids from the N-terminus are missing; Loop L4 in MxB corresponds to amino acid 580-609. Full-length (fl) MxA (662 amino acids), (fl) MxB (715 amino acids), (fl) THOV NP (454 amino acids), (fl) DHOV NP (458 amino acids), (fl) IFAV (H1N1/H5N1) NP (498 amino acids).

2.2.11 Isolation of plasmid DNA

Isolation of the plasmids was carried out using the QIAprep Spin Miniprep Kit according to the manufacture's protocol.

2.2.12 DNA sequencing

Analysis of the sequencing samples was processed by Eurofins MWG (Ebersberg, Germany) or Source Bioscience (Berlin-Buch, Germany).

2.2.13 Sequence alignment

Sequences alignment was performed using the ClustalOmega algorithm (145) and subsequently modified using Genedoc.

2.3 Biochemical methods

2.3.1 Sodium dodecyl sulfate polyacrylamide gel electrophoresis (SDS-PAGE)

Protein separation of different molecular weight was performed according to (146) using a denaturing gradient SDS-polyacrylamide gel electrophoresis (SDS-PAGE) kit (Invitrogen, Karlsruhe) and NuPAGE© MOPS SDS Buffer Kit Invitrogen (Karlsruhe) at a neutral pH (147) according to the manufacture's protocol .

2.3.2 Viral NP over-expression and solubility test

The over-expression of the wild type NPs was tested by growing a 5 mL overnight LB *E. coli* BL21 (DE3) Rosetta culture supplemented with the desired antibiotics at 37°C carrying the desired plasmid. This preculture was used to inoculate (1:100) a 100 mL TB medium supplemented with the respective antibiotics (1:1000).Cells were grown under shaking to an OD_{600} of 0.5 at 37°C and 30 min before induction with 40 µM isopropyl-β-D-thiogalactopyranoside (IPTG) temperature was decreased to 18°C for overnight expression (18 h). Bacteria were collected by centrifugation at 4500 rpm for 15 min and pellets were

resuspended in ice-cold 25 mL resuspension buffer per pellet from 1 L bacteria culture. Cells were disrupted by passing the resuspension three times through a microfluidizer (Microfluidics). The lysate was centrifuged at 40.000g and 4°C for 45 min in an Optima L-100 K ultracentrifuge using a type 35 rotor. The supernatant was filtered through a 0.2 µm filter. Samples were taken from the non-induced (NI), induced (I), supernatant (S) and pellet (P) fraction for SDS-PAGE analysis (see also 2.3.1).

2.3.3 Large scale protein over-expression and purification

Human wildtype and mutants of MxA (Expasy accession P20591), MxB (Expasy accession P20592) as well as viral THOV- (Expasy accession P89216) and DHOV-NPs (Expasy accession D6PT87) were expressed as N-terminal (6x) His-fusions followed by a PreScission™ cleavage site in *E. coli* BL21 (DE3) competent Rosetta cells (Novagen) from pSKB-LNB (pET28a+PreScission™ cleavage site) vector.

Bacterial cultures were grown and expressed in analogy to 2.3.2, except 6-12L TB medium supplemented with the respective antibiotics was used. After filtration of the soluble cell extract (0.2 µm), the supernatant was applied to a Ni^{2+}-NTA column (GE-Healthcare) equilibrated with equilibration buffer. The column was extensively washed with wash buffer 1, and afterwards with wash buffer 2. Following protein elution by elution buffer, the protein was incubated overnight at 4°C in the presence of 250 µg GST-tagged PreScission™ protease to cleave the N-terminal His_6 tag. The cleaved protein was concentrated and applied to a Superdex 200 16/60 (GE) gel filtration column equilibrated with gel filtration buffer. PreScission™ protease was removed using a GST column. Fractions containing the desired protein were pooled, concentrated (Amicon centrifugal filter) and flash frozen in liquid nitrogen and stored in small aliquots at -80°C. Samples were taken from all purification steps for SDS-PAGE analysis (see also 2.3.1).

2.3.4 Expression of selenomethionine (SeMet) incorporated protein

For the expression of SeMet-labeled THOV $NP^{\Delta 188\text{-}196}$ and subsequent structure determination, the medium was prepared as follows. M9 medium plus 1 mM $MgSO_4$, 0.1 mM $CaCl_2$, 0.4% glucose, 1 g/L NH_4Cl, and vitamin mix containing 1 mg/L riboflavin, 1 mg/L niacin amide, 0.1 mg/L pyridoxine monohydrochloride and 1 mg/L thiamine. M9 minimal medium supplemented with the respective antibiotics was inoculated with an overnight LB culture of the respective

clone in a 1:100 dilution. Cells were grown to an OD_{600} of 0.5 at 37°C, followed by addition of an amino acid mix containing L-lysine, L-phenylalanine, L-threonine (100 mg/L each), L-isoleucine, L-leucine, L-valine (50 mg/L each). 30 min before induction with 40 µM IPTG, 50 mg/L L-selenomethionine (Calbiochem-Novabiochem, Schwalbach) was added to suppress endogenous bacterial methionine biosynthesis and to incorporate SeMet (148). The culture was cooled to 20°C and protein expression was done overnight. Harvesting of the cells and purification was performed in the same way as for the native protein (see also 2.3.2 and 2.3.3).

2.3.5 Protein concentration determination

The extinction coefficient of different protein constructs was determined online at the Expasy homepage (https://web.expasy.org/prot/param/) according to (149) and protein concentration was subsequently determined at a wavelength λ = 280 nm.
As an alternative for protein concentration determination, for example in case that nucleotide contaminations existed, Quick Start™ Bradford Protein Assay from Bio-Rad was used and measured at λ = 595 nm.

2.3.6 Protein storage

Purified proteins in gel filtration buffer were aliquoted (25 µL) and flash frozen in liquid nitrogen for subsequent storage at -80°C.

2.3.7 Circular dichroism spectroscopy (CD)

CD-spectroscopy is a powerful method to evaluate the secondary structure, folding and stability of an expressed protein. The method is based on the unequal absorption of left (LCPL)- and right (RCPL)-handed circularly polarized light by a molecule containing one or more chiral chromophores showing in the following basic equation:

$$\Delta A = \Delta A_{LCPL} - \Delta A_{RCPL} \ (M^{-1}m^{-1})$$

Equation 1: Absorption difference of left (LCPL)- and right (RCPL)-handed circularly polarized light.

UV CD-spectroscopy was carried out to investigate the secondary structure content of the purified wt THOV NP and qualitative comparison with the IFAV NP. Spectra were recorded on a qCD Chirascan spectrometer (Applied Photophysics) from 190 to 260 nm in a 0.1 cm cell. Proteins were dialyzed overnight using the CD spectroscopy buffer (see 2.1.10). 200 µL of a 0.2 mg/mL protein solution was used for the measurements. Measurements were performed in triplicate and baseline-corrected by subtraction of the buffer.

2.3.8 Nucleotide detection via reverse-phase HPLC

Reversed phase high-pressure liquid chromatography (HPLC) assays were carried out according to (150) nucleotide separation. The principle of the assay is based on the basis of the interaction between the hydrophobic static phase from the column and the ion pair of nucleotide and tetrabutylammonium bromide (TBAB) in the mobile phase. Depending on the number of phosphates, a variable number of TBAB ions are bound by the nucleotide which increases the retention time (t_R) on the column. Peak integration was used for quantification of the kinetic study of nucleotide hydrolysis.

To check if the purified protein was already loaded with nucleotide from *E. coli*, 40 µM protein sample (in GTPase buffer) was applied on a HPLC system and separated via a reversed-phase column via a reversed-phase Hypersil ODS-2 C18 column. During the assay, the sample was running with a buffer containing 100 mM potassium phosphate (pH 6.5), 10 mM TBAB, 7,5%

acetonitrile. Denatured proteins were adsorbed at a C18 guard column. Nucleotide peaks were detected by measuring absorption at 254 nm and compared with standard nucleotide samples (40µM).

2.3.9 Nucleotide binding assay

Nucleotide binding was detected using isothermal titration calorimetry (ITC). ITC directly measures endothermic or exothermic reactions of a macromolecule-ligand interaction. ITC data provides a full thermodynamic profile of this interaction including the stoichiometry of the interaction (n), the association constant (K_A), the Gibbs free energy (ΔG), enthalpy (ΔH), entropy (ΔS), and the heat capacity of binding (ΔCp).

Nucleotide dissociation constants (K_D) were determined at 8°C on a VP-Isothermal Titration Calorimetry (VP-ITC) system (MicroCalTM, GE Healthcare, Freiburg). 1 mM nucleotide in ITC Buffer (see 2.1.10) was titrated in 8 µL steps into a reaction chamber containing 50 µM of MxA^{M527D} (or the indicated M527D mutants) in the same buffer. For the MxA^{K83A} mutant, an iTC200 (Microcal) was used with 200 µM protein and 4 mM guanosine 5'-O-[gamma-thio] triphosphate (GTPγS). The resulting heat change upon injection was integrated over a time range of 240 sec, and the obtained values were fitted to a standard single-site binding model using Origin®.

2.3.10 RNA/DNA binding assay

To elucidate the binding/reaction mechanism of the wt THOV NP binding to single-stranded (ss) RNA or ssDNA, a thermodynamic profile (ΔG, ΔH and –TΔS) was calculated according to the equation of the Gibbs free energy:

$$\Delta G(p,T) = \Delta H - T\Delta S$$

Equation 2: The Gibbs free energy can be partitioned into its enthalpic, ΔH, and entropic, TΔS, contributions. T is the temperature and p the pressure.

Single-stranded RNA and ssDNA binding affinity for the THOV and DHOV NP were determined and analyzed in analogy to 2.3.9, with the exception of using 10 µM of protein and 150 µM of RNA or DNA.

2.3.11 Nucleotide hydrolysis assay

GTPase activities of human MxA and MxB mutants were determined at 37°C in GTPase buffer (see 2.1.10). Saturating concentrations of GTP or xanthosine 5'-triphosphate (XTP) (1 mM) were used for each reaction (multiple turnover assay). Reactions were initiated by the addition of protein to the final reaction solution. For the heteromeric stimulation reactions, the concentration of MxA^{M527D} was kept constant at 2.5 µM, and increasing concentrations of the indicated MxA mutants were added. At different time points, reaction aliquots were 20-fold diluted in GTPase buffer and quickly transferred into liquid nitrogen. Separation of different nucleotides was achieved according to 2.3.8. Nucleotide peaks were detected by measuring adsorption at 254 nm and compared with standard nucleotide samples. GTP and hydrolysis product GDP in the samples were quantified by integration of the corresponding absorption peaks. Rates derived from a linear fit to the initial rate of the reaction (<40% GTP hydrolyzed) were plotted against the protein concentrations and the k_{obs} values were calculated. For data analysis, the program GraFit5 (Erithacus Software) was used.

2.3.12 Analytical gel filtration

MxA mutants were analysed using an FPLC Akta Purifier (GE Healthcare) equipped with a Superdex 200 10/300 column in the absence or presence of nucleotides. The running buffer contained 20 mM HEPES (pH 7.5), 150 mM NaCl, 2 mM $MgCl_2$, but no nucleotides. The mutants were pre-incubated for 15 min with 2 mM GDP/xanthosine 5'-diphosphate (XDP), 2 mM $AlCl_3$ and 20 mM NaF at 4°C in gel filtration buffer. 50 µL of a 2 mg/mL protein solution was subsequently applied to the column. A flow rate of 0.5 mL/min was used. Chromatograms were recorded at λ = 280 nm. For MxB as well as for the THOV and DHOV NPs, the same parameters were used as for MxA, except that no nucleotide was used.

2.3.13 Right angle light scattering (RALS)

A coupled RALS system and Refractive Index detector (Malvern) was connected in line to an analytical gel filtration column Superdex 200 10/300 to determine absolute molecular masses of the applied proteins. Gel filtration buffer was used as running buffer (see 2.1.10) with a flow rate of 0.5 mL/min. For each protein sample, 50 µL of a 2 mg/ml or 4 mg/mL solution were applied. Data analysis was performed with the provided software (Omnisec).

2.3.14 Analytical ultracentrifugation (AUC)

Oligomeric state determination of the NPs was performed by AUC in gel filtration buffer (150 mM NaCl) using a XLI type analytical ultracentrifuge (Beckman) equipped with ultraviolet absorbance optics. Samples were measured in an An-50 Ti rotor at a wavelength of 280 nm with a radial spacing of 0.003 cm. The protein was used in a concentration of 0.5 mg/mL. Sedimentation velocity experiments were carried out at 35000 r.p.m., 10 °C using two-channel cells with a 12 mm optical path length and a 400 µL sample volume. For the estimation of the partial specific volume $\bar{\upsilon}$ from the amino acid composition as well as the density ρ and viscosity η of the buffer, the program Sednterp (http://bitcwiki.sr.unh.edu/index.php/Main_Page) was used. Data were then analyzed with the program Sedfit (151) using a continuous c(s) distribution model. Theoretical sedimentation coefficients for a trimeric protein species were calculated using the following equation:

$$s_{20,w} = \frac{M_w \times (1 - \rho_{20,w} \times \bar{\upsilon})}{N_A \left(\frac{f}{f_0}\right) 6\pi\eta_{20,w} \times \sqrt[3]{\frac{3M_w\bar{\upsilon}}{\pi N_A}}}$$

Equation 3: Theoretical sedimentation coefficient in aqueous solution.

$\rho_{20,w}$ and $\eta_{20,w}$ are the density and viscosity of water at 20°C, respectively, N_A Avogadro's constant and M_W and f/f_0 the molecular weight and frictional ratio, respectively.

Using the equation 1, a frictional ratio of about 1.3 for the THOV/DHOV NPs in a trimeric state was calculated. Frictional ratios were calculated using the molecular weight of 52 kDa for

the wt THOV NP and wt DHOV NP. Using this frictional ratio of 1.3, a sedimentation coefficient of 7.5 was calculated for a protein with a molecular mass of 52 kDa.

2.3.15 Electron microscopy (EM)

To visualize the architecture of THOV and DHOV NPs bound to ssRNA, NPs at a final concentration of 1 mg/mL were incubated with an *in vitro* transcribed 8-kb single-stranded (ss) RNA comprising a Green Fluorescent Protein (GFP) expression construct (152) at a final concentration of 0.2 mg/mL (5:1, NP:ssRNA) or 0.1 mg/mL (10:1). Protein and ssRNA was diluted in EM buffer (see 2.1.10). NPs without ssRNA and the native vRNPs isolated form THOV (obtained from Prof. Dr. Georg Kochs, Freiburg, Germany) were visualized at a final concentration of 0.2 mg/mL. 10 µL of these solutions were spotted onto carbon-coated grids. Preparations and measurements were performed at room temperature. The sample was stained with 2 % uranyl acetate and analyzed using a Zeiss EM910 electron microscope at magnifications between 50 and 70k.

2.3.16 Oligomerization assay

Oligomerization assays were carried out at 1 mg/mL protein concentration. Samples were incubated at room temperature for 10 min in a buffer containing 20 mM HEPES (pH 7.5), 150 mM NaCl and 2 mM $MgCl_2$ or the indicated NaCl concentration. After ultracentrifugation at 75.000 rpm, 25°C for 10 min, equivalent amounts of supernatant and pellet were loaded on SDS–PAGE.

2.3.17 Homology modeling

For homology modeling also known as comparative modeling or knowledge-based modeling the fully automated protein structure homology-modeling server, accessible via the ExPASy web server was used (153). This procedure develops a three-dimensional model of the "target" protein from a protein sequence based on known structures of homologous proteins ("template"). For the MxA G domain, the calculated model was then superimposed to the

recently solved GDP-AlF_4^--bound GG dimer of human dynamin 1 (88) using COOT (Crystallographic Object-Oriented Toolkit) (154). For the THOV NP model, the crystal structure of the IFBV NP (PDB code: 3TJ0, (46)) was used.

2.3.18 Other assays and techniques

Other assays and techniques whose outcome appears in chapter 3.1.4 and 3.1.5, including cell- and virus-based assays, influenza A and THOV virus minireplicon system, Western blot analysis and immunofluorescence analysis were performed in our collaborator's lab in Freiburg (group of Prof. Dr. Georg Kochs, Ph.D. student Laura Graf). A detailed description of these assays and techniques can be found in (75).

2.4 Crystallographic and computational methods

2.4.1 Crystallization

Protein crystallization of highly purified native and selenomethione-substituted protein was performed at 10 mg/mL. Stored protein (-80°C) was gently thawed and prior crystallization setup centrifuged at 13200 rpm, 4°C for around 20 min.. The protein was diluted in gel filtration buffer (150 mM NaCl) (see also 2.1.10). For complex formation of the NP with single-stranded RNA, the RNA was diluted in the same buffer prepared with RNAse free ddH_2O. Commercially available RNA in highest purity was obtained from Integrated DNA Technologies, Inc., Leuven, Belgium. Extensive screening using the sitting-drop method in 96-well plates of commercially available screens (see also 2.1.5) at 20 and 4°C was performed. In contrast, non-automated crystallization trials were done using the hanging drop vapor diffusion method in 24-well plates. No precipitation over several days (3-5 days) was observed for the NPs at room temperature, indicating high stability. However, due to size limitations of initial crystals (for THOV NP as well as for DHOV NP), subsequent crystallization setups were done at 4°C to decelerate the nucleation process. Hanging drops were set up at different protein solution/reservoir ratios (1 µL:1 µL, 1 µL:2 µL, and 2 µL:1 µL). Concerning the automated 96-well crystallization trials, the drop consisted of 300 nL protein solution and 300 nL reservoir solution. The drops were placed on the 96-well plate using the Gryphon LCP 96-Chanel dispenser.

2.4.2 Cryo-protection

To avoid freezing damage of the crystals, and mitigate damage during data collection, the crystals were treated with suitable cryo-protectant. The cryo-solutions were composed of the protein solution and reservoir solution from the corresponding crystallization condition in equal volumes. Additionally, the concentration of PEG200, PEG400, ethylenglycol, MPD and glycerol was varying between 20-30%. The crystals were soaked in 2 µL of the cryo-solution for 5-10 sec. and flash frozen in $N_{2,l}$.

2.4.3 Data collection

The dataset for the native THOV $NP^{\Delta 188\text{-}196}$ crystals was recorded at BL14.1 at BESSY II, Berlin-Adlershof, using a Pilatus 6M detector. For data collection from a single crystal, the rotation method was applied with an φ increment of 0.3° at 100 K, a wavelength λ of 0.979733 Å and a detector distance of 553 mm. 2400 images with 1 sec. exposure time were collected.

The dataset for the selenomethione-substituted crystal of THOV $NP^{\Delta 188\text{-}196}$ was collected at the DESY synchrotron radiation facility in Hamburg, Petra III (P11) at the selenium peak (see Table 7) with a wavelength λ of 0.98 Å and a detector distance of 622.7 mm for 2000 images (for one peak dataset) with 1 s exposure time and 0.1° oscillation range for each image. The beamline was equipped with a Pilatus 6M detector. Both peak datasets were merged, and initial indexing for both datasets and determination of an optimal data collection strategy was performed with Mosflm (155). Recorded intensities were integrated and scaled with the program XDS (156).

2.4.4 Protein structure solution

In the following chapter a brief description is given over the theoretical background of X-ray crystallography. For a more detailed description please be referred to (157).

X-ray crystallography is an experimental technique allowing the determination of the three-dimensional structure of a macromolecule by interaction of the X-rays with a scattering matter in a crystal. Macromolecular crystals are made up from atoms or molecules which are arranged

in a three-dimensionally periodic manner. Per definition, the unit cell is the building block by which the crystal can be generated by applying translational operations. However, the asymmetric unit (ASU) is the smallest unit of a crystal structure, and space group symmetry operations (inversion, rotation or reflection) generate the unit cell of the crystal. The unit cell is built up from three noncolinear vectors a, b, and c. Generally, these vectors have unequal magnitudes and their angles deviate from 90°. The space group is defined by the dimensions of the unit cell and the symmetry operations applied to the asymmetric unit. The symmetry operations inversion or reflection cannot be applied to chiral molecules, therefore only 65 out of 230 possible space groups are found in protein crystals (158).

Diffraction of X-ray beams from the molecules within the crystal give information about the content of the crystal. This elastic scattering process (energy of the scattered wave is equal to the energy of the incident wave) is also known as Thomson scattering. In particular, the direction of the diffracted X-ray beams contains the information of the unit cell dimensions and thus the crystallographic symmetry. The intensities of the diffracted X-ray beams contain the information about the content of the unit cell, the spatial arrangement of the atoms of the crystallized molecule and therefore the information about the electron density distribution.

Assuming the unit cell contain n atoms at positions r_j (j = 1, 2, 3, . . , n) with respect to the origin of the unit cell. With their nuclei as origins, the atoms diffract according to their atomic scattering factor f. Transferring the origin to the origin of the unit cell, changes the phase angles by $2\pi rj \cdot S$. Where $\vec{S} = \vec{s} - \overrightarrow{s_0}$ with $\vec{s}$ as the scattered wave vector and $\overrightarrow{s_0}$ as incident wave vector. If summarizing all the individual atoms in the unit cell, the structure factor $\vec{F}(S)$ can be described as a function of the electron density distribution in the unit cell:

$$\vec{F}(S) = \sum_{j=1}^{n} f_j e^{\left(2\pi i \vec{r}_j \cdot \vec{S}\right)}.$$

Equation 4: The structure factor $\vec{F}(S)$ as the sum of all scattered atoms within the unit cell. Explanation can be found within the text.

With the translational vectors a, b, and c as well as the assumption that a crystal consists of a large number of unit cells: n_1 in direction $\vec{a}$, n_2 in direction $\vec{b}$ and n_3 in direction $\vec{c}$. To obtain the scattering of the whole crystal, the scattering contribution of all the unit cells with respect to a single origin needs to be added. The unit cell position can then be described as $t \cdot \vec{a} + u \cdot \vec{b} +$

$\nu \cdot \vec{c}$, with t, u, and ν are whole numbers. The total wave $\vec{K}(S)$ scattered by the crystal is obtained by summation over all unit cells:

$$\vec{K}(S) = \vec{F}(S) \times \sum_{t=0}^{n_1} e^{(2\pi i t \vec{a} \cdot \vec{S})} \times \sum_{u=0}^{n_2} e^{(2\pi i u \vec{b} \cdot \vec{S})} \times \sum_{\nu=0}^{n_3} e^{(2\pi i \nu \vec{c} \cdot \vec{S})}.$$

Equation 5: Total wave $\vec{K}(S)$ scattered by a crystal. Explanation can be found within the text.

Because n1, n2, and n3 are very large, the summation over t, u, and ν almost always equals zero (no scattering is observed) unless $\vec{a} \cdot \vec{S}$ is an integer h, $\vec{b} \cdot \vec{S}$ is an integer k, and $\vec{c} \cdot \vec{S}$ is an integer l. This condition is also known as the Laue condition, and h, k, l are the Miller-indices, representing equivalent crystal lattice planes in the reciprocal space. If the Laue condition is fulfilled, all unit cells scatter in phase, and the amplitude of the total scattered wave $\vec{K}(S)$ is proportional to the amplitude of the structure factor $\vec{F}(S)$ and the unit cell number in the crystal. As a consequence, reflections can be observed as discrete intensity maxima of the diffracted X-ray beam on the detector.

Instead of summing up over all the atoms, we can integrate over all electrons in the unit cell:

$$\vec{F}(S) = \int_{cell} \rho(\vec{r}) e^{(2\pi i \vec{r_j} \cdot \vec{S})} dv.$$

Equation 6: Structure factor $\vec{F}(S)$ of a unit cell as integration over all atoms. Explanation can be found within the text.

Where $\rho(\vec{r})$ is the electron density at position $\vec{r}$ in the unit cell. If x, y, and z are fractional coordinates in the unit cell ($0 \leq x < 1$; the same for y and z) and V is the volume of the unit cell, then is $dv = V \cdot dxdydz$ and $\vec{r} \cdot \vec{S} = (\vec{a} \cdot x + \vec{b} \cdot y + \vec{c} \cdot z) \cdot \vec{S} = hx + ky + lz$. Therefore, $\vec{F}(S)$ can be written as $\vec{F}(h\ k\ l)$:

$$\vec{F}(h\ k\ l) = V \int_{x=0}^{1} \int_{y=0}^{1} \int_{z=0}^{1} \rho(x\ y\ z) e^{(-2\pi i(hx+ky+lz))} dx\ dy\ dz.$$

Equation 7: Structure factor $\vec{F}(S)$ expressed as a function of h k l. Explanation can be found within the text.

To calculate now the electron density ρ at every position x, y, z in the unit cell, Fourier transformation has to be applied. $\vec{F}(h\,k\,l)$ is the Fourier transform of ρ (x y z), and vice versa. Consequently, ρ (x y z) can be expressed as a function of all $\vec{F}(h\,k\,l)$. Together with the information from the Laue conditions, that diffraction occurs only in discrete directions, the integration can be replaced by a summation. Considering $\vec{F} = |F|e^{i\alpha}$ we can also write:

$$\rho(x\,y\,z) = \frac{1}{V}\sum_h \sum_k \sum_l |F(h\,k\,l)|e^{-2\pi i(hx+ky+lz)+i\alpha(h\,k\,l)}.$$

Equation 8: Electron density ρ (x y z) of a crystal according to the Laue conditions. Explanation can be found within the text.

$|F(h\,k\,l)|$ terms can be easily obtained experimentally from the intensities of the scattered X-ray beam. However, the phase angles α(h k l) cannot be derived straightforward from the diffraction signals. This is also known as the 'crystallographic phase problem'.

Several methods are known to overcome this problem and obtain the phases which are lost during an experimental measurement. A more in-depth description can be found in (159). If the sequence identity of a structurally similar macromolecule is >25%, Molecular Replacement (MR) can be applied. Another method, the so called isomorphous replacement method implies the finding of heavy atoms which were added to the crystallized protein by soaking the protein in the heavy atom solution or co-crystallization. Differences in the reflection amplitudes of the heavy atom substituted and native crystal can be used to approximate the heavy atom structure factor amplitudes. Heavy atom positions can be determined using Patterson or direct methods. The protein phase angles can be estimated using the heavy atom phase angles.

The direct incorporation of selenomethionine into the protein during cellular expression can be used by anomalous scattering methods to calculate the phases. This method is using a phenomenon called anomalous differences, resulting from differences in reflection pairs $\vec{F}$(h k l) and $\vec{F}$(-h - k - l) when the energy of incident X-ray photons is almost equal to the absorption edge of an atom such as selenium. The reflection with indices (-h -k -l) is referred to as the Friedel mate of (h k l). The positions and thus the phase angles can be calculated from these anomalous scatterers.

The calculated electron density map (from direct methods, experimental phasing or molecular replacement) is than used to build a reasonable macromolecular model, and several cycles of refinement are necessary to obtain a model which is in good agreement with the experimental data (160). The agreement of the observed data and the model is given by the comparison of the observed structure factors with those of the calculated from the model. The R-factor evaluates the agreement between F_{obs}(h k l) and F_{calc}(h k l), and new phases are computed after each refinement step to update the electron density map. The refinement process therefore maximize the agreement between F_{obs}(h k l) and F_{calc}(h k l) by varying the parameter of the model.

2.4.4.1 Protein structure solution for the THOV NP

Initial molecular replacement trials with the native dataset of the apo form of THOV $NP^{\Delta 188\text{-}196}$ using the crystal structures of IFAV H1N1 NP (PDB code: 2IQH) and IFBV NP (PDB code: 3TJ0) were not successful. Consequently, SeMet-substituted protein was expressed (see 2.3.4) and crystallized in the apo form.

The phases for the THOV $NP^{\Delta 188\text{-}196}$ structure were obtained using the SAD method (single wavelength anomalous dispersion), and the 11 selenium atoms were found with SHELXD (161) using the anomalous signal of the peak data sets. Initial phases were calculated with the program SHELXE (161) and HKL2MAP (162).

2.4.5 Atomic model building and data refinement

Model building and fitting into the electron density map was done manually with COOT (154) using the homology model of THOV NP based on IFBV NP (PDB code: 3TJ0), and selenomethionine positions were used to allocate the sequence. Refinement has been done in Phenix (163) using TLS (Translational, libration, screw rotation displacement) refinement (164). 5% of the measured X-ray intensities were set aside from the refinement for cross-validation (165).

2.4.6 Structure analysis and figure preparation

The refinement process of the THOV NP$^{\Delta 188\text{-}196}$ structure is still in process, and so far 305 out of 445 amino acid side chains could be placed into the electron density map. The electrostatic surface calculations were performed in Chimera (166), the missing amino acid side chains were placed into the THOV NP$^{\Delta 188\text{-}196}$ structure with Swiss-PDBViewer (167), followed by an automated energy minimization step for local constraint release. The conservation plot was calculated using the Consurf server (168) and visualized with Chimera (166). Figures were prepared in PyMol (169) and Chimera (166).

3 Results

3.1 Nucleotide binding for G domain dimerization, GTPase activation and antiviral activity of MxA

To understand the role of nucleotide binding for the catalytic and antiviral mechanism of MxA, a combined biochemical and cell-based approach was chosen. Based on the crystal structure of the human dynamin 1 G domain dimer in the presence of a transition state mimic (88) and previous functional experiments (75), a systematic biochemical characterization of several previously described and novel MxA mutants in the G domain was performed to explore the mechanism of nucleotide binding and hydrolysis in MxA. For this project, I performed the biochemical experiments, whereas the cell-based experiments were performed by our collaboration partners Prof. Georg Kochs and Laura Graf, based on my cloned constructs. The majority of this work has been published in the Journal of Biological Chemistry (142).

3.1.1 Expression of G domain mutants

To generate the desired MxA point mutants for biochemical studies, a panel of MxA variants with mutations in the G domain were expressed as N-terminal His_6-fusions in *E. coli* and purified via affinity chromatography (see 2.3.3). After the final gel filtration run, the protein was at least 95% pure, as analyzed by SDS-PAGE (Figure 17A, B). The protein did not contain nucleotide retained from the bacteria, as analyzed by HPLC analysis (Figure 17C, see 2.3.8). Several of the generated point mutants were introduced into the background of a monomeric variant of MxA, MxA^{M527D}. This mutant harbors a mutation in the stalk domain that prevents higher order assembly (75), shows greater solubility than the wild-type (wt) protein and can be prepared in high quantities from bacterial lysates without aggregation. Nucleotide binding to this mutant can be measured reliably by isothermal titration calorimetry (ITC), without considering competing reactions such as higher order assembly via the stalk domains. A typical purification procedure is shown for MxA^{M527D} in Figure 17.

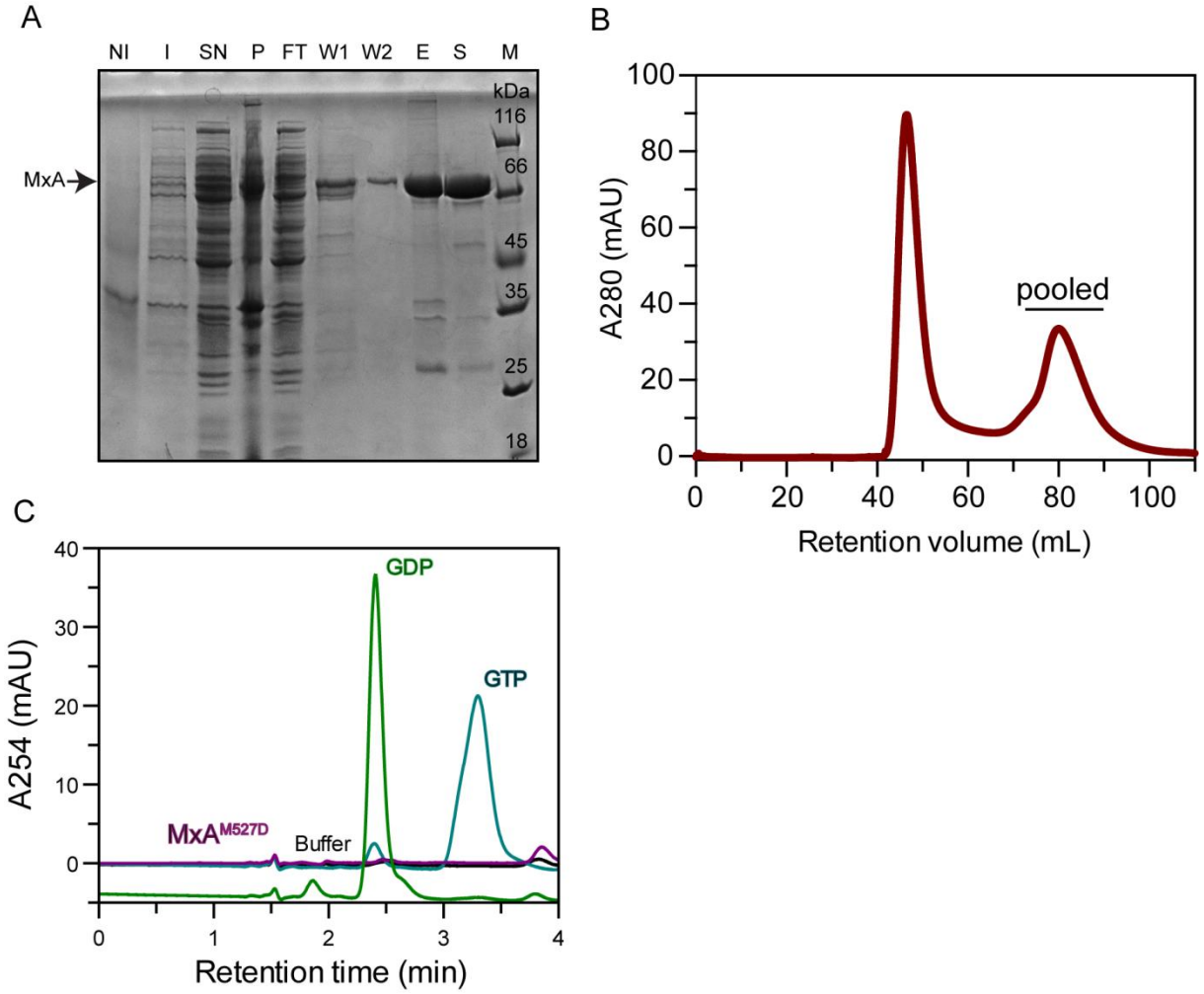

Figure 17: Expression and purification of hsMxA^{M527D}.

(A) SDS-PAGE of hsMxA^{M527D} purification. NI, whole cell *E.coli* lysate; I, IPTG-induced whole cell E. coli lysate; SN, supernatant fraction of the cell lysate; P, pellet fraction; FT, flow-through of the soluble extract on Ni^{2+}-NTA column; W1, flow-through of the high-salt and ATP wash (wash 1); W2, flow-through of the high-imidazole wash (wash 2); E, elution fraction; S,.SEC fractions 34-40; M, protein molecular weight marker. (B) Gel filtration profile of MxB^{M527D}. Pooled fractions are indicated. (C) The nucleotide-loading status of MxA analyzed by HPLC. The GTP standard is shown in cyan, GDP in green, buffer in black and purified MxA in purple. 40 µM of protein was applied.

3.1.2 The GTPase mechanism of MxA

To gain insights into the GTPase mechanism of MxA, I modeled the G domain dimer of MxA based on the structure of the GDP-AlF_4^--bound dynamin (88) (Figure 18A). The majority of the residues in the catalytic center are highly conserved between MxA and dynamin, for example, the G4 loop that mediates specificity for guanine binding (Figure 18B), suggesting a conserved catalytic mechanism of these proteins. The modeled dimer interface was recently confirmed by crystal structures of a stalkless MxA construct determined in the absence of nucleotide, in the presence of GDP or of the non-hydrolyzable GTP analogue GMP-PCP (77).

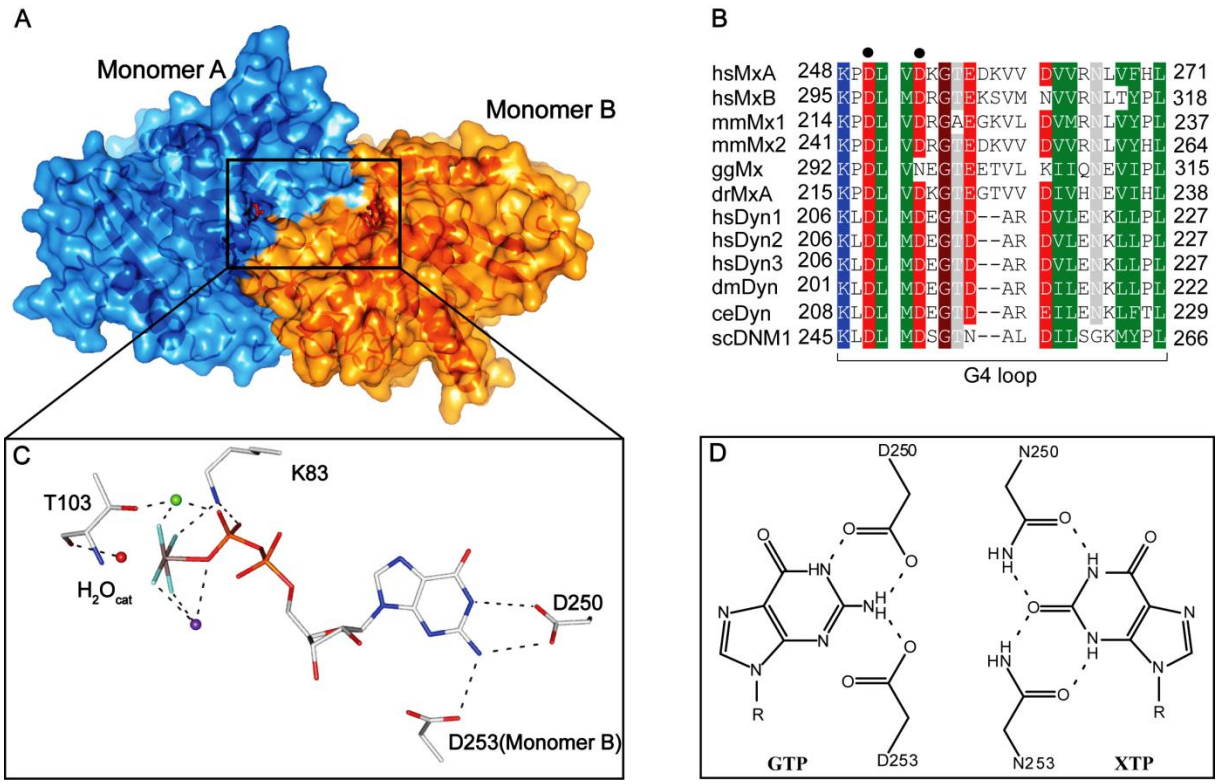

Figure 18: G domain architecture of MxA.

(A) Homology model of the MxA GTPase domain dimer (residues 69-340) based on the crystal structure of the human dynamin1 GTPase domain-BSE construct in the GDP-AlF_4^--bound state (pdb 2X2E). (B) Sequence alignment of Mx and dynamin proteins in the G4 loop. Sequences of human MxA (Swiss-Prot accession P20591), human MxB (P20592), mouse (mm) Mx1 (P09922), mmMx2 (Q9WVP9), chicken (gg) Mx (Q90597), zebrafish (dr) MxA (Q8JH68), human dynamin1 (Q05193), human dynamin2 (P50570), human dynamin3 (Q9UQ16), *Drosophila melanogaster* (dm) dynamin (P27619), *Caenorhabditis elegans* (ce) dynamin (Q9U9I9) and *Saccharomyces cerevisiae* (sc) dynamin-related protein DNM1 (P54861) were aligned and manually adjusted. Residues with a conservation of greater than 70% are color-coded (D, E in red; R, K, H in blue; N, Q, S, T in grey; A, L, I, V, F, Y, W, M, C in green and P, G in brown). Asp250 and Asp253 are marked with a dot. (C) Details of the catalytic site. The red ball represents the catalytic water, the green ball a Mg^{2+}- and the purple ball a Na^+-ion. Asp250 stabilizes the purine base in *cis* and Asp253 of the neighboring monomer binds to it in *trans*. (D, left) Scheme showing the proposed binding mode of the guanine base by D250 in *cis* and D253 of the opposing molecule in *trans.* (Right) Xanthosine base-binding by N250 and envisaged binding mode of N253. Hydrogen bonds are depicted as dashed lines.

For the present study, I focused on residues close to the catalytic center of the G domain (Figure 18C): Lys83 in the highly conserved phosphate-binding loop (130), Thr103 in the switch I region that is crucial for stabilizing the transition-state of GTP hydrolysis (131), Asp250 which contacts the purine base in *cis*, and Asp253 stabilizing the G interface by contacting the purine base of the opposing G domain in *trans* (Figure 18C).

Initially, I determined the nucleotide binding affinities of MxA^{M527D}. It bound to the slowly-hydrolysable GTP analogue GTPγS with an affinity of 15 µM (Figure 19A, Table 3 for a summary of all data), which was in agreement with previous measurements using fluorescence analysis (75).

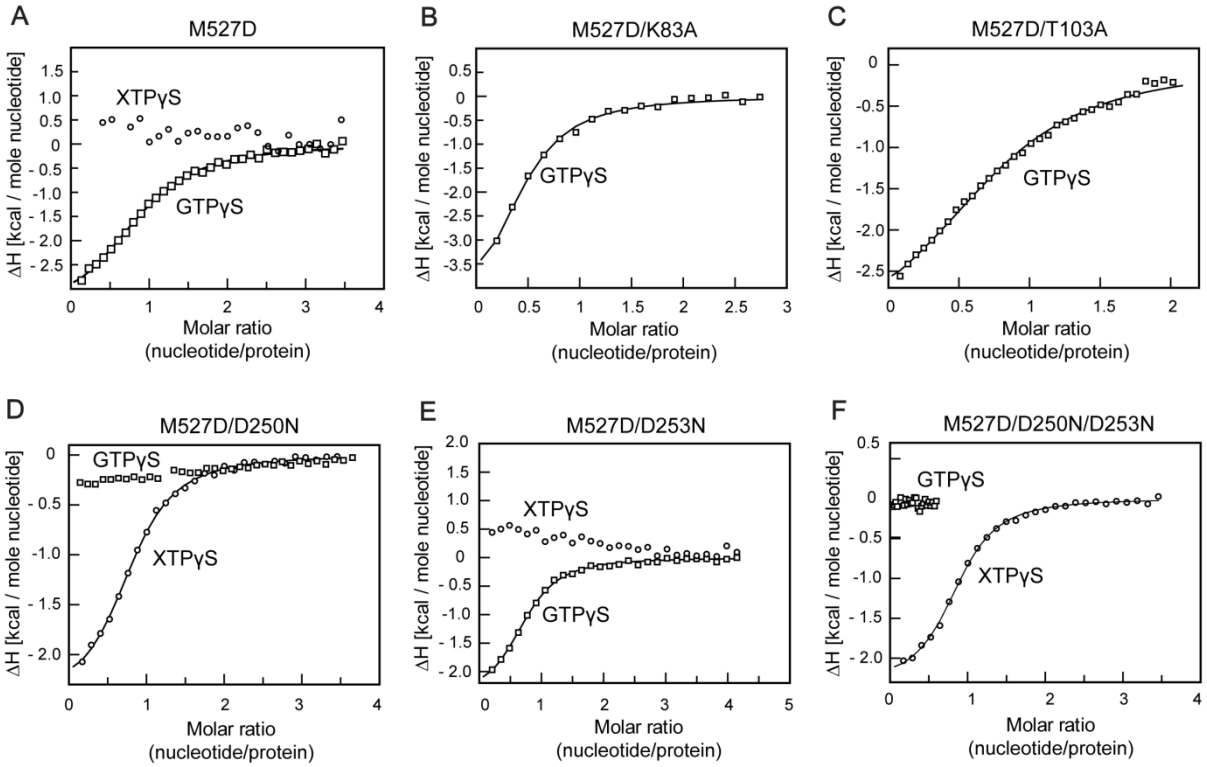

Figure 19: Nucleotide binding analysis.

1 mM solutions of the indicated nucleotide were stepwise titrated into 50 µM solutions of the indicated MxA mutants at 8°C in an ITC device. Resulting heat changes were integrated and the obtained values fitted to a quadratic binding equation. The corresponding K_D values were derived from the fittings. (A) M527D for GTPγS: K_D=15±1 µM, n=0.92±0.02, (B) M527D/K83A for GTPγS: K_D=39±6 µM, n=0.42±0.03, (C) M527D/T103A for GTPγS: K_D=28±2 µM, n=0.81±0.02, (D) M527D/D250N for XTPγS: K_D=7.8±0.5 µM, n=0.82±0.01, (E) M527D/D253N for GTPγS: K_D=9±1 µM, n=0.73±0.01 and (F) M527D/D250N/D253N for XTPγS: K_D=5.6±0.4 µM, n=0.87±0.01. GTPγS (□), XTPγS (○). Due to the reduced heat signal upon nucleotide binding, higher protein and ligand concentrations were used for the T103A and K83A mutants. For K83A, this resulted in increased protein precipitation that may explain the lower binding number.

In gel filtration experiments, the MxA^{M527D} mutant eluted as a monomer in the presence of GTPγS, GDP or in the absence of nucleotide (Figure 20). However, in the presence of GDP-AlF_4^-, that mimics the transition state of GTP hydrolysis, MxA^{M527D} dimerized, suggesting that trapping of the GTPase transition-state is accompanied by G domain dimerization (Figure 20A).

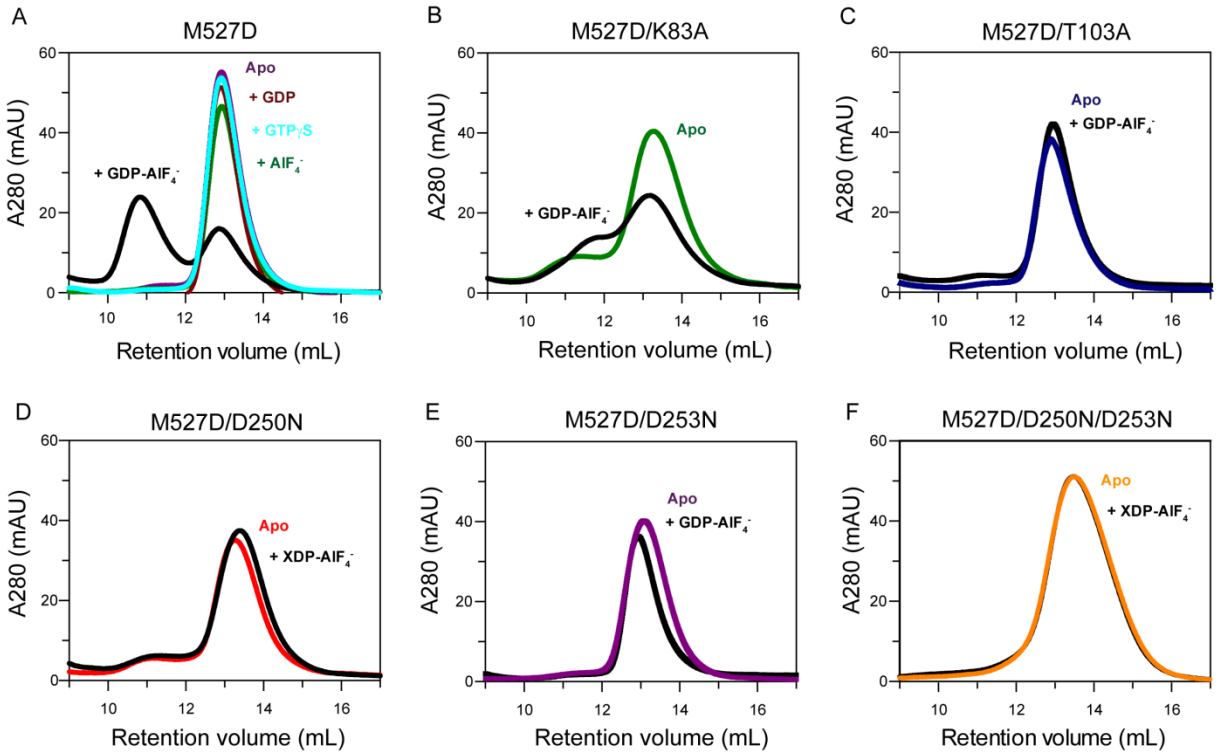

Figure 20: Analytical gel filtration analysis.

Upon 15 min incubation with 2 mM of the indicated nucleotide solutions, 50 µl of the indicated MxA mutants at a concentration of 2 mg/mL were applied to an S200 gel filtration column. (A) M527D with GTPγS, GDP-AlF_4^-, GDP, AlF_4^- alone or in the absence of nucleotides. (B) M527D/K83A, (C) M527D/T103A, (D) M527D/D250N, (E) M527D/D253N and (F) M527D/D250N/D253N in the absence and presence of the indicated nucleotides.

Mutation	K_D for GTPγS (µM)*	K_D for XTPγS (µM)*	k_{obs} for GTP (min^{-1})*,#	k_{obs} for XTP (min^{-1})*,#	Dimerization (GDP-AlF_4^-)*	THOV NP binding	FLUAV/THOV antiviral activity
wild type	15 ± 1	No binding	21.6 ± 0.1	n.d.	+++	Yes	Yes
K83A	39 ± 6	n.d.	< 1	n.d.	+	Yes	No
T103A	28 ± 2	n.d.	< 1	n.d.	-	Yes	No
V185Y	n.d.	n.d.	n.d.	n.d.	n.d.	Yes	No
D250N	No binding	7.8 ± 0.5	< 1	< 1	- (XDP-AlF_4^-)	Yes	No
D253N	9 ± 1	No binding	< 1	< 1	-	Yes	No
G255E	n.d.	n.d.	1.6 ± 0.1	n.d.	-	n.d.	No
V268M	n.d.	n.d.	7.7 ± 0.1	n.d.	+	n.d.	Reduced
D250N+D253N	No binding	5.6 ± 0.4	< 1	< 1	- (XDP-AlF_4^-)	Yes	No

Table 3: Summary of the biochemical and antiviral activity of the studied mutants.

*** experiments were performed with the monomeric M527D mutant**
 # at 20 µM protein concentration
n.d. – not determined

In agreement with previous results (75), MxA^{M527D} showed a robust intrinsic GTPase activity that cooperatively increased with higher protein concentrations (Figure 21), again indicating that the formation of a G interface leads to stimulated GTP hydrolysis.

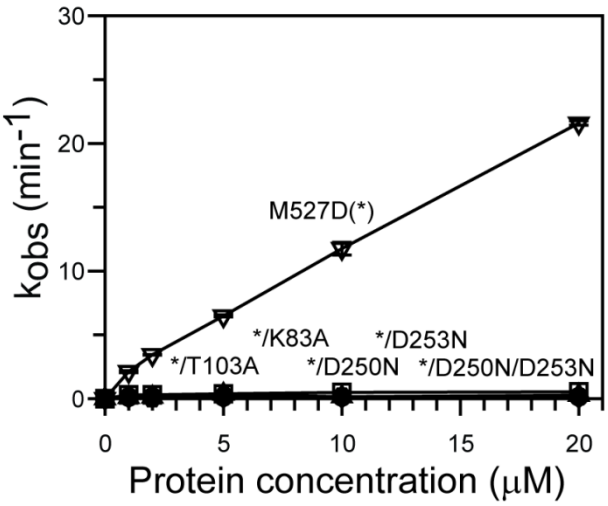

Figure 21: Protein concentration-dependent GTPase/XTPase activity of MxA mutants.

All reactions were carried out in the presence of 1 mM nucleotide at 37°C and GTP/XTP hydrolysis was monitored by HPLC analysis. The mean k_{obs} was calculated from two independent experiments for each concentration, with the error bar showing the range of the two data points. M527D (GTP) (∇), M527D/K83A (GTP) (◇), M527D/T103A (GTP) (⬢), M527D/D250N (XTP) (Δ), M527D/D253N (GTP) (□), M527D/D250N/D253N (XTP) (○). The asterisk represents the M527D mutation.

Lys83 in MxA is located in the P-loop, suggesting that it may be involved in phosphate binding. In dynamin, the corresponding K44A mutant was originally designed as a GTP-binding deficient mutant, based on homology to the Ras GTPase (170). In dynamin, the K44A mutant is now widely used to block clathrin-mediated endocytosis (171). Interestingly, recent cryo EM data show that the dynamin K44A mutant can form a super-constricted helix in the presence of GTP (172). This data suggested the K83A mutation might affect GTP binding in MxA (130). Nevertheless, the ITC assays showed binding of GTPγS by MxA$^{M527D/K83A}$ with a dissociation constant of 39 µM, i.e. with a slightly reduced affinity compared to MxA^{M527D} (Figure 19B). Dimerization of this mutant in the presence of GDP-AlF_4^- was greatly reduced (Figure 20B) and nucleotide hydrolysis was completely blocked for MxA$^{M527D/K83A}$ (Figure 21).

Thr65 in dynamin is located in switch I and was shown to stabilize the attacking water molecule for GTP hydrolysis via a main chain interaction (88). Furthermore, the side chain of Thr65 coordinates the catalytic Mg^{2+}-ion. The T65A mutation was proposed to affect only GTP hydrolysis (173), although others suggested it may reduce nucleotide binding as well (174). The corresponding T103A exchange in MxA was considered to block GTP hydrolysis, but not GTP

binding (131). In ITC experiments, $MxA^{M527D/T103A}$ bound GTPγS with a slightly reduced affinity (K_D = 28 µM) compared to MxA^{M527D}, indicating that the T103A exchange did not considerably affect nucleotide binding (Figure 19C). However, this mutant did not dimerize in the presence of GDP-AlF_4^- (Figure 20C) and showed a complete loss of basal and stimulated GTPase activity (Figure 21), suggesting that it cannot stabilize a GTPase transition-state.

To create a bona-fide GTP-binding deficient mutant, I turned towards an amino acid exchange in the guanine-nucleotide substrate specificity (G4) motif. The mutation of an aspartate to an asparagine in the G4 motif of the small GTPase Ras and the signal recognition particle GTPase (99,175,176), abrogates GTP binding and allows binding of the related XTP. In agreement with these observations, also the corresponding MxA mutant $MxA^{M527D/D250N}$ lost its ability to bind GTPγS, but bound XTPγS with a dissociation constant of 7.8 µM (Figure 18D, Figure 19D), whereas MxA^{M527D} did not bind to XTPγS with appreciable affinity (Figure 19A). However, addition of XDP-AlF_4^- did not result in dimerization of $MxA^{M527D/D250N}$ (Figure 20D), and the mutant neither showed stimulated XTPase activity (Figure 21) nor GTPase activity (data not shown). Thus, not only nucleotide binding, but also the nature of the bound nucleotide itself contributes to dimerization and dimerization-stimulated GTP hydrolysis.

In dynamin, Asp211 adjacent to the G4 motif mediates dimerization by contacting the nucleotide in the opposing molecule via a contact to the guanine base (88). This residue is also conserved in MxA (Asp253) and contacts the guanine base (Figure 18C) (77). I reasoned that the lack of XTPase reaction in $MxA^{M527D/D250N}$ mutant might be caused by the inability of Asp253 to contact the xanthosine base in *trans*. To explore this hypothesis, I sought to restore this putative contact in MxA by additionally introducing the D253N mutation, which in principle should be able to form two hydrogen bonds with the xanthosine base in *trans* (Figure 18D). The $MxA^{M527D/D253N}$ mutant bound GTPγS with comparable affinity to MxA^{M527D} (K_D = 9 µM) (Figure 19E), but did not dimerize in the presence of GDP-AlF_4^- (Figure 20E). It also did not display any GTPase activity (Figure 21), indicating an involvement of D253 in dimerization-induced catalysis of MxA. The $MxA^{M527D/D250N/D253N}$ mutant bound with a dissociation constant of 5.6 µM to XTPγS but not to GTPγS (Figure 19F). However, also for this mutant, I did not observe XDP-AlF_4^--induced dimerization (Fig. 3F) and no stimulated XTPase (Figure 21) and GTPase (data not shown) activity, indicating that the D253N mutation cannot restore a putative contact to XTP in *trans*. I speculate that the D250N mutant binds the xanthosine base with a slightly different geometry compared to the genuine guanine-base binding mode. Such a difference may then affect the overall geometry of the catalytic site in a way that is not compatible with G domain dimerization and initiation of nucleotide hydrolysis.

3.1.3 A single intact catalytic center is sufficient for nucleotide hydrolysis

To further characterize the requirements for formation of the G domain interface, I analyzed the ability of the different mutants to stimulate the GTPase activity of the wt G domain of monomeric MxA^{M527D} in a mixed GTPase assay. For these experiments, I employed a constant low concentration of 2.5 µM of MxA^{M527D} and added increasing amounts of MxA$^{M527D/T103A}$, a mutant defective in GTP hydrolysis, nucleotide binding (D250N) or G interface formation (D253N). Strikingly, the monomeric T103A mutant stimulated the GTPase activity of MxA^{M527D} as efficiently as monomeric MxA^{M527D}, (compare Figure 22A with Figure 21) whereas the G interface mutant D253N was a less potent activator, indicating that one functional GTPase site is sufficient for the formation of a functional G interface with a GTP-binding competent mutant.

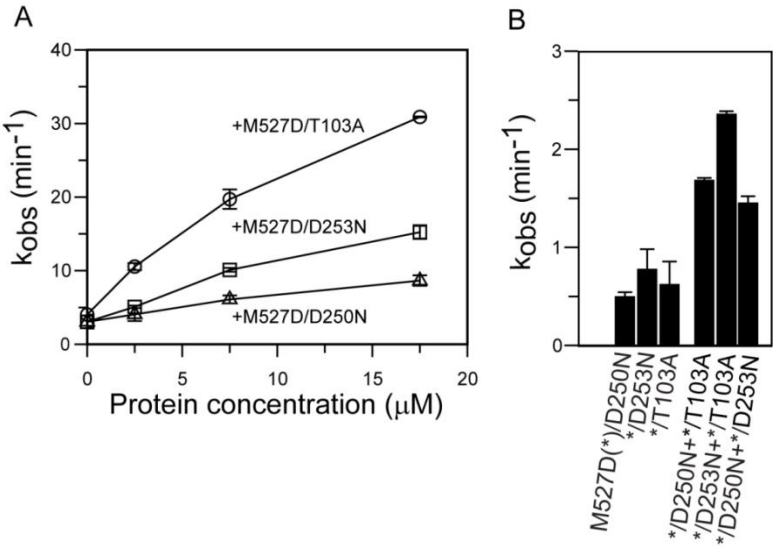

Figure 22: Analysis of the GTPase activity.

(A) The GTPase activity of M527D can be stimulated by monomeric G domain mutants of MxA. 2.5 µM of M527D was incubated with the indicated concentrations of the corresponding mutant (see x-axis). The mean k_{obs} calculated from two independent experiments is indicated, with the error bar showing the range of the two data points. M527D+M527D/T103A (○), M527D+M527D/D250N (Δ), M527D+M527D/D253N (□). (B) Mixed GTPase assays. 37.5 µM of each indicated M527D mutant was used. The mean k_{obs} was calculated from two independent experiments, with the error bar showing the range of the two data points. When two monomeric G domain mutants were incubated together, their GTPase reactions were mostly additive, e.g. no significant additional GTPase stimulation was observed.

The GTP-binding deficient D250N mutant showed only minor GTPase activation of MxA^{M527D}, indicating that the loss of nucleotide binding (D250N) in one molecule interferes with dimerization-induced GTP hydrolysis. GTP hydrolysis by the monomeric T103A, D250N or

D253N mutants could not be restored by any of the other defective mutants (Figure 22B), indicating that defects in both partner molecules completely abrogate GTPase activity.

3.1.4 Nucleotide binding and hydrolysis are required for the antiviral function of MxA

In hand of the biochemically described set of G domain mutants, we explored the role of nucleotide binding and hydrolysis for the antiviral activity of MxA. Initially, the inhibition of the polymerase complex of THOV, which shows high sensitivity to the antiviral effect of MxA (177,178) was investigated. A minireplicon reporter assay was used to study the polymerase activity of THOV (79). For the reconstitution of vRNPs, we co-expressed the viral polymerase subunits and the viral NP, together with an artificial RNA minigenome encoding the *firefly* luciferase reporter gene. These vRNPs are active in transcription and replication of the minigenome. Additional expression of wt MxA suppressed viral polymerase activity to 2% relative to control (Figure 23A). Interestingly, all G domain amino acid substitutions tested led to a partial or complete loss of the antiviral function (Figure 23A, Table 3) indicating that the complete cycle of GTP binding, hydrolysis and G domain dimerization is crucial for the antiviral effect.

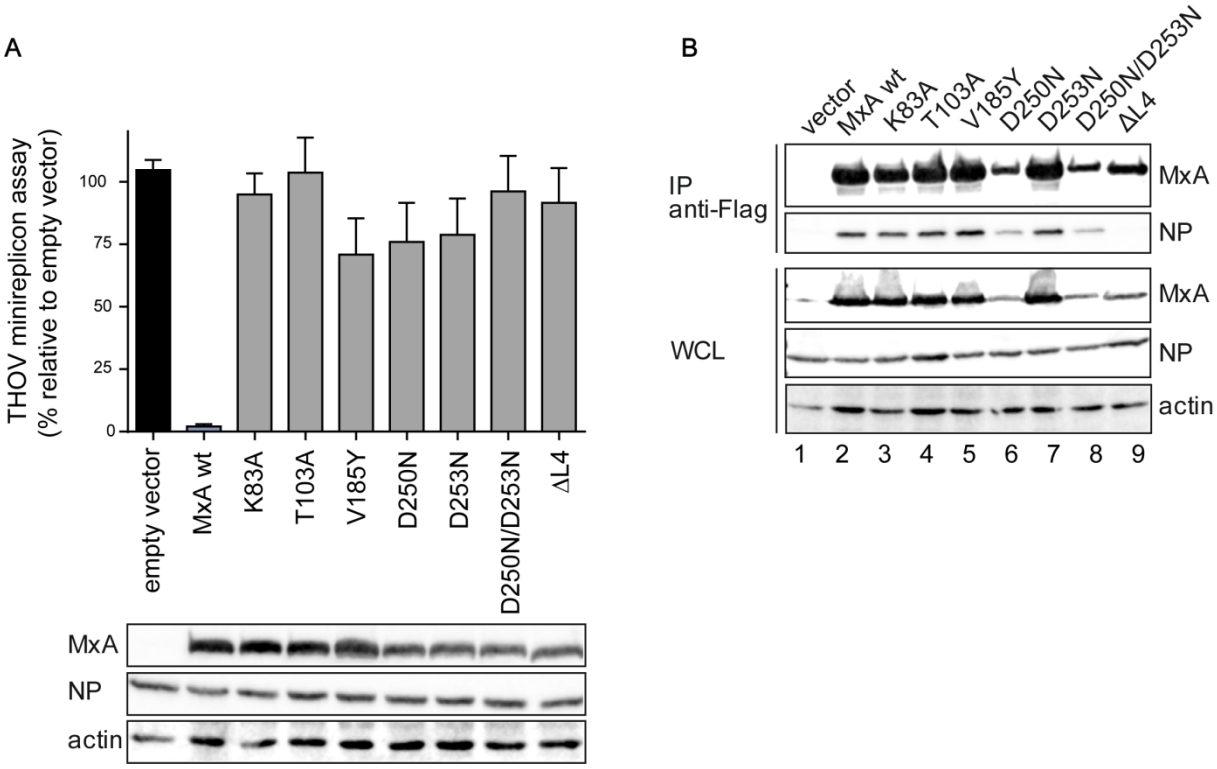

Figure 23: G domain mutants interact with the viral NP.

(A) 293T cells were co-transfected with expression plasmids for the THOV-minireplicon system, consisting of the viral polymerase subunits (10 ng each), NP (50 ng), and the pPolI-FF-Luc minigenome encoding *firefly* luciferase (50 ng) as well as expression plasmids for MxA or MxA mutants (100 ng) for 24 h. *Firefly* luciferase activity determined in the cell lysates was normalized to the activity of *Renilla* luciferase encoded by the co-transfected pRL-SV40 plasmid (10 ng). The activity in the absence of MxA, empty vector control, was set to 100%. Results are presented as means of technical duplicates of three independent experiments. Protein expression of Flag-tagged Mx, viral NP, and β-actin were determined by Western blot analysis. (B) Co-precipitation of viral NP with MxA. 293T cells were transfected with Flag-tagged MxA constructs and infected with THOV (10 MOI). At 24 h post infection, the cell lysates were subjected to Flag-specific immunoprecipitation. Flag-MxA and co-precipitated THOV-NP as well as whole cell lysates (WCL) were analyzed by Western blot. One representative result for three individual experiments is shown. These experiments were performed by Laura Graf in Freiburg.

A direct interaction of MxA with the NP of THOV, the major constituent of the viral RNPs, has been demonstrated (179). It involves loop L4 at the tip of the stalk that directly interacts with the viral NP (79) (see also 1.6.3). To test the influence of the G domain mutations on viral target interaction, cells expressing the respective Flag-tagged MxA mutants were infected with THOV, and viral NP was co-precipitated from the cell lysates using a Flag-specific antibody. Only in the presence of wt MxA, we were able to co-precipitate the viral NP, but not by an MxA mutant with a deletion of loop L4 (ΔL4) which represents the putative NP interaction site (Figure 23B, lane 9) (79). Interestingly, in pull-down experiments, the G domain mutants K83A, T103A, D250N, D253N, D250N/D253N efficiently precipitated THOV NP from the infected cells (Figure 23B). V185Y was included in the analysis because this exchange was recently shown to disrupt formation of the G interface (77). This mutant also bound efficiently

to the NP (Fig. 5B, lane 5), but showed reduced antiviral activity (Figure 23A). These results indicate that nucleotide binding and hydrolysis of MxA are not required for THOV RNP binding but are essential for executing the subsequent antiviral effect against THOV.

Similarly, the inhibition of a highly pathogenic H5N1 influenza A virus (180) was assessed using a previously described minireplicon reporter assay for IFAV (138). In these assays, wt MxA inhibited viral replication by 80% (Figure 24A). However, all tested G domain mutations completely abrogated antiviral activity.

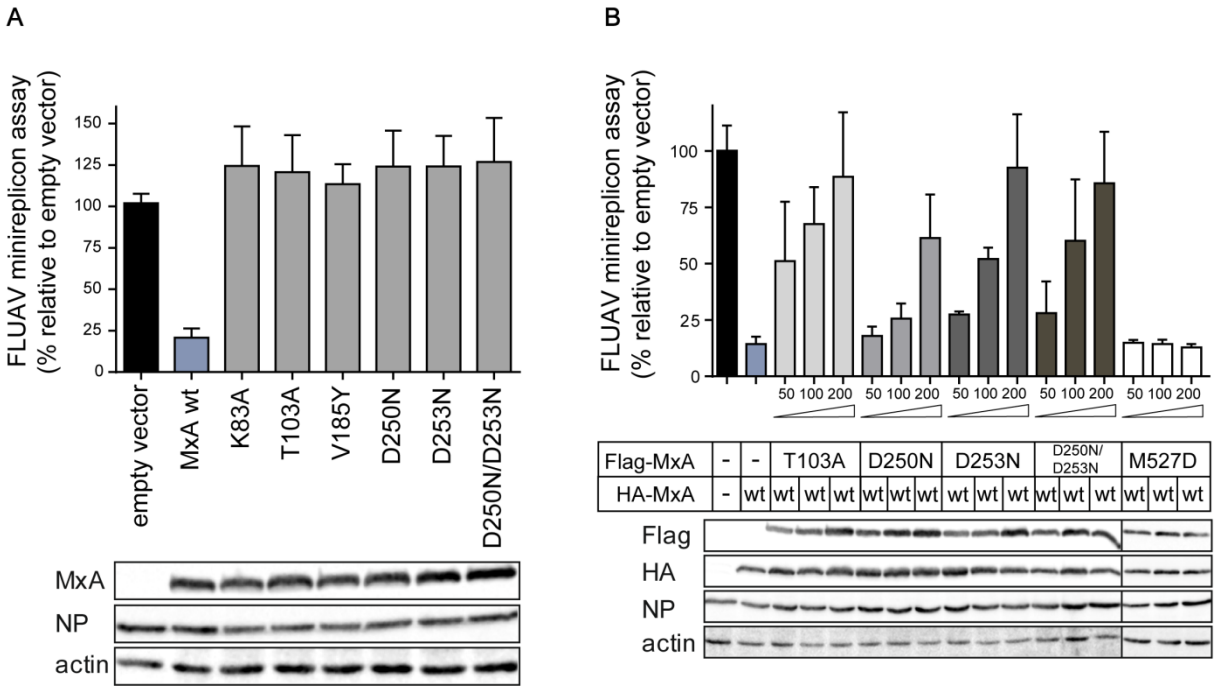

Figure 24: A functional GTPase is crucial for antiviral activity.

(A) 293T cells were co-transfected with expression plasmids for the IFAV minireplicon system of VN/04, consisting of the viral polymerase subunits (10 ng each), NP (100 ng), and the pPolI-FF-Luc minigenome encoding *firefly* luciferase under the control of the viral promoter (50 ng) as well as expression plasmids for MxA or MxA mutants (300 ng). After 24 h, *firefly* luciferase activity was determined in the cell lysates and normalized to the activity of *Renilla* luciferase encoded by the co-transfected pRL-SV40 plasmid (10 ng). The activity in the absence of MxA, empty vector control, was set to 100%. Protein expression of Flag-tagged MxA, viral NP, and β-actin were determined by Western blot analysis. (B) Dominant-negative effect of MxA mutants on wt MxA activity. HA-tagged wt MxA (300 ng) was co-transfected with the components of the VN/04 minireplicon system as described for panel A and increasing amounts (50 ng, 100 ng, 200 ng) of the indicated Flag-tagged MxA mutants. Results are presented as means of technical duplicates of three independent experiments. These experiments were performed by Laura Graf in Freiburg.

To further explore the effect of these mutants, co-expression of some of these mutants with wt MxA was performed, expecting a stimulatory effect, as detected for the stimulation of the GTPase activity in Figure 22A. Interestingly, the co-expressed the G domain mutants even at low concentrations, interfered with the antiviral activity of wt MxA in a dominant-negative fashion (Figure 24B). However, the oligomerization-defective mutant MxA^{M527D} that was

shown to be antivirally inactive (75) did not affect the antiviral activity of wt MxA in these co-expression experiments, presumably because it is not incorporated into wt MxA oligomers due to its inability to for higher-oligomers. This suggests that incorporation of GTP-binding or GTPase-deficient MxA molecules into a hetero-oligomeric complex hampers the antiviral activity of wt MxA.

3.1.5 Role of nucleotide binding and hydrolysis in formation of cytoplasmic MxA assemblies

To further characterize the role of GTP binding and hydrolysis on intracellular distribution of MxA, we transfected HeLa cells with the different GTP binding deficient mutants and analyzed their localization by immunofluorescence using a MxA specific antibody (181). In agreement with previous data, wt MxA showed a diffuse cytosolic staining with some punctate structures (Figure 25).

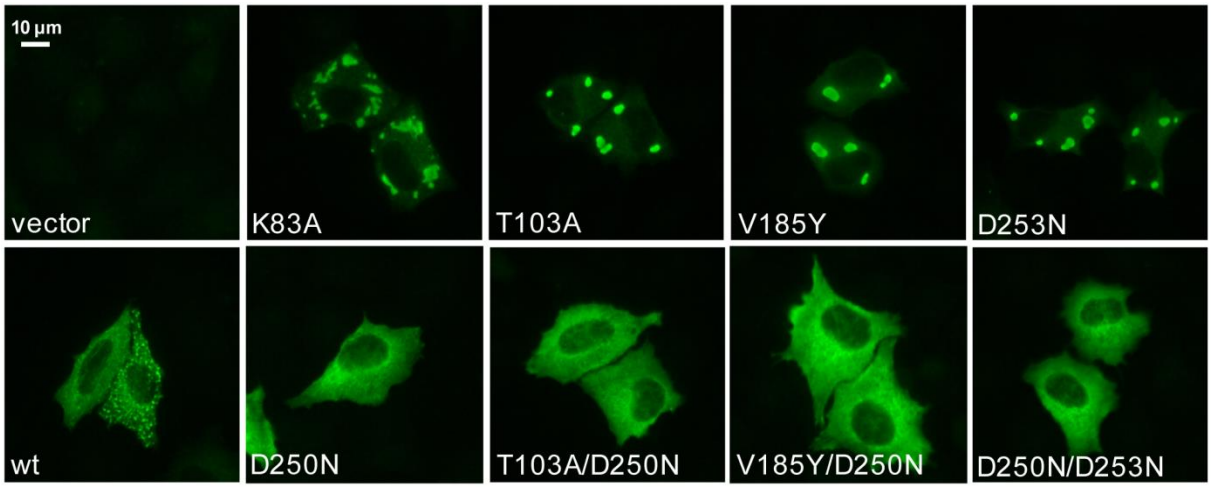

Figure 25: Intracellular distribution of MxA G domain mutants.

HeLa cells were transfected with expression plasmids for wt MxA or MxA mutants (50 ng). 24 h post transfection, cells were fixed and stained with a specific antibody against MxA. Results are representative of three individual experiments. These experiments were performed by Laura Graf in Freiburg.

These structures co-localized with Syntaxin 17, a marker of the smooth ER indicating an association of wt MxA with this membrane compartment (Figure 26), as reported previously (101). In contrast, the GTPase-deficient mutants, K83A, T103A, V185Y and D253N, that showed GTP binding but no GTP hydrolysis, aggregated in large cytosolic clusters (Figure 25). These clusters also co-localized with the smooth ER marker Syntaxin 17 (Figure 26). However, MxA^{D250N}, the only mutant defective in GTP binding, showed a cytosolic distribution without

punctate aggregates (Figure 25), pointing to a role of GTP binding for the formation of intracellular MxA assemblies that are associated with Syntaxin 17-positive membranes. This finding was supported by the observation that introduction of the D250N mutation into GTPase-deficient MxA mutants also led to an cytoplasmic distribution, as shown for MxA^{T103A}, MxA^{V185Y}, and MxA^{D253N} versus the respective double mutants (Figure 25 and Figure 26).

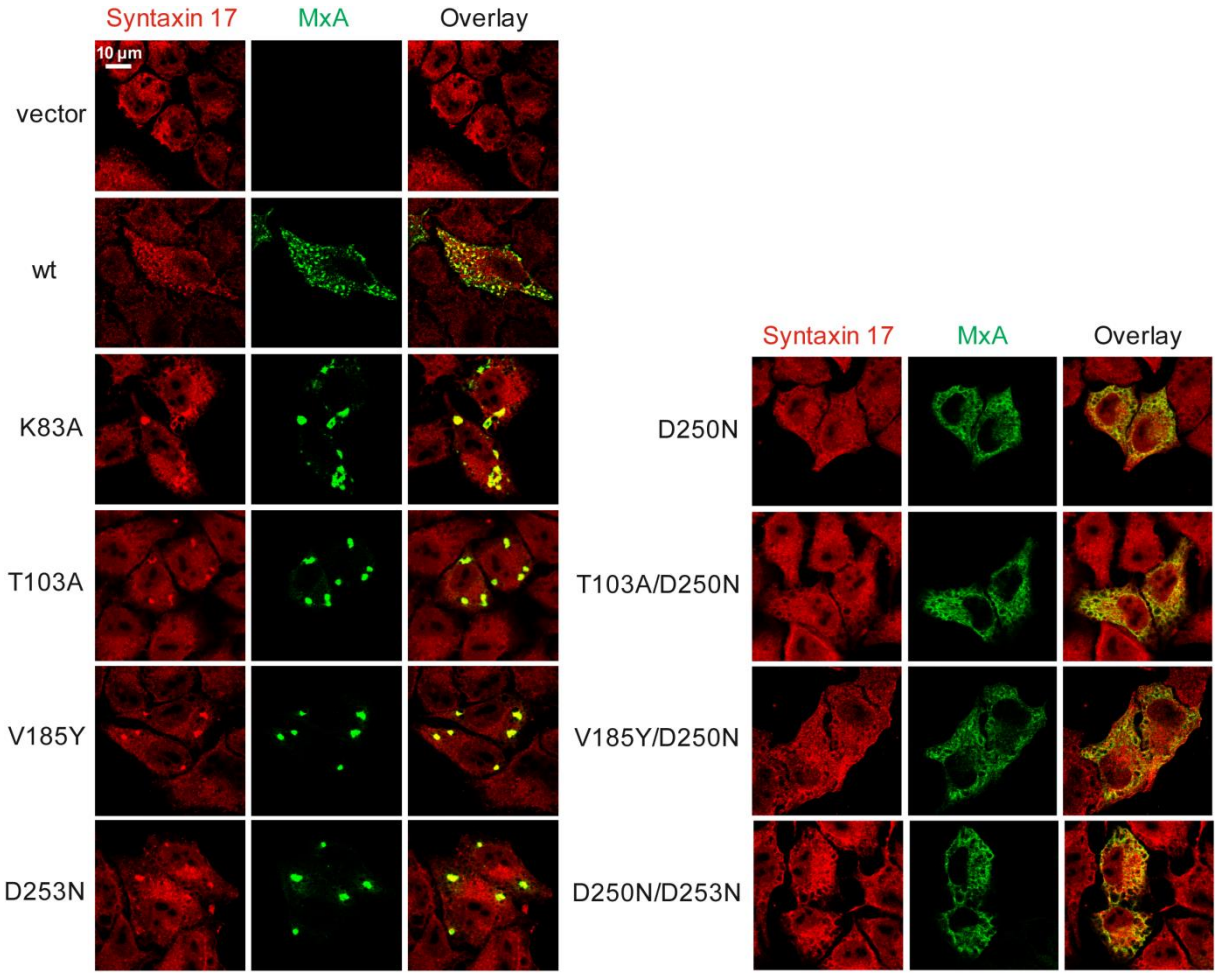

Figure 26: Co-localization study of MxA G domain mutants with Syntaxin 17.

HeLa cells were transfected with expression plasmids for wt MxA or MxA mutants (50 ng). At 24 h post transfection, cells were fixed and stained with specific antibodies against MxA (green) and Syntaxin 17 (red). Immunofluorescence analysis was performed using a confocal laser-scanning microscope. These experiments were performed by Laura Graf.

In further experiments, we tested the intracellular redistribution of the MxA mutants induced by LACV infection. LACV replicates in the cytoplasm, and the viral nucleoprotein (N) accumulates in the Golgi area at a late phase of the replication cycle (Figure 27, vector, white arrow).

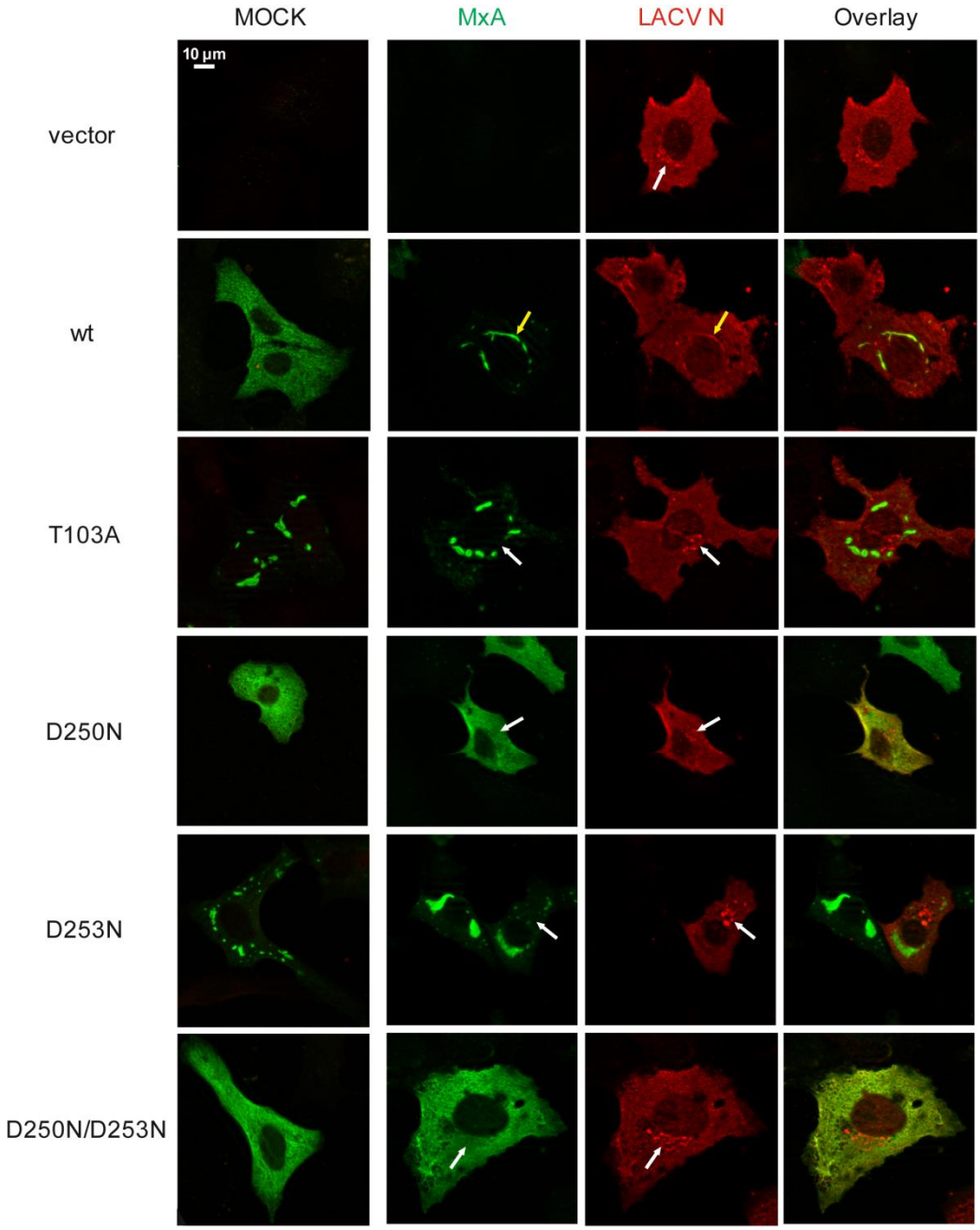

Figure 27: Complex formation of MxA with the LACV nucleoprotein (N).

Vero cells were transfected with the indicated MxA expression constructs (50 ng) and infected with LACV. At 18 h post infection, cells were fixed and immunofluorescence analysis was performed using specific antibodies against MxA (green) and LACV-N (red). The mock panel shows overlay images of transfected and mock-infected cells. The white arrows indicate accumulation of N protein in the Golgi area that is devoid of an MxA signal. In wt MxA-expressing cells, yellow arrows indicate formation of ER resident MxA-N assemblies. Experiments were performed by Laura Graf.

During the process of MxA-mediated restriction of LACV replication, MxA was able to associate with newly synthesized viral N protein and sequesters it into large perinuclear MxA-N assemblies, which could be used as a readout for the antiviral effect (104). Accordingly, wt MxA formed the characteristic perinuclear assemblies with the viral N upon infection with LACV (Figure 27, wt, yellow arrow). In contrast, the GTPase-deficient mutants, MxA^{T103A} and

MxA^{D253N}, that spontaneously aggregated into MxA assemblies, did not show obvious redistribution upon viral infection and thus did not limit viral replication, as indicated by the localization of N to the Golgi area (Figure 27, white arrows). Interestingly, the GTP-binding deficient mutants MxA^{D250N} and $MxA^{D250N/D253N}$ showed a diffuse cytoplasmic staining pattern and did not form a complex with viral N (Figure 27). Taken together, these results suggest that MxA mutants defective in GTP binding, G domain dimerization and GTP hydrolysis lose antiviral activity against orthomyxoviruses and LACV.

3.1.6 G255E and V268M are natural genetic variations in the putative G interface

Human MxA is highly conserved with only few allelic variations in the human population. A recent analysis of genomic DNA from healthy individuals identified some rare variants in the *MX1* gene (182). Two of them are located in the G interface and lead to an exchange of glycine to glutamic acid at position 255 and valine to methionine at position 268, respectively (182) (Figure 28A).

I tested whether these polymorphisms affect the catalysis and function of MxA. Interestingly, the $MxA^{M527D/V268M}$ and $MxA^{M527D/G255E}$ mutants displayed reduced or a complete loss of GDP-AlF_4^--induced dimerization (Figure 28B, C). Correspondingly, these polymorphisms also led to a reduction and a complete loss of GTPase activation, respectively (Figure 28D), suggesting that these mutations decrease the capacity to form a functional G interface to different extents. Furthermore, the G255E mutation completely abolished the antiviral activity of MxA in the IFAV minireplicon assay and led to cytoplasmic aggregates when expressed in HeLa cells. The MxA^{V268M} mutant showed a slight, but significant reduction of antiviral activity (Figure 28E) and a diffuse cytosolic staining with small punctate assemblies that were different from the few large aggregates formed by MxA^{G255E}. The pattern was reminiscent of that observed for wt MxA (Figure 28F, Figure 25).

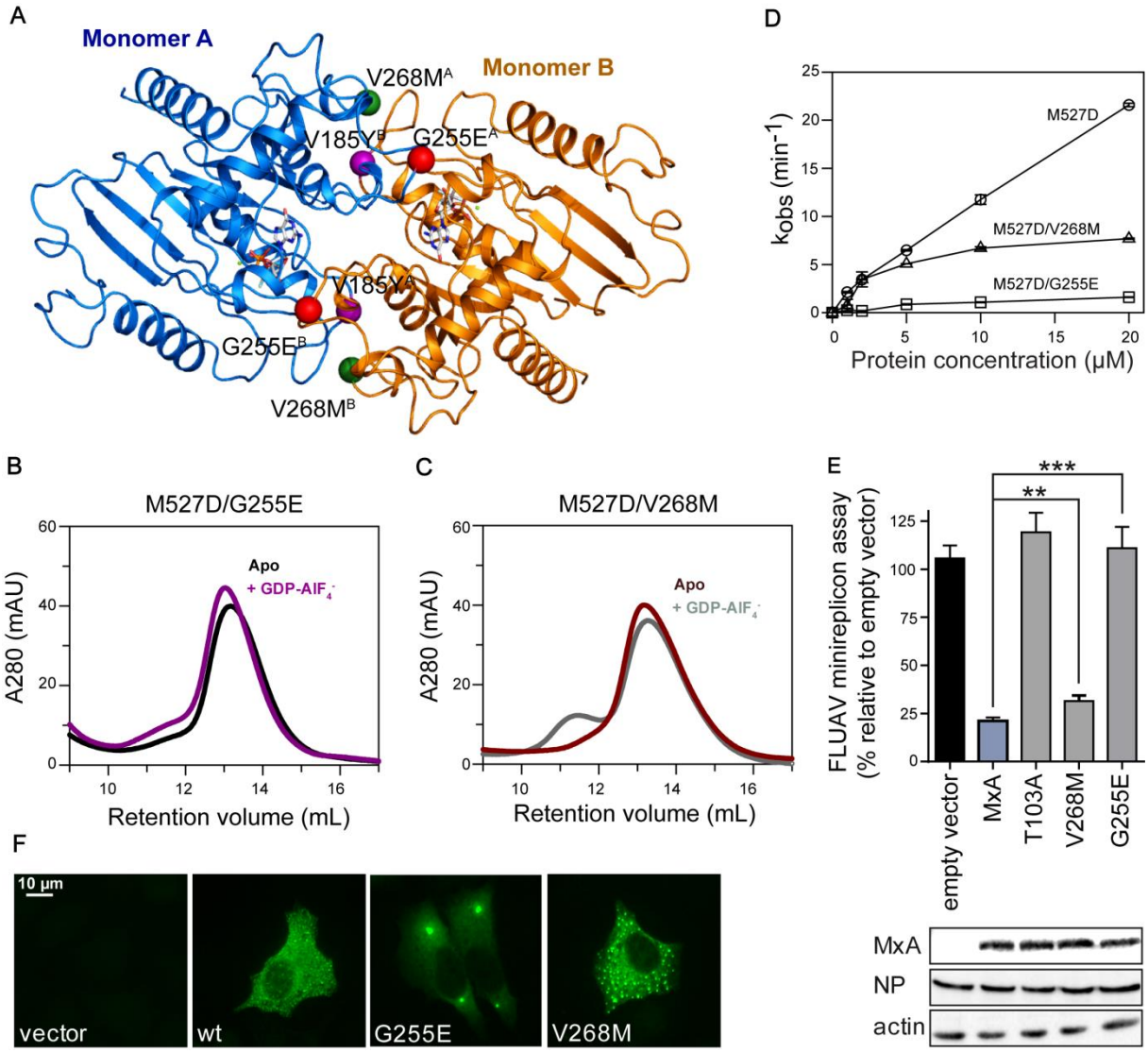

Figure 28: Effects of MxA polymorphisms in the G interface.

(A) Homology model of the MxA GTPase domain dimer as in Figure 18A. Interface residues are depicted as balls: V185 (purple), G255 (red), V268 (green) with the subscript indicating monomer A or B, respectively. (B and C) Analytical gel filtration analysis of M527D/G255E and M527D/V268M as in Figure 20. (D) Protein concentration-dependent GTPase activities of M527D (○), M527D/V268M (□) and M527D/G255E (Δ) as in Figure 21. (E) IFAV-minireplicon system of VN/04, as described in Figure 24A. Significance was calculated with Student's t test (n=3). **p=0.0058; ***p=0.0002. (F) Intracellular distribution of G255E and V268M in HeLa cells, as in Figure 25. Experiments in E and F were performed by Laura Graf.

3.2 Biochemical characterization of the human MxB GTPase

MxA and MxB share 63 % sequence identity and despite minor differences like a 43 residue N-terminal extension in MxB, which contains a nuclear localization signal within the first 25 residues (NLS, nuclear MxB), they show a high degree of structural similarity (see 1.6) (80,81). Recently it was shown, that the myxovirus resistant protein 2 (Mx2 or MxB), but not MxA, is an interferon-induced potent inhibitor of the human immunodeficiency virus type I (HIV-I) (70-72). Furthermore, it was shown that MxB inhibits HIV-I nuclear import by interacting with the viral capsid protein or destabilization of the nuclear viral DNA (70-72). MxA has no antiviral activity against HIV-I but is a potent restriction factor for DNA and RNA viruses like the *Orthomyxoviridae* family (IFAV, THOV). MxA interacts and blocks the import of vRNPs into the nucleus. Interestingly, it was postulated that the MxB antiviral activity is nucleotide-independent (72), which is contrary to the GTP-dependent antiviral activity of MxA (75,76). In the following chapter, I sought to biochemically characterize the MxB protein to deduce possible differences to MxA which may be important for the differential antiviral spectrum.

3.2.1 Expression of a soluble MxB construct

To get sufficient amounts of a soluble MxB construct for subsequent biochemical characterization, the human MxB cDNA was cloned into a bacterial expression vector (see 2.2), expressed in *E. coli* and purified via affinity chromatography and gelfiltration (see 2.3.3). Most of the MxB constructs listed in Table 2 (see 2.2.10) were insoluble, even in high salt conditions (500 mM NaCl) and therefore not suitable for biochemical characterization. Nonetheless, I could generate a soluble constructs, $MxB^{\Delta N85/\Delta L4}$ (L4 corresponds to amino acid 580-609), and the point mutant T151A of this construct. T151 in MxB corresponds to T103A in MxA, and the T103A exchange in MxA was shown to block GTP hydrolysis, but not GTP binding (see 3.1.2 and 3.1.3).

As an example, the purification of $MxB^{\Delta N85/\Delta L4}$ is illustrated in Figure 29. Figure 29C shows the gel filtration chromatogram of the purified protein. Despite a relatively high tendency of aggregation, a reasonable fraction of a lower order species could be obtained (Figure 29C, Fractions from 60-70 mL) for biochemical studies. The nucleotide loading status of purified MxB was monitored by HPLC analysis (see 2.3.8) (Figure 29D). Both MxB variants were nucleotide-free after purification.

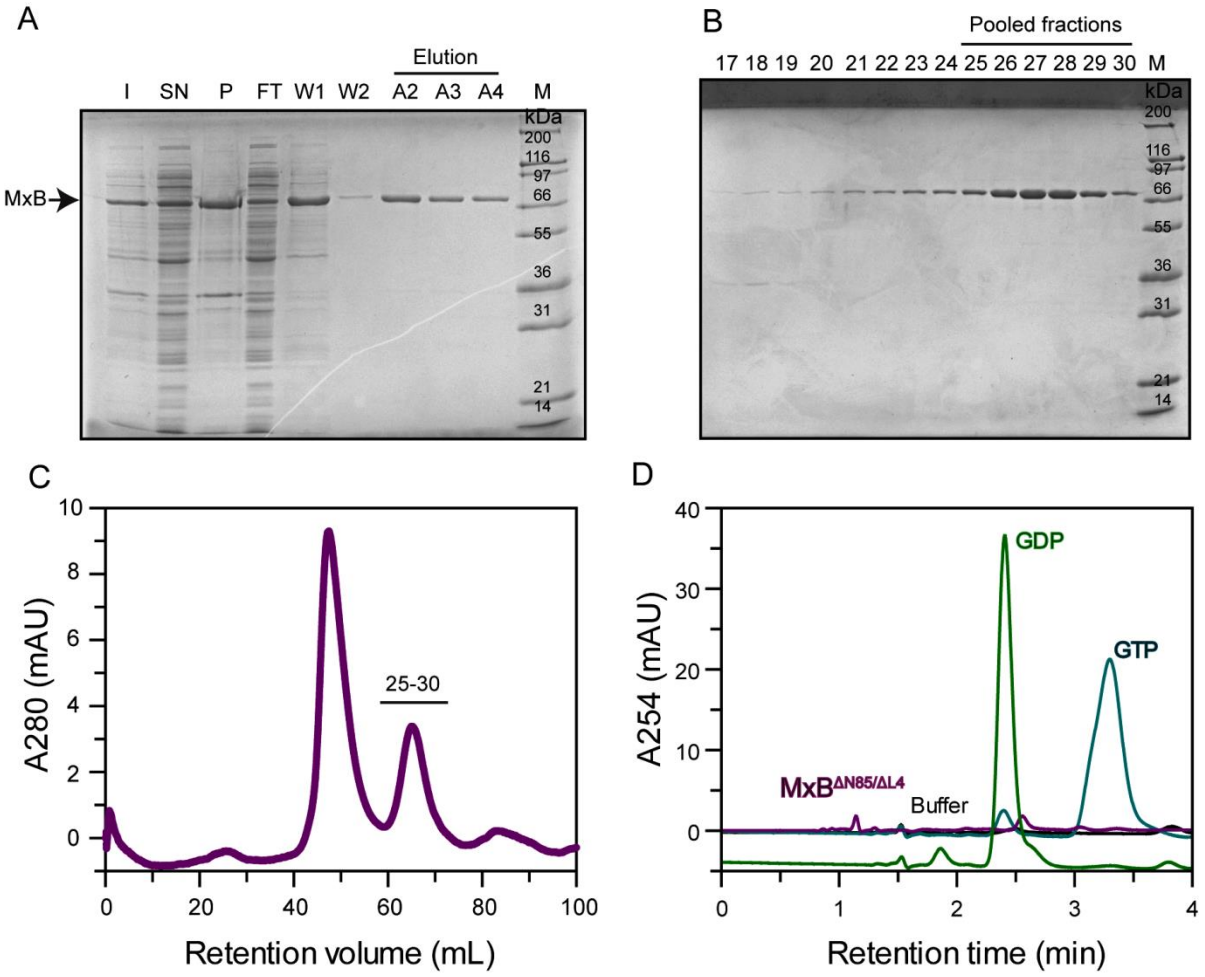

Figure 29: Expression and purification of hsMxB$^{\Delta N85+\Delta L4}$.

(A) SDS-PAGE of hsMxB$^{\Delta N85/\Delta L4}$ purification. I, induced whole cell *E. coli* lysate; SN, supernatant fraction of the cell lysate; P, pellet fraction; FT, flow-through of the soluble extract on Ni^{2+}-NTA column; W1, flow-through of the high-salt and ATP wash (wash 1); W2, flow-through of the high-imidazole wash (wash 2); A2-A4, elution fractions; M, protein molecular weight marker. (B) SDS-PAGE of the SEC profile seen in C. Fractions 25-30 were pooled for biochemical analysis. The molecular weights of the markers are indicated. (C) Gel filtration profile of MxB$^{\Delta N85/\Delta L4}$. (D) The nucleotide-loading status was analyzed by HPLC. The GTP standard is shown in cyan, GDP in green, buffer in black and purified MxB in purple. 40 µM of protein was applied.

3.2.2 The oligomerization state of MxB

The human MxA protein is a tetramer in solution and further oligomerization is a prerequisite for its antiviral activity in the cell (75,76). To probe the oligomerization state of the expressed cytoplasmic MxB construct (MxB$^{\Delta N85/\Delta L4}$), gel filtration analysis combined with right angle light scattering (RALS) was performed (see 2.3.12 and 2.3.13).

Under the used conditions, the protein showed a dimeric state (Figure 30), which is in agreement with recently published studies, where a construct lacking the first 84 amino acids was used (80,81). Likewise, analytical ultracentrifugation studies of MxA lacking the loop L4 showed a stable dimer (75). Dimeric MxB was also demonstrated to be the antiviral active form (80), although a construct including the L4 was used. This indicates that, in contrast to MxA loop L4 is not important for MxB tetramerization.

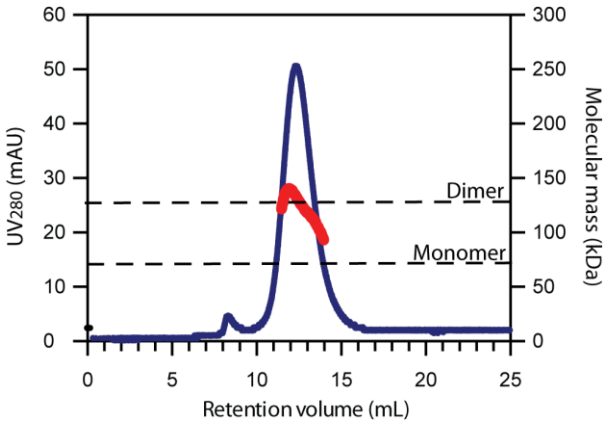

Figure 30: Right angle light scattering analysis of MxB $^{\Delta N85/\Delta L4}$.

The protein was separated using a S200 10/300 gel filtration column and detected at 280 nm. The RALS data indicates a dimeric species for MxB$^{\Delta N85/\Delta L4}$. Experiments were performed in gel filtration buffer (500 mM NaCl) at 4°C using a protein-concentration of 2 mg/mL.

3.2.3 Concentration-dependent GTP hydrolysis of MxB

GTP hydrolysis (130,131) and oligomerization of MxA via the stalk (75,76,183,184) are important for its antiviral activity. Furthermore, a protein concentration-dependent increase in GTPase activity is characteristic for the dynamin superfamily. Together with the group of Prof. Kochs, I could show in chapter 3.1 that nucleotide binding and formation of a G interface is critical for the intracellular localization and the antiviral function of MxA.

To obtain information on the GTPase activity of the engineered cytoplasmic MxB construct (ΔN85/ΔL4) and on its protein concentration-dependent GTPase activity, multiple turnover assays were performed (see 2.3.11), using 1 mM GTP and various protein concentrations (Figure 31). In previous studies, it was shown that wt MxA has a k_{max} of approx. 6 min^{-1} (75), and a similar value was obtained here for MxB. Furthermore, MxB$^{\Delta N85/\Delta L4}$ displayed a protein-concentration dependent GTPase activity increase (Figure 31), like MxA and other dynamin family members, and showed a similar GTPase activity compared to wt MxA.

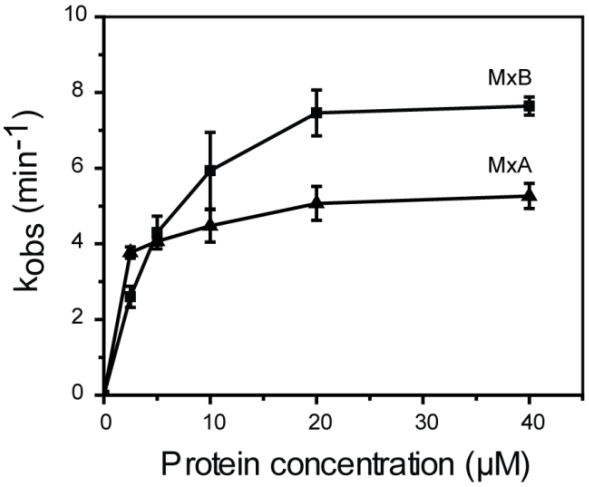

Figure 31: GTPase activity of MxB compared to MxA.

Protein-concentration-dependent GTPase activities of MxB$^{\Delta N85/\Delta L4}$ (■) and wt MxA (▲) were determined at 37°C and 150 mM NaCl. 1 mM of GTP and the indicated protein concentrations were used. The mean of k_{obs} calculated from two independent experiments is indicated with the error bar showing the range of the two data points.

3.2.4 MxA stimulates the GTPase activity of MxB

MxA blocks the import of viral ribonucleoprotein complexes (vRNPs) into the nucleus and an interaction of MxA protein with viral NPs or vRNPs was demonstrated for influenza A virus (IFAV), Thogoto virus (THOV) and LACV (108,111,136). In contrast, MxB has recently been shown to be a potent inhibitor of HIV and other lentiviruses (70-72,134). Cytoplasmic (76 kDa) and nuclear (78 kD) forms of MxB exist (135,185), and at least the cytoplasmic form could in principle interact with the highly homologues cytoplasmic MxA. Therefore, the possibility of a putative interaction and GTPase regulation of MxA and MxB was investigated in this chapter.

I analyzed the ability of MxB$^{\Delta N85/\Delta L4}$ to stimulate the GTPase activity of the wt monomeric MxA^{M527D} in a mixed GTPase assay according to the experiments performed in chapter 3.1.3. For these experiments, I employed a constant low concentration of 2.5 µM of MxA^{M527D} and added increasing amounts of MxA$^{M527D/T103A}$ or MxB$^{\Delta N85/\Delta L4/T151A}$ mutants defective in GTP hydrolysis (Figure 32A). As shown already in 3.1.3, the monomeric T103A mutant stimulated the GTPase activity of MxA^{M527D} as efficiently as monomeric MxA^{M527D}, whereas MxB$^{\Delta N85/\Delta L4/T151A}$ could not stimulate the GTPase activity of MxA^{M527D} (Figure 32A).

Next, I used a constant low concentration of 2.5 µM of MxB$^{\Delta N85/\Delta L4}$ and added increasing concentrations of MxA$^{M527D/T103A}$ or MxB$^{\Delta N85/\Delta L4/T151A}$. Surprisingly, MxA$^{M527D/T103A}$ could

stimulate the GTPase activity of MxB$^{\Delta N85/\Delta L4}$, albeit to a lower degree compared to the monomeric MxA variant in Figure 32A. The addition of the GTPase-deficient MxB$^{\Delta N85/\Delta L4/T151A}$ mutant did not show any stimulatory effect on the GTPase activity. These data support the hypothesis of an MxA-MxB interaction and a putative regulatory mechanism of their GTPase activities. However, since MxA performs its GTPase stimulation via G domain dimerization, and MxB was used in a dimeric state (see 3.2.2), further investigations using a monomeric MxB construct could shed additional light on this mechanism.

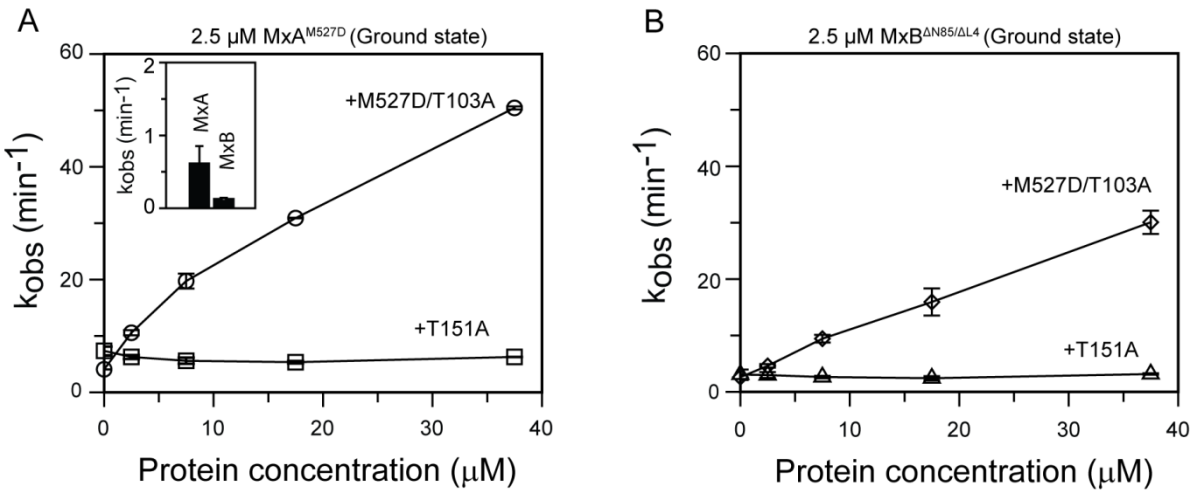

Figure 32: Analysis of the GTPase activity of MxA and MxB.

(A) The GTPase activity of MxA^{M527D} can be stimulated by a monomeric MxA G domain mutant T103A (see also 3.1.3) but not by a dimeric MxB mutant (T151A). 2.5 µM of MxA^{M527D} was incubated with the indicated concentrations of the corresponding (MxA$^{M527D/T103A}$ or MxB$^{\Delta N85/\Delta L4/T151A}$) mutant (see x-axis). The insert shows the GTPase activity of MxA$^{M527D/T103A}$ (a) or MxB$^{\Delta N85/\Delta L4/T151A}$ (b) at 37.5 µM and 1 mM GTP. The mean k_{obs} calculated from two independent experiments is indicated, with the error bar showing the range of the two data points. MxA^{M527D}+M527D/T103A (○), MxA^{M527D}+MxB$^{\Delta N85/\Delta L4/T151A}$ (□). (B) The GTPase activity of MxB$^{\Delta N85/\Delta L4}$ can be stimulated by a monomeric MxA G domain mutant T103A, but not by the T151A variant of the dimeric MxB variant. 2.5 µM of MxB$^{\Delta N85/\Delta L4}$ was incubated with the indicated concentrations of the corresponding (MxA$^{M527D/T103A}$ or MxB$^{\Delta N85/\Delta L4/T151A}$) mutant (see x-axis). The mean k_{obs} calculated from two independent experiments is indicated, with the error bar showing the range of the two data points. MxB$^{\Delta N85/\Delta L4}$+MxA$^{M527D/T103A}$ (◇), MxB$^{\Delta N85/\Delta L4}$+MxB$^{\Delta N85/\Delta L4/T151A}$ (Δ).

3.3 Biochemical and structural characterization of the THOV and DHOV NP

3.3.1 Protein over-expression and solubility tests

Some of the *Orthomyxoviridae* family members including IFAV, IFBV NPs were object of comprehensive functional and structural investigations during the last years, and crystal structures of some of those (44-46) led to a better understanding of the viral replication cycle. However, the atomic structure of the THOV NP, which shares approximately 19% sequence identity with the IFV NPs, has not been elucidated. As a main target of the human MxA protein (108), the THOV NP was subject of biochemical and structural investigations during this study. At the beginning of the NP project, I sought to express the IFAV NP (H5N1 and two variations of H1N1, Figure 33) and the THOV NP as GST- and His_6-fusions. To test the expression and solubility of the NPs, the cDNAs were cloned into bacterial expression vectors (see 2.2) and expressed in *E. coli* (see 2.3.2).

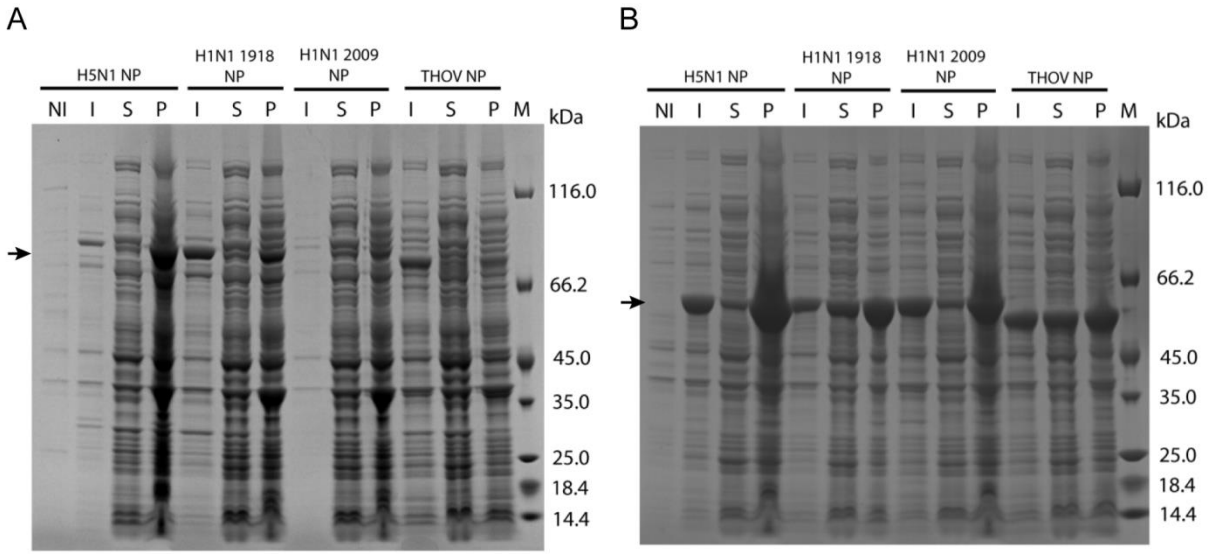

Figure 33: Expression and solubility test of IFAV and THOV NPs.

(A) SDS-PAGE of wt NPs expressed as N-terminal GST-fusion in pGEX-6P1 for over-expression and solubility test. NI, non-induced; I, induced whole cell *E. coli* lysate; SN, supernatant fraction of the cell lysate; P, pellet fraction; M, protein molecular weight marker. (B) SDS-PAGE of wt NPs expressed as N-terminal His_6-fusion in the pSKB-LNB vector for over-expression and solubility test.

In test expression experiments, a clear over-expression band was visible for the GST-tagged H1N1 1918 NP with a size of 82 kDa including the GST tag, the H5N1 NP (82 kDa), and the THOV NP (78 kDa). Only low expression levels were detected for the H1N1 2009 NP (82 kD, Figure 33). However, all NPs expressed as a GST-fusions were insoluble and were consequently found in the pellet (P) fraction (Figure 33A). Dimerization of the GST protein may facilitate the unspecific oligomerization/aggregation of the viral NP.

In contrast to the GST-fusions, all NPs were highly over-expressed when expressed as His_6 fusions with the pSKB-LNB vector. The 56 kDa band represents the IFAV NPs and the 52 kDa band represents the THOV NP in the IPTG-induced fractions (I) (Figure 33B). Even if soluble protein was found in the supernatant for the IFAV NPs, the majority of the protein remained insoluble in the pellet (P) fraction. The THOV NP showed the highest amount of soluble protein in the supernatant (S) (Figure 33B), and further studies were therefore focused on the THOV NP.

3.3.2 Large scale NP expression and purification

As shown in chapter 3.3.1, the THOV NP was best expressed and showed sufficient solubility using the pSKB-LNB vector providing an N-terminal His_6-tag. For structural studies, sufficient amounts of highly pure protein are indispensable. To achieve this, a large scale purification was performed (see 2.3.3). The purification procedure included one affinity chromatography and one size exclusion chromatography step (see 2.3.3). The purification resulted in NP of over 95% purity, as assessed by SDS-PAGE (Figure 34A for THOV NP and Figure 35A for DHOV NP). The NPs eluted in a single peak at 150 mM NaCl on a Superdex 200 16/60 (Figure 34B for THOV NP, and Figure 35B for DHOV NP).

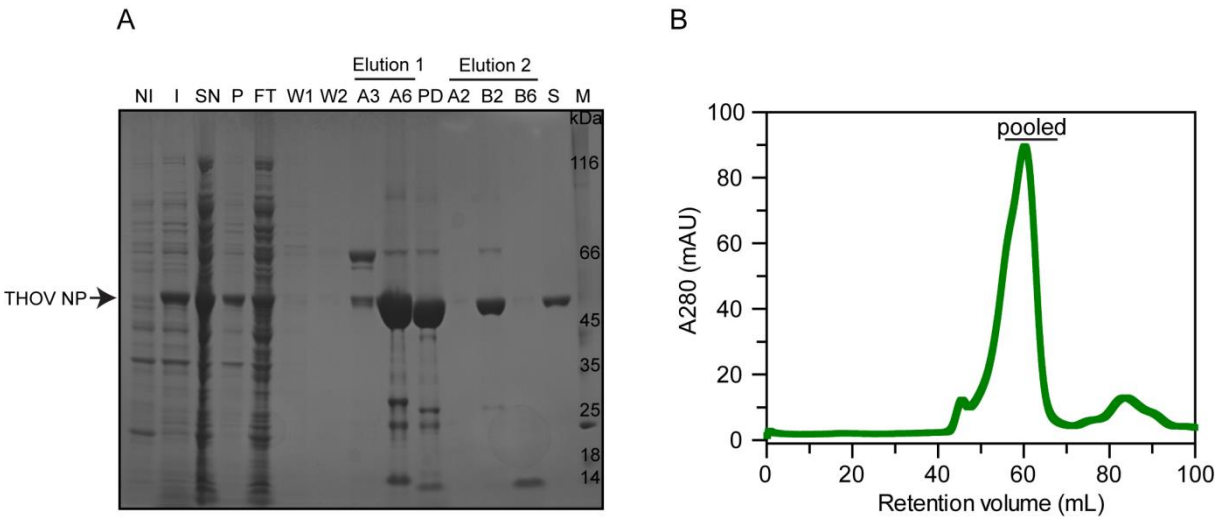

Figure 34: Expression and purification of the wt THOV NP.

(A) Typical SDS-PAGE of wt THOV NP purification. NI, non-induced; I, induced whole cell E. coli lysate; SN, supernatant fraction of the cell lysate; P, pellet fraction; FT, flow-through of the soluble extract on Ni^{2+}-NTA column; W1, flow-through of the high-salt and ATP wash (wash 1); W2, flow-through of the high-imidazole wash (wash 2); A3 and A6, elution 1 fractions; PD, post digestion with PreScission™ protease (visible at approx. 42 kDa); A2, B2 and B6, elution 2 fractions (removal of the GST-tagged protease via

GSH-column); S, SEC fraction 24 to 27; M, protein molecular weight marker. (B) Gel filtration profile of wt THOV NP on a Superdex 200 16/60 column. Pooled fractions are indicated.

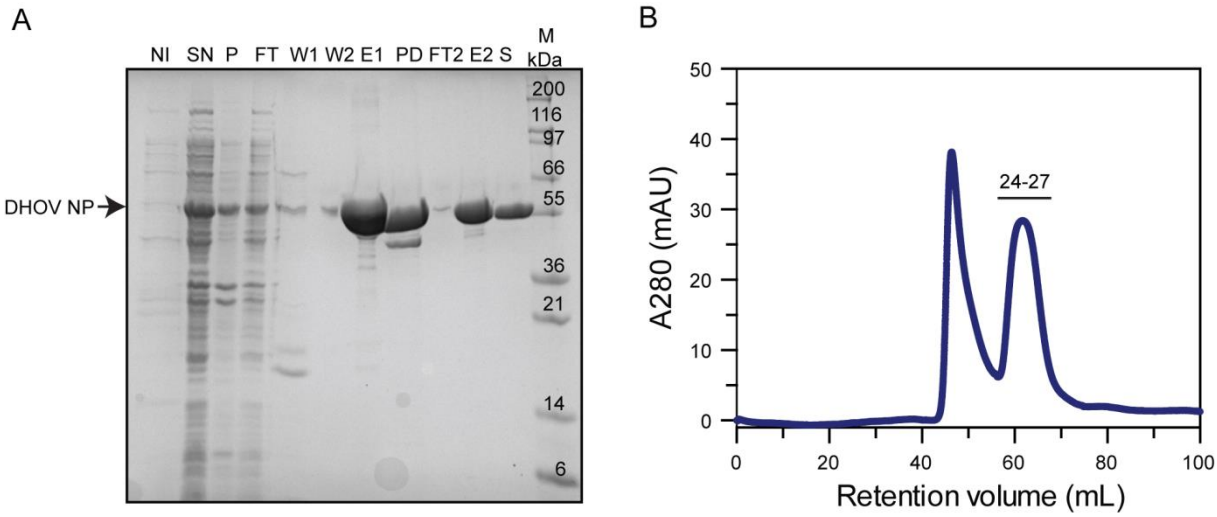

Figure 35: Expression and purification of the wt DHOV NP.

(A) Typical SDS-PAGE of wt DHOV NP purification. NI, non-induced; SN, supernatant fraction of the cell lysate; P, pellet fraction; FT, flow-through of the soluble extract on Ni^{2+}-NTA column; W1, flow-through of the high-salt and ATP wash (wash 1); W2, flow-through of the high-imidazole wash (wash 2); E1, elution 1 fractions; PD, post digestion with PreScission™ protease (visible at approx. 42 kDa); FT2, flow-through 2 (removal of the GST-tagged protease via a GSH-column); E2, elution 2 fractions; S, SEC fraction 60-70mL; M, protein molecular weight marker. (B) Gel filtration profile of wt DHOV NP on a Superdex 200 16/60 column.

3.3.3 Salt and protein concentration optimization

For buffer optimization of the THOV NP, the NaCl concentration was optimized (50 mM–500 mM) using an ultracentrifugation spin assay (see 2.3.16). The stability of the protein was monitored by the supernatant/pellet ratio after a quick ultracentrifugation run. Unstable proteins tend to aggregate and can be found in the pellet (P), whereas stable proteins are present in the supernatant (S) fraction. Equivalent amounts of supernatant (S) and pellet (P) were loaded on SDS–PAGE. As can be seen in Figure 36A, the THOV NP is stable in the range of 50 mM to 500 mM NaCl, because all of the protein was found in the soluble (S) fraction.

Protein crystallization requires a relatively high protein concentration. To test if the THOV (Figure 36B) and DHOV NP (Figure 36C) fulfill this requirement without the tendency of aggregation, the same spin assay experiments, with varying concentrations were performed. Both NPs show high stability up to 15 mg/mL. In conclusion, for the crystallization trials, protein concentrations between 10 and 15 mg/ mL were used.

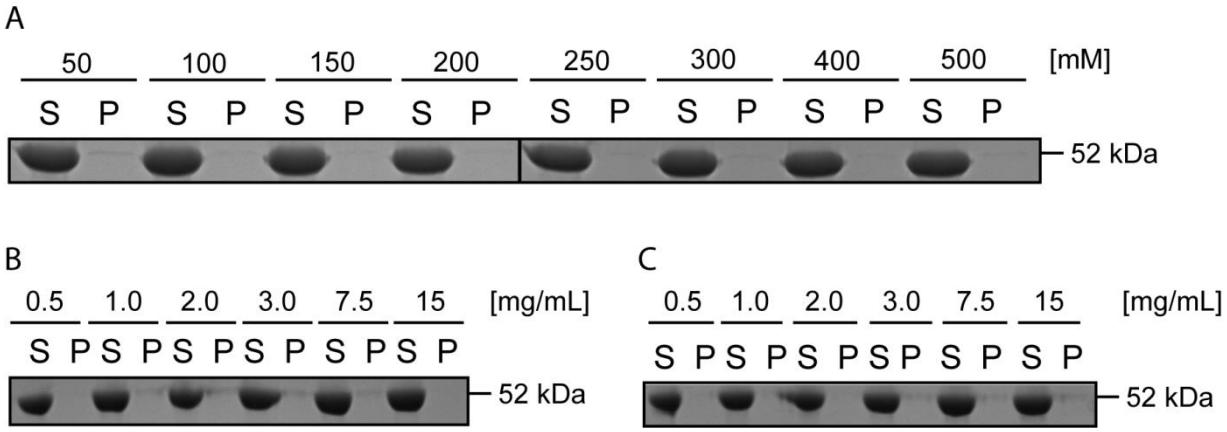

Figure 36: Salt and protein concentration optimization for THOV and DHOV NP.

(A) Wt THOV NP stability under different NaCl concentration at 25°C. Wt THOV (B) and DHOV (C) NP stability under different protein concentrations at 25°C. S - Supernatant, P - Pellet.

3.3.4 Folding status of the THOV NP

For structural investigation of a protein, a homogenous and properly folded sample is a prerequisite for the success of the project. Therefore, qualitative CD-spectra were recorded, according to 2.3.7. As an example, the wt THOV NP CD spectrum is shown in Figure 37. The spectrum was compared to the IFAV H1N1 1918 NP (Figure 37). The crystal structure of the IFAV H1N1 NP was solved in 2006 (44) and is mainly α-helical, which is substantiated by the CD-spectrum in Figure 37 (black curve).

The *Orthomyxoviridae* family shows a low sequence similarity within their NPs (see Appendix D - *Orthomyxoviridae* nucleoprotein alignment). However, the THOV NP displays a similar, mainly α-helical CD-profile with negative absorption bands at approximately 222 nm and 208 nm, as well a positive absorption band at 190 nm (Figure 37, green curve). In conclusion, the CD-profile shows a properly folded THOV NP, confirming an appropriate expression and purification strategy.

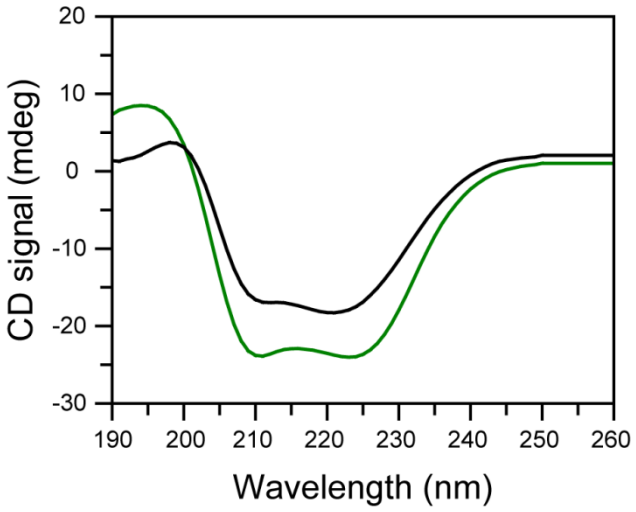

Figure 37: CD-spectra of the wt THOV NP and wt IFAV H1N1 NP.

Spectra were recorded on a qCD Chirascan spectrometer (Applied Photophysics) from 190 to 260 nm in a 0.1 cm cell. 0.2 mg/mL of protein was used for the measurements in a phosphate buffer (see 2.1.10). Measurements were performed in triplicate and baseline-corrected by subtraction of the buffer.

3.3.5 RNA and DNA binding

The THOV and DHOV contain a segmented, negative strand RNA genome, like the IFA, B and C virus. Each RNA segment is covered by multiple copies of the NP and is associated with the heterotrimeric polymerase complex into viral ribonucleoprotein (vRNP) particles. At first, the influence of the length of a poly-uracil RNA oligomer (polyU or pU) on NP binding was tested calorimetrically by ITC (see 2.3.9 and 2.1.10) (

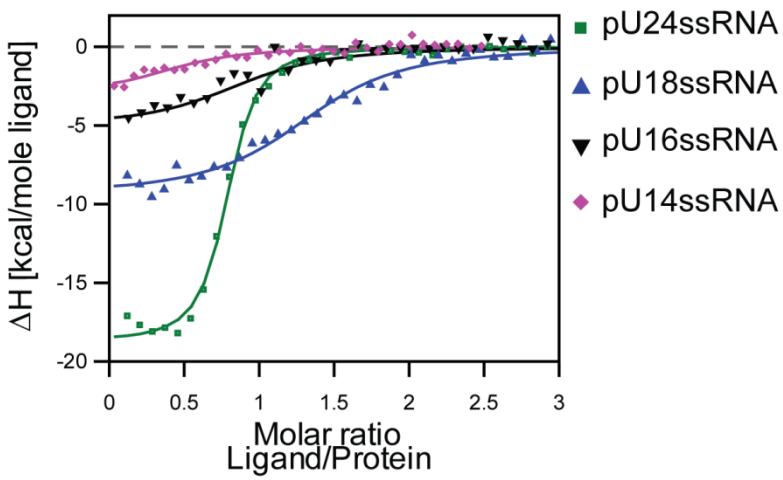

Figure 38). A polyU sequence was chosen to avoid possible secondary structures of the RNA. THOV NP showed the highest affinity towards a polyU24 molecule with a calculated

dissociation constant (K_D) of 130 ± 20 nM. Shortening the RNA ligands resulted in a clear affinity decrease, with the lowest affinity for the pU14 (K_D = 2 ± 1 µM) (Table 4).

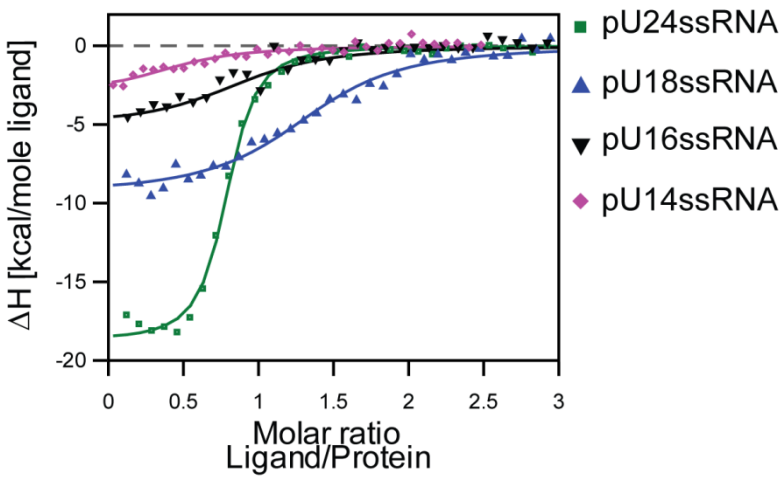

Figure 38: Wt THOV NP bound to polyU-molecules of different length.

Integrated ITC signals for the wt THOV NP bound to different oligos. 150 µM solutions of the indicated RNA oligo were stepwise titrated into 10 µM solutions of wt THOV NP at 8°C in an ITC device. Resulting heat changes were integrated and the obtained values fitted to a quadratic binding equation. The following K_D values were derived from the fittings. pU14: K_D=2.1±1 µM, n=0.5±0.08, pU16: K_D=1.2±0.4 µM, n=0.9±0.06, pU18: K_D=427±86 nM, n=1.4±0.03, pU24: K_D=133±17 nM, n=0.8±0.01. Experiments were performed in ITC buffer (see 2.1.10).

As can be seen from the high negative ΔH-value, the binding of the THOV NP towards the pU24mer is mainly enthalpy-driven. This binding event requires a high extent of conformational changes of the RNA upon binding, indicated by the highly unfavorable entropic factor (Figure 39, pU24). One possible explanation is that there are RNA-induced large scale changes. However, another reason might be the solvent contribution in changing the free binding energy arises from reorganization (solvation/desolvation) of solvent-solvent or solvent solute (protein and RNA) interactions. Similar to the pU24mer, the pU18mer shows a mostly favorable enthalpic binding mechanism, although to a lower extent. The shorter the oligo, the less entropically unfavorable conformational changes are required upon binding as can be seen for the pU16 and pU14 oligo.

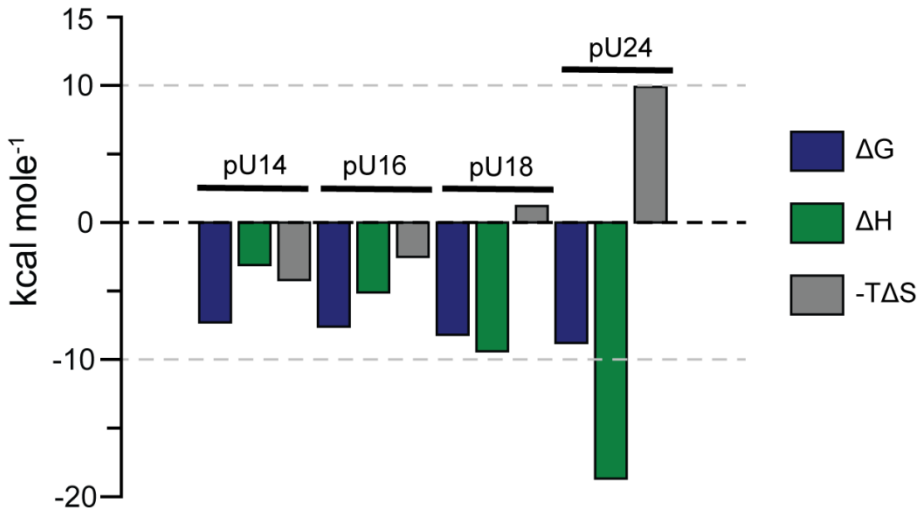

Figure 39: Thermodynamic parameters for the wt THOV NP bound to different polyU oligos.

The thermodynamic binding parameters obtained from the ITC measurements in Figure 38.

Next, I also tested the ability of THOV NP binding to ssDNA. Accordingly, ssDNA (polyT) was used as a ligand, and a 5-fold lower affinity for the wt THOV NP towards pT24 was observed (Figure 40A). Finally, DHOV NP was tested for its binding affinity towards the 24mer pU molecule. Wt DHOV NP bound to pU24 with a similar affinity as wt THOV NP (Figure 40B).

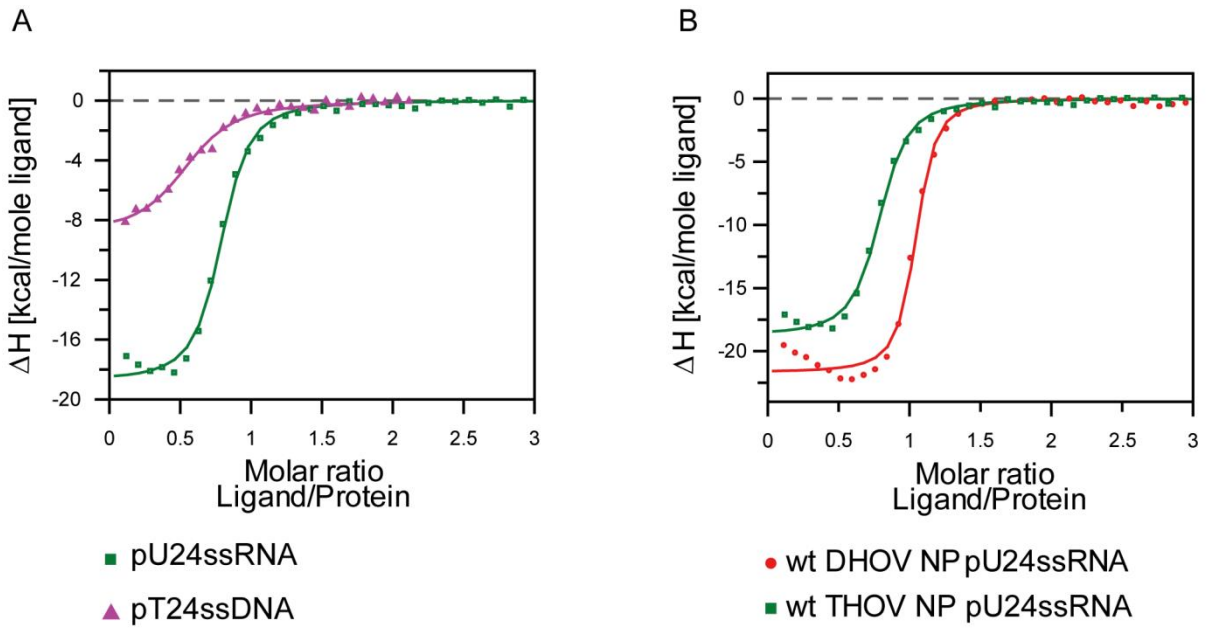

Figure 40: RNA binding assays for THOV and DHOV NP.

150 µM solutions of the indicated RNA oligo were stepwise titrated into 10 µM solutions of THOV or DHOV NP at 8°C in an ITC device. Resulting heat changes were integrated and the obtained values fitted to a quadratic binding equation. The following K_D values were derived from the fittings. (A) RNA vs. DNA binding for the wt THOV NP. pU24: K_D=133±17 nM, n=0.8±0.01, pT24: K_D=598±107µM, n=0.60±0.02. (B) Wt DHOV NP binds to a pU24mer with similar affinity like THOV NP. pU24 (DHOV NP): K_D=50±10 nM, n=1.0±0.01 (see 2.1.10).

IFAV NPs are believed to bind nonspecifically to the single-stranded viral RNA genome (186). The only viral protein with sequence specificity is the viral polymerase that binds the 5′ viral RNA and the 5′-3′ panhandle structure (26,187-190). Sequence analysis indicates that the first 12 nucleotides from the 3’ end and the first 13 nucleotides from the 5’end are highly conserved among the eight IFAV segments (191). These regions are termed the untranslated regions (UTRs), and form the promotor for the transcription and replication. These conserved regions are bound by the RNA-dependent RNA polymerase (RdRp), whereas the rest of the pseudo-circularized vRNA is coated with NP. Recently, structural information was obtained on the mechanism of promotor binding (192,193).

To analyse if the THOV NP can discriminate between the coding and non-coding (UTRs) regions of the viral segment, binding affinities towards RNA oligos comprising the first 10 nucleotides from the 3’ and 5’ends of segment 5, which encodes the NP itself, were tested for THOV NP. Surprisingly, THOV NP bound these sequence with a 10-fold (for the 3’ sequence) and a 6-fold (for the 5’ sequence) lower affinity compared to the pU18-ssRNA (Figure 41A).

Using DNA instead of RNA, the effect was less obvious (Figure 41B). However, more experiments are inevitable to get a more detailed view on this mechanism of binding.

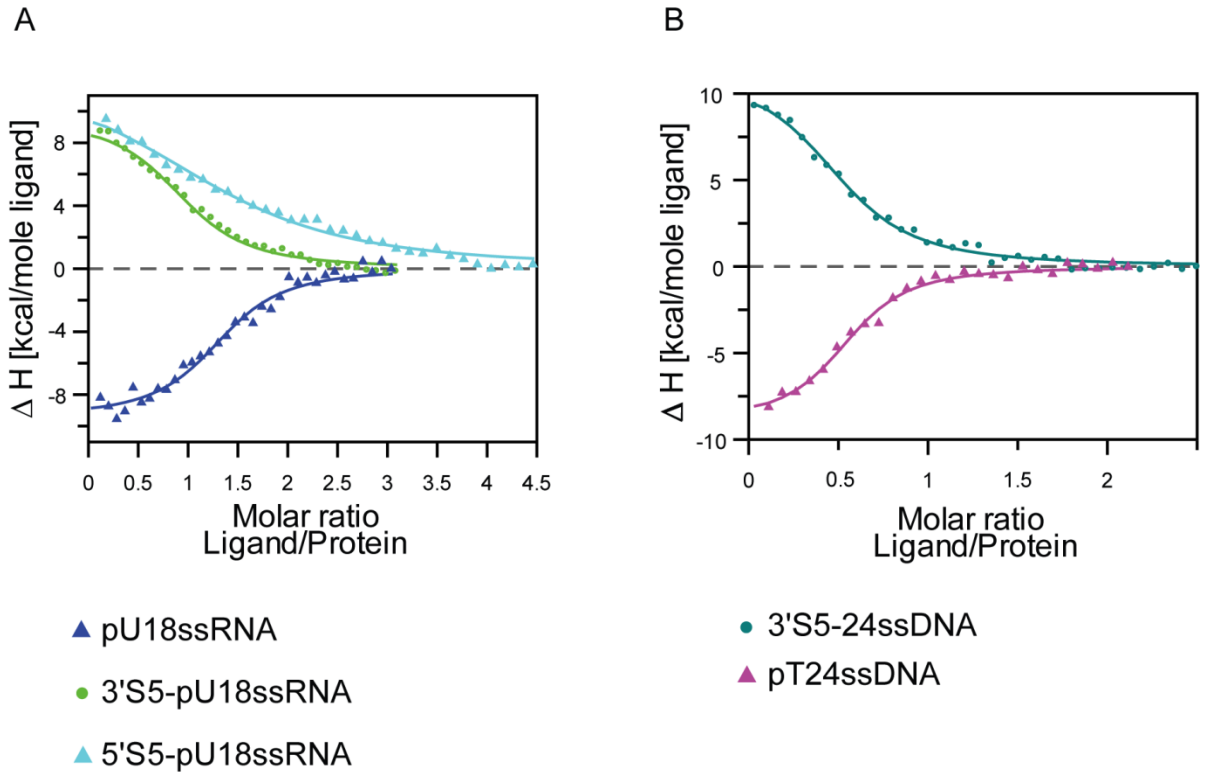

Figure 41: Integrated ITC graphs for the wt THOV bound to viral UTRs.

150 µM solutions of the indicated RNA oligo were stepwise titrated into 10 µM solutions of wt THOV NP at 8°C in an ITC device. Resulting heat changes were integrated and the obtained values fitted to a quadratic binding equation. The following K_D values were derived from the fittings. (A) RNA sequence specificity of wt THOV NP towards segment 5 (encodes the NP). pU18: K_D=427±86 nM, n=1.4±0.03, 3'S5-pU18ssRNA: K_D=4.1±0.6 µM, n=1±0.03, 5'S5-pU18ssRNA: K_D=2.3±0.2 µM, n=1.5±0.01. (B) DNA sequence specificity of wt THOV NP towards segment 5. pT24: K_D=598±107 µM, n=0.6±0.02, 3'S5-pU18ssRNA: K_D=1.06±0.14 µM, n=0.5±0.02 (see 2.1.10).

Analysis of the thermodynamic profiles of the binding to the 3' and 5' ends of segment 5 indicates an endothermic character of RNA binding (Figure 42, compare A, B and C with D). This can be interpreted by the ability of the THOV NP to unwind possible secondary structures of the used RNA. Furthermore, the calorimetric data suggests a so called "enthalpy-entropy compensation". This means that favorable changes in binding enthalpy are compensated by opposite changes in binding entropy and vice versa. This results in very small changes in the overall free binding energy. The sequences used and the binding affinities together with the stoichiometry are summarized in Table 4.

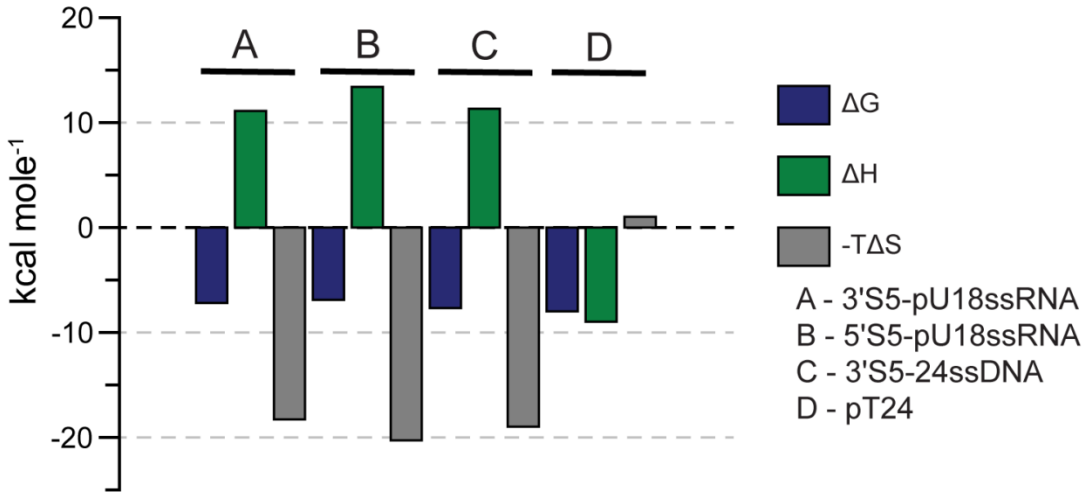

Figure 42: Thermodynamic parameters for the wt THOV NP bound to viral UTRs.

The thermodynamic binding parameters obtained from the ITC measurements in Figure 41.

Oligo	Sequence	Binding affinity (K_D)	Stoichiometry (n)
pU14	UUUUUUUUUUUUUU	2.1±1.0 µM	0.5±0.08
pU16	UUUUUUUUUUUUUUUU	1.2±0.4 µM	0.9±0.06
pU18	UUUUUUUUUUUUUUUUUU	427±86 nM	1.4±0.03
pU24	UUUUUUUUUUUUUUUUUUUUUUUU	133±17 nM	0.8±0.01
pT24	TTTTTTTTTTTTTTTTTTTTTT	598±107 nM	0.6±0.02
3'S5-24ssDNA	CCAAAAAACTGCCTTGATTTCTCT	1.06±0.14 µM	0.5±0.02
3'S5-pU18ssRNA	UUUUUUUUUGAUUUCUCU	4.1±0.6 µM	1.0±0.03
5'S5-pU18ssRNA	AGCAAAAACAUUUUUUUU	2.3±0.2 µM	1.5±0.01

Table 4: RNA/DNA sequences and binding parameters for the wt THOV NP.

3.3.6 Oligomeric state of the NPs

The IFAV NPs are mainly trimeric in solution (44,45,194) and IFBV NP shows a tetrameric character (46). To investigate the oligomerization state of the expressed THOV and DHOV NPs, the NPs were subjected to analytical gel filtration coupled to an “in-line” RALS device (see 2.3.13) and sedimentation velocity analytical ultracentrifugation experiments (see 2.3.14) to determine their relative molecular mass.

A RALS device measures the scattered laser light intensity at 90° to the incident beam. From the measured intensity and the sample concentration, the sample’s molecular weight and oligomeric state can be directly calculated. Using RALS analysis, THOV NP showed a mainly trimeric character in the absence of RNA (Apo) (Figure 43A). An apparent molecular mass of 160 kDa corresponds to a THOV NP trimer (MW of a monomer is 52 kDa). DHOV NP (MW of a monomer is 52 kDa) elutes at the same retention volume (12.5 mL) as the THOV NP, indicating the same oligomeric state for the DHOV NP (Figure 43B).

In sedimentation velocity analytical ultracentrifugation (AUC), the movement of solutes in a centrifugal field is interpreted using hydrodynamic theory to define the size, shape and interactions of macromolecules. In agreement with the analytical gel filtration/RALS experiments, the AUC results indicate a trimeric species for both NPs in the apo form (Figure 43C).

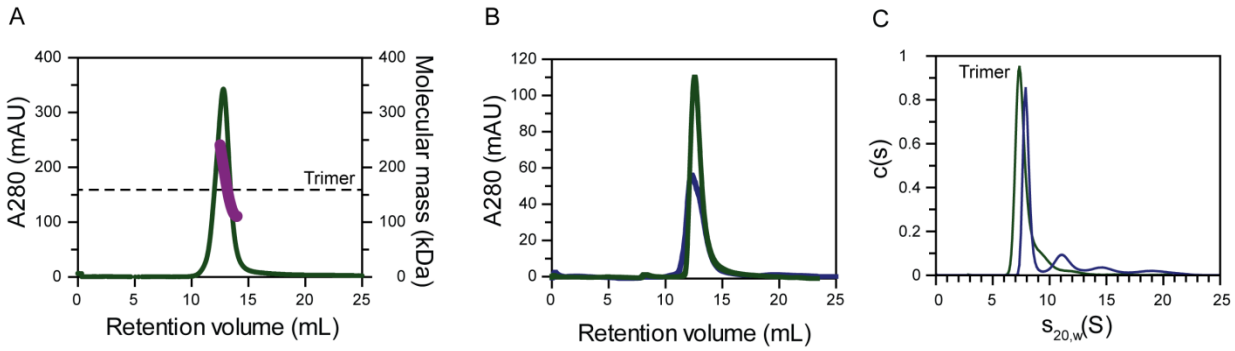

Figure 43: Oligomeric state of the wt THOV and wt DHOV NP in solution.

(A) 50 µl of THOV NP at a concentration of 4 mg/mL was applied on a S200 10/300 gel filtration column connected to a RALS detector in gel filtration buffer (150 mM NaCl). The purple curve refers to the right y-axis and indicates the average molecular mass within the eluted peak. (B) Retention volume comparison on a S200 10/300 column of THOV (green curve) and DHOV NP (blue curve) at an initial concentration of 2 mg/mL (C) Analytical ultracentrifugation sedimentation velocity experiments of THOV and DHOV NP at 0.5 mg/mL in gel filtration buffer (150 mM NaCl). The relative protein concentration c(s) as a function of the normalized sedimentation coefficient $s_{20,w}$ is plotted.

To test if RNA binding causes THOV NP self-association, the NP was incubated with a pU24mer ssRNA (1:0.5, NP:RNA) and RALS experiments were performed. RNA-binding to an NP trimer did not affect NP-NP association or further oligomerization (compare Figure 43A with Figure 44).

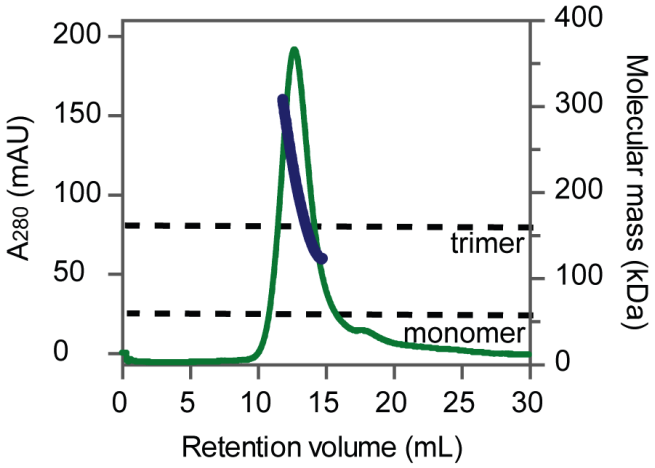

Figure 44: Trimeric form of wt THOV NP bound to a pU24mer ssRNA.

(A) Upon preincubation of THOV NP at a concentration of 2 mg/mL with a pU24mer ssRNA oligo (1:0.5, NP:RNA), 50 µL were applied on a S200 10/300 gel filtration column connected to a RALS detector in gel filtration buffer (150 mM NaCl). The blue curve indicates the average molecular mass within the eluted peak.

3.3.7 The isolated MxA loop L4 does not bind THOV NP *in vitro*

Previous *in vivo* studies showed that the human MxA protein interacts with the nucleocapsids of the THOV (179) and prevents the intracellular transport of the nucleocapsids into the cell nucleus, blocking viral transcription and replication (108). The disordered loop L4 which protrudes from the stalk is a key determinant of antiviral specificity against orthomyxoviruses such as IFAV and THOV (75,76) (see also 1.6.3). Furthermore, key residues within this loop L4 were identified being responsible for the antiviral activity of the MxA protein (73,79).

To identify a possible interaction of the loop L4 of MxA with the THOV NP *in vitro,* commercially synthesized peptides (see Table 5) of the loop L4 were subjected to ITC experiments with THOV NP (see 2.3.9 and 2.3.10).

Peptide	Sequence
Peptide-1	^{533}CQDQVYRGALQKVREKELEEEKKKKSW**DFGAFQ**SSSATD^{571}
Peptide-2	^{560}DFGA^{563}
Peptide-3	^{560}DFGAFQ^{565}

Table 5: Peptides used in this study for ITC experiments.

Initially, a peptide comprising amino acids 533-571 (peptide-1) of the loop L4 in MxA was used (Table 5). No binding signal was detected for peptide-1 in a 1:5 (NP:peptide-1) ratio (Figure 45A).

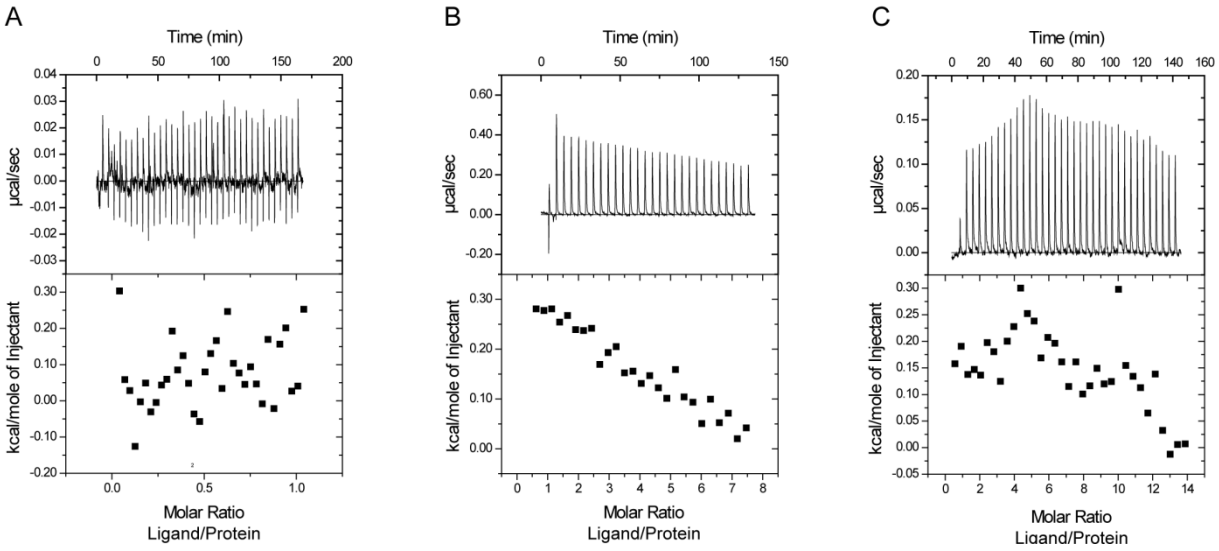

Figure 45: Loop L4-peptide-1 binding analysis.

(A) 0.5 mM loop L4 (peptide-1) was stepwise titrated into 100 µM solution of the THOV NP at 8°C in an ITC device. (B) 1.8 mM loop L4 (peptide-1) was stepwise titrated into 50 µM solution of THOV NP at 8°C. (C) 1 mM loop L4 (peptide-1) was stepwise titrated into 15 µM solution of the wt THOV NP-pU24 complex at 8°C. The NP-RNA complex was prepared by mixing NP and pU24ssRNA in a 1:0.5 molar ratio prior the ITC experiment. Thermograms (upper box) and integrated heat signals (lower box) are depicted. Due to the low heat signal, data fitting was not possible.

Consequently, a higher excess of peptide-1 over NP (1:36) was used. However, even at such high peptide-1 concentrations, no binding signal could be observed (Figure 45B).

Next, I tried to decorate the NP with ssRNA (pU24mer, see Table 4) prior subjecting it to ITC. Excess of ssRNA was removed by applying the complex on a gel filtration S200 10/300 column. No binding of peptide-1 to the NP-RNA complex was detectable (Figure 45C).

Assuming that the length of peptide-1 influences the binding to the NP or NP-RNA complex negatively, shorter peptides were used (see Table 5, peptide-2 and peptide-3). Phe561 and

Gly562 were recently identified as key residues in the antiviral activity against orthomyxoviruses (73,79), and therefore are included in the used peptides.

However, also peptide-2 and-3 did not bind to the wt THOV NP under these conditions (Figure 46A and B, respectively). This indicates that the isolated loop L4 (residues 533-571) or portions of it (residues 560-563/565) are not sufficient to bind to the wt apo or RNA-bound THOV NP *in vitro* under these conditions.

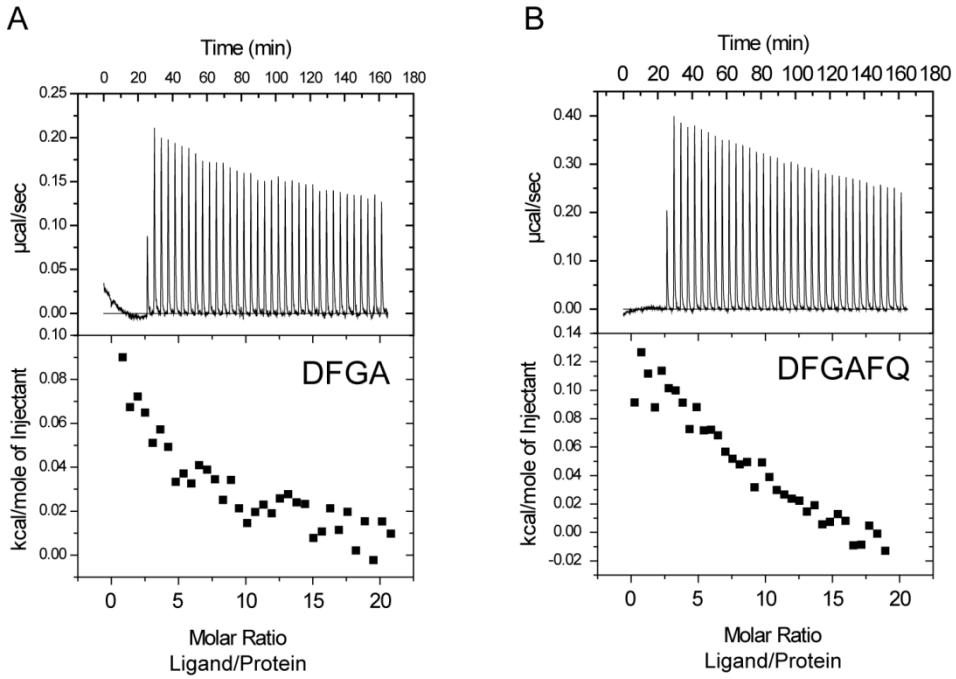

Figure 46: Loop L4-peptide-2 and-3 binding analysis.

(A) 5 mM loop L4 (peptide-2 and -3) was stepwise titrated into 50 µM solution of the wt THOV NP at 8°C in an ITC device. The peptide sequence is shown in the lower box. Thermograms (upper box) and integrated heat signals (lower box) are depicted. Due to the low heat signal, data fitting was not possible.

3.4 Structure of the THOV NP

3.4.1 Crystallization

To get insight into the three-dimensional architecture of the native THOV and DHOV NPs, purified NPs were subjected to crystallization trials (see 2.4.1).

Extensive screening at 20 and 4°C (see 2.1.5) was not successful for the apo form of the THOV NP. Consequently, the NP was mixed with different ssRNA oligos described in Table 4 (see 3.3.5 for stochiometry) (Figure 47A-D).

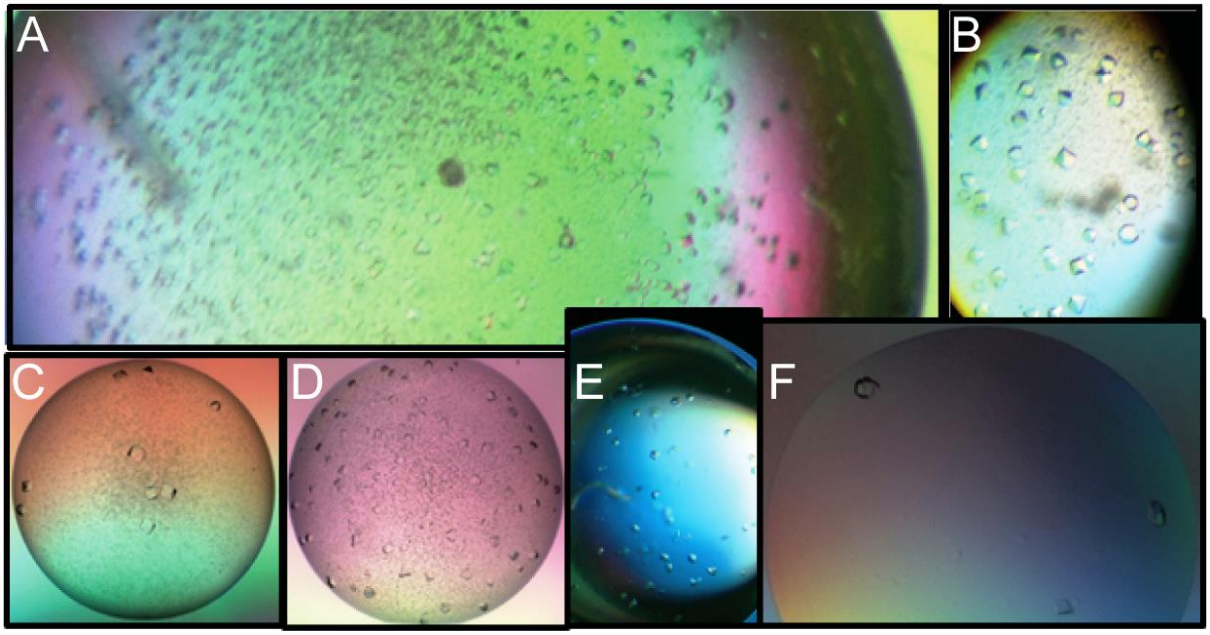

Figure 47: Examples of THOV NP crystals.

(A) Initial crystals of wt THOV NP bound to a pU24mer (24-well plates). (B) Optimized wt THOV NP bound to a pU24mer crystals (24-well plate). (C) Optimized wt THOV NP bound to a pU24mer crystals (96-well plate). (D) Optimized wt THOV NP bound to a pU18mer crystals (96-well plate). (E) Optimized native THOV NP$^{\Delta 188\text{-}196}$ in the apo form (24-well plate) and (F) SeMet-substituted (96-well plate).

Crystals only appeared for the THOV NP bound to pU24mer and pU18mer. For the NP-pU24mer complex, crystals appeared after one hour at 4°C in 8 % PEG 4000, 100 mM Sodium acetate, pH 4.6, but the size of the crystals was to small for structural analyses (Figure 47A). Thus, the same NP:RNA complex was subjected to 24-well plate crystal screening using a 1:1, 1:2 and 2:1 ratio of protein and precipitant for size optimization. Also in 24-well plates, crystal size could not be increased. Consequently, optimizations using glycerol, sucrose, ethylenglycol and MPD in concentrations (w/v) between 4 and 12% were used to slow down the nucleation process. Bigger crystals were obtained using 12% glycerol and 8% sucrose in addition to the

original condition (Figure 47B). The single crystals showed a clear tetragonal-bipyramidal shape, surrounded by a slight precipitation (Figure 47B). Further optimization by varying the PEG and the sodium acetate concentration as well as the pH was not successful. Therefore, an additive screen was performed for the NP:pU24mer complex to improve the quality of the crystals. Single crystal grew upon addition of 3 mM of the reducing agent TCEP-HCl (Figure 47C).

The NP bound to a pU18mer crystallized with 16 % PEG 3350, 100 mM Sodium acetate pH 4.6, 0.3% (v/v) DMSO, at 4°C after one day and the crystals had a tetragonal-pyramidal shape (Figure 47D). The same screening procedure was performed for the full-length DHOV NP. In contrast to the THOV NP, DHOV NP did crystallize in the apo form (9 % (w/v) PEG 8000, 200 mM $MgCl_2$, 100 mM Tris-HCl pH 7.4°C within 3 days) (Figure 48A), but also in complex with a pU24mer (10 % (w/v) PEG 4000, 200 mM $MgCl_2$, 100 mM MES sodium salt pH 6.5, 4°C, 2 weeks, Figure 48B or in 8 % (w/v) PEG 8000, 200 mM LiCl, 50 mM $MgSO_4$, 4°C, 3days, Figure 48C). Many crystals could be obtained from the DHOV NP construct and some could be optimized in their shape. Three are depicted in Figure 48.

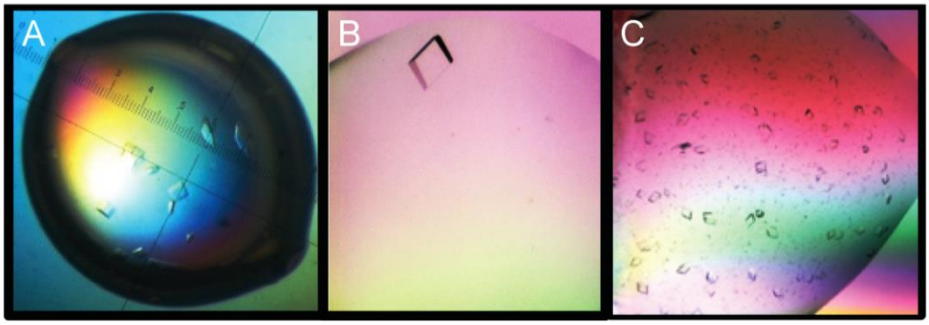

Figure 48: Examples of wt DHOV NP crystals.

(A) Initial wt DHOV NP crystals in the apo form (24-well plate). (B) Initial wt DHOV NP crystals bound to a pU24mer crystals (96-well plates). (C) Optimized wt DHOV NP bound to a pU18mer crystals (96-well plate).

However, the crystals composed of NP and RNA were highly fragile and very difficult to handle. Therefore, only the apo form of the DHOV NP crystals could be tested at the BESSY synchrotron radiation facility in Berlin. To reduce radiation damage during X-ray exposure, the crystals were transferred into a cryo-solution composed of the mother liquor and glycerol, MPD or ethylenglycol in concentration from 20 to 30% (w/v) as cryoprotectants. Crystals were immediately cryo-cooled in liquid nitrogen ($N_{2,l}$) according to (195). However, all the crystals obtained from the full-length NPs diffracted X-ray only up to 6-7 Å at a synchrotron source.

Deletion constructs, lacking flexible regions of both NPs were designed based on secondary structure prediction (predicted with Jpred3, (196)) and the known crystal structures of the IFAV (44), (45) and IFBV NPs (46). The constructs which crystallized with or without RNA are depicted in Table 6. From all the constructs tested, only crystals of the THOV NP$^{\Delta 188\text{-}196}$ in the apo form diffracted X-rays to a maximum resolution of 3.2 Å (native, Figure 47E) and 3.8 Å (SeMe- substituted, Figure 47F), and a complete X-ray data set could be collected (see 3.4.3). Native crystals appeared in 20% (w/v) PEG 3350, 200 mM ammonium citrate pH 7.0 after 2 weeks at 4°C. SeMet-substituted crystals grew in 20% (w/v) PEG 3350, 200-300 mM NaCl after 1 week at 4°C.

Construct	Apo or RNA bound
THOV NP$^{\Delta 7}$	Apo & RNA
THOV NP$^{\Delta 14}$	Apo & RNA
THOV NP$^{\Delta 22}$	Apo & RNA
THOV NP$^{\Delta 188\text{-}196}$	Apo & RNA
DHOV NP$^{\Delta 28}$	Apo & RNA
DHOV NP$^{\Delta 194\text{-}200}$	Apo
DHOV NP$^{\Delta 28+\Delta 194\text{-}200}$	Apo

Table 6: Crystallizable deletion constructs of the THOV and DHOV NP.

All ssRNA oligos from Table 4 were used for complex preparation.

3.4.2 Structure determination of the THOV NP$^{\Delta 188\text{-}196}$

Initially, only the native dataset (BESSY II synchrotron radiation facility in Berlin, BL14.1) was collected and molecular replacement was applied using the IFAV (44) and IFBV NP (46) structures as a search-model. However, due to the low sequence similarity (19% to IFAV and 28% to IFBV NP), no suitable structure solution could be obtained. Consequently, the crystals were soaked in different lanthanides like $Ce(SO_4)_2$, $Sm(CH_3CO_2)_3$, $EuCl_3$, $YbCl_3$, $GdCl_3$ or heavy atom components like K_2PtCl_3 or Amino-2,4,6-triiodoisophthalic acid (I3C, JBS Phasing Kit) varying the concentration (0.5-50 mM) and incubation time. However, experimental phase determination using the anomalous signal of these compounds was not successful, likely due to insufficient heavy atom incorporation. Therefore, SeMet-substituted crystals were produced

and an anomalous dataset recorded for initial phase determination (see 2.4.4, with the data statistics shown in Table 7).

Data collection	Native	SeMet[a] peak
Space group	R3 (146)	R3 (146)
Unit cell dimensions		
a, b, c (Å)	119.7, 119.7, 88.5	119.4, 119.4, 85.2
α, β, γ (°)	90, 90,120	90, 90,120
Wavelength (Å)	0.979733	0.98
Resolution (Å)*	44.69 (3.18) - 3.0	50.00 (3.72) - 3.63
Unique reflections	18,917 (2993)	10,149 (733)
Completeness (%)*	99.7 (98.3)	98.8 (92.1)
R_{meas}*	9.9 (164.3)	9.2 (78.8)
$I/\sigma(I)$*	16.4 (1.55)	9.0 (1.76)
Redundancy*	10.4 (9.9)	2.9 (2.2)

Table 7: Data collection statistics of native and SeMet THOV NPΔ$^{188\text{-}196}$ crystals.

* Numbers in brackets represent values from the highest resolution shell.
[a] For the SeMet data, Friedel pairs were treated as separate observations.

The crystals belong to space group R3 (146) with a solvent content of 47.3% based on the Matthews coefficient corresponding to 1 molecule in the asymmetric unit (ASU). 11 Selenium atoms were found in the ASU of the crystals (see Figure 49) using the anomalous signal. For structure determination, an experimental map was calculated using a SAD protocol (Map-model CC = 0.58, FOM (figure of merit) = 0.38) (see Figure 50). However, these phases were not accurate enough to allow automated model building.

Subsequently, a THOV NP homology model was derived from the influenza B virus NP (46) (see 2.3.17) and fitted into the experimental map. Together with the determined positions of 11 selenium atoms, the backbone of the model could be placed manually in some regions of the electron density map. This was followed by iterative model building and refinement, using experimental phase restraints to avoid model bias. The partial model was further refined against the native 3.2 Å dataset, using positional, grouped B-factors and TLS refinement protocols, until a preliminary model with an R_{work} value of 34.3% and an R_{free} value of 35.8% was obtained (Table 8).

Refinement	Native
Resolution (Å)	44.69 - 3.0
Unique reflections	14,155
R_{work}[a] / R_{free}[b] [%]	34.3/35.8
Molecules / asymmetric unit	1
Number of atoms	
Protein	2,922
Ligand / Ion	-
Water	-
Average B-factors (Å^2)	
Protein	88.6
Water	-
R.m.s.deviations	
Bond lengths (Å)	0.005
Bond angles (°)	1.257

Table 8: Refinement statistics for the THOV NPΔ$^{188\text{-}196}$.

[a] $R_{work} = \frac{\Sigma_{h,k,l}||F_{obs}(h,k,l)|-|F_{calc}(h,k,l)|}{\Sigma_{h,k,l}|F_{obs}(h,k,l)|}$.

[b] R_{free} was calculated with 5% of the data excluded from the refinement.

The preliminary model includes amino acids 20-454 of THOV NP$^{\Delta 188\text{-}196}$. Residues 1-19 are predicted to be disordered and no electron density was found for them. Residues 188-196 were deleted to facilitate crystallization. From the electron density map, it was apparent that the THOV NP$^{\Delta 188\text{-}196}$ trimerized via the 3-fold crystallographic symmetry axis (Figure 51). So far, 89.4% of all residues are in the favored regions of the Ramachandran plot (Figure 52).

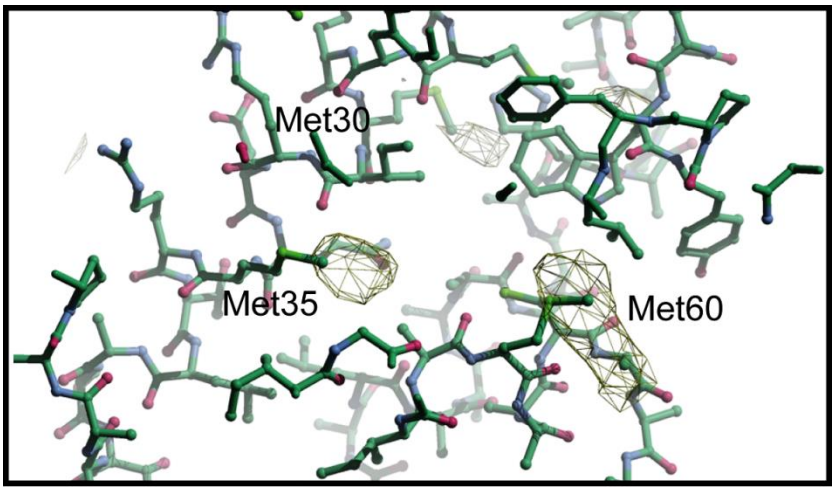

Figure 49: Anomalous difference map of the THOV NP$^{\Delta 188\text{-}196}$.

Selected region of the model, with the anomalous difference map is shown in brown mesh at 3σ. The fitted methionines are labelled.

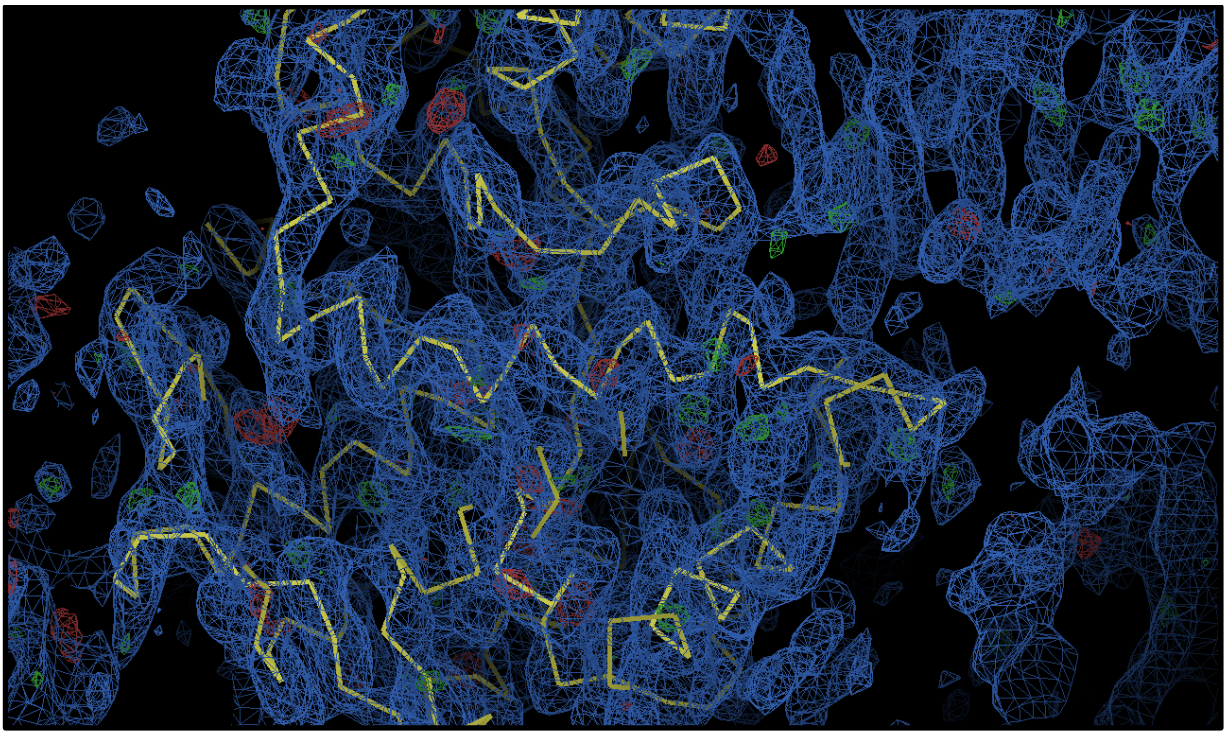

Figure 50: Initial 2Fo-Fc, Fo-Fc and anomalous difference map of THOV NP$^{\Delta 188\text{-}196}$ crystal.

The 2Fo-Fc map is shown in blue mesh at a contour level of 1.0σ, the Fo-Fc map is shown in green (positive) and red (negative) mesh at 3σ.

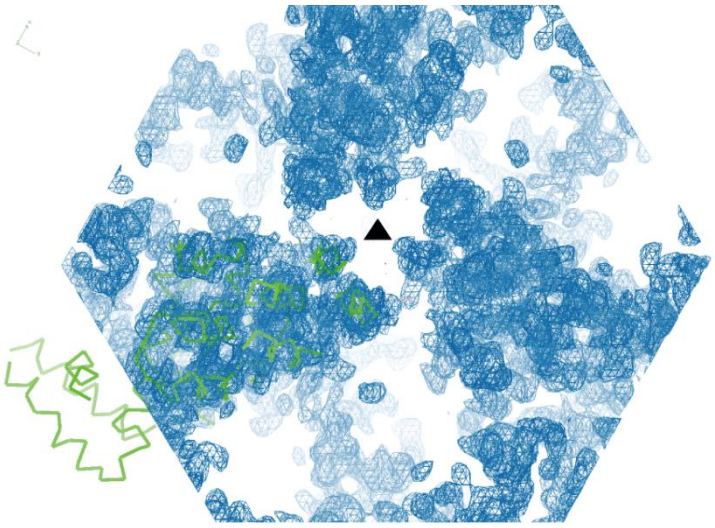

Figure 51: Three-fold symmetry of the THOV NP$^{\Delta 188\text{-}196}$ within the crystal lattice

Refined 2Fo-Fc electron density, contoured at 1σ, is shown as blue mesh. The refined working model is shown as green C_α-trace. The crystallographic 3-fold symmetry is indicated by a triangle.

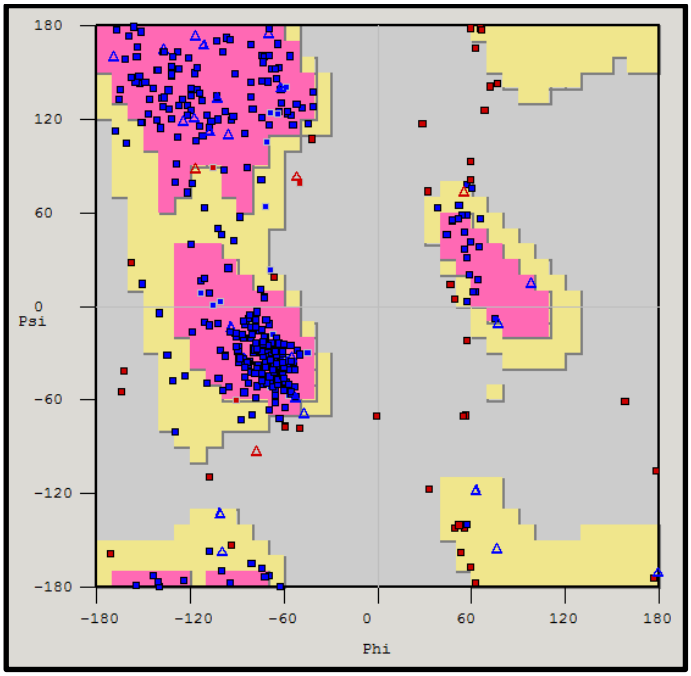

Figure 52: Ramachandran plot of the THOV NP$^{\Delta 188\text{-}196}$ structure.

79.0% of all residues are in the most favoured region and 10.4% in allowed regions of the Ramachandran plot. 10.6% of the residues (45) are still in the disallowed region.

3.4.3 Structural analysis of the THOV NP$^{\Delta 188\text{-}196}$ structure

In agreement with the CD-spectroscopy data (see 3.3.4), the structure of the THOV NP is mainly α-helical. The separation into a body and a head domain and the tail loop at the tip of the head are clearly apparent (Figure 53).

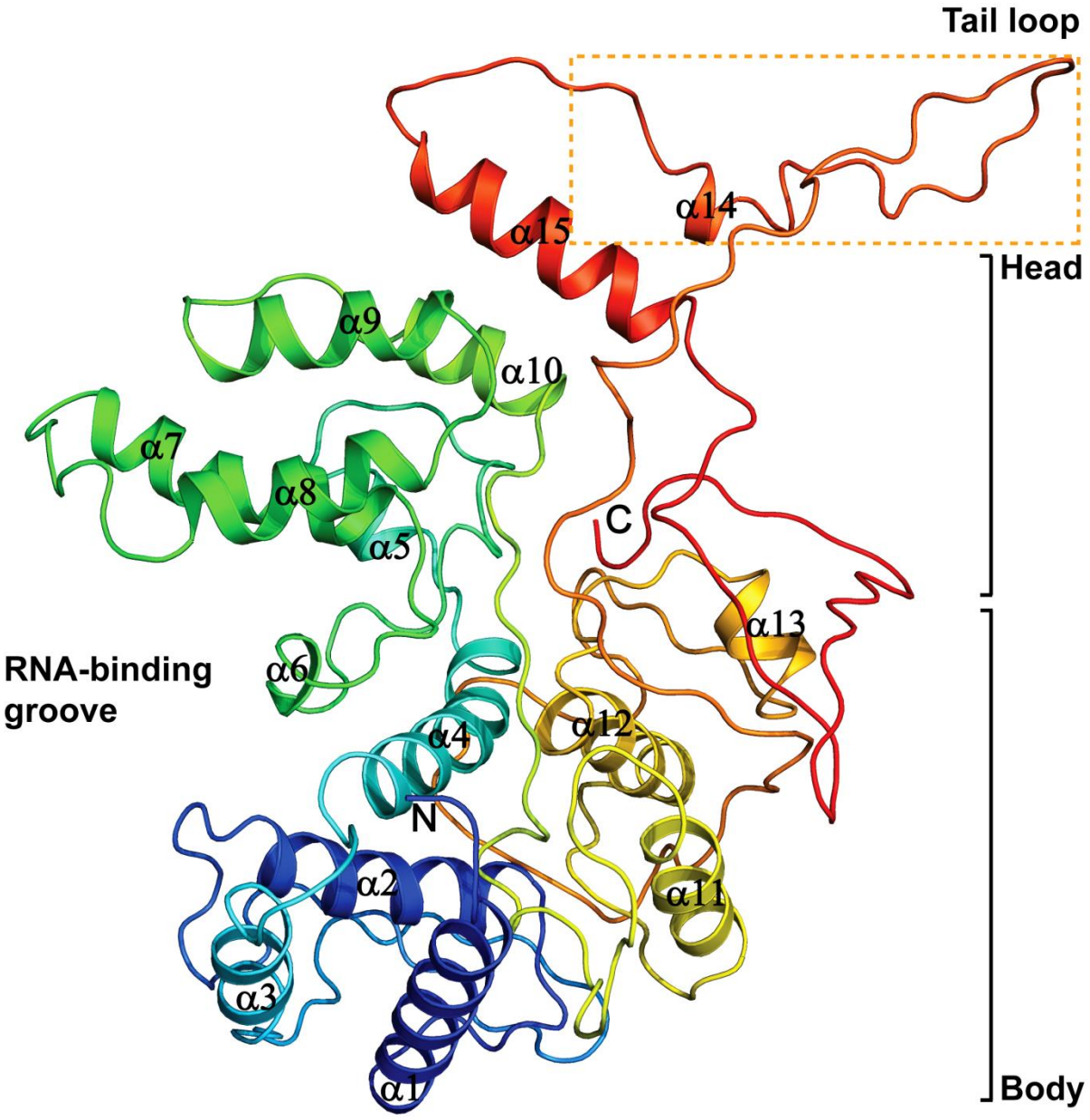

Figure 53: THOV NP$^{\Delta 188\text{-}196}$ monomer.

Rainbow colored ribbon type representation of the THOV NP $^{\Delta 188\text{-}196}$ monomer. From the N-terminus (N, blue) to the C-terminus (C, red). The putative RNA-binding site, the head and the body domain, and the tail loop (orange box) are indicated.

The head and body domain are connected by non-contiguous regions in two segments, a helix-loop-helix motif (α4-loop-α5, amino acid 116-140) and an elongated loop (residues 227-238). The polypeptide chain goes back and forth between the head and body domain, providing stability to the whole globular molecule.

The head domain is formed by residues 135–252 and 398–424, and the body domain consists of the three polypeptide segments 20-134, 253-363 and 425-454. The tail loop (amino acids 364-397) is located at the tip of the head domain (Figure 54).

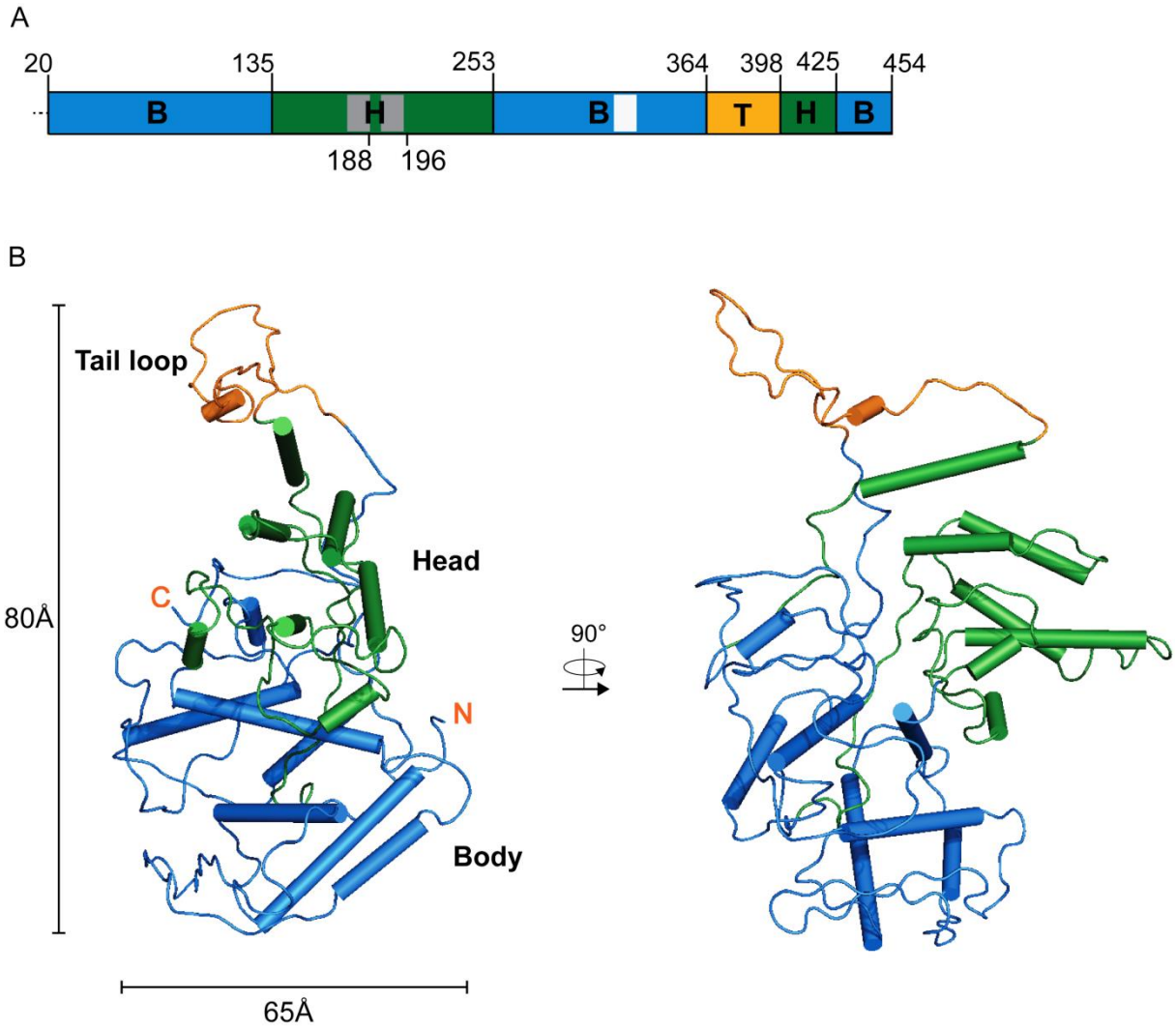

Figure 54: Structure and domain architecture of the THOV NP$^{\Delta 188-196}$.

(A) Schematic representation of the domain architecture of THOV NP$^{\Delta 188-196}$ (deleted residues 188 to 196 are indicated). The Classical/Bipartite NLS (cNLS) is indicated in grey, amino acid 179-193 and the nuclear accumulation signal (NAS) in white, amino acid 313-322 (197). (B) Cylinder representation of the front (left) and side (right) views of THOV NP$^{\Delta 188-196}$. The N- and C-terminus is labelled in orange. The first visible amino acid is Thr20. B: Body domain, H: Head domain, T: Tail loop.

THOV NP$^{\Delta 188\text{-}196}$ crystallized as a trimer. The positively charged tail loop, which is located at the C-terminus of the molecule, is facing into the groove between the head and the body domain of the neighboring molecule. In addition to the tail loop, helix α15 is in close proximity for putative inter-subunit contacts with the neighboring helix α14 in the crystal (Figure 55).

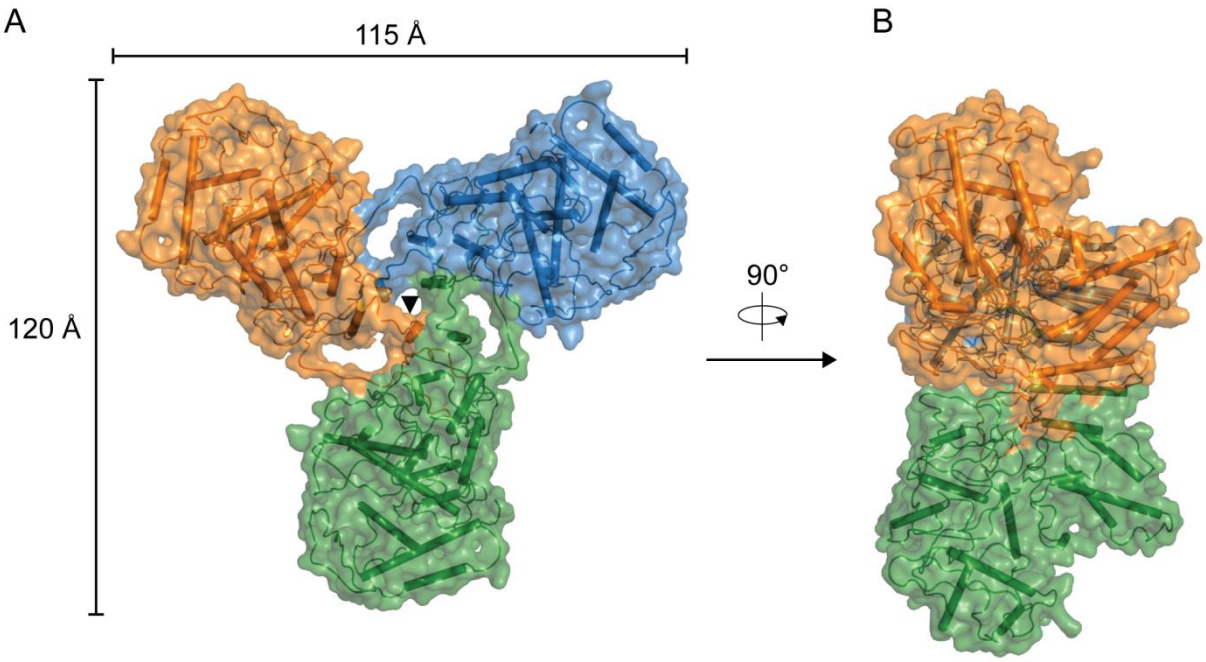

Figure 55: The crystallographic trimer of THOV NP$^{\Delta 188\text{-}196}$.

(A) Front and (B) side view of the crystallographic trimer. The NP protomer in the asymmetric unit forms a crystallographic trimer with its symmetry-related counterparts. Each NP molecule in the trimer inserts its tail loop into the neighboring protomer.

The positively charged groove between the head and the body domain is the putative RNA-binding site in IFAV, IFBV and ISAV NP (45-47). However, there are no structures of these NPs bound to RNA. In the crystal structure of the THOV NP$^{\Delta 188\text{-}196}$, many basic residues are located in this region, including Arg67, Arg70, Lys74, Lys109, Lys111, Lys126, Lys128, Lys135, Lys158, Arg160, Lys162, Arg213, Arg248 (Figure 56A). Additionally, basic residues are found in the body domain (α1), Lys26, Arg32, Arg36 and in the helix α11, Lys269, Lys273, Lys277, Lys278. Altogether, this may suggest an involvement of the groove in binding the RNA backbone. Tyr148 in IFAV NP is known to abolish RNA binding and to stabilize the trimeric form (194). In the THOV NP$^{\Delta 188\text{-}196}$ structure, Trp133 at one end of helix α4 could have a similar function (Figure 56B). Moreover, Tyr115, Phe117 together with Trp133 and Tyr136, some of them are conserved (see Appendix D - *Orthomyxoviridae* nucleoprotein

alignment) and may function as two gates (each on one side) for RNA binding, providing π-π-stacking interactions with the RNA bases. There was clear electron density for these four residues.

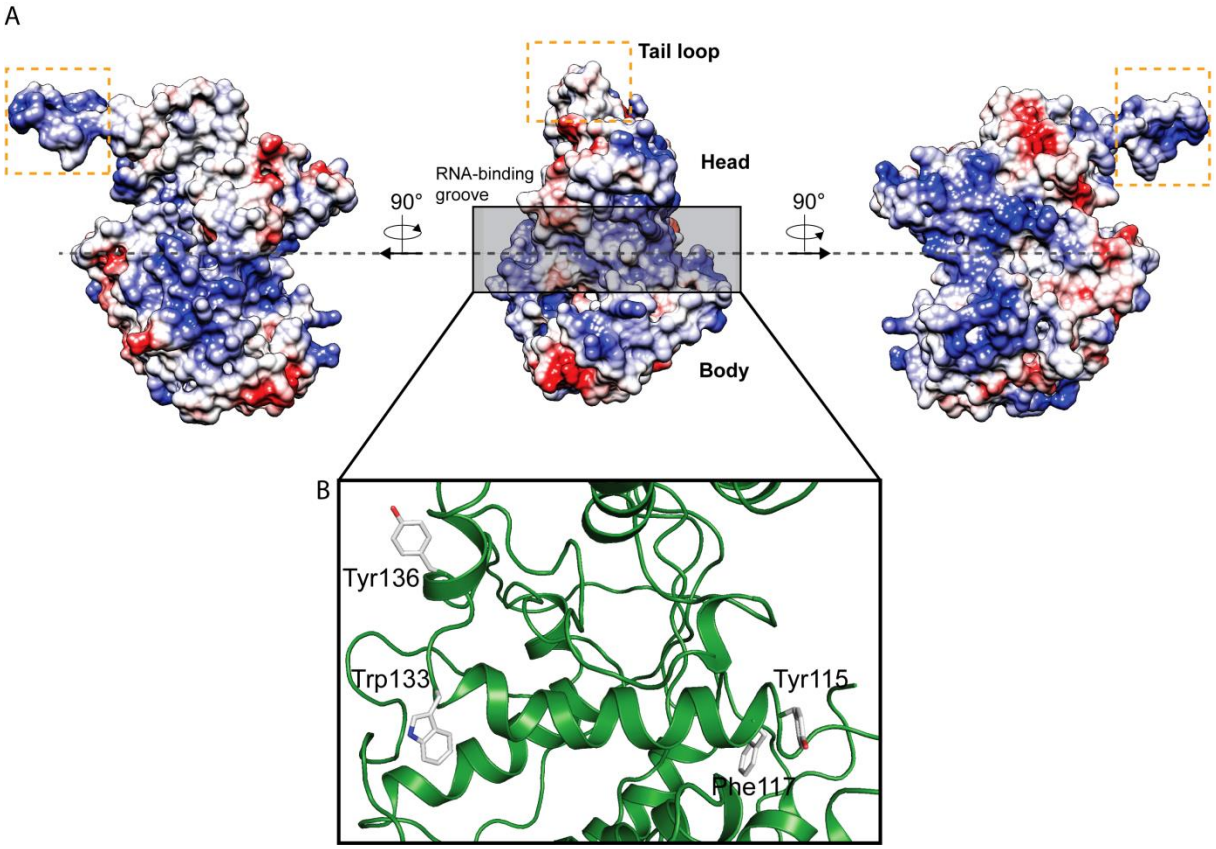

Figure 56: Electrostatic surface potential of THOV NP$^{\Delta 188\text{-}196}$.

(A) Front view (center) and side views (left and right). The RNA-binding side between the head and the body domain is highlighted in light grey and the tail loop is within the orange box. The color range is from -10 kcal/mole*e (red) to +10 kcal/mole*e (blue). (B) Detailed view of the aromatic gate in the RNA binding groove of THOV NP$^{\Delta 188\text{-}196}$. The four aromatic residues (Tyr115, Phe117, Trp133 and Tyr136) are located at each side of the RNA-groove. The electrostatic surface calculation was done with Chimera (166).

3.4.4 Structural comparison with negative-sense single-stranded RNA viruses (NSRVs)

Knowledge of vRNP formation and function is essential to understand the mechanisms of the NSRV life cycle. Structural comparisons of the THOV NP$^{\Delta 188\text{-}196}$ structure with other known crystal structures of the *Orthomyxoviridae* family members shows remarkable structural similarities despite the very low sequence homology of their NPs (19% to IFAV, 28% to IFBV and 12% to ISAV (Figure 57).

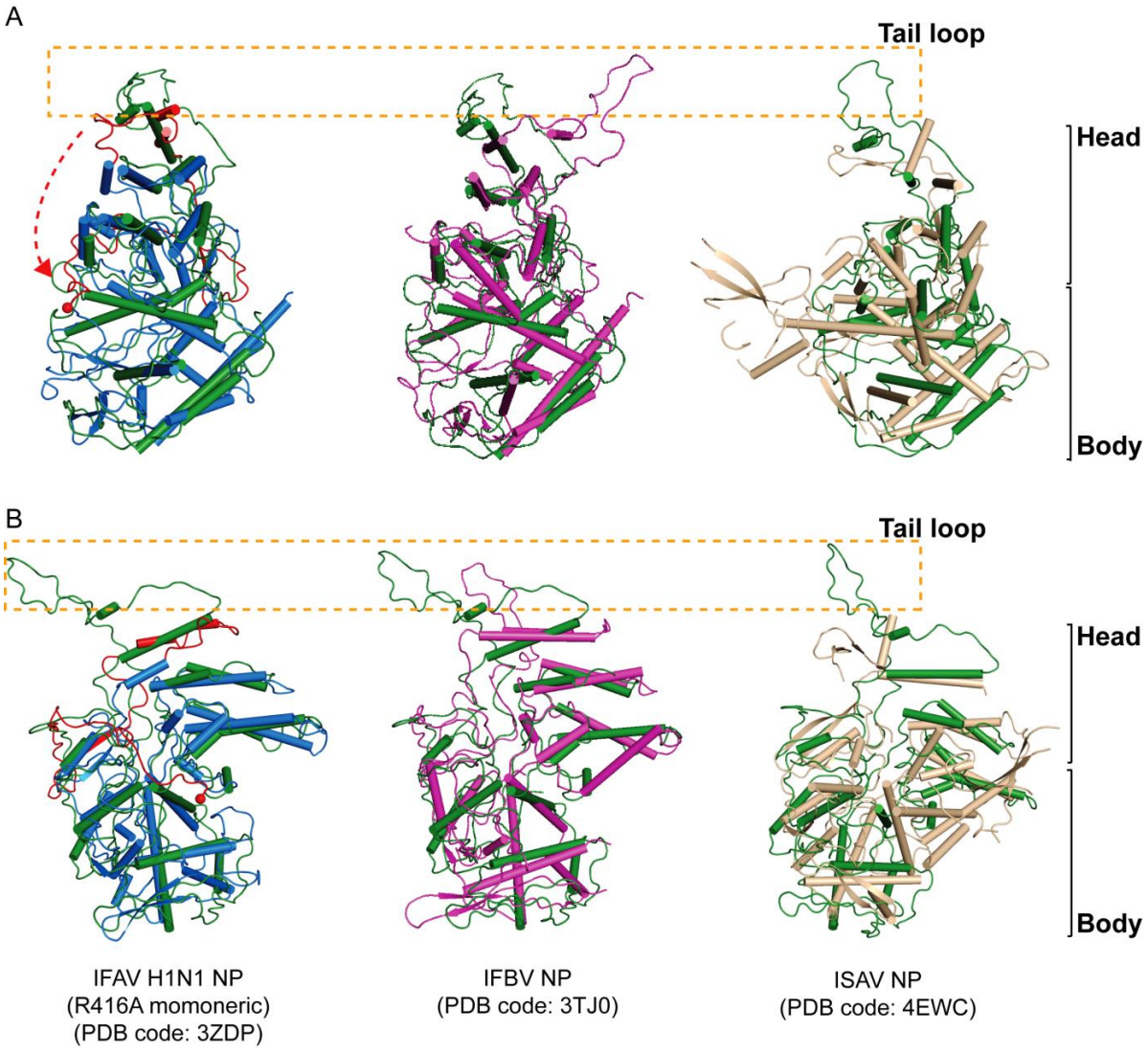

Figure 57: Structural comparison of orthomyxovirus NPs.

Topology-based structural C_α atom alignment of the know crystal structures of the *Orthomyxoviridae* family, together with r.m.s.d values obtained from structural comparison. Front view (A) and side view (B). The tail loop region is highlighted with an orange box. IAFV H1N1 NP (R416A, monomeric, in blue) (50) vs. THOV NP$^{\Delta 188\text{-}196}$ (r.m.s.d of 2.9 Å over 322 residues)). IABV NP (in purple) (46) vs. THOV NP$^{\Delta 188\text{-}196}$ (r.m.s.d of 2.9 Å over 345 residues). ISAV NP (in fawn) (47) vs. THOV NP$^{\Delta 188\text{-}196}$ (r.m.s.d of 2.9 Å over 298 residues). The C-terminal region (429-498 in red) of the IFAV H1N1 (R416A, monomeric) folds back into the RNA binding groove and the last residue (Asn498) is indicated by a red dot.

The NPs are all composed of two (head and body) helical domains, which form a banana-shaped molecule. A long tail loop, which is important for NP oligomerization and therefore for vRNP assembly, is located at the C-terminal end of the head domain and interacts with the adjacent protomer in the trimeric (IFAV and THOV) or in a tetrameric form (IFBV) (Figure 57). However, it folds back into the RNA binding groove in the monomeric state (IFAV). Furthermore, there is a different orientation of the tail loop in the present THOV NP$^{\Delta 188\text{-}196}$ structure compared with the IFBV NP (46).

Moreover, comparisons with other segmented (La Crosse virus, LACV, *Bunyaviridae*), or non-segmented (Vesicular Stomatitis Virus (VSV) and rabies virus, both *Rhabdoviridae*) NSRV NPs show similar topology of the NPs despite differences in size (LACV NP: 235 residues, VSV NP: 422 residues, Rabies virus NP: 398 residues, THOV NP 454 residues). The head and body domain are connected via a loop region and a central helix-loop-helix (HLH) motif surrounding the RNA binding groove (amino acid 116-140 in THOV NP$^{\Delta 188\text{-}196}$) (Figure 58, indicated in purple). These regions are spread throughout the whole sequence. Furthermore, a C-terminal tail loop region for oligomerization is present in all of the NPs. Together, similarity and structural conservation of the NSRV NPs indicate an important role of this architecture for vRNA encapsidation.

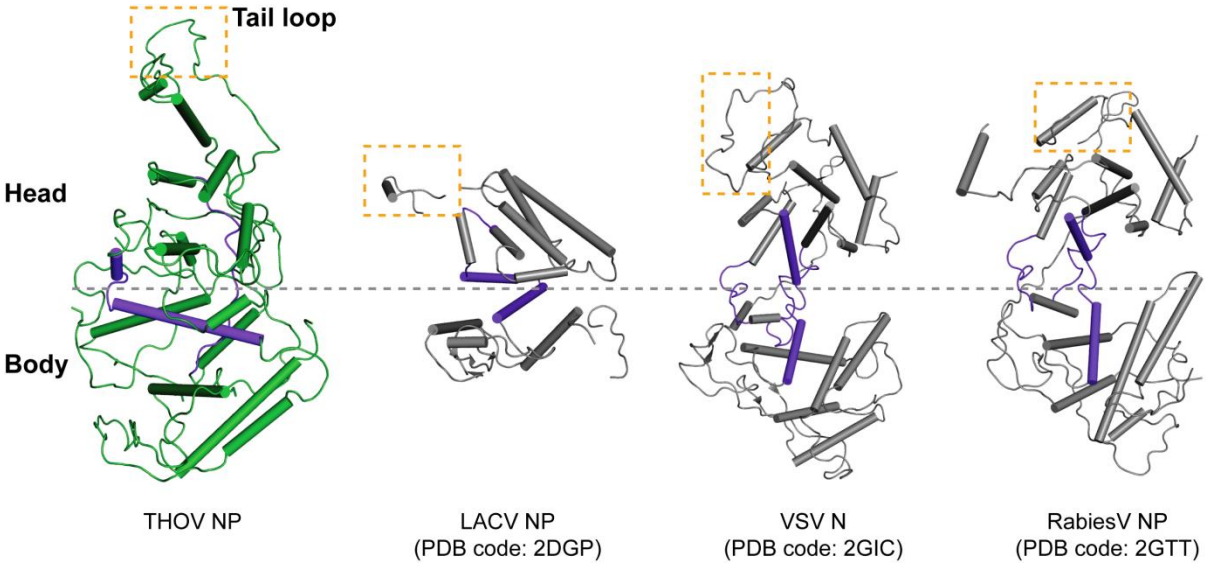

Figure 58: Structural comparison of NSRV NPs.

All NPs are composed of a head and a body domain which are connected via a loop region and a helix-loop-helix-motif (purple). The tail region is indicated with an orange box located near the C-terminus.

3.4.5 Functional analysis of the THOV NP$^{\Delta 188-196}$ structure

3.4.5.1 Single-stranded RNA/DNA binding

To characterize the role of the flexible regions, Δ188-196 in THOV NP and the corresponding Δ194-200 deletion in DHOV NP in RNA binding, I subjected this mutants to ITC experiments with a pU24mer oligo (Figure 59A, Table 9).

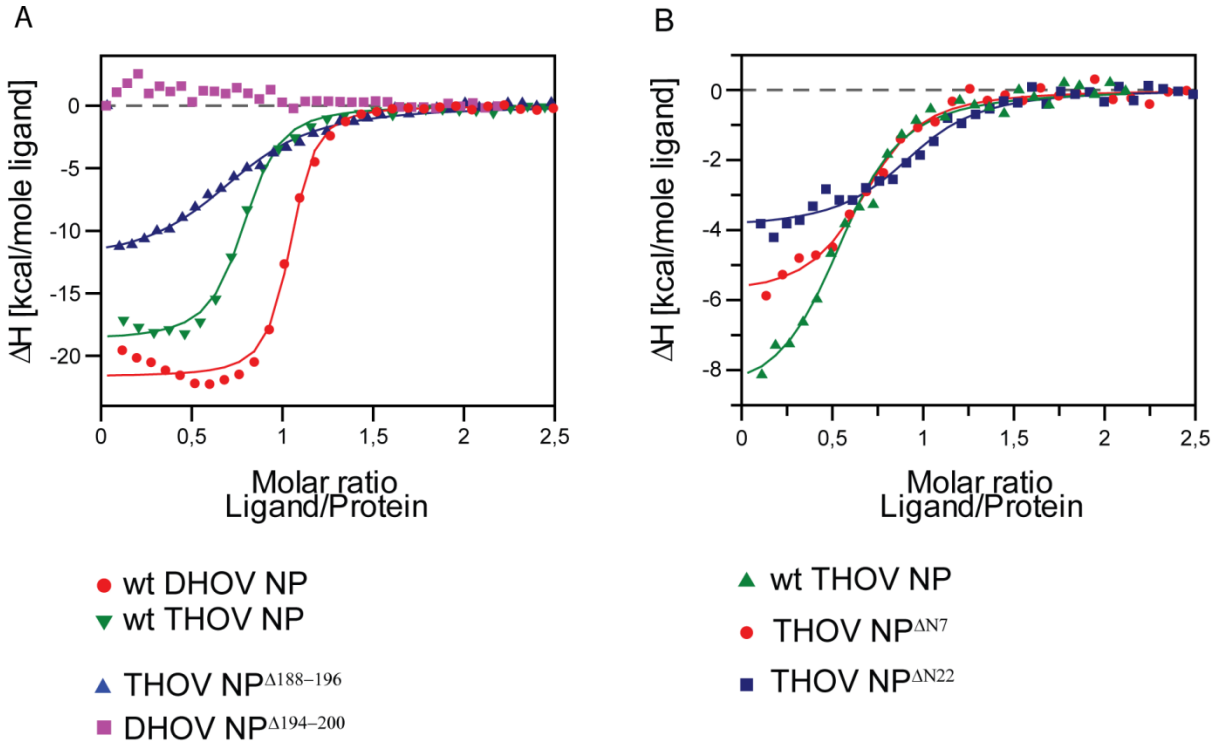

Figure 59: Binding to ssRNA/ssDNA of internal and N-terminal deletion constructs.

(A) Integrated ITC signals for the THOV NP$^{\Delta 188-196}$ (Δ, blue curve, K_D=1.1±0.1 µM, n=0.8±0.02), wt THOV NP (∇, green curve, K_D=133±17 nM, n=0.8±0.01), DHOV NP$^{\Delta 194-200}$ (□, purple curve, no binding) and wt DHOV NP (○, red curve, K_D=51±9 nM, n=1.0±0.01) bound to a pU24mer. (B) Integrated ITC signals for the wt THOV NP (Δ, green curve, K_D=598±107 nM, n=0.6±0.02), THOV NP$^{\Delta N7}$ (○, red curve, K_D=404±83 nM, n=0.7±0.02), THOV NP$^{\Delta N22}$ (□, blue curve, K_D=555±123 nM, n=0.9±0.02) bound to a pT24mer. Resulting heat changes were integrated and the obtained values fitted to a quadratic binding equation. The indicated K_D values were derived from the fittings. 150 µM solutions of the pU24mer or pT24mer oligo were stepwise titrated into 10 µM solutions of the indicated mutant at 8°C in an ITC device. Experiments were performed in ITC buffer (see 2.1.10)

Both deletions were introduced to facilitate crystallization, but only in the case of the THOV NP, the structure could be obtained. Lys190, Lys192 and Lys193 (within Δ188-196) located in the upper part of the RNA binding groove influence THOV NP RNA binding, because deletion

of these residues reduced the binding affinity of the mutant to a pU24mer oligo approximately 8-times compared to wildtype (wt) THOV NP (Figure 59A). Moreover, the DHOV NP$^{\Delta 194\text{-}200}$ mutant (including the deletion of Lys196, Arg198 and Lys199) completely lost its ability to bind to ssRNA, indicating a more important role of this region on RNA binding (Figure 59).

Next, I was also interested in the role of the flexible N-terminus of the THOV NP for binding to RNAs/DNAs. Two lysine residues are found at the N-terminus, Lys14 and Lys15. However, deletion of the first 7 or 22 residues did not influence the pT24mer binding of the THOV NP (Figure 59B). The K_D values and the stoichiometry are summarized in Table 9.

Mutant	Oligo	Binding affinity (K_D)	Stoichiometry (n)
Wt THOV NP	pU24	133±17 nM	0.8±0.01
Wt THOV NP	pT24	598±107 nM,	0.6±0.02
THOV NP$^{\Delta 188\text{-}196}$	pU24	1.1±0.1 µM	0.8±0.02
THOV NP$^{\Delta N7}$	pT24	404±83 nM	0.7±0.02
THOV NP$^{\Delta N22}$	pT24	555±123 nM	0.9±0.02
Wt DHOV NP	pU24	51±9 nM	1.0±0.01
DHOV NP$^{\Delta 194\text{-}200}$	pU24	No binding	No binding

Table 9: Binding characteristics of the deletion mutants of THOV and DHOV NP.

3.4.5.2 Oligomerization

The internal deletion of residues 188 to 196 in the THOV NP did not interfere with trimerization as proven by the crystal structure (see 3.4.3). Furthermore, THOV NP$^{\Delta 188\text{-}196}$ eluted at the same retention volume compared to the wt protein in analytical gel filtration experiments (Figure 60A, compare purple with green curve, see also Figure 43).

The crystal structure of the ISAV NP, a member of the orthomyxovirus family was solved by deleting an acidic patch at the very C-terminal tail of the protein (47). Consequently, Glu415 and Glu416 in THOV NP, and Glu420, Phe421, Glu422 and Glu423 in DHOV NP were mutated to alanine's for crystallization at the beginning of the project. Crystals never appeared for both of the NPs. Interestingly, in gel filtration experiments THOV NP$^{E415,\ 416\text{-}2A}$ eluted in a monomer/trimer equilibrium (Figure 60A, red curve). The additional deletion of THOV NP residues 378 to 387 within the tail loop in the Δ188-196 and EE415-416AA background disrupted trimerization completely and the protein eluted as a monomer (Figure 60A, black

curve), indicating an important role of the tail loop in trimerization. In IFAV NP, Glu449 (Glu415 in THOV NP) is known to make a salt bridge to Arg422 of the adjacent NP (in the trimer) in IFAV H1N1 NP and to Lys430 of the same NP in IFAV H5N1 NP (45). Mutating Glu449 to alanine in IFAV H5N1 NP resulted in a mixture of different types of higher-oligomers (198).

Mutating residues Glu420, Phe421, Glu422 and Glu423 to alanine's in the DHOV NP, however, were sufficient to disrupt trimerization and the protein eluted as a monomer (Figure 60B, orange curve). These results indicate an involvement of these acidic residues in trimerization of the THOV and DHOV NP but in comparison to the IFAV H5N1 NP did not form higher-oligomers. However, in the present THOV NP$^{\Delta 188\text{-}196}$ crystal structure Glu415 and Glu416 is not resolved.

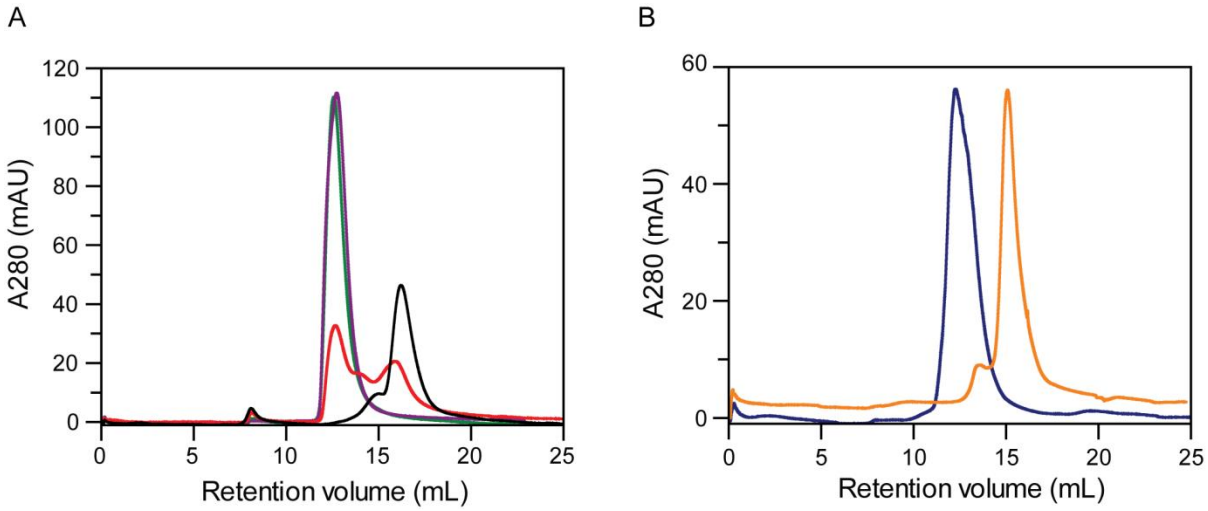

Figure 60: Analytical gel filtration analysis.

(A) Wt THOV NP (trimer, green curve), THOV NP$^{\Delta 188\text{-}196}$ (trimer, purple curve), THOV NP$^{E415,\ 416\text{-}2A}$ (trimer/monomer, red curve), THOV NP$^{\Delta 188\text{-}196,\ \Delta 378\text{-}387,\ E415,\ 416\text{-}2A}$ (monomer, black curve). (B) Wt DHOV NP (trimer, blue curve), DHOV NP$^{E420\text{-},\ F421\text{-},\ E422\text{-},\ D423\text{-}4A}$ (monomer, orange curve). 50 µl of NP at a concentration of 2 mg/mL was applied to an S200 10/300 gel filtration column. System was equilibrated with gel filtration buffer (150 mM NaCl, see 2.1.10) and runs were performed at 0.5 mL/min and 4°C.

3.4.5.3 Electron microscopy (EM) analysis of THOV/DHOV-RNPs

For the visualization of THOV and DHOV NPs in the apo form or bound to a 8-kb long ssRNA (152), I reconstituted these RNPs *in vitro* and observed the particles by negative-stained electron microscopy (see 2.3.15). Different molar ratios (5:1 and 10:1, NP:ssRNA) were used for complex preparation. Wt THOV and wt DHOV NP images are shown here as a reference for NP trimers before addition of ssRNA (Figure 61C and Figure 62A). Nevertheless, upon addition of ssRNA in a 5:1 molar ratio (Figure 61D), THOV NPs formed small ring-like structures with a diameter between 25 and 35 nm and the electron micrographs are distinct from the apo trimeric NP. The size of the rings indicated binding of NP to fractions of degraded ssRNA. Therefore, no accurate NP number could be derived for the rings. Nevertheless, the formation of ring-like NP structures is in agreement with reconstituted IFAV RNPs, where 9 NPs formed a mini-RNP together with the heterotrimeric polymerase subunits (PB1, PB2 and PA) (199,200).

The crystallized mutant THOV $NP^{\Delta 188\text{-}196}$, which exhibits defects in RNA-binding (Table 9), still showed ring-like structures (Figure 61E), indicating that these residues are not essential for oligomerization. Surprisingly, when using a 10:1 molar ratio (NP:ssRNA), aggregated structures for the THOV NP were observed, as shown in Figure 61F and G (two representative spots on the grid). Similarly to the THOV NP, also DHOV NP showed ring-like (Figure 62B and C, 5:1 ratio) and filamentous (Figure 62D, 10:1 ratio) structures in the electron micrographs when incubated with ssRNA. Furthermore, I visualized purified RNPs extracted from THOV virions. They are similar in architecture compared to the IFAV vRNPs (52,53,190), showing a rod-like structure with a loop region visible on one side (Figure 61H).

Altogether, EM analysis hints at oligomer formation, depending on the NP:nucleic acid ratio, which suggests cooperative effects on long RNA fragments if a sufficient NP concentration is provided.

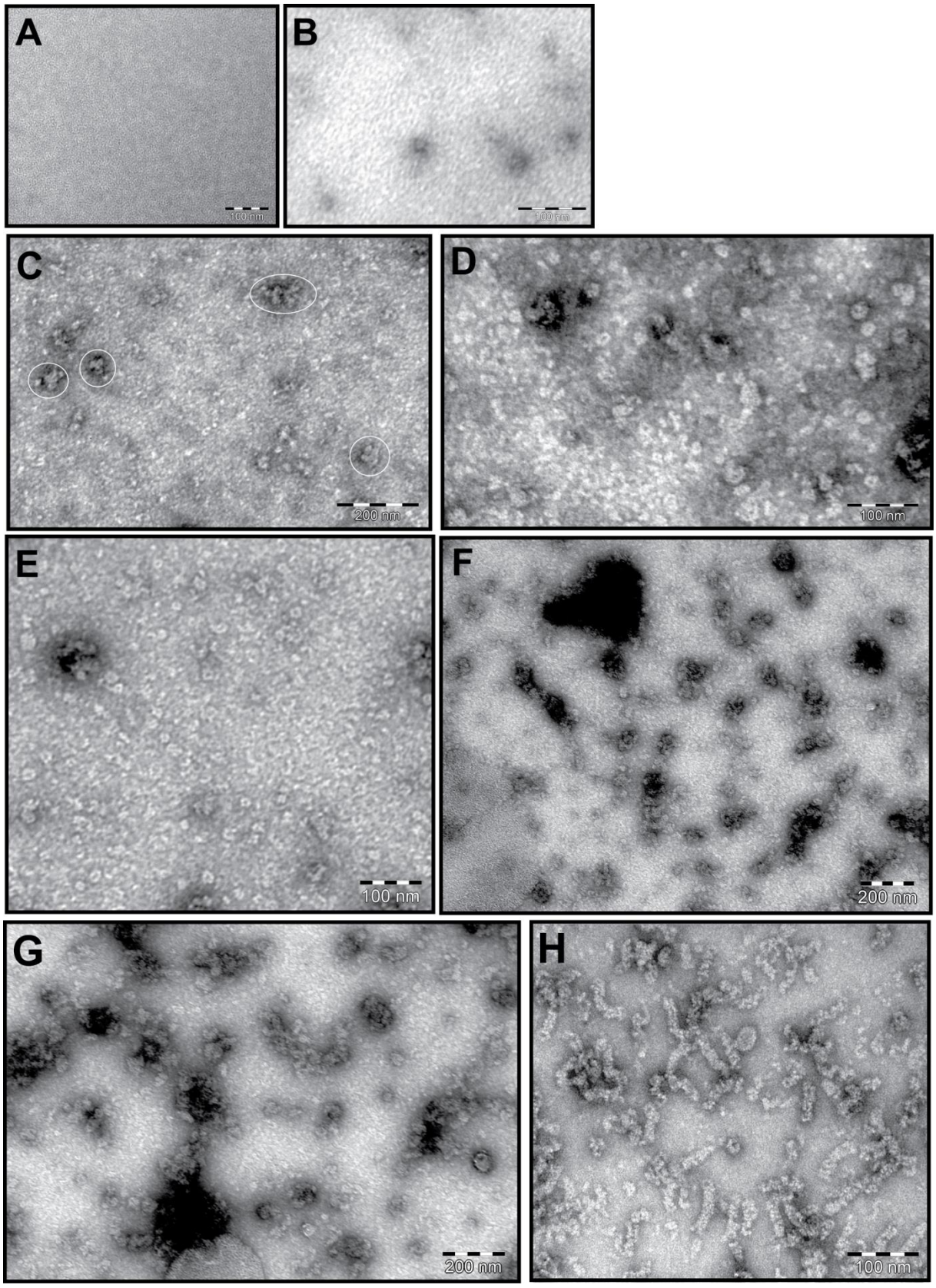

Figure 61: NP visualization on ssRNA by electron microscopy.

(A) EM buffer (see 2.1.10). (B) 8-kb long ssRNA (152). (C) Wt THOV NP (Apo). Circles highlight the trimeric protein. (D) Wt THOV NP + ssRNA (5:1). (E) THOV NP$^{\Delta 188\text{-}196}$ + ssRNA (5:1). (F, G) Wt THOV

NP + ssRNA (10:1) at two different grid positions. (H) Purified RNPs extracted from virions of the THOV. The samples were negatively stained with 2% uranyl acetate. The scale bar in nm is indicated.

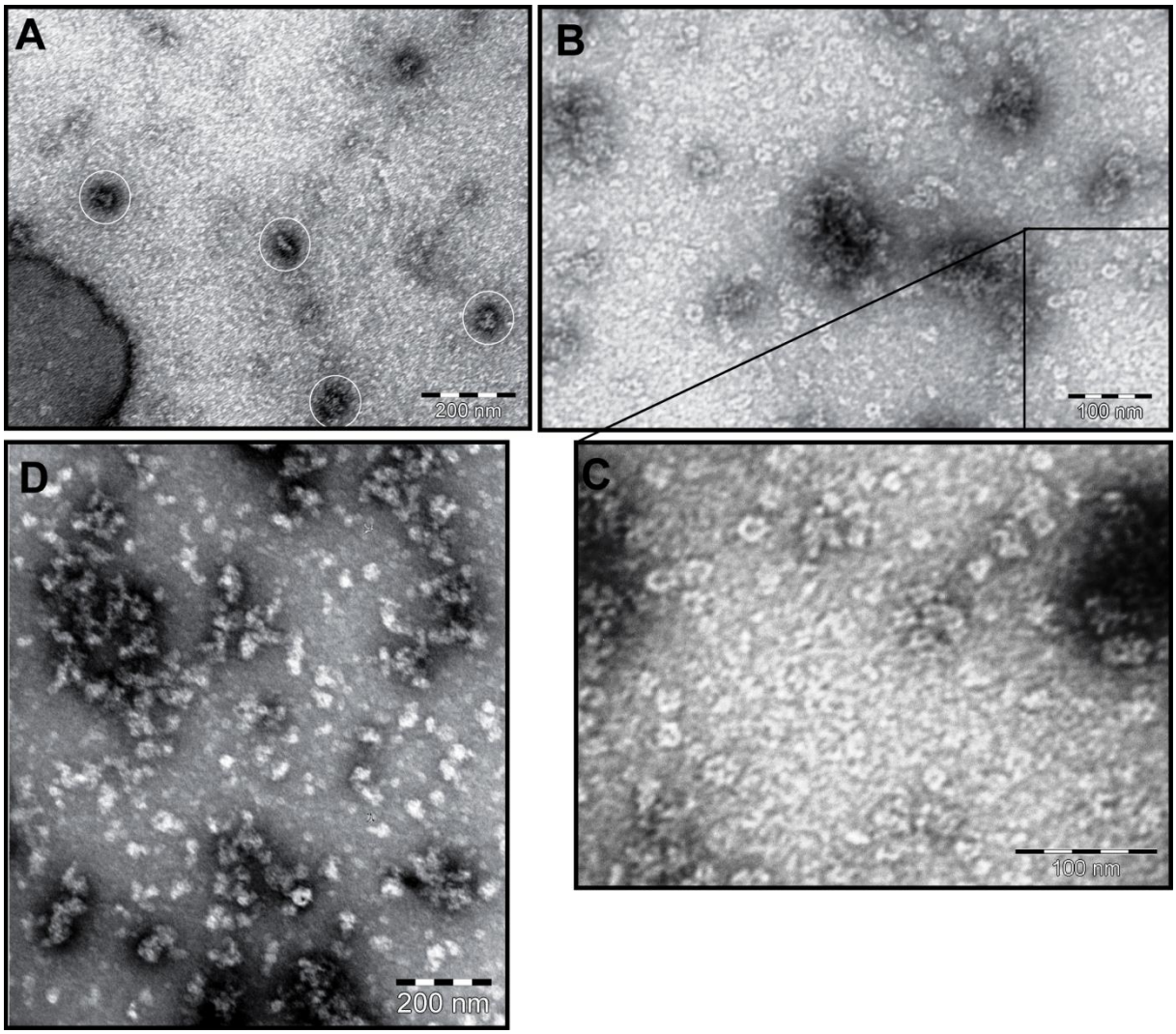

Figure 62: Electron microscopy of wt DHOV NP at different NP:nucleic acid ratios.

(A) Wt DHOV NP (Apo). Circles highlight the trimeric protein. (B, C) Wt DHOV NP + ssRNA (5:1). (D) Wt DHOV NP + ssRNA (10:1). The samples were negatively stained with 2% uranyl acetate. The scale bar in nm is indicated.

4 Discussion

4.1 G domain dimerization of MxA and its role for the antiviral activity

The dynamin superfamily is characterized by their concentration-dependent increase of GTPase activity. For dynamin and dynamin-related proteins, such as MxA or the guanylate binding protein 1, GTPase activation is mediated by nucleotide-dependent dimerization of the G domains via the G interface which induces rearrangements of catalytic residues in the active site (77,84,88). In dynamin and dynamin related-proteins, the GTPase activity has been implicated in the nucleotide-dependent remodeling of cellular membranes. However, the exact function of the GTPase activity for the antiviral action of MxA has remained unclear. Current knowledge indicates that the antiviral activity of MxA is dependent on GTP hydrolysis (130,131) and oligomerization via the stalk (75,76,183,184). In this doctoral thesis, a panel of G domain mutants was used to demonstrate that nucleotide binding and formation of the G interface are critical for the intracellular localization and the antiviral function of MxA.

Structure analysis indicates that the G domain dimer of dynamin and MxA is formed by direct contacts between the two switch regions and the *trans* stabilizing loop (77,88). Additionally, Asp253 from the G4 loop stabilizes this interaction by contacting the guanine base of the opposite G domain in *trans*. The nucleotide base, in turn, is bound in *cis* by the highly conserved Asp250 in the G4 loop which determines nucleotide-binding specificity (see also 1.6.2.2 and 3.1.2). Accordingly, the D250N mutation switched the nucleotide binding preference from guanosine to xanthosine triphosphates, as described previously for Ras-like GTPases and the signal recognition particle (176,201,202). MxA^{K83A} was previously annotated as a nucleotide-binding deficient mutant (130). However, in this study this mutant was still able to bind nucleotide (see Table 3), albeit with reduced affinity. However, MxA^{K83A} was deficient for GTP hydrolysis, and essentially behaved as MxA^{T103A} (131) in all assays carried out. These two mutants were previously used to assess the effects of GTP binding and hydrolysis for the antiviral effect of MxA against IFAV and vesicular stomatitits virus (130,131) and recently of the MxA paralog MxB against HIV-1 (70,72). In light of the biochemical results of this doctoral thesis, some of the interpretations previously drawn from analysis of the K83A mutant may have to be revisited or experiments repeated using, for example, the nucleotide-binding deficient D250N mutant.

In agreement with the recently published result from Rennie et al. (77), the monomeric MxA^{M527D} (75) dimerized in solution via the G domain in the presence of the transition state

analogue GDP-AlF_4^- (see also 3.1.2). However, MxA^{M527D} did not dimerize in the presence of GTPγS, GDP, AlF_4^- alone, or GMP-PCP (data not shown), indicating that a high affinity dimer is only formed in the transition state of GTP hydrolysis, and that dimer formation via the G interface is generally a low affinity, transient process. Furthermore, the MxA mutants MxA^{D250N} and MxA^{D253N}, with defects in binding the guanine base in *cis* or in *trans* lost their GDP-AlF_4^--induced dimerization via the G interface, as recently described for the V185Y mutation at the center of the G interface (77). In native assemblies, MxA may oligomerize via the stalk region (75,76), and the G interfaces may be stabilized by the simultaneous formation of multiple interactions within the large oligomers.

In mixed GTPase assays G domain mutants, with defects in their own hydrolysis, could still effectively stimulate the GTPase activity of an opposing wt G domain (see also 3.1.3). The T103A mutant, deficient in GTP hydrolysis, stimulated the GTPase of an opposing wt G domain to a similar extent as wt MxA. However, losing the capability for GTP binding, like shown for the D250N mutant, greatly reduced GTPase stimulation.These data demonstrate a crucial role of GTP binding for the induction of a G domain dimerization-competent conformation in MxA. Furthermore, the analysis of the MxA^{T103A} mutant indicates no coupling between the GTPase activity of two interacting G domains, and each G domain can independently hydrolyze GTP upon dimerization.

All G domain mutants in the context of the oligomerization-competent wt MxA protein lost their antiviral activity against THOV and IFAV (see also 3.1.4). In addition, the formation of MxA assemblies with the viral N protein in LACV-infected cells, a measure of MxA-mediated block of viral replication (104), was not observed for the G domain mutants. Interestingly, all G domain mutants had a dominant-negative effect on the antiviral activity of wt MxA. This supports a model wherein the incorporation of a small number of GTP-binding or GTPase-deficient mutants into wt MxA oligomers impedes MxA activity that requires formation of MxA oligomers around viral nucleocapsids, coordinated GTP hydrolysis and structural transformations in the MxA oligomers. In pull-down experiments, the binding of the viral NP in THOV-infected cells was not affected by introducing mutations in the G domain. This indicates that the recognition of the viral target by MxA is uncoupled from the GTPase cycle.

Nucleotide binding facilitates the oligomerization of MxA (76,203), probably by the additional nucleotide-driven association between G domains stabilizing the MxA oligomer. Accordingly, wt MxA that cycles between GTP and GDP-bound states showed a typical dispersed cytoplasmic localization with a few small assemblies that co-localized with markers of the smooth ER (101,183) (see also 3.1.5). However, the intracellular localization/distribution of the

G domain mutants showed significant differences compared to wt MxA. Nucleotide-binding competent but hydrolysis-defective mutants such as K83A, T103A and D253A formed few large intracellular aggregates which co-localized with the smooth ER marker Syntaxin 17 (204). In contrast, the nucleotide-binding deficient D250N mutant was uniformly dispersed throughout the cytoplasm of the transfected cells. The G domain mutants that prevent hydrolysis were combined with the D250N mutant that prevents GTP binding, to exclude the possibility that the formation of the large MxA granules is not a consequence of structural disturbance of the mutant proteins but rather a function of the nucleotide-binding status of MxA. Intriguingly, the double mutants showed the same diffuse distribution as previously observed for the nucleotide-binding deficient mutant, indicating that constant GTP binding stabilizes membrane-associated MxA aggregates. GTP hydrolysis and possibly release of the nucleotides is thus a prerequisite for dissociating these assemblies. As previously suggested (75,90), dimeric or tetrameric forms of MxA might be released from these membrane-associated stores to initiate the antiviral action.

Only a few single nucleotide polymorphisms are described in the human population of the highly conserved *MX1* gene (205). However, a recent study analyzed variations in the MxA genes of 267 healthy individuals and identified two rare nucleotide changes that result in amino acid exchanges at positions 255 and 268 (182). The structural information of the G domain dimer indicates, that these exchanges are localize in the G interface and might influence its formation or function. Interestingly, the V268M substitution showed diminished GTP hydrolysis, but only a slightly reduced antiviral activity (see also 3.1.6). The V268M variation was found homozygotic in a single individual (182). However, the G255E mutation completely abolished GTPase and antiviral activity of MxA in our analysis. Gly255 is closely located to Asp250 and Asp253, and raises the possibility that the G255E mutation interferes with the formation of the G interface. The rare occurrence of polymorphic changes in the G domain of MxA like the G255E mutation that was found only heterozygotic in two individuals (182) underlines the importance of this structural element for the antiviral function of MxA and suggests a central role of MxA for the antiviral host defense in humans. Therefore, it would be very interesting for a future study whether such polymorphisms are enriched in patients suffering from severe influenza symptoms as it has been described recently for IFITM3, another IFN-induced antiviral restriction factor against influenza A virus (206).

In summary, the present biochemical data suggest a dual role for the GTPase activity in MxA function and leads to the following proposed model (Figure 63). Viral infection leads to the induction of MxA by interferons, newly synthesized MxA is initially deposited close to ER

membranes. Upon GTP hydrolysis, dynamic redistribution of MxA from these depots to the viral RNPs or nucleocapsids takes place, which represent the target of MxA action. In the absence of GTPase activity, this release is prevented and MxA, most likely in its GTP-bound state, stays inactive in the membrane-associated deposits. The regular oligomerization of MxA molecules into ring-like structures around the viral RNPs allows multiple contacts with viral NPs as a main component of the RNPs. The affinity for these RNPs might cooperatively increase, facilitated by multiple interactions of MxA. GTP binding may not be necessary for the initial recognition of viral targets, but might stabilize the MxA-NP complex (Figure 63). How nucleotide hydrolysis is additionally required for inactivation of the viral target structure or for the recycling of RNP-bound MxA is a matter of future investigations.

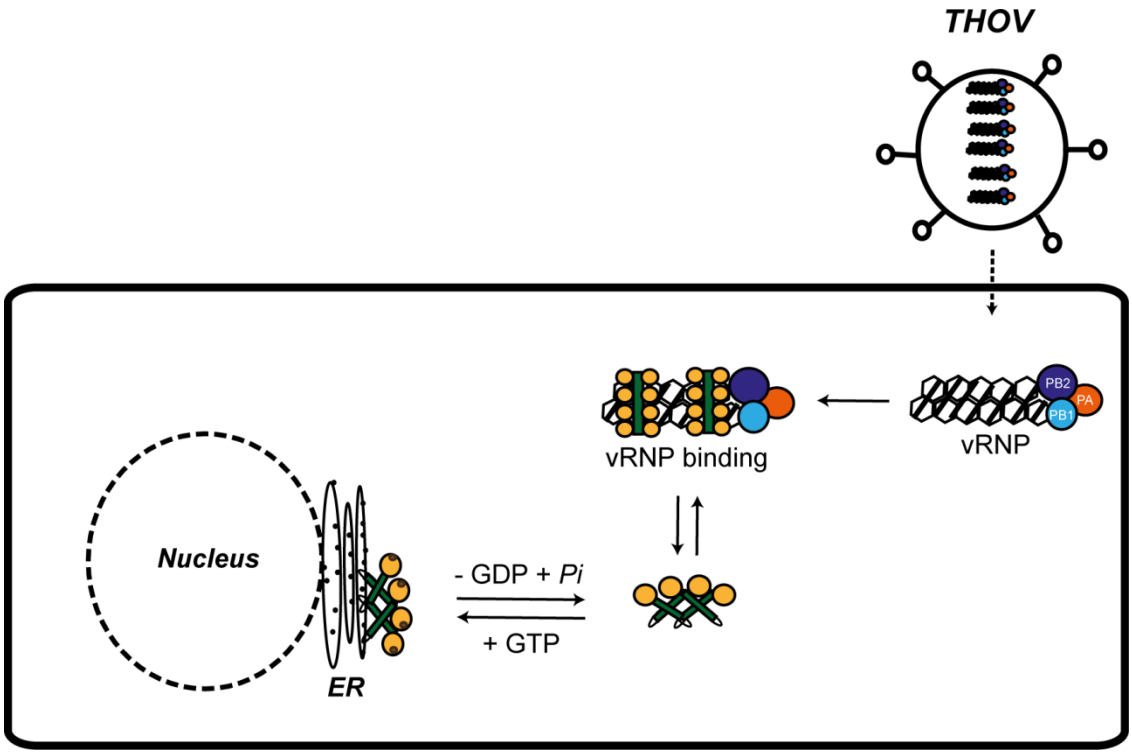

Figure 63: Role of nucleotide in the antiviral activity of human MxA.

The description of the figure is described in the text above.

4.2 MxA as a regulator of the MxB GTPase

The role of the interferon-induced cytoplasmic MxA protein in restricting a broad spectrum of ssRNA and DNA viruses has been subject of numerous investigations over the last decades. Its antiviral activity seems to depend on its cellular localization (see 1.6, and Table 1). For

example, MxA locates to the cytosol and interferes with nuclear translocation of IFAV vRNPs, and in this way inhibits secondary transcription and replication of IFAV genomes. Membrane binding, however, may be important for inhibiting viruses that replicate on membrane sites, such as bunyaviruses, positive-strand RNA viruses, the African Swine Fever virus, and poxviruses (102-104). The formation of higher-order oligomers, as well as GTP binding and hydrolysis seems to be a prerequisite for antiviral activity (75,76,142) (see also 3.1), with the only exception of hepatitis B virus restriction, which was demonstrated to be GTPase-independent (122).

The closely related human MxB protein was recently identified as a potent restriction factor for HIV-1 and other lentiviruses, in addition to its already known involvement in regulating nucleocytoplasmic transport and cell-cycle progression (70-72,106,132,134,207). However, no antiviral activity against the MxA-sensitive viruses was observed (70-72). In contrast to MxA, the MxB protein was shown to target the assembled capsid (CA) of HIV-1 (80). The antiviral mechanism is still poorly understood, but studies suggest that MxB prevents integration of the viral DNA into the host genome by interfering with uncoating (132), nuclear uptake (70,72), or integration by the viral pre-integration complex (PIC) (71,72) (see also 1.6.3 and 1.6.2). In contrast to MxA, oligomerization and GTPase activity are not critical for HIV-1 restriction. MxB exist in a long nuclear 78 kDa (+NLS), and a short cytoplasmic 76 kDa (-NLS) isoform. No antiviral or cellular activity has yet been described for the short 76 kDa isoform. However, hetero-oligomerization with the long 78 kDa isoform was observed (135), indicating that the short isoform may regulate the function of the long isoform. No interaction of the long 78 kDa isoform with the cytoplasmic MxA protein was observed (135), suggesting that nuclear MxB does not co-translocate MxA into the nucleus.

In the present study (see 3.2), a soluble dimeric MxB construct ($MxB^{\Delta N85/\Delta L4}$) was generated, representing the short cytoplasmic 76 kDa isoform of MxB. RALS analysis confirmed that this mutant is a dimeric protein. Dimerization of MxB was shown to be crucial for antiviral activity, as proven by other groups (80,81). Furthermore, in mixed GTPase assays, I found that a monomeric MxA mutant could stimulate the basal GTPase activity of MxB by approximately 12-fold (see 3.2.4, Figure 32B). However, no stimulatory effect of MxB on the GTPase of MxA could be observed (see Figure 32A). These results indicate that at least in vitro an interaction of MxA with the MxB protein takes place. It likely involves the G interface, as observed for MxA homo-dimers (see also 3.1). Whether this interaction is crucial for the antiviral activity is still not clear. For example, it could play a role in uncoating of the HIV-1 capsids, since this

process takes place in the cytoplasm of infected cell, and an interaction of the short MxB variant with the HIV-1 capsid was demonstrated, although to a lower extent compared to the long MxB variant (80).

The antiviral activity of MxB seems to be independent of nucleotide binding and hydrolysis. However, there is evidence suggesting that MxB plays a role in regulating nucleocytoplasmic transport and/or cell-cycle progression in a nucleotide dependent manner, since GTP binding was crucial for localization to the cytoplasmic face of the nuclear pore (106).
A GTPase-deficient MxB mutant (T151A) did also disrupt the nuclear import of a reporter protein, indicating that GTP hydrolysis is required for nuclear import (106). It can be speculated that the modulation of the GTPase activity of MxB by MxA may have an influence on the nucleocytoplasmic transport mechanism.
Furthermore, cells expressing the GTPase deficient mutant (T151A) showed a significant delay in progression from G_0/G_1 into S phase in the cell-cycle (106). The MxA-MxB interaction and the resulting increase in the GTPase activity of MxB may possibly have a regulatory effect on the cell-cycle progression of a dividing cell.

Retroviruses like HIV-1 are dependent on host resources, in particular on cellular proteins that are expressed at specific stages of the cell-cycle. Infection of human T cells ($CD4^+$) with HIV-1 causes cell-cycle arrest or delay in the G_2 phase, and leads ultimately to the cell death. Accessory proteins such as Vpr and Vif are known to be key players in this arrest (208). The GTPase coupling between MxA and MxB and the resulting increase in GTPase activity of MxB may be part of a complex machinery to overcome this cell-cycle arrest.

Finally, it remains an open question to date how potent the human MxB GTPase is against HIV-1 compared to other known restriction factors such as SAMHD1 or APOBEC, and how important the here presented observation in stimulating the GTPase activity of MxB by MxA is *in vivo*.

4.3 Structural comparison of the THOV NP within the *Orthomyxoviridae* family

The *Orthomyxoviridae* family belongs to the segmented negative-strand RNA viruses (sNSVs) (see 1.3 and Figure 2). This family is characterized by its segmented ssRNA genome which is decorated with viral NP, and which forms the vRNP together with the heterotrimeric polymerase. The vRNPs act as an independent molecular entity, providing a template for transcription and replication in the nucleus. In the last years, atomic resolution structures of RNA-free NPs became available for several of these NPs (44-47).

In the present work I determined the crystal structure of the RNA-free orthomyxovirus NP from THOV. The structural analysis indicates a similar overall architecture compared to IFA/BV NP (44-46), and the ISAV NP (47). A putative RNA-binding groove between head and body domain, and a C-terminal tail loop region responsible for oligomerization were identified (see also 3.4.3). Surface conservation analysis of THOV NP revealed high conservation within the members of its own genus Thogoto virus (including DHOV, see Appendix D - *Orthomyxoviridae* nucleoprotein alignment) (Figure 64A) and within the *Orthomyxoviridae* family (including IFA/B and C virus) (Figure 64B). Two prominent regions with high conservation are present in the structure: (1) the positively charged RNA-binding groove between the head and the body domain, and (2) the C-terminal tail loop. These observations indicate an important functional role of these elements throughout the *Orthomyxoviridae* family for RNA binding and oligomerization, respectively.

A B-factor (Debye-Waller factor) analysis revealed that the present THOV NP$^{\Delta 188\text{-}196}$ structure comprises a high flexible tail loop region (Figure 65), allowing the formation of irregular, supercoiled structures of the THOV RNPs (see 3.4.5.3, and Figure 61D-H), consistent with observations of other segmented NRVs, such as IFAV (see 1.1, and Figure 8C, D and E). The region between the head and the body domain shows low B-factors, reflecting a more rigid region of the molecule.

Crystallization trials of the wildtype THOV NP were successful, however, these crystals diffracted poorly. Generating a construct lacking amino acid 188-196 resulted in crystals that diffracted X-ray well enough to allow the structure determination. Even without these 9 residues, the solvent-exposed region surrounding this stetch shows still high flexibly (Figure 65, dashed box marked with an asterisk). Interestingly, the conventional NLS (cNLS, amino acid 179-193) of the THOV NP was reported to be located in this region (see also 3.4.3, and Figure 54A).

With the present structure, it is obvious that this cNLS is exposed and accessible for putative import machineries, such as importin-α. Deletion of these residues (^{188}NPKTKKPLE^{196}) also reduced the RNA-binding affinity for a pU24mer by approximately 10-fold (see also 3.4.5.1, and Table 9), suggesting a dual role of this region in cNLS-mediated nucleocytoplasmic transport and RNA-binding of THOV NP/vRNPs.

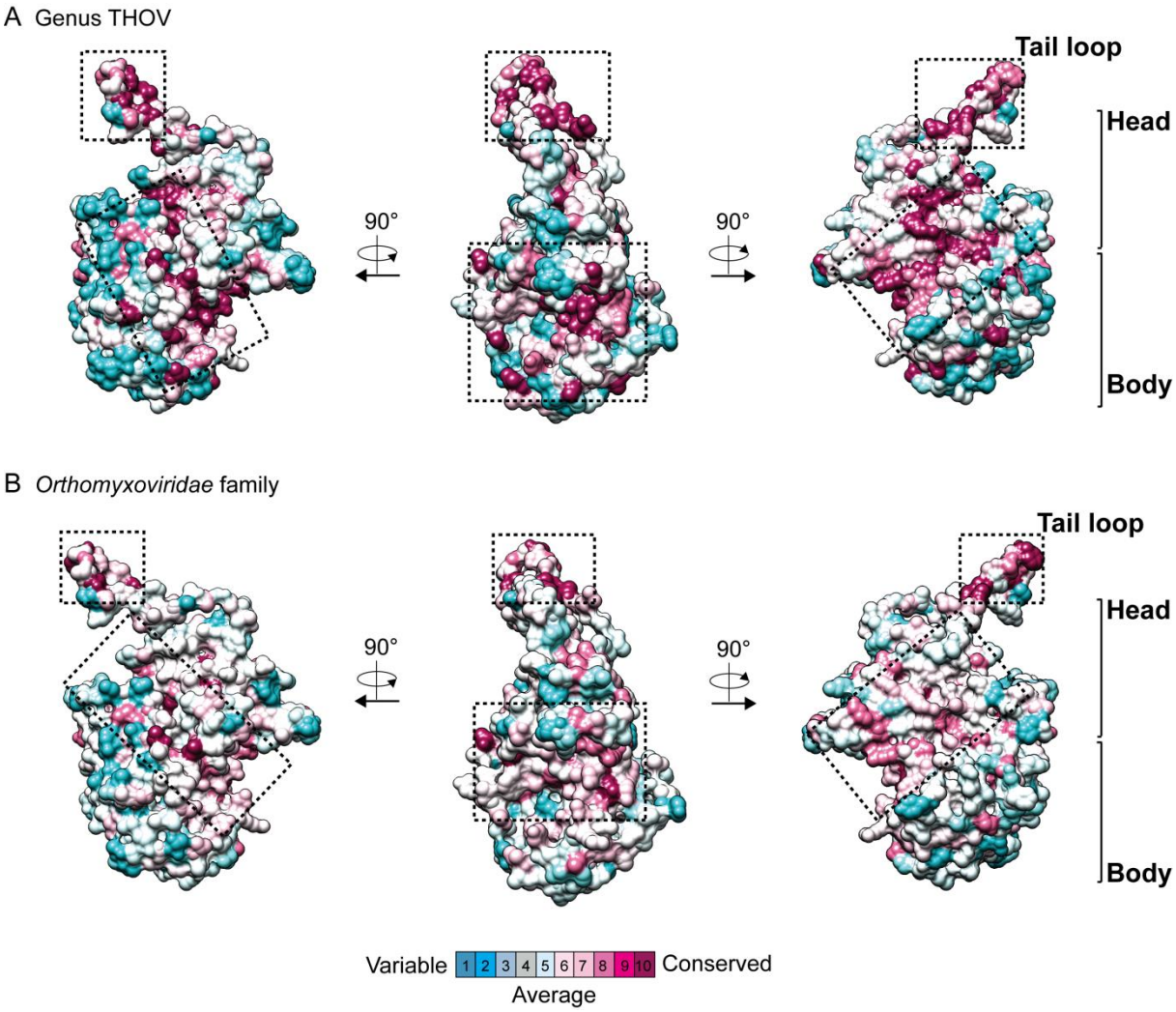

Figure 64: Surface conservation plot of THOV NP$^{\Delta 188\text{-}196}$.

Surface conservation plot (see 2.4.6) of the THOV NP$^{\Delta 188\text{-}196}$. Conserved residues are highlighted in purple and non-conserved residues in cyan. (A) Sequence conservation of the genus THOV mapped on the solvent-accessible surface of the THOV NP$^{\Delta 188\text{-}196}$ structure (see also Figure 5, excluding IFA, B and CV). (B) Sequence conservation of the whole *Orthomyxoviridae* family (including IFA (H1N1 & H5N1), B and C virus).

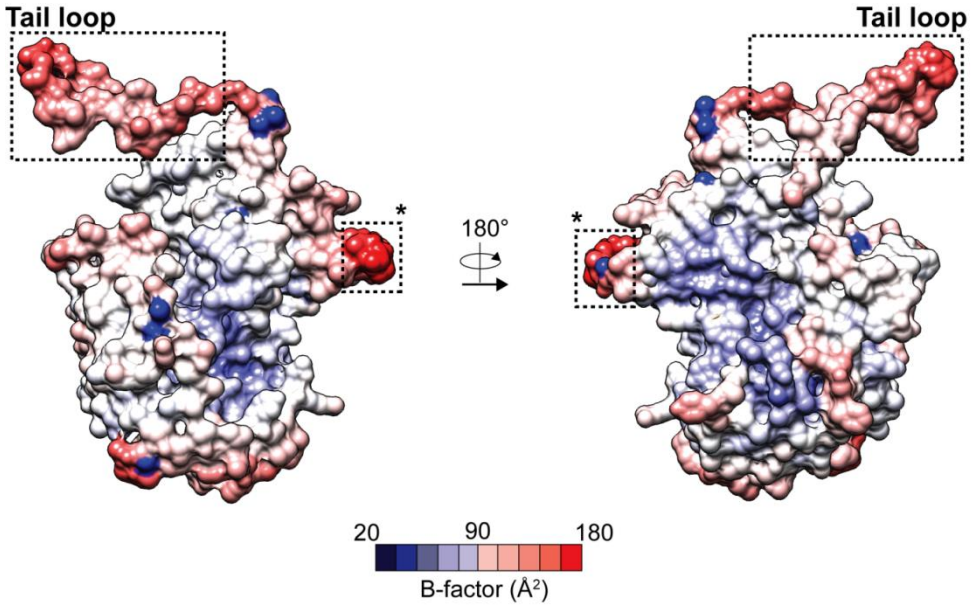

Figure 65: Surface B-factor plot of THOV NP$^{\Delta 188\text{-}196}$.

Regions with low B-factors are represented in blue and high B-factors in red. The asterisk highlights the cNLS (see also 3.4.3 and Figure 54A).

4.4 THOV NP sensitivity towards the antiviral MxA GTPase

Zoonotic transmission of influenza A virus from waterfowls, the natural host, into the human population is rare. However, in the last century, two dramatic cases were reported, 1918 ('Spanish' H1N1) and 2009 (pH1N1, reassortant virus from two swine influenza viruses) introducing a novel NP segment, resulting in pandemics with thousands of deaths. In 2013, a new H7N9 variant was transmitted from birds to humans (209). Multiple adaptations are necessary to overcome the interspecies barrier and establish a human lineage (210). This includes the adaptation to cellular factors such as the hemagglutinin (211), altered binding to cellular importins (212), but also adaptation to host restriction factors, such as the human MxA protein, to overcome the innate defense system. Host adaptation (viral mutations) of viral strains provides hints which viral structures are targeted by the human MxA protein. In Table 10, several surface-exposed amino acid adaptions to MxA in the body domain of the IFAV NP are summarized (140,213).

	Amino acid positions											
H1N1 1918			**I/V100**	**P283**			**Y313**					
pH1N1 2009		**D53**	**I/V100**		H289	K305		M316	K350	K351	I353	K357
H7N9	**N52**											
THOV	I44	P45	**V90**	N262			L289			**R328**		**R332**
DHOV	I52	D53	V90	V267			I292			V331		R335
BOUV	V54	D55	V100	V269			I294			E333		R337

Table 10: Amino acids responsible for MxA resistance.

Amino acids responsible for MxA resistance in the IFAV H1N1 NP (1918 & 2009), in the corresponding THOV/DHOV and bourbon virus (BOUV) NP. Amino acids which are linked to strong MxA resistance are underscored, and amino acids with a minor contribution to MxA resistance are shown in black (140,213). Residues from the THOV NP (Arg328 and Arg332) are highlighted in orange and may have the same role as Lys351 and Lys 357 in H1N1 2009 NP due to similar chemical properties. For the THOV/DHOV and BOUV NP, no experimental data are available. Consequently, the MxA resistance contribution is only an assumption.

The human MxA protein also inhibits the replication of the THOV (see also 1.6.3, and Table 1) (108,179,214), however, MxA shows higher sensitivity to THOV than to IFAV (177,178,215). Clearly, additional cellular host factors play an important role in determining the NP sensitivity of MxA, but nevertheless, the present THOV NP structure provides a possible explanation for the increased sensitivity. The pandemic influenza strains H1N1 1918 and pH1N1 2009 display surface-exposed residues on the backside of the NPs body domain which have been shown to be important for MxA resistance, these include Ile/Val100, Pro283 and Tyr313 in H1N1 1918, Asp53 and Ile/Val100 in pH1N1 2009 (216). Additionaly, Asn52 was identified on the body domain of the recently identified H7N9 NP (213) Figure 66A.

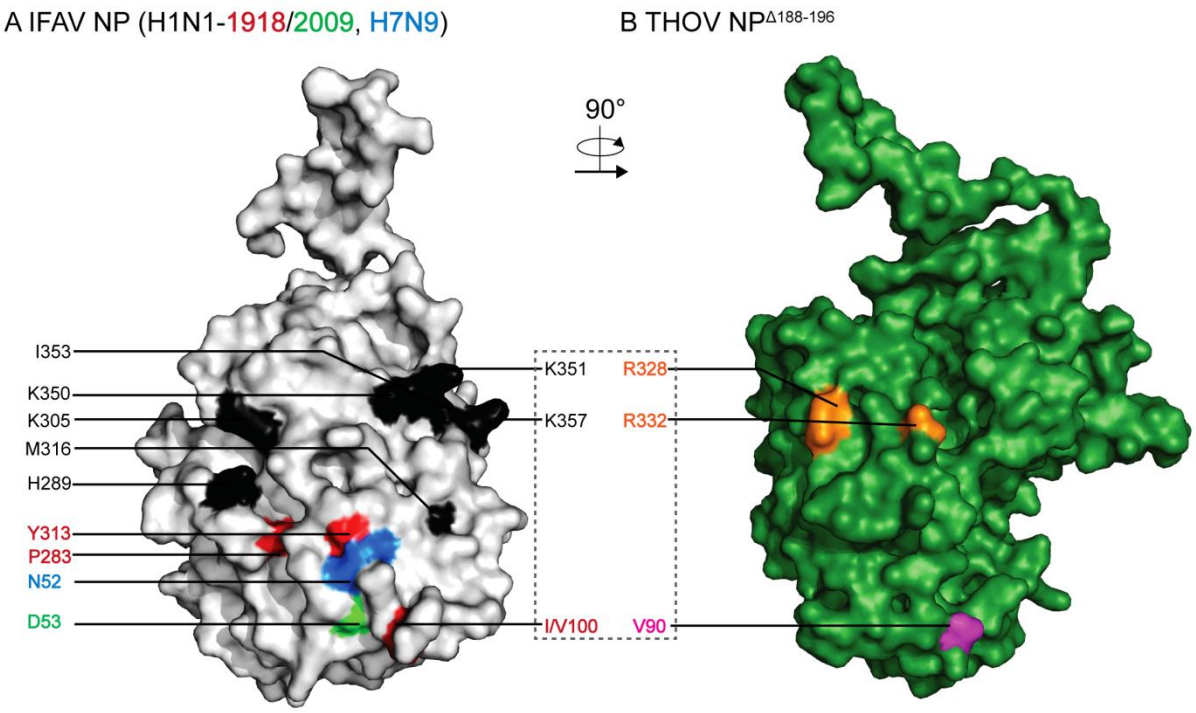

Figure 66: Amino acid cluster mediating MxA resistance.

(A) Amino acids important for MxA resistance in IFAV NP H1N1 1918 (A/Brevig Mission/1/1918, in red) and 2009 (A/Hamburg/4/2009, in green). The position of the recently identified H7N9 (A/Shanghai/1/2013) MxA resistance mutation is shown in blue. Minor contributing amino acids shown in black (140,213). (B) The corresponding amino acids on the THOV NP$^{\Delta 188\text{-}196}$ surface (grey dashed box). Val90 was present on the NP surface (shown in magenta). The orange highlighted residues correspond to IFAV NP amino acids with minor contribution to MxA resistance (see also Table 10).

However, the THOV NP structure exposes a corresponding Val90 together with Arg328 and Arg332 that were shown to contribute minorly to MxA resistance (Arg328 and Arg332) (Figure 66B). The DHOV NP, which is not MxA-sensitive (177), however, carries an Asp53 at this position (comparable to pH1N1 2009 NP).

The bourbon virus, a member of the THOV genus, was responsible for the death of a man in 2014 (31). The bourbon virus NP shares 45% sequence identity with the THOV NP, and sequence analysis revealed that the bourbon virus NP possess an Asp at position 55, comparable with the corresponding Asp53 in IFAV H1N1 2009. This MxA-resistant mutation in the bourbon virus NP may also be responsible for the severe course of the disease.

4.5 Oligomeric model of the THOV-RNP

Segmented negative-sense RNA viruses (sNSVs) encapsulate their genomic RNA with multiple copies of the NPs, leading to formation of the transcriptionally active vRNPs together with the heterotrimeric polymerase (see also 1.4). vRNPs are irregular, flexible, supercoiled structures. They are responsible for the transcription and replication of the virus during the life-cycle in the host cell. Cryo-EM analysis revealed the architecture of several RNPs including native (52), reconstituted RNPs (53) or mini-RNPs (200). On the basis of native RNPs (PDB code: 4BBL) isolated from virions, and the electron microscopy data, I modeled the central filamentous region of the THOV-RNP (see also 3.4.5.3, Figure 61H), and mapped the amino acids responsible for MxA resistance on this model (Figure 67).

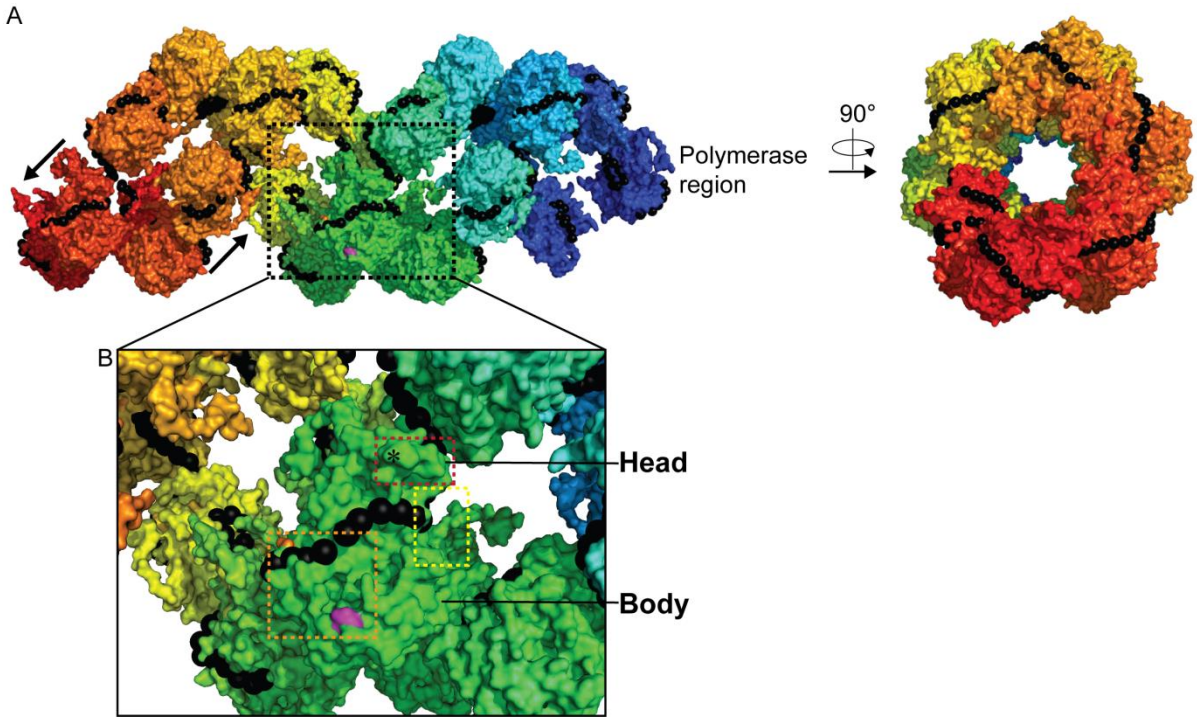

Figure 67: Model of the THOV-RNP.

(A) Side and front view of the central filament region of the THOV-RNP in surface representation (rainbow colored). Single-stranded RNA (polyU) is shown in black. The antiparallel orientation of the NPs is indicated by the arrows. In the left-handed helix, 12 NPs are required to form one turn. (B) Detailed view of one monomer. The dashed orange boxes indicate the MxA resistance amino acid positions (magenta for major MxA resistance, and orange for minor MxA resistance). The dashed red box shows the cNLS, and the yellow dashed box the N-terminal region. The cryo-EM structure of the IFAV RNP (PDB code: 4BBL, (52)) was used to model the THOV-RNP.

The NPs in the helical model arrange in an antiparallel fashion (indicated by the arrows) and bind to ssRNA (polyU) with the RNA-binding site facing to the outside. The RNA is therefore

partially exposed. The MxA-sensitive amino acids in the body domain of the THOV NP are on the outer surface of the model and therefore accessible for putative interactions with cellular factors such as the human MxA protein. Furthermore, a DEAD box RNA helicase, UAP-56, which prevents dsRNA formation might interact with the THOV NP N-terminal region (Figure 67B, dashed yellow box), as shown for the IFAV NP. UAP-56 has also been shown to interact with MxA and the IFAV NP (137). In the IFAV NP, Lys351 and Lys357 are minor MxA-resistance determinants (Table 10). The corresponding Arg328 and Arg332 (Figure 67B, in orange) are located close to the RNA and might have a second role in RNA binding in addition to determining MxA sensitivity.

Using electron microscopy, I visualized THOV and DHOV NP bound to 8-kb long ssRNA. When using a 5:1 ratio (see 3.4.5.3, Figure 61D-E and Figure 62B-C) ring-like structures varying in diameter from 25-35 nm were the main species visible on the electron micrographs. However, larger aggregates were observed using a higher NP:ssRNA ratio (10:1). The ring-like structures might be explained by binding of the NPs to degraded fractions of ssRNA. Nevertheless, ring-like structures were predominantly found and might represent a stable NP-ssRNA structure.

In addition to the central filament region and the polymerase region of the viral RNP as described in chapter 1.4, a loop region can be found at one end of the RNP (see also 1.4, Figure 9). The ring-like structures observed in this thesis support the model of ring/loop formation in THOV RNPs. On the basis of a biologically active IFAV miniRNP cryo-EM structure, where 9 NPs bound to 248 nucleotides, I docked the THOV NP structure to model a THOV 9mer shown in Figure 68. In this arrangement, the tail loop (amino acid 361-396) could connect to the adjacent NP so that the backside of the NP is facing into the inside of the ring (Figure 68B), exposing the ssRNA to the outside of the ring.

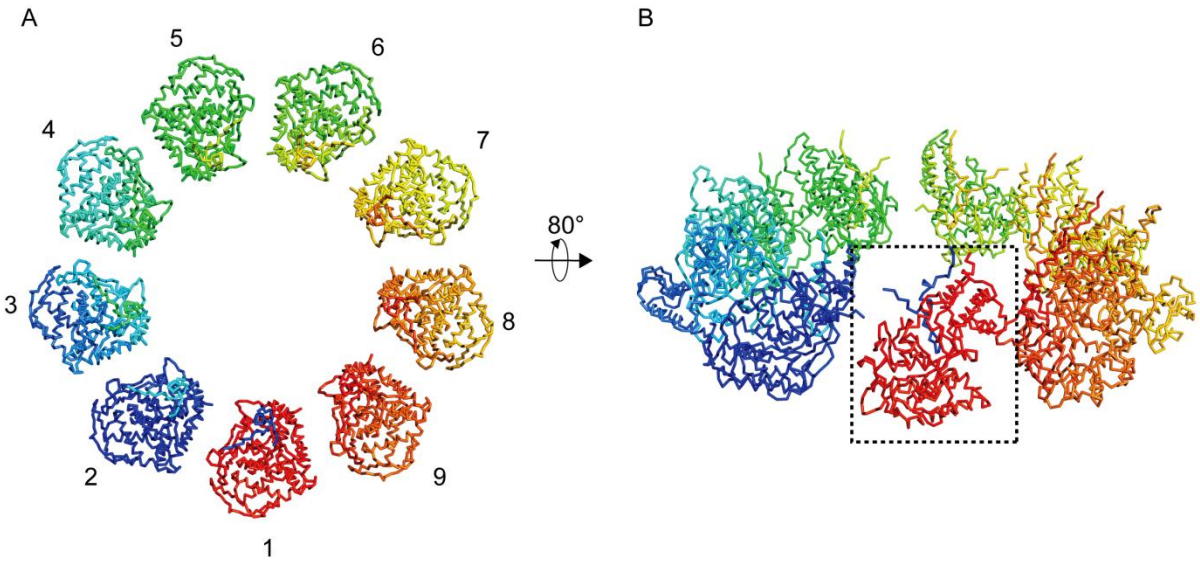

Figure 68: Model of the THOV-miniRNP.

(A) Front view of the of a THOV miniRNP (9mer) model in ribbon-type representation (rainbow colored). (B) Side view of the miniRNP. The dashed box shows one monomer with the inserted tail loop (amino acids 361-396) from the adjacent NP. The model was manually adjusted based on the cryoEM structure of an IFAV miniRNP (PDB code: 2WFS, (45,200)).

Both models, the helical RNP in Figure 67 and the ring-like mini-RNP in Figure 68 demonstrate the capability of the THOV NP to form structural diverse assemblies. This diversity is mainly facilitated by the flexibility of the C-terminal tail loop of the NP. The helical arrangement of the NP together with the heterotrimeric polymerase represents the native and biological active form, whereas the formation of the ring-like structures might be an artifact, and it remains speculative if such structures are of biological importance. Finally, the visualization of such THOV- or IFV-RNP structures in complex with the human MxA GTPase is of great importance for possible drug design efforts in the future.

Appendix A – Instruments

Instrument	Manufacturer (location)
Agarose Gel Electrophoresis System	OLS, Bremen, Germany
Amicon centrifugal filter devices	Millipore, Billerica, USA
Analytical Ultracentrifuge XL-1	Beckman Coulter, Krefeld, Germany
Automated imaging and storing system (Rock Imager)	Formulatrix, Waltham, Germany
Benchtop Centrifuge 5415 R	Eppendorf, Hamburg, Germany
Benchtop Centrifuge 5804 R	Eppendorf, Hamburg, Germany
Binocular Microscope MZ 7.5	Leica, Wetzlar, Germany
Blockheater Rotilabo H250	Roth, Karlsruhe, Germany
Chromatography column GSTrap HP 1 ml	GE Healthcare, Piscataway, USA
Chromatography column material GSH Sepharose 4B	GE Healthcare, Piscataway, USA
Chromatography columns Superdex 200 16/60, 26/60	GE Healthcare, Piscataway, USA
Centrifuge Avanti J-26 XP	Beckman Coulter, Krefeld, Germany
Fluidizer	Microfluidics, Newton, USA
FPLC Äkta Prime Plus	GE Healthcare, Piscataway, USA
FPLC Äkta Purifier	GE Healthcare, Piscataway, USA
HPLC 1260 Infinity LC	Agilent, Santa Clara, USA
Imaging system LAS4000 mini	FujiFilm, Düsseldorf, Germany
Isothermal Titration Calorimeter VP-ITC	GE Healthcare, Piscataway, USA
Isothermal Titration Calorimeter iTC_{200}	GE Healthcare, Piscataway, USA
Nanodrop 2000	Thermo Scientific, Wilmington, USA
Nucleosil 100 C18 HPLC precolumn	Knauer, Berlin, Germany
PCR Thermocycler	Biometra, Göttingen, Germany
C1000 Touch™ Thermal Cycler	Bio-Rad, München, Germany
Peristaltic Pump ISM 827 B	Ismatec, Glattbrugg, CH
pH-Meter	Mettler-Toledo, Gießen, Germany
Pipetting robot Hydra-Plus-One	Thermo Scientific, Dreieich, Germany
Pipetting robot Gryphon LCP	Art Robbins Instruments, Sunnyvale, USA
RALS 270 dual detector	Malvern Instruments, Worcestershire, U.K.
Refrective index detector VE 3580	Malvern Instruments, Worcestershire, U.K.
Reversed-phase ODS-2 hypersil	Thermo Scientific, Dreieich, Germany
Scales	Sartorius, Göttingen, Germany
SDS PAGE System Xcell Sure Lock	Invitrogen, Darmstadt, Germany
Shaker Incubator	New Brunswick Scientific, Edison, USA
Thermoblock MKR13	HLC Biotech, Bovenden, Germany
Ultracentrifuge Optima L-100 K	Beckman Coulter, Krefeld, Germany
Vacuum pump	Vacuubrand, Wertheim, Germany
Vortex Genie 2	Bender+Hobien, Zurich, CH

Appendix B – Chemicals

Chemical/ Enzyme/ Kit	Cat.-No.	Manufacturer (location)
10 x cloned Pfu reaction buffer	600153-82	Stratagene (La Jolla, USA)
Acetic Acid	3783.5	Roth (Karlsruhe)
Acetonitrile	CN20.2	Roth (Karlsruhe)
ATP	NU-1010-10G	Jena Bioscience (Jena)
β-Mercaptoethanol	4227.3	Roth (Karlsruhe)
Chloramphenicol	3886.3	Roth (Karlsruhe)
Coomassie brillant blue R 250	3862.2	Roth (Karlsruhe)
dATP	NU-1001	Jena Bioscience (Jena)
dCTP	NU-1002	Jena Bioscience (Jena)
dGTP	NU-1003	Jena Bioscience (Jena)
dTTP	NU-1003	Jena Bioscience (Jena)
di-Potassium hydrogen phosphate anhydrous	P749.2	Roth (Karlsruhe)
DMSO	D8418	Sigma-Aldrich (Steinheim)
DNAse I	04 716 728 001	Roche (Mannheim)
DOGS-NTA	790528	Avanti (Alabaster, USA)
*Dpn*I	R0176S	New England Biolabs (Frankfurt am Main)
DTT	6908.2	Roth (Karlsruhe)
Ethanol	5054.2	Roth (Karlsruhe)
GDP	NU-1172S	Jena Bioscience (Jena)
GeneAmp© dNTPs	N8080007	Roche Molecular Systems (Branchburg, USA)
Glutathione Sepharose™ 4B	27-4574-01	Amersham (Piscatawy, USA)
Glycerol	3783.1	Roth (Karlsruhe)
GTP	NU-1012-1G	Jena Bioscience (Jena)
Guanidinehydrochloride	0037.1	Roth (Karlsruhe)
HEPES	9105.4	Roth (Karlsruhe)
hsMxA cDNA		ImaGenes (Berlin, Germany)
Imidazole	3899.3	Roth (Karlsruhe)
IPTG	CN08.2	Roth (Karlsruhe)
Isopropanol	9866.5	Roth (Karlsruhe)
Kanamycinsulfate	T823.4	Roth (Karlsruhe)
Mark12™ unstained standard	LC5677	Invitrogen (Karlsruhe)
Magnesium chloride Hexahydrate	63065	Sigma-Aldrich (Steinheim)
Fermentas unstained standard	SM0431	Fermentas GmbH (St. Leon-Rot)
NuPAGE© LDS Sample Buffer (4x)	NP0007	Invitrogen (Karlsruhe)
NuPAGE© MOPS SDS Buffer Kit	NP0050	Invitrogen (Karlsruhe)
NuPAGE© Novex 4-12% Bis-Tris Gel 1,5 mm, 10 / 15 well	NP0335BOX / NP0336BOX	Invitrogen (Karlsruhe)
Pefabloc© SC-Protease inhibitor	A154.2	Roth (Karlsruhe)
Pfu DNA polymerase	00153	Stratagene (La Jolla, USA) Potassium
dihydrogen phosphate	3904.1	Roth (Karlsruhe)
PreScission™ Protease	27-0843-01	GE Healthcare (München)
Primers diverse		EurofinsMWG (Ebersberg)
QIAprep™ Spin Miniprep Kit	27106	Qiagen (Hilden)
Sodium chloride	9265.2	Roth (Karlsruhe)
Terrific-Broth medium	HP61.1	Roth (Karlsruhe)
Tetrabutylammonium bromide	86860-500G	Sigma-Aldrich (Steinheim)

Appendix C – Dynamin superfamily alignment

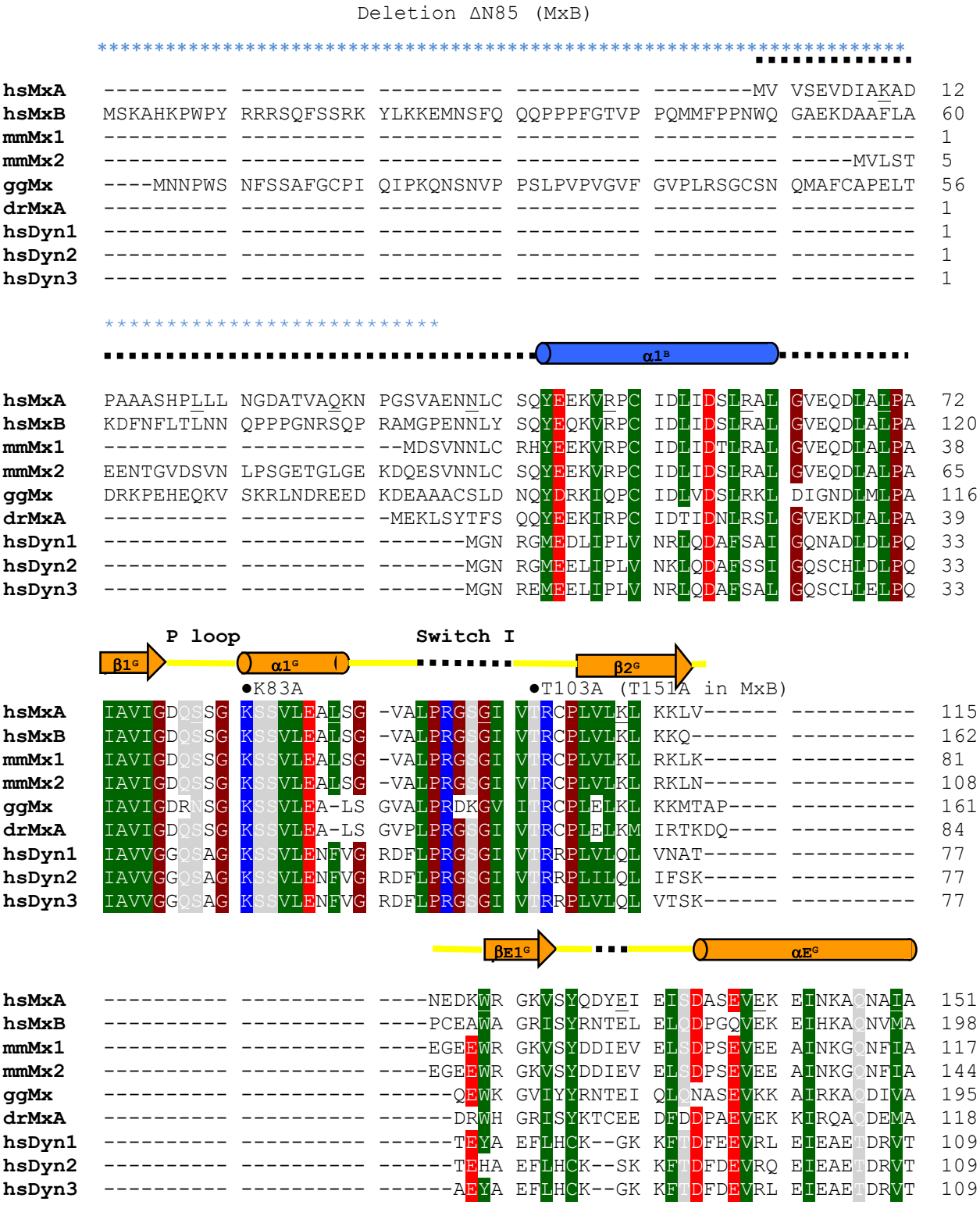

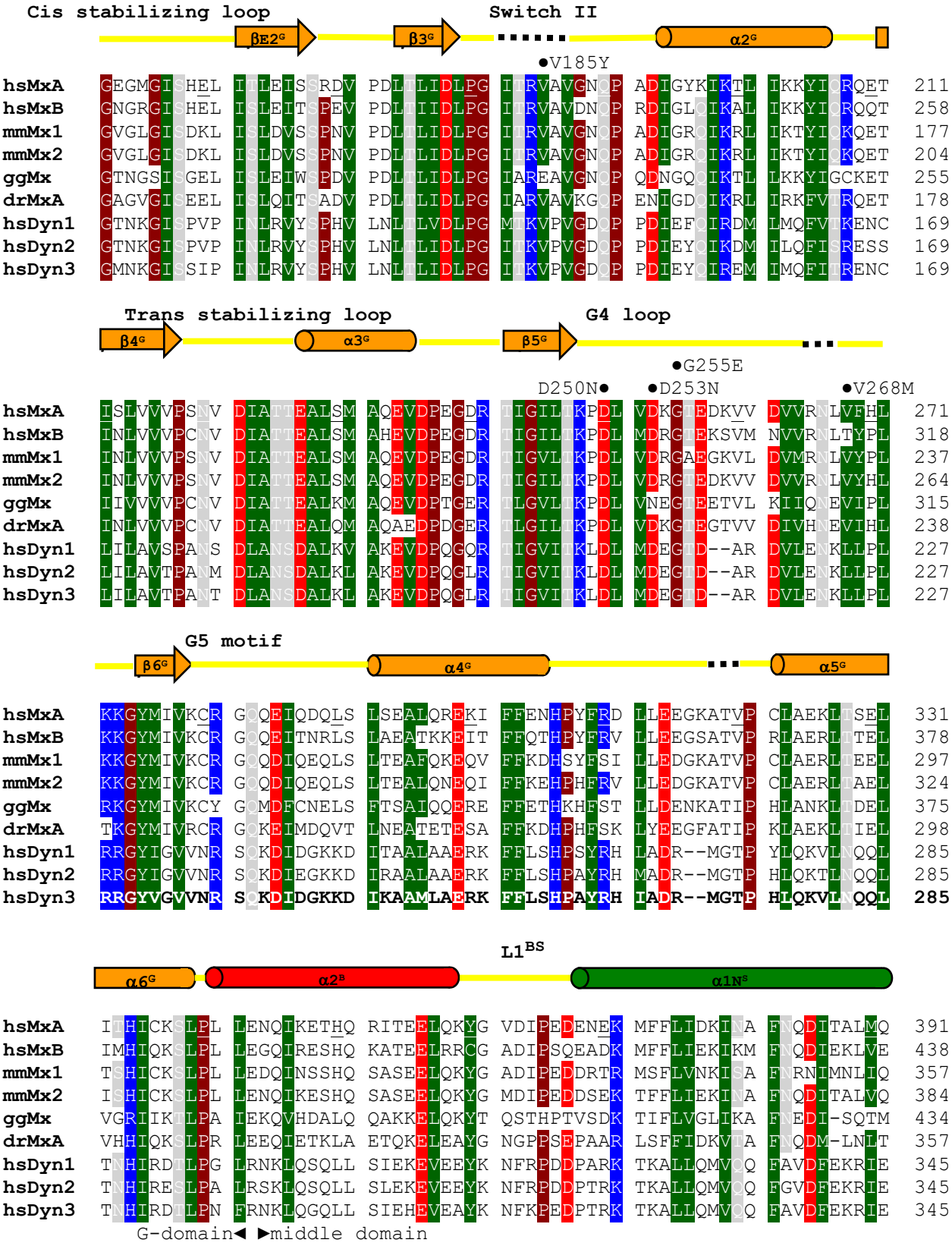
Cis stabilizing loop
Switch II
βE2G
β3G
α2G
●V185Y
hsMxA GEGMGISHEL IVLEISSRDV PDLVLIDLPG IVRVAVGNQP ADIGYKIKTL IKKYIQRQET 211
hsMxB GNGRGISHEL ISLEITSPEV PDLVIIDLPG IVRVAVDNQP RDIGLQIKAL IKKYIQRQQT 258
mmMx1 GVGLGISDKL ISLDVSSPNV PDLVLIDLPG IVRVAVGNQP ADIGRQIKRL IKTYIQKQET 177
mmMx2 GVGLGISDKL ISLDVSSPNV PDLVLIDLPG IVRVAVGNQP ADIGRQIKRL IKTYIQKQET 204
ggMx GTNGSISGEL ISLEIWSPDV PDLVLIDLPG IAREAVGNQP QDNGQQIKTL LKKYIGCKET 255
drMxA GAGVGISEEL ISLQITSADV PDLVLIDLPG IARVAVKGQP ENIGDQIKRL IRKFVTRQET 178
hsDyn1 GTNKGISPVP INLRVYSPHV LNLVLVDLPG MTKVPVGDQP PDIEFQIRDM LMQFVTKENC 169
hsDyn2 GTNKGISPVP INLRVYSPHV LNLVLIDLPG ITKVPVGDQP PDIEYQIKDM ILQFISRESS 169
hsDyn3 GMNKGISSIP INLRVYSPHV LNLVLIDLPG ITKVPVGDQP PDIEYQIREM IMQFITRENC 169
Trans stabilizing loop
G4 loop
β4G
α3G
β5G
●G255E
D250N●
●D253N
●V268M
hsMxA ISLVVVPSNV DIATTEALSM AQEVDPEGDR TIGILTKPDL VDKGTEDKVV DVVRNLVFHL 271
hsMxB INLVVVPCNV DIATTEALSM AHEVDPEGDR TIGILTKPDL MDRGTEKSVM NVVRNLTYPL 318
mmMx1 INLVVVPSNV DIATTEALSM AQEVDPEGDR TIGVLTKPDL VDRGAEGKVL DVMRNLVYPL 237
mmMx2 INLVVVPSNV DIATTEALSM AQEVDPEGDR TIGILTKPDL VDRGTEDKVV DVVRNLVYHL 264
ggMx IIVVVVPCNV DIATTEALKM AQEVDPTGER TLGVLTKPDL VNEGTEETVL KIIQNEVIPL 315
drMxA INLVVVPCNV DIATTEALQM AQAEDPDGER TLGILTKPDL VDKGTEGTVV DIVHNEVIHL 238
hsDyn1 LILAVSPANS DLANSDALKV AKEVDPQGQR TIGVITKLDL MDEGTD--AR DVLENKLLPL 227
hsDyn2 LILAVTPANM DLANSDALKL AKEVDPQGLR TIGVIKLDL MDEGTD--AR DVLENKLLPL 227
hsDyn3 LILAVTPANT DLANSDALKL AKEVDPQGLR TIGVIKLDL MDEGTD--AR DVLENKLLPL 227
G5 motif
β6G
α4G
α5G
hsMxA KKGYMIVKCR GVQEIQDQLS LSEALQREKI FFENHPYFRD LLEEGKATVP CLAEKLISEL 331
hsMxB KKGYMIVKCR GVQEITNRLS LAEATKKEIT FFQTHPYFRV LLEEGSATVP RLAERLTTEL 378
mmMx1 KKGYMIVKCR GVQDIQEQLS LTEAFQKEQV FFKDHSYFSI LLEDGKATVP CLAERLTEEL 297
mmMx2 KKGYMIVKCR GVQDIQEQLS LTEALQNEQI FFKEHPHFRV LLEDGKATVP CLAERLTAEL 324
ggMx RKGYMIVKCY GVMDFCNELS FTSAIQQERE FFETHKHFST LLDENKATIP HLANKLIDEL 375
drMxA TKGYMIVRCR GVKEIMDQVT LNEATETESA FFKDHPHFSK LYEEGFATIP KLAEKLTIEL 298
hsDyn1 RRGYIGVVNR SQKDIDGKKD ITAALAAERK FFLSHPSYRH LADR--MGTP YLQKVLNQQL 285
hsDyn2 RRGYIGVVNR SQKDIEGKKD IRAALAAERK FFLSHPAYRH MADR--MGTP HLQKTLNQQL 285
hsDyn3 RRGYVGVVNR SQKDIDGKKD IKAAMLAERK FFLSHPAYRH IADR--MGTP HLQKVLNQQL 285
L1BS
α6G
α2B
α1NS
hsMxA ITHICKSLPL LENQIKETHQ RITEELQKYG VDIPEDENEK MFFLIDKINA FNQDITALMQ 391
hsMxB IMHIQKSLPL LEGQIRESHQ KATEELRRCG ADIPSQEADK MFFLIEKIKM FNQDIEKLVE 438
mmMx1 TSHICKSLPL LEDQINSSHQ SASEELQKYG ADIPEDDRTR MSFLVNKISA FNRNIMNLIQ 357
mmMx2 ISHICKSLPL LENQIKESHQ SASEELQKYG MDIPEDDSEK TFFLIEKINA FNQDITALVQ 384
ggMx VGRIIKSLPA IEKQVHDALQ QAKKELQKYT QSTHPTVSDK TIFLVGLIKA FNEDI-SQTM 434
drMxA VHHIQKSLPR LEEQIETKLA ETQKELEAYG NGPPSEPAAR LSFFIDKVTA FNQDM-LNLT 357
hsDyn1 TNHIRDSLPG LRNKLQSQLL SIEKEVEEYK NFRPDDPARK TKALLQMVCQ FAVDFEKRIE 345
hsDyn2 TNHIRESLPA LRSKLQSQLL SLEKEVEEYK NFRPDDPTRK TKALLQMVCQ FGVDFEKRIE 345
hsDyn3 TNHIRDSLPN FRNKLQGQLL SIEHEVEAYK NFKPEDPTRK TKALLQMVCQ FAVDFEKRIE 345
G-domain◄ ►middle domain

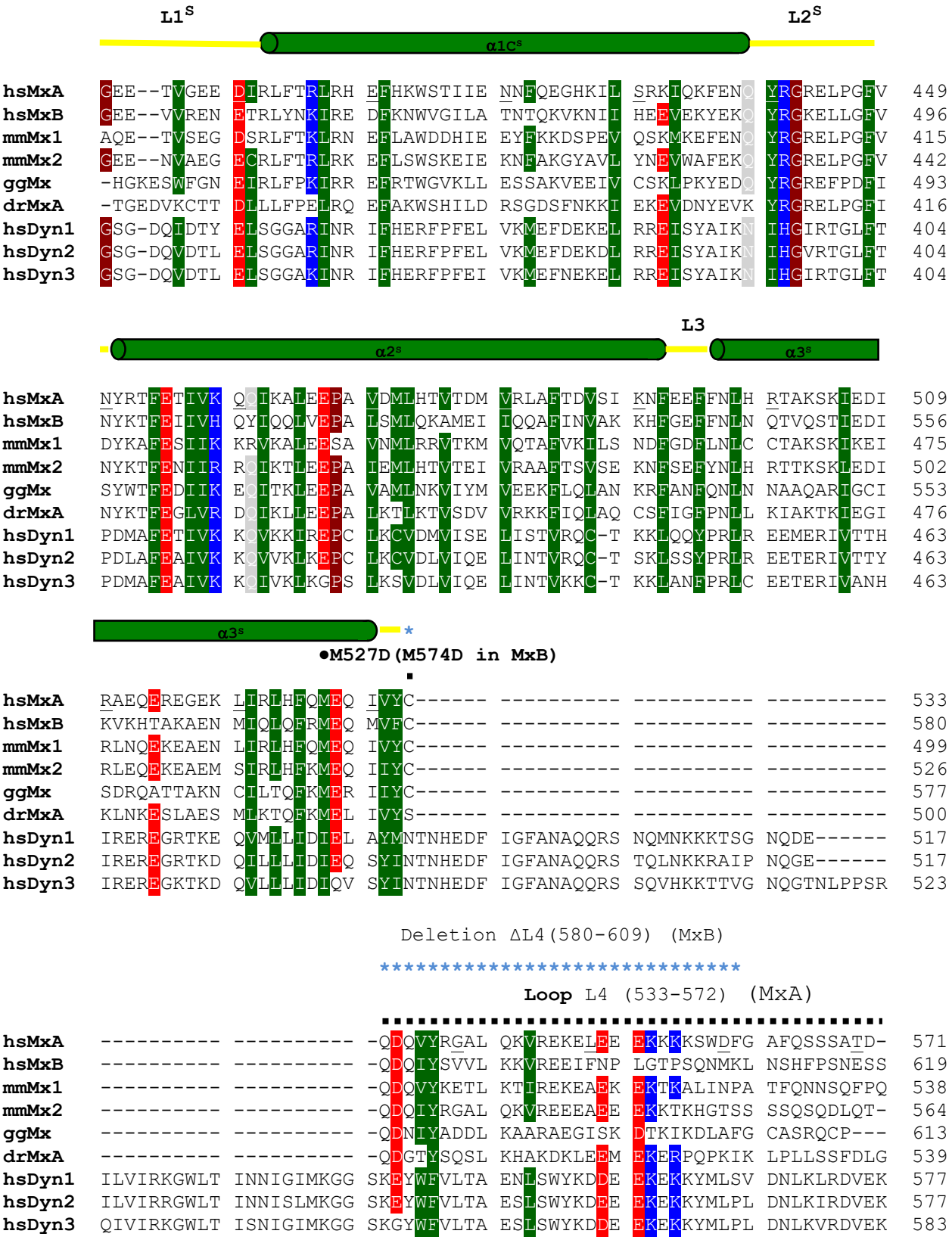
L1S
L2S
α1CS
L3
α2S
α3S
α3S
•M527D(M574D in MxB)
Deletion ΔL4(580-609) (MxB)
Loop L4 (533-572) (MxA)
hsMxA 449
hsMxB 496
mmMx1 415
mmMx2 442
ggMx 493
drMxA 416
hsDyn1 404
hsDyn2 404
hsDyn3 404
hsMxA 509
hsMxB 556
mmMx1 475
mmMx2 502
ggMx 553
drMxA 476
hsDyn1 463
hsDyn2 463
hsDyn3 463
hsMxA 533
hsMxB 580
mmMx1 499
mmMx2 526
ggMx 577
drMxA 500
hsDyn1 517
hsDyn2 517
hsDyn3 523
hsMxA 571
hsMxB 619
mmMx1 538
mmMx2 564
ggMx 613
drMxA 539
hsDyn1 577
hsDyn2 577
hsDyn3 583

```
hsMxA   ---------- ---------- ---------- ---------- ---------- ----------  571
hsMxB   V--------- ---------- ---------- ---------- ---------- ----------  620
mmMx1   KG-------- ---------- ---------- ---------- ---------- ----------  540
mmMx2   ---------- ---------- ---------- ---------- ---------- ----------  564
ggMx    ---------- ---------- ---------- ---------- ---------- ----------  613
drMxA   TDNH------ ---------- ---------- ---------- ---------- ----------  543
hsDyn1  GFMSSK--HI FALFNTEQRN VYKDYRQLEL ACETQEEVDS WKASFLRAGV YPERVGDKEK  635
hsDyn2  GFMSNK--HV FAIFNTEQRN VYKDLRQIEL ACDSQEDVDS WKASFLRAGV YPE------K  629
hsDyn3  SFMSSK--HI FALFNTEQRN VYKDYRFLEL ACDSQEDVDS WKASLLRAGV YPD------K  635
```


```
hsMxA   ---------- ---------- -SSMEEIFQH LMAYHQEASK RISSHIPLII QFFMLQTYGQ  610
hsMxB   ---------- ---------- -SSFTEIGIH LNAYFLETSK RLANQIPFII QYFMLRENGD  659
mmMx1   ---------- ---------- -LTTTEMTQH LKAYYQECRR NIGRQIPLII QYFILKTFGE  579
mmMx2   ---------- ---------- -SSMAEIFQH LNAYRQEAHN RISSHVPLII QYFILKMFAE  603
ggMx    ---------- ---------- -SFALEMVSH VKAYFTGASK RLSNQIPLII LSTVLHDFGN  652
drMxA   ---------- ---------- -AILREMRLH LKSYYTIASK RLADQIPMVI RYMLLQEAAL  582
hsDyn1  ASETEENGSD SFMHSMDPQL ERQVETIRNL VDSYMAIVNK TVRDLMPKTI MHLMINNTKE  695
hsDyn2  DQAENEDGAQ ENTFSMDPQL ERQVETIRNL VDSYVAIINK SIRDLMPKTI MHLMINNTKA  689
hsDyn3  SVAENDENGQ AENFSMDPQL ERQVETIRNL VDSYMSIINK CIRDLIPKTI MHLMINNVKD  695
```


```
hsMxA   QLQKAMLQLL QDKDTYSWLL KERSDTSDKR KFLKERLARL TQARRRLAQF PG--------  662
hsMxB   SLQKAMMQIL QEKNRYSWLL QEQSETATKR RILKERIYRL TQARHALCQF SSKEIH----  715
mmMx1   EIEKMMLQLL QDTSKCSWFL EEQSDTREKK KFLKRRLLRL DEARQKLAKF SD--------  631
mmMx2   RLQKGMLQLL QDKDSCSWLL KEQSDTSEKR KFLKERLARL AQARRRLAKF PG--------  655
ggMx    YLQTSMLHLL QGKEEINYLL QEDHEAANQQ KLLTSRISHL NKAYQYLVDF KSL-------  705
drMxA   ELQRNMLQLL QDKDGVDNLL KEDCDIGQKR ENLLSRQTRL IEGTQPLGHL LEVTFIDYCN  642
hsDyn1  FIFSELLANL YSCGDQNTLM EESAEQAQRR DEMLRMYHAL KEALSIIGDI NTTTVSTPMP  755
hsDyn2  FIHHELLAYL YSSADQSSLM EESADQAQRR DDMLRMYHAL KEALNIIGDI STSTVSTPVP  749
hsDyn3  FINSELLAQL YSSEDQNTLM EESAEQAQRR DEMLRMYQAL KEALGIIGDI STATVSTPAP  755

hsMxA   ---------- ---------- ---------- ---------- ---------- ----------  662
hsMxB   ---------- ---------- ---------- ---------- ---------- ----------  715
mmMx1   ---------- ---------- ---------- ---------- ---------- ----------  631
mmMx2   ---------- ---------- ---------- ---------- ---------- ----------  655
ggMx    ---------- ---------- ---------- ---------- ---------- ----------  705
drMxA   ILMQ------ ---------- ---------- ---------- ---------- ----------  646
hsDyn1  PPVDDSWLQV QSVPAGRRSP TSSPTPQRRA PAVPPARPGS RGPAPGPPPA GSALGGAPPV  815
hsDyn2  PPVDDTWLQS ASSHSPTPQR RPVSSI-HPP GRPPAVRGPT PGPPLIPVPV GAAASFSAPP  808
hsDyn3  PPVDDSWIQH SRRSPPPSPT TQRRPTLSAP LARPTSGRGP APAIPSPGPH SGAPPVPFRP  815

hsMxA   ---------- ---------- ---------- ---------- ---------- ----------  662
hsMxB   ---------- ---------- ---------- ---------- ---------- ----------  715
mmMx1   ---------- ---------- ---------- ---------- ---------- ----------  631
mmMx2   ---------- ---------- ---------- ---------- ---------- ----------  655
ggMx    ---------- ---------- ---------- ---------- ---------- ----------  705
drMxA   ---------- ---------- ---------- ---------- ---------- ----------  646
hsDyn1  PSRPGASPDP FGPPPQVPSR PNRAPPGVPS RSGQASPSRP ESPRPPFDL- ----------  864
hsDyn2  IPSRPGPQSV FANSDLFPAP PQIPSRPVRI PPGIPPGVPS RRPPAAPSRP TIIRPAEPSL  868
hsDyn3  GPLPPFPSSS DSFGAPPQVP SRPTRAPPSV PSRRPPPSPT RPTIIRPLES SLLD------  869
```

```
hsMxA    ---------- - 662
hsMxB    ---------- - 715
mmMx1    ---------- - 631
mmMx2    ---------- - 655
ggMx     ---------- - 705
drMxA    ---------- - 646
hsDyn1   ---------- - 864
hsDyn2   LD-------- - 870
hsDyn3   ---------- - 869
```

Sequence alignment of Mx and human dynamin proteins. Amino acid sequences of human MxA (Swiss-Prot accession P20591), human MxB (P20592), mouse (mm) Mx1 (P09922), mouse Mx2 (Q9WVP9), chicken (gg) Mx protein (Q90597), zebrafish (dr) MxA protein (Q8JH68), human dynamin1 (Q05193), human dynamin2 (P50570), human Dynamin3 (Q9UQ16) were aligned using CLUSTAL W (145) and manually adjusted. Residues with a conservation of greater than 70% are color-coded (D, E in red; R, K, H in blue; N, Q, S, T in grey; A, L, I, V, F, Y, W, M, C in green and P, G in brown). α-helices are shown as cylinders and β-strands as arrows, and the MxA stalk was depicted as gray cylinders under the sequences. Mutations within the G domain and the G interface as described in 3.1 for MxA (black dot) and 3.2 for MxB (in brackets, and deletions represented by blue asterisk) are specified at the corresponding positions. Sequence alignment was modified from (75,76).

Appendix D - *Orthomyxoviridae* nucleoprotein alignment

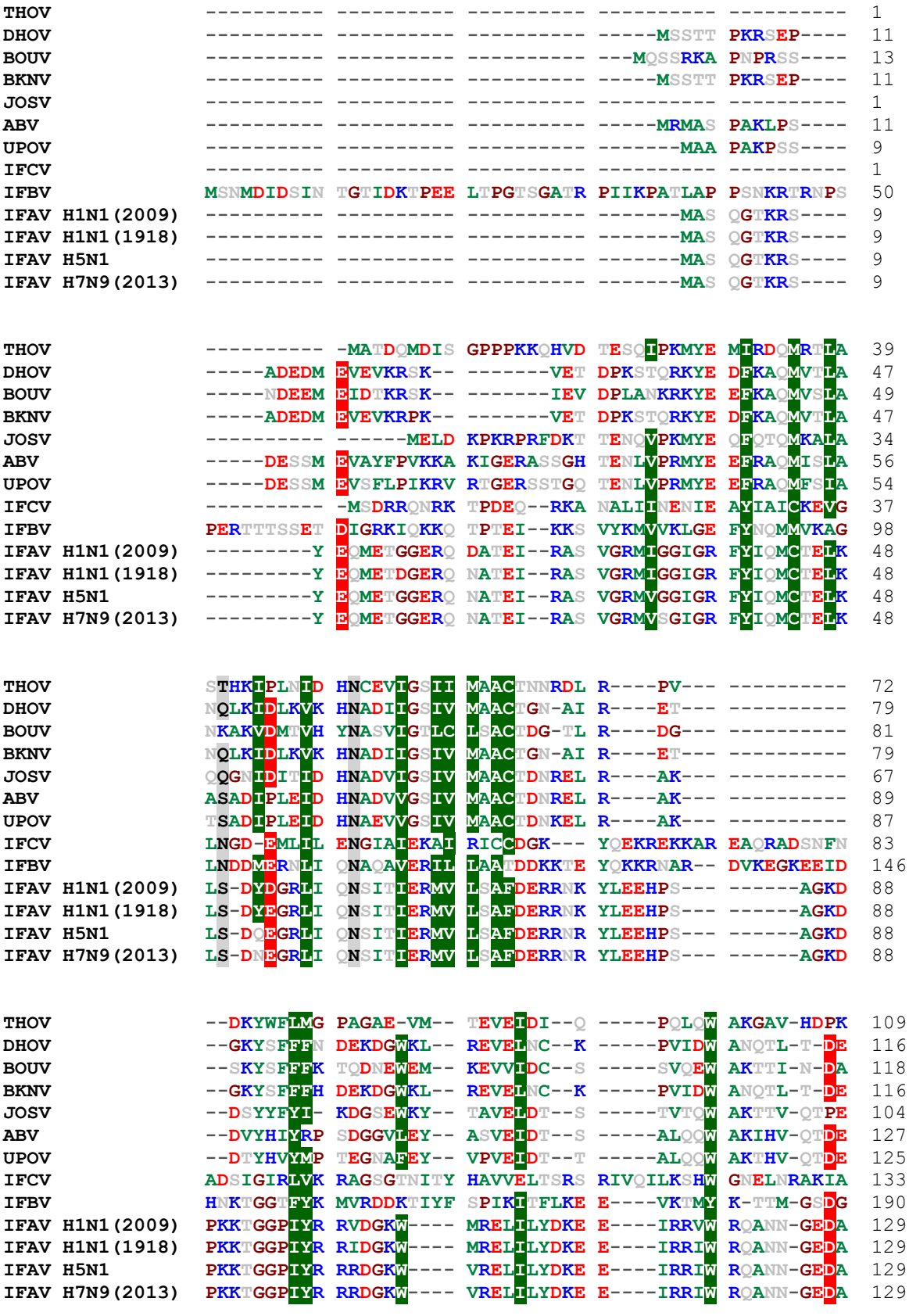

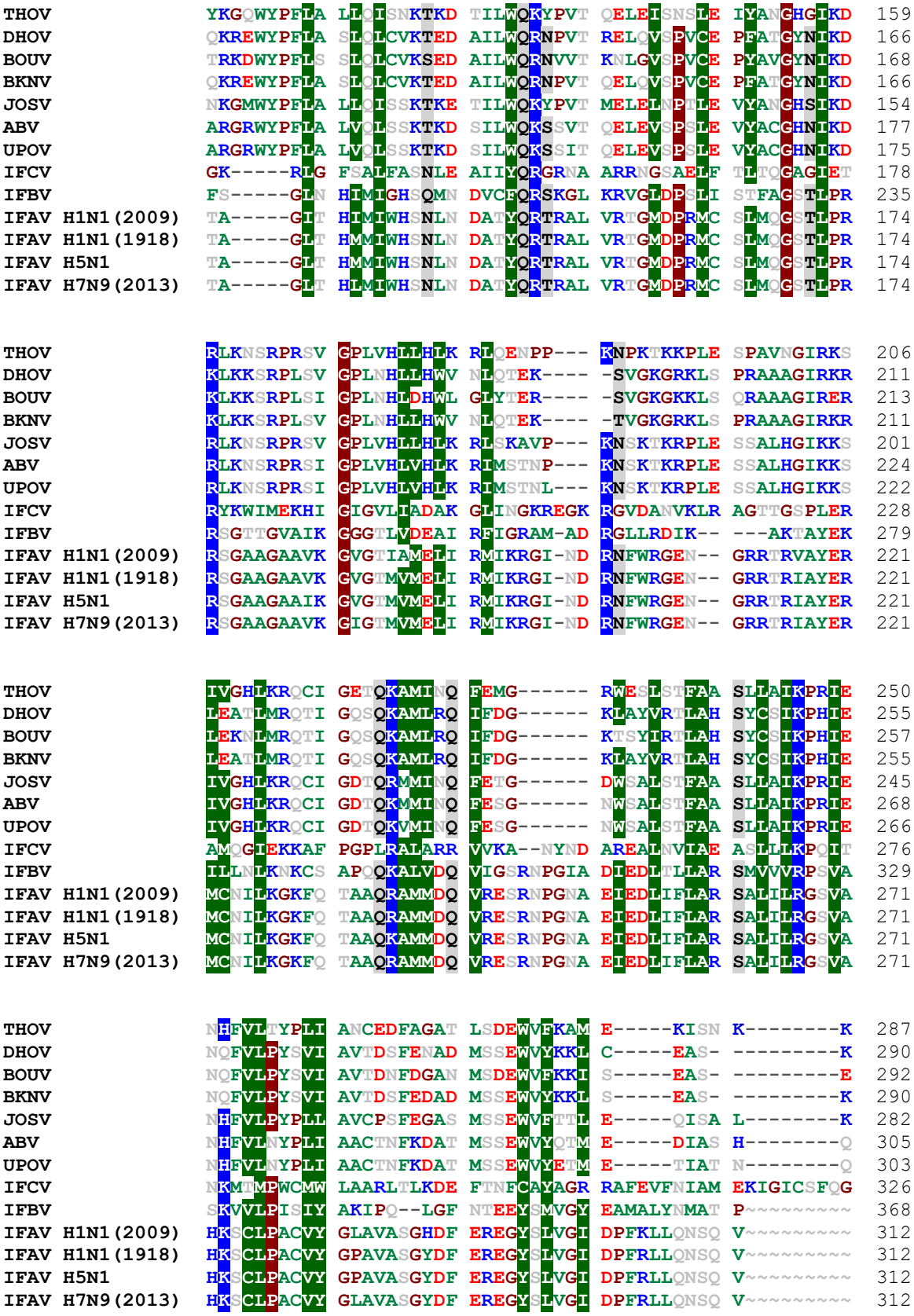
THOV YKGQWYPFLA LLQISNKTKD TILWQKYPVT QELEISNSLE IYANGHGIKD 159
DHOV QKREWYPFLA SLQLCVKTED AILWQRNPVT RELQVSPVCE PFATGYNIKD 166
BOUV TRKDWYPFLS SLQLCVKSED AILWQRNVVT KNLGVSPVCE PYAVGYNIKD 168
BKNV QKREWYPFLA SLQLCVKTED AILWQRNPVT QELQVSPVCE PFATGYNIKD 166
JOSV NKGMWYPFLA LLQISSKTKE TILWQKYPVT MELELNPLE VYANGHSIKD 154
ABV ARGRWYPFLA LVQLSSKTKD SILWQKSSVT QELEVSPSLE VYACGHNIKD 177
UPOV ARGRWYPFLA LVQLSSKTKD SILWQKSSIT QELEVSPSLE VYACGHNIKD 175
IFCV GK-----RLG FSALFASNLE AIIYQRGRNA ARRNGSAELF TLTQGAGIET 178
IFBV FS-----GLN HIMIGHSQMN DVCFQRSKGL KRVGIDPSLI STFAGSTLPR 235
IFAV H1N1(2009) TA-----GIT HIMIWHSNLN DATYQRTRAL VRTGMDPRMC SLMQGSTLPR 174
IFAV H1N1(1918) TA-----GLT HMMIWHSNLN DATYQRTRAL VRTGMDPRMC SLMQGSTLPR 174
IFAV H5N1 TA-----GLT HMMIWHSNLN DATYQRTRAL VRTGMDPRMC SLMQGSTLPR 174
IFAV H7N9(2013) TA-----GLT HLMIWHSNLN DATYQRTRAL VRTGMDPRMC SLMQGSTLPR 174
THOV RLKNSRPRSV GPLVHLLHLK RLQENPP--- KNPKTKKPLE SPAVNGIRKS 206
DHOV KLKKSRPLSV GPLNHLLHWV NLQTEK---- -SVGKGRKLS PRAAAGIRKR 211
BOUV KLKKSRPLSI GPLNHLDHWL GLYTER---- -SVGKGKKLS QRAAAGIRER 213
BKNV KLKKSRPLSV GPLNHLLHWV NLQTEK---- -TVGKGRKLS PRAAAGIRKR 211
JOSV RLKNSRPRSV GPLVHLLHLK RLSKAVP--- KNSKTKRPLE SSALHGIKKS 201
ABV RLKNSRPRSI GPLVHLVHLK RIMSTNP--- KNSKTKRPLE SSALHGIKKS 224
UPOV RLKNSRPRSI GPLVHLVHLK RIMSTNL--- KNSKTKRPLE SSALHGIKKS 222
IFCV RYKWIMEKHI GIGVLIADAK GLINGKREGK RGVDANVKLR AGTTGSPLER 228
IFBV RSGTTGVAIK GGGTLVDEAI RFIGRAM-AD RGLLRDIK-- ---AKTAYEK 279
IFAV H1N1(2009) RSGAAGAAVK GVGTIAMELI RMIKRGI-ND RNFWRGEN-- GRRTRVAYER 221
IFAV H1N1(1918) RSGAAGAAVK GVGTMVMELI RMIKRGI-ND RNFWRGEN-- GRRTRIAYER 221
IFAV H5N1 RSGAAGAAIK GVGTMVMELI RMIKRGI-ND RNFWRGEN-- GRRTRIAYER 221
IFAV H7N9(2013) RSGAAGAAVK GIGTMVMELI RMIKRGI-ND RNFWRGEN-- GRRTRIAYER 221
THOV IVGHLKRQCI GETQKAMINQ FEMG------ RWESLSTFAA SLLAIKPRIE 250
DHOV LEATLMRQTI GQSQKAMLRQ IFDG------ KLAYVRTLAH SYCSIKPHIE 255
BOUV LEKNLMRQTI GQSQKAMLRQ IFDG------ KTSYIRTLAH SYCSIKPHIE 257
BKNV LEATLMRQTI GQSQKAMLRQ IFDG------ KLAYVRTLAH SYCSIKPHIE 255
JOSV IVGHLKRQCI GDTQRMMINQ FETG------ DWSALSTFAA SLLAIKPRIE 245
ABV IVGHLKRQCI GDTQKMMINQ FESG------ NWSALSTFAA SLLAIKPRIE 268
UPOV IVGHLKRQCI GDTQKVMINQ FESG------ NWSALSTFAA SLLAIKPRIE 266
IFCV AMQGIEKKAF PGPLRALARR VVKA--NYND AREALNVIAE ASLLLKPQIT 276
IFBV ILLNLKNKCS APQQKALVDQ VIGSRNPGIA DIEDLTLLAR SMVVVRPSVA 329
IFAV H1N1(2009) MCNILKGKFQ TAAQRAMMDQ VRESRNPGNA EIEDLIFLAR SALILRGSVA 271
IFAV H1N1(1918) MCNILKGKFQ TAAQRAMMDQ VRESRNPGNA EIEDLIFLAR SALILRGSVA 271
IFAV H5N1 MCNILKGKFQ TAAQKAMMDQ VRESRNPGNA EIEDLIFLAR SALILRGSVA 271
IFAV H7N9(2013) MCNILKGKFQ TAAQRAMMDQ VRESRNPGNA EIEDLIFLAR SALILRGSVA 271
THOV NHFVLTYPLI ANCEDFAGAT LSDEWVFKAM E-----KISN K--------K 287
DHOV NQFVLPYSVI AVTDSFENAD MSSEWVYKKL C-----EAS- ---------K 290
BOUV NQFVLPYSVI AVTDNFDGAN MSDEWVFKKI S-----EAS- ---------E 292
BKNV NQFVLPYSVI AVTDSFEDAD MSSEWVYKKL S-----EAS- ---------K 290
JOSV NHFVLPYPLL AVCPSFEGAS MSSEWVFTTL E-----QISA L--------K 282
ABV NHFVLNYPLI AACTNFKDAT MSSEWVYQTM E-----DIAS H--------Q 305
UPOV NHFVLNYPLI AACTNFKDAT MSSEWVYETM E-----TIAT N--------Q 303
IFCV NKMIMPWCMW LAARLTLKDE FTNFCAYAGR RAFEVFNIAM EKIGICSFQG 326
IFBV SKVVLPISIY AKIPQ--LGF NTEEYSMVGY EAMALYNMAT P~~~~~~~~~ 368
IFAV H1N1(2009) HKSCLPACVY GLAVASGHDF EREGYSLVGI DPFKLLQNSQ V~~~~~~~~~ 312
IFAV H1N1(1918) HKSCLPACVY GPAVASGYDF EREGYSLVGI DPFRLLQNSQ V~~~~~~~~~ 312
IFAV H5N1 HKSCLPACVY GPAVASGYDF EREGYSLVGI DPFRLLQNSQ V~~~~~~~~~ 312
IFAV H7N9(2013) HKSCLPACVY GLAVASGYDF EREGYSLVGI DPFRLLQNSQ V~~~~~~~~~ 312

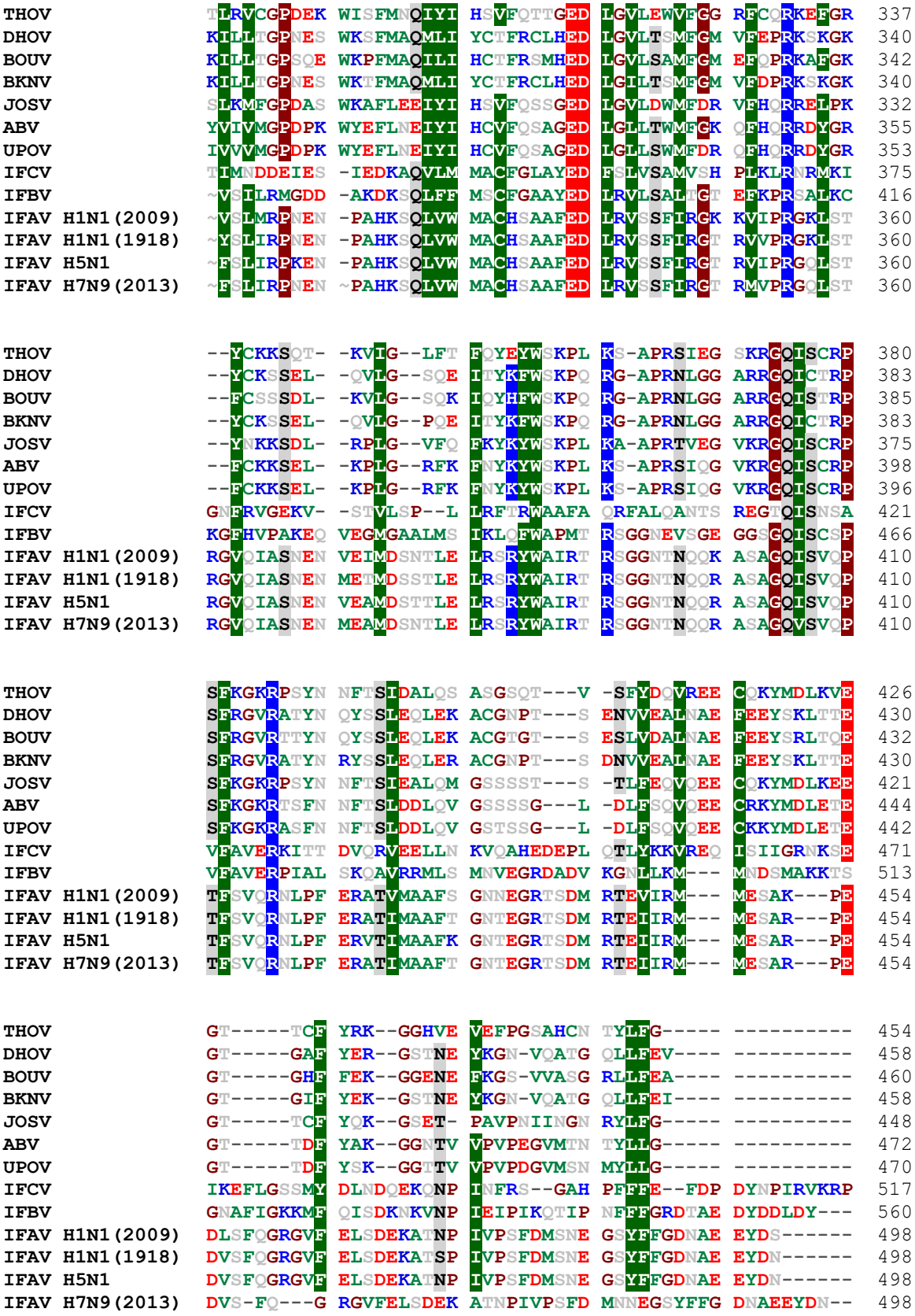
THOV
DHOV
BOUV
BKNV
JOSV
ABV
UPOV
IFCV
IFBV
IFAV H1N1(2009)
IFAV H1N1(1918)
IFAV H5N1
IFAV H7N9(2013)

```
THOV              ---------- ---------- ---------- ---------- ----------  454
DHOV              ---------- ---------- ---------- ---------- ----------  458
BOUV              ---------- ---------- ---------- ---------- ----------  460
BKNV              ---------- ---------- ---------- ---------- ----------  458
JOSV              ---------- ---------- ---------- ---------- ----------  448
ABV               ---------- ---------- ---------- ---------- ----------  472
UPOV              ---------- ---------- ---------- ---------- ----------  470
IFCV              KKPIAKRNSN ISRLEEEGMD ENSEIGQAKK MKPLDQLAST SSNIPGEN--  565
IFBV              ---------- ---------- ---------- ---------- ----------  560
IFAV H1N1(2009)   ---------- ---------- ---------- ---------- ----------  498
IFAV H1N1(1918)   ---------- ---------- ---------- ---------- ----------  498
IFAV H5N1         ---------- ---------- ---------- ---------- ----------  498
IFAV H7N9(2013)   ---------- ---------- ---------- ---------- ----------  498


THOV              ---- 454
DHOV              ---- 458
BOUV              ---- 460
BKNV              ---- 458
JOSV              ---- 448
ABV               ---- 472
UPOV              ---- 470
IFCV              ---- 565
IFBV              ---- 560
IFAV H1N1(2009)   ---- 498
IFAV H1N1(1918)   ---- 498
IFAV H5N1         ---- 498
IFAV H7N9(2013)   --   498
```

Sequence alignment of THOV NP and other NP members of the orthomyxovirus family. Amino acid sequences of THOV NP (Swiss-Prot accession A0A0B6VKB5), DHOV NP (D6PT87), Bourbon virus (BOUV) NP (A0A0C5I425), Batken virus (BKNV) NP (Sequence derived from Prof. Dr. Georg Kochs), Jos virus (JOSV) NP (H6SW55), Aransas Bay virus (ABV) NP (X2CUE7), Upolu virus (UPOV) NP (X2CWU1), influenza C virus (IFCV) NP (P08028), influenza B virus (IFBV) NP (P04665), influenza A virus H1N1 (2009) (IFAV) NP (C4RU37), influenza A virus H1N1 (1918) (IFAV) NP (Q5UEW0), influenza A virus H5N1 (IFAV) NP (O92784), influenza A virus H7N9 (2013) (IFAV) NP (A0A067Y7E0) were aligned using CLUSTAL Omega (145) and manually adjusted. Residues with a conservation of greater than 70% are color-coded (D, E in red; R, K, H in blue; N, Q, S, T in grey; A, L, I, V, F, Y, W, M, C in green and P, G in brown).

Appendix E – Abbreviations

''	Minute
Å	Ångström (0.1 nm)
ABV	Aransas Bay virus
AC	Affinity chromatography
AIDS	Acquired immune deficiency syndrome
AIM	Absent in melanoma
Amp	Ampicillin
AUC	Analytical ultracentrifugation
ASFV	African swine fever virus
ASU	Asymmetric unit
BKNV	Batken virus
BSE	Bundle signaling element
C-terminus	Carboxy-terminus
CCHFV	Crimean-congo hemorrhagic fever virus
CD	Circular dichroism
cGAS	cyclic GMP-AMP synthase
COOT	Crystallographic Object-Oriented Toolkit
cRNA	copyRNA
DAI	DNA-dependent activator of IRF
dd	Double deionised
DHOV	Dhori virus
DMSO	Dimethyl sulfoxide
DNA	Deoxyribonucleic acid
DNAse	Deoxyribonuclease
DTT	Dithiothreitol
dNTP	Deoxynucleotide triphosphate
Dpn	*Diplococcus pneumonia*
EBV	Epstein-bar virus
E. coli	*Escherichia coli*
EDTA	Ethylenediaminetetraacetic acid
EM	Electron microscopy
ER	Endoplasmic reticulum
EtOH	Ethanol
fr.	Fraction
fw.	Forward
G domain	Guanine nucleotide binding domain
G protein	Guanine nucleotide binding protein
GAP	GTPase-activating protein
GBP	Guanylate binding protein
GDP	Guanosine-5'-diphosphate
GED	GTPase effector domain
GIMAP	GTPase of immunity-associated proteins
GTP	Guanosine-5'-triphosphate
GMP-PCP	Guanosine-5′-[(β,γ)-methyleno]triphosphate
GMP-PNP	Guanosine-5’-[(β,γ)-imido]triphosphate
GNBP	Guanine Nucleotide Binding Protein
GSH	Reduced Glutathione
GST	Glutathione-S-transferase
GTP	Guanosine-5'-triphosphate
GTP-γ-S	Guanosine-5’-O-[(γ)-thio]triphosphate

GTPase	Guanosine-5'-triphosphate hydrolase
HA	Hemagglutinine
HEPES	4-(2-hydroxyethyl)-1-piperazineethanesulfonic acid
HPLC	High Performance Liquide Chromatography
HPV	Human papillomavirus
Hs	*Homo Sapiens*
kb	Kilobase
kDa	Kilodalton
k_{obs}	observed turnover number
IFITM(P)	IFN-induced transmembrane (protein)
IFN	Interferon
IFNAR	IFN α/β receptor
IF(A/B/C)V	Influenza (A/B/C) virus
IL	Interleukine
IPTG	Isopropyl (β)-D-1-thiogalactopyranoside
IRF	IFN-regulatory factor
ISAV	Infectious salmon anemia virus
ISG	IFN-stimulated gene
ITC	Isothermal titration calorimetry
IRG	Immunity-related GTPases
Jak	Janus kinase
JOSV	Jos virus
Kan	Kanamycin
λ	Wavelength
LACV	La Crosse virus
LB	Luria Bertani
M1/2	Matrix protein 1/2
M^7G	7-Methylguanylate
mAU	Milli absorbance unit
MDA5	Melanoma differentation-associated protein5
MDC	Max-Delbrück-Centrum für Molekulare Medizin Berlin-Buch
MOPS	3-(N-morpholino) propanesulfonic acid
MPD	2-Methyl-2,4-pentanediol
min(s)	Minute(s)
MxA/B	Myxovirus resistance protein A/B
N	Nucleocapsid
N-terminus	Amino-terminus
NS1/2	Non-structural protein 1/2
NA	Neuroaminidase
NAS	Nuclear accumulation signal
NF-κB	Nuclear factor κB
NLR(P)	Nucleotide-binding and oligomerization leucine-rich (protein)
NLS	Nuclear localization signal
NP	Nucleoprotein
(s/ns)NSV	(segmented/non-segmented) Negative strand RNA virus
OD	Optical density
P-loop	Phosphate-binding loop
PA	Poly acidic
PAMP	Pathogen associated molecular pattern
PB	Poly basic
PCR	Polymerase Chain Reaction
PDB	Protein Data Bank
PEG	Polyethylene glycol
Pfu	*Pyrococcus furiosus*
PRR	Pattern recognition receptor
RALS	Right Angle Light Scattering

Ras	Rat sarcoma
RdRp	RNA-dependent RNA polymerase
RIG-I	Retinoic acid-inducible gene-I
rv.	Reverse
RVFV	Rift valley fever virus
SA	Sialic acid
SDS PAGE	Sodiumdodecylsulfate polyacrylamide gel electrophoresis
SEC	Size-exclusion chromatography
SeMet	Selenomethionine
SFV	Semliki forest virus
SRP	Signal recognition particle
SR	Signal recognition particle receptor
STAT	Signal transducer and activator of transcription
STING	Stimulator of IFN genes
TB	Teriffic-Broth
TBA(B)	Tetrabutylammonium (bromide)
THOV	Thogoto virus
TLR	Toll-like receptor
TLS	Translation, libration screw rotation displacement
UPOV	Upolu virus
vRNP	Viral ribonucleoparticle
VSV	Vesicular stomatitis virus
XDP	Xanthosine-5’diphosphate
XTP	Xanthosine-5’triphosphate

For amino acids, the one and three letter code was used

A Ala alanine	I Ile isoleucine	R Arg arginine
C Cys cysteine	K Lys lysine	S Ser serine
D Asp aspartate	L Leu leucine	T Thr threonine
E Glu glutamate	M Met methionine	V Val valine
F Phe phenylalanine	N Asn asparagine	W Trp tryptophane
G Gly glycine	P Pro proline	Y Tyr tyrosine
H His histidine	Q Gln glutamine	x any amino acid

Bibliography

1. David M. Knipe, P. M. H. (2007) *Fields Virology*, Lippincott Williams & Wilkins
2. Stanley, M. A., Winder, D. M., Sterling, J. C., and Goon, P. K. (2012) HPV infection, anal intra-epithelial neoplasia (AIN) and anal cancer: current issues. *BMC cancer* **12**, 398
3. Baltimore, D. (1971) Expression of animal virus genomes. *Bacteriological reviews* **35**, 235-241
4. Ruigrok, R. W., Crepin, T., and Kolakofsky, D. Nucleoproteins and nucleocapsids of negative-strand RNA viruses. *Curr Opin Microbiol* **14**, 504-510
5. Rey, F. A. (2010) Virology: One protein, many functions. *Nature* **468**, 773-775
6. Andrew M.Q. King, M. J. A., Eric B. Carstens, Elliot J. Lefkowitz. (2012) *Virus Taxonomy*, Elsevier
7. Hedlund, M., Larson, J. L., and Fang, F. (2010) Antiviral strategies for pandemic and seasonal influenza. *Viruses* **2**, 1766-1781
8. Taubenberger, J. K., and Morens, D. M. (2009) Pandemic influenza--including a risk assessment of H5N1. *Revue scientifique et technique* **28**, 187-202
9. Taubenberger, J. K., and Kash, J. C. (2010) Influenza virus evolution, host adaptation, and pandemic formation. *Cell host & microbe* **7**, 440-451
10. Johnson, N. P., and Mueller, J. (2002) Updating the accounts: global mortality of the 1918-1920 "Spanish" influenza pandemic. *Bulletin of the history of medicine* **76**, 105-115
11. Shrestha, S. S., Swerdlow, D. L., Borse, R. H., Prabhu, V. S., Finelli, L., Atkins, C. Y., Owusu-Edusei, K., Bell, B., Mead, P. S., Biggerstaff, M., Brammer, L., Davidson, H., Jernigan, D., Jhung, M. A., Kamimoto, L. A., Merlin, T. L., Nowell, M., Redd, S. C., Reed, C., Schuchat, A., and Meltzer, M. I. (2011) Estimating the burden of 2009 pandemic influenza A (H1N1) in the United States (April 2009-April 2010). *Clin Infect Dis* **52 Suppl 1**, S75-82
12. Ghedin, E., Sengamalay, N. A., Shumway, M., Zaborsky, J., Feldblyum, T., Subbu, V., Spiro, D. J., Sitz, J., Koo, H., Bolotov, P., Dernovoy, D., Tatusova, T., Bao, Y., St George, K., Taylor, J., Lipman, D. J., Fraser, C. M., Taubenberger, J. K., and Salzberg, S. L. (2005) Large-scale sequencing of human influenza reveals the dynamic nature of viral genome evolution. *Nature* **437**, 1162-1166
13. Horimoto, T., and Kawaoka, Y. (2005) Influenza: lessons from past pandemics, warnings from current incidents. *Nat Rev Microbiol* **3**, 591-600
14. Gamblin, S. J., and Skehel, J. J. (2010) Influenza hemagglutinin and neuraminidase membrane glycoproteins. *J Biol Chem* **285**, 28403-28409
15. Portela, A., and Digard, P. (2002) The influenza virus nucleoprotein: a multifunctional RNA-binding protein pivotal to virus replication. *J Gen Virol* **83**, 723-734
16. Martin, K., and Helenius, A. (1991) Nuclear transport of influenza virus ribonucleoproteins: the viral matrix protein (M1) promotes export and inhibits import. *Cell* **67**, 117-130
17. Schnell, J. R., and Chou, J. J. (2008) Structure and mechanism of the M2 proton channel of influenza A virus. *Nature* **451**, 591-595
18. Alonso-Caplen, F. V., Nemeroff, M. E., Qiu, Y., and Krug, R. M. (1992) Nucleocytoplasmic transport: the influenza virus NS1 protein regulates the transport of spliced NS2 mRNA and its precursor NS1 mRNA. *Genes Dev* **6**, 255-267
19. Lu, Y., Wambach, M., Katze, M. G., and Krug, R. M. (1995) Binding of the influenza virus NS1 protein to double-stranded RNA inhibits the activation of the protein kinase that phosphorylates the elF-2 translation initiation factor. *Virology* **214**, 222-228
20. Neumann, G., Hughes, M. T., and Kawaoka, Y. (2000) Influenza A virus NS2 protein mediates vRNP nuclear export through NES-independent interaction with hCRM1. *EMBO J* **19**, 6751-6758
21. Drake, J. W. (1993) Rates of spontaneous mutation among RNA viruses. *Proc Natl Acad Sci U S A* **90**, 4171-4175
22. Das, K., Aramini, J. M., Ma, L. C., Krug, R. M., and Arnold, E. (2010) Structures of influenza A proteins and insights into antiviral drug targets. *Nat Struct Mol Biol* **17**, 530-538

23. Wu, W. W., and Pante, N. (2009) The directionality of the nuclear transport of the influenza A genome is driven by selective exposure of nuclear localization sequences on nucleoprotein. *Virology journal* **6**, 68
24. Ulmanen, I., Broni, B. A., and Krug, R. M. (1981) Role of two of the influenza virus core P proteins in recognizing cap 1 structures (m7GpppNm) on RNAs and in initiating viral RNA transcription. *Proc Natl Acad Sci U S A* **78**, 7355-7359
25. Plotch, S. J., Bouloy, M., Ulmanen, I., and Krug, R. M. (1981) A unique cap(m7GpppXm)-dependent influenza virion endonuclease cleaves capped RNAs to generate the primers that initiate viral RNA transcription. *Cell* **23**, 847-858
26. Hagen, M., Chung, T. D., Butcher, J. A., and Krystal, M. (1994) Recombinant influenza virus polymerase: requirement of both 5' and 3' viral ends for endonuclease activity. *J Virol* **68**, 1509-1515
27. Nemeroff, M. E., Barabino, S. M., Li, Y., Keller, W., and Krug, R. M. (1998) Influenza virus NS1 protein interacts with the cellular 30 kDa subunit of CPSF and inhibits 3'end formation of cellular pre-mRNAs. *Mol Cell* **1**, 991-1000
28. Newcomb, L. L., Kuo, R. L., Ye, Q., Jiang, Y., Tao, Y. J., and Krug, R. M. (2009) Interaction of the influenza a virus nucleocapsid protein with the viral RNA polymerase potentiates unprimed viral RNA replication. *J Virol* **83**, 29-36
29. Haig, D. A., Woodall, J. P., and Danskin, D. (1965) Thogoto Virus: A Hitherto Underscribed Agent Isolated from Ticks in Kenya. *Journal of general microbiology* **38**, 389-394
30. Anderson, C. R., and Casals, J. (1973) Dhori virus, a new agent isolated from Hyalomma dromedarii in India. *The Indian journal of medical research* **61**, 1416-1420
31. Olga, I. K., Amy, J. L., Dana, J. H., Daniel, M. P., Cynthia, S. G., Hunt, D. C., and Staples, J. E. (2015) Novel Thogotovirus Associated with Febrile Illness and Death, United States, 2014 *Emerging Infectious Disease journal* **21**
32. Butenko, A. M., Leshchinskaia, E. V., Semashko, I. V., Donets, M. A., and Mart'ianova, L. I. (1987) [Dhori virus--a causative agent of human disease. 5 cases of laboratory infection]. *Voprosy virusologii* **32**, 724-729
33. Mateo, R. I., Xiao, S. Y., Lei, H., AP, D. A. R., and Tesh, R. B. (2007) Dhori virus (Orthomyxoviridae: Thogotovirus) infection in mice: a model of the pathogenesis of severe orthomyxovirus infection. *The American journal of tropical medicine and hygiene* **76**, 785-790
34. Staunton, D., Nuttall, P. A., and Bishop, D. H. (1989) Sequence analyses of Thogoto viral RNA segment 3: evidence for a distant relationship between an arbovirus and members of the Orthomyxoviridae. *J Gen Virol* **70 (Pt 10)**, 2811-2817
35. Fuller, F. J., Freedman-Faulstich, E. Z., and Barnes, J. A. (1987) Complete nucleotide sequence of the tick-borne, orthomyxo-like Dhori/Indian/1313/61 virus nucleoprotein gene. *Virology* **160**, 81-87
36. Morse, M. A., Marriott, A. C., and Nuttall, P. A. (1992) The glycoprotein of Thogoto virus (a tick-borne orthomyxo-like virus) is related to the baculovirus glycoprotein GP64. *Virology* **186**, 640-646
37. Noton, S. L., Simpson-Holley, M., Medcalf, E., Wise, H. M., Hutchinson, E. C., McCauley, J. W., and Digard, P. (2009) Studies of an influenza A virus temperature-sensitive mutant identify a late role for NP in the formation of infectious virions. *J Virol* **83**, 562-571
38. Albertini, A. A., Wernimont, A. K., Muziol, T., Ravelli, R. B., Clapier, C. R., Schoehn, G., Weissenhorn, W., and Ruigrok, R. W. (2006) Crystal structure of the rabies virus nucleoprotein-RNA complex. *Science* **313**, 360-363
39. Green, T. J., Zhang, X., Wertz, G. W., and Luo, M. (2006) Structure of the vesicular stomatitis virus nucleoprotein-RNA complex. *Science* **313**, 357-360
40. Tawar, R. G., Duquerroy, S., Vonrhein, C., Varela, P. F., Damier-Piolle, L., Castagne, N., MacLellan, K., Bedouelle, H., Bricogne, G., Bhella, D., Eleouet, J. F., and Rey, F. A. (2009) Crystal structure of a nucleocapsid-like nucleoprotein-RNA complex of respiratory syncytial virus. *Science* **326**, 1279-1283
41. Rudolph, M. G., Kraus, I., Dickmanns, A., Eickmann, M., Garten, W., and Ficner, R. (2003) Crystal structure of the borna disease virus nucleoprotein. *Structure* **11**, 1219-1226

42. Carter, S. D., Surtees, R., Walter, C. T., Ariza, A., Bergeron, E., Nichol, S. T., Hiscox, J. A., Edwards, T. A., and Barr, J. N. (2012) Structure, function, and evolution of the Crimean-Congo hemorrhagic fever virus nucleocapsid protein. *J Virol* **86**, 10914-10923
43. Ferron, F., Li, Z., Danek, E. I., Luo, D., Wong, Y., Coutard, B., Lantez, V., Charrel, R., Canard, B., Walz, T., and Lescar, J. The hexamer structure of Rift Valley fever virus nucleoprotein suggests a mechanism for its assembly into ribonucleoprotein complexes. *PLoS Pathog* **7**, e1002030
44. Ye, Q., Krug, R. M., and Tao, Y. J. (2006) The mechanism by which influenza A virus nucleoprotein forms oligomers and binds RNA. *Nature* **444**, 1078-1082
45. Ng, A. K., Zhang, H., Tan, K., Li, Z., Liu, J. H., Chan, P. K., Li, S. M., Chan, W. Y., Au, S. W., Joachimiak, A., Walz, T., Wang, J. H., and Shaw, P. C. (2008) Structure of the influenza virus A H5N1 nucleoprotein: implications for RNA binding, oligomerization, and vaccine design. *FASEB journal : official publication of the Federation of American Societies for Experimental Biology* **22**, 3638-3647
46. Ng, A. K., Lam, M. K., Zhang, H., Liu, J., Au, S. W., Chan, P. K., Wang, J., and Shaw, P. C. Structural basis for RNA binding and homo-oligomer formation by influenza B virus nucleoprotein. *J Virol* **86**, 6758-6767
47. Zheng, W., Olson, J., Vakharia, V., and Tao, Y. J. (2013) The crystal structure and RNA-binding of an orthomyxovirus nucleoprotein. *PLoS Pathog* **9**, e1003624
48. Qi, X., Lan, S., Wang, W., Schelde, L. M., Dong, H., Wallat, G. D., Ly, H., Liang, Y., and Dong, C. Cap binding and immune evasion revealed by Lassa nucleoprotein structure. *Nature* **468**, 779-783
49. Reguera, J., Cusack, S., and Kolakofsky, D. (2014) Segmented negative strand RNA virus nucleoprotein structure. *Current opinion in virology* **5C**, 7-15
50. Chenavas, S., Estrozi, L. F., Slama-Schwok, A., Delmas, B., Di Primo, C., Baudin, F., Li, X., Crepin, T., and Ruigrok, R. W. Monomeric nucleoprotein of influenza a virus. *PLoS Pathog* **9**, e1003275
51. Raymond, D. D., Piper, M. E., Gerrard, S. R., and Smith, J. L. Structure of the Rift Valley fever virus nucleocapsid protein reveals another architecture for RNA encapsidation. *Proc Natl Acad Sci U S A* **107**, 11769-11774
52. Arranz, R., Coloma, R., Chichon, F. J., Conesa, J. J., Carrascosa, J. L., Valpuesta, J. M., Ortin, J., and Martin-Benito, J. The Structure of Native Influenza Virion Ribonucleoproteins. *Science*
53. Moeller, A., Kirchdoerfer, R. N., Potter, C. S., Carragher, B., and Wilson, I. A. Organization of the Influenza Virus Replication Machinery. *Science*
54. Kawai, T., and Akira, S. (2006) Innate immune recognition of viral infection. *Nature immunology* **7**, 131-137
55. Keating, S. E., Baran, M., and Bowie, A. G. (2011) Cytosolic DNA sensors regulating type I interferon induction. *Trends in immunology* **32**, 574-581
56. Diamond, M. S., and Farzan, M. (2013) The broad-spectrum antiviral functions of IFIT and IFITM proteins. *Nat Rev Immunol* **13**, 46-57
57. Ma, Z., and Damania, B. (2016) The cGAS-STING Defense Pathway and Its Counteraction by Viruses. *Cell host & microbe* **19**, 150-158
58. Takeuchi, O., and Akira, S. (2009) Innate immunity to virus infection. *Immunol Rev* **227**, 75-86
59. Theofilopoulos, A. N., Baccala, R., Beutler, B., and Kono, D. H. (2005) Type I interferons (alpha/beta) in immunity and autoimmunity. *Annual review of immunology* **23**, 307-336
60. Der, S. D., Zhou, A., Williams, B. R., and Silverman, R. H. (1998) Identification of genes differentially regulated by interferon alpha, beta, or gamma using oligonucleotide arrays. *Proc Natl Acad Sci U S A* **95**, 15623-15628
61. de Veer, M. J., Holko, M., Frevel, M., Walker, E., Der, S., Paranjape, J. M., Silverman, R. H., and Williams, B. R. (2001) Functional classification of interferon-stimulated genes identified using microarrays. *J Leukoc Biol* **69**, 912-920
62. Sze, A., Olagnier, D., Lin, R., van Grevenynghe, J., and Hiscott, J. (2013) SAMHD1 host restriction factor: a link with innate immune sensing of retrovirus infection. *J Mol Biol* **425**, 4981-4994
63. Praefcke, G. J., and McMahon, H. T. (2004) The dynamin superfamily: universal membrane tubulation and fission molecules? *Nat Rev Mol Cell Biol* **5**, 133-147

64. Lindenmann, J. (1962) Resistance of mice to mouse-adapted influenza A virus. *Virology* **16**, 203-204
65. Haller, O., Stertz, S., and Kochs, G. (2007) The Mx GTPase family of interferon-induced antiviral proteins. *Microbes and infection / Institut Pasteur* **9**, 1636-1643
66. Arnheiter, H., Frese, M., Kambadur, R., Meier, E., and Haller, O. (1996) Mx transgenic mice--animal models of health. *Curr Top Microbiol Immunol* **206**, 119-147
67. P. Staeheli, H., W. Boll,, and Weissmann, J. L. a. C. (1986) Mx Protein: Constitutive Expression in 3T3 Cells Transformed with Cloned Mx cDNA Confers Selective Resistance to Influenza Virus. *Cell* **44**, 147-158
68. Staeheli, P., and Sutcliffe, J. G. (1988) Identification of a second interferon-regulated murine Mx gene. *Mol Cell Biol* **8**, 4524-4528
69. THOMAS ZURCHER, J. P. A. P. S. (1992) Nuclear Localization of Mouse Mxl Protein Is Necessary for Inhibition of Influenza Virus. *JOURNAL OF VIROLOGY* **66**, 5059-5066
70. Goujon, C., Moncorge, O., Bauby, H., Doyle, T., Ward, C. C., Schaller, T., Hue, S., Barclay, W. S., Schulz, R., and Malim, M. H. (2013) Human MX2 is an interferon-induced post-entry inhibitor of HIV-1 infection. *Nature* **502**, 559-562
71. Liu, Z., Pan, Q., Ding, S., Qian, J., Xu, F., Zhou, J., Cen, S., Guo, F., and Liang, C. (2013) The interferon-inducible MxB protein inhibits HIV-1 infection. *Cell host & microbe* **14**, 398-410
72. Kane, M., Yadav, S. S., Bitzegeio, J., Kutluay, S. B., Zang, T., Wilson, S. J., Schoggins, J. W., Rice, C. M., Yamashita, M., Hatziioannou, T., and Bieniasz, P. D. (2013) MX2 is an interferon-induced inhibitor of HIV-1 infection. *Nature* **502**, 563-566
73. Mitchell, P. S., Patzina, C., Emerman, M., Haller, O., Malik, H. S., and Kochs, G. (2012) Evolution-guided identification of antiviral specificity determinants in the broadly acting interferon-induced innate immunity factor MxA. *Cell host & microbe* **12**, 598-604
74. Haller, O., Staeheli, P., Schwemmle, M., and Kochs, G. (2015) Mx GTPases: dynamin-like antiviral machines of innate immunity. *Trends in microbiology* **23**, 154-163
75. Gao, S., von der Malsburg, A., Paeschke, S., Behlke, J., Haller, O., Kochs, G., and Daumke, O. (2010) Structural basis of oligomerization in the stalk region of dynamin-like MxA. *Nature* **465**, 502-506
76. Gao, S., von der Malsburg, A., Dick, A., Faelber, K., Schroder, G. F., Haller, O., Kochs, G., and Daumke, O. (2011) Structure of myxovirus resistance protein a reveals intra- and intermolecular domain interactions required for the antiviral function. *Immunity* **35**, 514-525
77. Rennie, M. L., McKelvie, S. A., Bulloch, E. M., and Kingston, R. L. (2014) Transient dimerization of duman MxA promotes GTP hydrolysis, resulting in a mechanical power stroke. *Structure* **22**, 1433-1445
78. von der Malsburg, A., Abutbul-Ionita, I., Haller, O., Kochs, G., and Danino, D. (2011) Stalk domain of the dynamin-like MxA GTPase protein mediates membrane binding and liposome tubulation via the unstructured L4 loop. *J Biol Chem* **286**, 37858-37865
79. Patzina, C., Haller, O., and Kochs, G. (2014) Structural requirements for the antiviral activity of the human MxA protein against Thogoto and influenza A virus. *J Biol Chem* **289**, 6020-6027
80. Fribourgh, J. L., Nguyen, H. C., Matreyek, K. A., Alvarez, F. J., Summers, B. J., Dewdney, T. G., Aiken, C., Zhang, P., Engelman, A., and Xiong, Y. (2014) Structural insight into HIV-1 restriction by MxB. *Cell host & microbe* **16**, 627-638
81. Xu, B., Kong, J., Wang, X., Wei, W., Xie, W., and Yu, X. F. (2015) Structural insight into the assembly of human anti-HIV dynamin-like protein MxB/Mx2. *Biochemical and biophysical research communications* **456**, 197-201
82. Staeheli, P., Pitossi, F., and Pavlovic, J. (1993) Mx proteins: GTPases with antiviral activity. *Trends in cell biology* **3**, 268-272
83. Warnock, D. E., Hinshaw, J. E., and Schmid, S. L. (1996) Dynamin self-assembly stimulates its GTPase activity. *J Biol Chem* **271**, 22310-22314
84. Ghosh, A., Praefcke, G. J., Renault, L., Wittinghofer, A., and Herrmann, C. (2006) How guanylate-binding proteins achieve assembly-stimulated processive cleavage of GTP to GMP. *Nature* **440**, 101-104

85. Saraste, M., Sibbald, P. R., and Wittinghofer, A. (1990) The P-loop--a common motif in ATP- and GTP-binding proteins. *Trends in biochemical sciences* **15**, 430-434
86. Wittinghofer, A., and Vetter, I. R. (2011) Structure-function relationships of the G domain, a canonical switch motif. *Annual review of biochemistry* **80**, 943-971
87. Gasper, R., Meyer, S., Gotthardt, K., Sirajuddin, M., and Wittinghofer, A. (2009) It takes two to tango: regulation of G proteins by dimerization. *Nat Rev Mol Cell Biol* **10**, 423-429
88. Chappie, J. S., Acharya, S., Leonard, M., Schmid, S. L., and Dyda, F. (2010) G domain dimerization controls dynamin's assembly-stimulated GTPase activity. *Nature* **465**, 435-440
89. Wenger, J., Klinglmayr, E., Frohlich, C., Eibl, C., Gimeno, A., Hessenberger, M., Puehringer, S., Daumke, O., and Goettig, P. (2013) Functional mapping of human dynamin-1-like GTPase domain based on x-ray structure analyses. *PLoS One* **8**, e71835
90. Haller, O., Gao, S., von der Malsburg, A., Daumke, O., and Kochs, G. (2010) Dynamin-like MxA GTPase: structural insights into oligomerization and implications for antiviral activity. *J Biol Chem* **285**, 28419-28424
91. Reubold, T. F., Faelber, K., Plattner, N., Posor, Y., Ketel, K., Curth, U., Schlegel, J., Anand, R., Manstein, D. J., Noe, F., Haucke, V., Daumke, O., and Eschenburg, S. (2015) Crystal structure of the dynamin tetramer. *Nature* **525**, 404-408
92. Mears, J. A., Ray, P., and Hinshaw, J. E. (2007) A corkscrew model for dynamin constriction. *Structure* **15**, 1190-1202
93. Sirajuddin, M., Farkasovsky, M., Hauer, F., Kuhlmann, D., Macara, I. G., Weyand, M., Stark, H., and Wittinghofer, A. (2007) Structural insight into filament formation by mammalian septins. *Nature* **449**, 311-315
94. Schwefel, D., Frohlich, C., Eichhorst, J., Wiesner, B., Behlke, J., Aravind, L., and Daumke, O. (2010) Structural basis of oligomerization in septin-like GTPase of immunity-associated protein 2 (GIMAP2). *Proc Natl Acad Sci U S A* **107**, 20299-20304
95. Byrnes, L. J., Singh, A., Szeto, K., Benvin, N. M., O'Donnell, J. P., Zipfel, W. R., and Sondermann, H. (2013) Structural basis for conformational switching and GTP loading of the large G protein atlastin. *EMBO J* **32**, 369-384
96. Focia, P. J., Shepotinovskaya, I. V., Seidler, J. A., and Freymann, D. M. (2004) Heterodimeric GTPase core of the SRP targeting complex. *Science* **303**, 373-377
97. Byrnes, L. J., and Sondermann, H. (2011) Structural basis for the nucleotide-dependent dimerization of the large G protein atlastin-1/SPG3A. *Proc Natl Acad Sci U S A* **108**, 2216-2221
98. Bian, X., Klemm, R. W., Liu, T. Y., Zhang, M., Sun, S., Sui, X., Liu, X., Rapoport, T. A., and Hu, J. (2011) Structures of the atlastin GTPase provide insight into homotypic fusion of endoplasmic reticulum membranes. *Proc Natl Acad Sci U S A* **108**, 3976-3981
99. Egea, P. F., Shan, S. O., Napetschnig, J., Savage, D. F., Walter, P., and Stroud, R. M. (2004) Substrate twinning activates the signal recognition particle and its receptor. *Nature* **427**, 215-221
100. Accola, M. A., Huang, B., Al Masri, A., and McNiven, M. A. (2002) The antiviral dynamin family member, MxA, tubulates lipids and localizes to the smooth endoplasmic reticulum. *J Biol Chem* **277**, 21829-21835
101. Stertz, S., Reichelt, M., Krijnse-Locker, J., Mackenzie, J., Simpson, J. C., Haller, O., and Kochs, G. (2006) Interferon-induced, antiviral human MxA protein localizes to a distinct subcompartment of the smooth endoplasmic reticulum. *Journal of interferon & cytokine research : the official journal of the International Society for Interferon and Cytokine Research* **26**, 650-660
102. Johnston, S. C., Lin, K. L., Connor, J. H., Ruthel, G., Goff, A., and Hensley, L. E. (2012) In vitro inhibition of monkeypox virus production and spread by Interferon-beta. *Virology journal* **9**, 5
103. Netherton, C. L., Simpson, J., Haller, O., Wileman, T. E., Takamatsu, H. H., Monaghan, P., and Taylor, G. (2009) Inhibition of a large double-stranded DNA virus by MxA protein. *J Virol* **83**, 2310-2320
104. Reichelt, M., Stertz, S., Krijnse-Locker, J., Haller, O., and Kochs, G. (2004) Missorting of LaCrosse virus nucleocapsid protein by the interferon-induced MxA GTPase involves smooth ER membranes. *Traffic* **5**, 772-784

105. Haller, O., and Kochs, G. (2002) Interferon-induced mx proteins: dynamin-like GTPases with antiviral activity. *Traffic* **3**, 710-717
106. King, M. C., Raposo, G., and Lemmon, M. A. (2004) Inhibition of nuclear import and cell-cycle progression by mutated forms of the dynamin-like GTPase MxB. *Proc Natl Acad Sci U S A* **101**, 8957-8962
107. Pavlovic, J., Haller, O., and Staeheli, P. (1992) Human and mouse Mx proteins inhibit different steps of the influenza virus multiplication cycle. *J Virol* **66**, 2564-2569
108. Kochs, G., and Haller, O. (1999) Interferon-induced human MxA GTPase blocks nuclear import of Thogoto virus nucleocapsids. *Proc Natl Acad Sci U S A* **96**, 2082-2086
109. Xiao, H., Killip, M. J., Staeheli, P., Randall, R. E., and Jackson, D. (2013) The human interferon-induced MxA protein inhibits early stages of influenza A virus infection by retaining the incoming viral genome in the cytoplasm. *J Virol* **87**, 13053-13058
110. Pavlovic, J., Zurcher, T., Haller, O., and Staeheli, P. (1990) Resistance to influenza virus and vesicular stomatitis virus conferred by expression of human MxA protein. *J Virol* **64**, 3370-3375
111. Kochs, G., Janzen, C., Hohenberg, H., and Haller, O. (2002) Antivirally active MxA protein sequesters La Crosse virus nucleocapsid protein into perinuclear complexes. *Proc Natl Acad Sci U S A* **99**, 3153-3158
112. Frese, M., Kochs, G., Feldmann, H., Hertkorn, C., and Haller, O. (1996) Inhibition of bunyaviruses, phleboviruses, and hantaviruses by human MxA protein. *J Virol* **70**, 915-923
113. Kanerva, M., Melen, K., Vaheri, A., and Julkunen, I. (1996) Inhibition of puumala and tula hantaviruses in Vero cells by MxA protein. *Virology* **224**, 55-62
114. Bridgen, A., Dalrymple, D. A., Weber, F., and Elliott, R. M. (2004) Inhibition of Dugbe nairovirus replication by human MxA protein. *Virus Res* **99**, 47-50
115. Andersson, I., Bladh, L., Mousavi-Jazi, M., Magnusson, K. E., Lundkvist, A., Haller, O., and Mirazimi, A. (2004) Human MxA protein inhibits the replication of Crimean-Congo hemorrhagic fever virus. *J Virol* **78**, 4323-4329
116. Staeheli, P., and Pavlovic, J. (1991) Inhibition of vesicular stomatitis virus mRNA synthesis by human MxA protein. *J Virol* **65**, 4498-4501
117. Schneider-Schaulies, S., Schneider-Schaulies, J., Schuster, A., Bayer, M., Pavlovic, J., and ter Meulen, V. (1994) Cell type-specific MxA-mediated inhibition of measles virus transcription in human brain cells. *J Virol* **68**, 6910-6917
118. Zhao, H., De, B. P., Das, T., and Banerjee, A. K. (1996) Inhibition of human parainfluenza virus-3 replication by interferon and human MxA. *Virology* **220**, 330-338
119. Chieux, V., Chehadeh, W., Harvey, J., Haller, O., Wattre, P., and Hober, D. (2001) Inhibition of coxsackievirus B4 replication in stably transfected cells expressing human MxA protein. *Virology* **283**, 84-92
120. Landis, H., Simon-Jodicke, A., Kloti, A., Di Paolo, C., Schnorr, J. J., Schneider-Schaulies, S., Hefti, H. P., and Pavlovic, J. (1998) Human MxA protein confers resistance to Semliki Forest virus and inhibits the amplification of a Semliki Forest virus-based replicon in the absence of viral structural proteins. *J Virol* **72**, 1516-1522
121. Mundt, E. (2007) Human MxA protein confers resistance to double-stranded RNA viruses of two virus families. *J Gen Virol* **88**, 1319-1323
122. Yu, Z., Wang, Z., Chen, J., Li, H., Lin, Z., Zhang, F., Zhou, Y., and Hou, J. (2008) GTPase activity is not essential for the interferon-inducible MxA protein to inhibit the replication of hepatitis B virus. *Arch Virol* **153**, 1677-1684
123. Li, N., Zhang, L., Chen, L., Feng, W., Xu, Y., Chen, F., Liu, X., Chen, Z., and Liu, W. (2012) MxA inhibits hepatitis B virus replication by interaction with hepatitis B core antigen. *Hepatology* **56**, 803-811
124. Haller, O., Frese, M., Rost, D., Nuttall, P. A., and Kochs, G. (1995) Tick-borne thogoto virus infection in mice is inhibited by the orthomyxovirus resistance gene product Mx1. *J Virol* **69**, 2596-2601
125. Verhelst, J., Parthoens, E., Schepens, B., Fiers, W., and Saelens, X. (2012) Interferon-inducible protein mx1 inhibits influenza virus by interfering with functional viral ribonucleoprotein complex assembly. *J Virol* **86**, 13445-13455

126. Robert Thimme, M. F., Georg Kochs, Otto Haller. Mx1 but not MxA confers resistance against tick-borne Dhori virus in mice. . *Virology* **211**, 296–301
127. Frese, M., Weeber, M., Weber, F., Speth, V., and Haller, O. (1997) Mx1 sensitivity: Batken virus is an orthomyxovirus closely related to Dhori virus. *J Gen Virol* **78 (Pt 10)**, 2453-2458
128. Jin, H. K., Yoshimatsu, K., Takada, A., Ogino, M., Asano, A., Arikawa, J., and Watanabe, T. (2001) Mouse Mx2 protein inhibits hantavirus but not influenza virus replication. *Arch Virol* **146**, 41-49
129. Zurcher, T., Pavlovic, J., and Staeheli, P. (1992) Mouse Mx2 protein inhibits vesicular stomatitis virus but not influenza virus. *Virology* **187**, 796-800
130. Pitossi, F., Blank, A., Schroder, A., Schwarz, A., Hussi, P., Schwemmle, M., Pavlovic, J., and Staeheli, P. (1993) A functional GTP-binding motif is necessary for antiviral activity of Mx proteins. *J Virol* **67**, 6726-6732
131. Ponten, A., Sick, C., Weeber, M., Haller, O., and Kochs, G. (1997) Dominant-negative mutants of human MxA protein: domains in the carboxy-terminal moiety are important for oligomerization and antiviral activity. *J Virol* **71**, 2591-2599
132. Fricke, T., White, T. E., Schulte, B., de Souza Aranha Vieira, D. A., Dharan, A., Campbell, E. M., Brandariz-Nunez, A., and Diaz-Griffero, F. (2014) MxB binds to the HIV-1 core and prevents the uncoating process of HIV-1. *Retrovirology* **11**, 68
133. Goujon, C., Moncorge, O., Bauby, H., Doyle, T., Barclay, W. S., and Malim, M. H. (2014) Transfer of the Amino-Terminal Nuclear Envelope Targeting Domain of Human MX2 Converts MX1 into an HIV-1 Resistance Factor. *J Virol* **88**, 9017-9026
134. Busnadiego, I., Kane, M., Rihn, S. J., Preugschas, H. F., Hughes, J., Blanco-Melo, D., Strouvelle, V. P., Zang, T. M., Willett, B. J., Boutell, C., Bieniasz, P. D., and Wilson, S. J. (2014) Host and viral determinants of Mx2 antiretroviral activity. *J Virol* **88**, 7738-7752
135. Melen, K., and Julkunen, I. (1997) Nuclear cotransport mechanism of cytoplasmic human MxB protein. *J Biol Chem* **272**, 32353-32359
136. Turan, K., Mibayashi, M., Sugiyama, K., Saito, S., Numajiri, A., and Nagata, K. (2004) Nuclear MxA proteins form a complex with influenza virus NP and inhibit the transcription of the engineered influenza virus genome. *Nucleic Acids Res* **32**, 643-652
137. Wisskirchen, C., Ludersdorfer, T. H., Muller, D. A., Moritz, E., and Pavlovic, J. Interferon-induced antiviral protein MxA interacts with the cellular RNA helicases UAP56 and URH49. *J Biol Chem* **286**, 34743-34751
138. Dittmann, J., Stertz, S., Grimm, D., Steel, J., Garcia-Sastre, A., Haller, O., and Kochs, G. (2008) Influenza A virus strains differ in sensitivity to the antiviral action of Mx-GTPase. *J Virol* **82**, 3624-3631
139. Zimmermann, P., Manz, B., Haller, O., Schwemmle, M., and Kochs, G. (2011) The viral nucleoprotein determines Mx sensitivity of influenza A viruses. *J Virol* **85**, 8133-8140
140. Manz, B., Dornfeld, D., Gotz, V., Zell, R., Zimmermann, P., Haller, O., Kochs, G., and Schwemmle, M. (2013) Pandemic influenza A viruses escape from restriction by human MxA through adaptive mutations in the nucleoprotein. *PLoS Pathog* **9**, e1003279
141. Oliver Daumke, S. G., Alexander von der Malsburg, Otto Haller and Georg Kochs. Structur of the MxA stalk elucidates the assembly of ring-like units of an antiviral module. *Landes Bioscience* **1**, 62 - 64
142. Dick, A., Graf, L., Olal, D., von der Malsburg, A., Gao, S., Kochs, G., and Daumke, O. (2015) Role of nucleotide binding and GTPase domain dimerization in dynamin-like myxovirus resistance protein A for GTPase activation and antiviral activity. *J Biol Chem* **290**, 12779-12792
143. Sambrook, J., and Russell, D.W. . (2001) Molecular cloning : a laboratory manual. *Cold Spring Harbor, N.Y., Cold Spring Harbor Laboratory Press* **3**
144. Chung, C. T., Niemela, S. L., and Miller, R. H. (1989) One-step preparation of competent Escherichia coli: transformation and storage of bacterial cells in the same solution. *Proc Natl Acad Sci U S A* **86**, 2172-2175
145. Thompson, J. D., Higgins, D. G., and Gibson, T. J. (1994) CLUSTAL W: improving the sensitivity of progressive multiple sequence alignment through sequence weighting, position-specific gap penalties and weight matrix choice. *Nucleic Acids Res* **22**, 4673-4680
146. Laemmli, U. K. (1970) Cleavage of structural proteins during the assembly of the head of bacteriophage T4. *Nature* **227**, 680-685

147. Moos, M., Jr., Nguyen, N.Y., and Liu, T.Y. . (1988) Reproducible high yield sequencing of proteins electrophoretically separated and transferred to an inert support. *J Biol Chem* **263**, 6005-6008

148. Doublie, S. (1997) Preparation of selenomethionyl proteins for phase determination. *Methods Enzymol* **276**, 523-530
149. Gill, S. C., and von Hippel, P.H. . (1989) Calculation of protein extinction coefficients from amino acid sequence data. *Anal Biochem* **182**, 319-326

150. Lenzen, C., Cool, R. H., and Wittinghofer, A. (1995) Analysis of intrinsic and CDC25-stimulated guanine nucleotide exchange of p21ras-nucleotide complexes by fluorescence measurements. *Methods Enzymol* **255**, 95-109
151. Schuck, P. (2000) Size-distribution analysis of macromolecules by sedimentation velocity ultracentrifugation and lamm equation modeling. *Biophys J* **78**, 1606-1619
152. Lundstrom, K. (2003) Semliki Forest virus vectors for large-scale production of recombinant proteins. *Methods in molecular medicine* **76**, 525-543
153. Arnold, K., Bordoli, L., Kopp, J., and Schwede, T. (2006) The SWISS-MODEL workspace: a web-based environment for protein structure homology modelling. *Bioinformatics* **22**, 195-201
154. Emsley, P., and Cowtan, K. (2004) Coot: model-building tools for molecular graphics. *Acta crystallographica. Section D, Biological crystallography* **60**, 2126-2132
155. Leslie, A. G. (2006) The integration of macromolecular diffraction data. *Acta crystallographica. Section D, Biological crystallography* **62**, 48-57
156. Kabsch, W. (2010) Xds. *Acta crystallographica. Section D, Biological crystallography* **66**, 125-132
157. Drenth, J. (2007) *Principles of Protein X-Ray Crystallography*, 3rd edition ed., Springer Science and Business Media LLC

158. Hahn., T. (2002) *International Tables for Crystallography Volume A: Space-group symmetry.*, Springer Science+Business Media
159. Taylor, G. L. (2010) Introduction to phasing. *Acta crystallographica. Section D, Biological crystallography* **66**, 325-338
160. Tronrud, D. E. (2007) Introduction to macromolecular refinement. *Methods Mol Biol* **364**, 231-254
161. Sheldrick, G. M. (2008) A short history of SHELX. *Acta crystallographica. Section A, Foundations of crystallography* **64**, 112-122
162. Schneider, T. P. a. T. R. (2004) HKL2MAP: a graphical user interface for macromolecular phasing with SHELX programs. *J. Appl. Cryst.*, 843-844
163. Afonine, P. V., Grosse-Kunstleve, R. W., Echols, N., Headd, J. J., Moriarty, N. W., Mustyakimov, M., Terwilliger, T. C., Urzhumtsev, A., Zwart, P. H., and Adams, P. D. (2012) Towards automated crystallographic structure refinement with phenix.refine. *Acta crystallographica. Section D, Biological crystallography* **68**, 352-367
164. M. D. Winn, M. N. I. a. G. N. M. (2001) Use of TLS parameters to model anisotropic displacements in macromolecular refinement. *Crystallogr D Biol Crystallogr*, 122-133
165. Brunger, A. T. (1997) Free R value: cross-validation in crystallography. *Methods Enzymol* **277**, 366-396
166. Pettersen, E. F., Goddard, T. D., Huang, C. C., Couch, G. S., Greenblatt, D. M., Meng, E. C., and Ferrin, T. E. (2004) UCSF Chimera--a visualization system for exploratory research and analysis. *Journal of computational chemistry* **25**, 1605-1612
167. Guex, N., and Peitsch, M. C. (1997) SWISS-MODEL and the Swiss-PdbViewer: an environment for comparative protein modeling. *Electrophoresis* **18**, 2714-2723
168. Landau, M., Mayrose, I., Rosenberg, Y., Glaser, F., Martz, E., Pupko, T., and Ben-Tal, N. (2005) ConSurf 2005: the projection of evolutionary conservation scores of residues on protein structures. *Nucleic Acids Res* **33**, W299-302
169. DeLano, W. L. (2002) The PyMol Molecular Graphics System.
170. Herskovits, J. S., Burgess, C. C., Obar, R. A., and Vallee, R. B. (1993) Effects of mutant rat dynamin on endocytosis. *J Cell Biol* **122**, 565-578

171. Damke, H., Baba, T., Warnock, D. E., and Schmid, S. L. (1994) Induction of mutant dynamin specifically blocks endocytic coated vesicle formation. *J Cell Biol* **127**, 915-934
172. Sundborger, A. C., Fang, S., Heymann, J. A., Ray, P., Chappie, J. S., and Hinshaw, J. E. (2014) A dynamin mutant defines a superconstricted prefission state. *Cell reports* **8**, 734-742
173. Marks, B., Stowell, M. H., Vallis, Y., Mills, I. G., Gibson, A., Hopkins, C. R., and McMahon, H. T. (2001) GTPase activity of dynamin and resulting conformation change are essential for endocytosis. *Nature* **410**, 231-235
174. Song, B. D., Leonard, M., and Schmid, S. L. (2004) Dynamin GTPase domain mutants that differentially affect GTP binding, GTP hydrolysis, and clathrin-mediated endocytosis. *J Biol Chem* **279**, 40431-40436
175. Shan, S. O., Stroud, R. M., and Walter, P. (2004) Mechanism of association and reciprocal activation of two GTPases. *PLoS biology* **2**, e320
176. Shan, S. O., and Walter, P. (2005) Molecular crosstalk between the nucleotide specificity determinant of the SRP GTPase and the SRP receptor. *Biochemistry* **44**, 6214-6222
177. Frese, M., Kochs, G., Meier-Dieter, U., Siebler, J., and Haller, O. (1995) Human MxA protein inhibits tick-borne Thogoto virus but not Dhori virus. *J Virol* **69**, 3904-3909
178. Pavlovic, J., Arzet, H. A., Hefti, H. P., Frese, M., Rost, D., Ernst, B., Kolb, E., Staeheli, P., and Haller, O. (1995) Enhanced virus resistance of transgenic mice expressing the human MxA protein. *J Virol* **69**, 4506-4510
179. Kochs, G., and Haller, O. (1999) GTP-bound human MxA protein interacts with the nucleocapsids of Thogoto virus (Orthomyxoviridae). *J Biol Chem* **274**, 4370-4376
180. Maines, T. R., Lu, X. H., Erb, S. M., Edwards, L., Guarner, J., Greer, P. W., Nguyen, D. C., Szretter, K. J., Chen, L. M., Thawatsupha, P., Chittaganpitch, M., Waicharoen, S., Nguyen, D. T., Nguyen, T., Nguyen, H. H., Kim, J. H., Hoang, L. T., Kang, C., Phuong, L. S., Lim, W., Zaki, S., Donis, R. O., Cox, N. J., Katz, J. M., and Tumpey, T. M. (2005) Avian influenza (H5N1) viruses isolated from humans in Asia in 2004 exhibit increased virulence in mammals. *J Virol* **79**, 11788-11800
181. Flohr, F., Schneider-Schaulies, S., Haller, O., and Kochs, G. (1999) The central interactive region of human MxA GTPase is involved in GTPase activation and interaction with viral target structures. *FEBS letters* **463**, 24-28
182. Duc, T. T., Farnir, F., Michaux, C., Desmecht, D., and Cornet, A. (2012) Detection of new biallelic polymorphisms in the human MxA gene. *Molecular biology reports* **39**, 8533-8538
183. Melen, K., Ronni, T., Broni, B., Krug, R. M., von Bonsdorff, C. H., and Julkunen, I. (1992) Interferon-induced Mx proteins form oligomers and contain a putative leucine zipper. *J Biol Chem* **267**, 25898-25907
184. Di Paolo, C., Hefti, H. P., Meli, M., Landis, H., and Pavlovic, J. (1999) Intramolecular backfolding of the carboxyl-terminal end of MxA protein is a prerequisite for its oligomerization. *J Biol Chem* **274**, 32071-32078
185. Melen, K., Keskinen, P., Ronni, T., Sareneva, T., Lounatmaa, K., and Julkunen, I. (1996) Human MxB protein, an interferon-alpha-inducible GTPase, contains a nuclear targeting signal and is localized in the heterochromatin region beneath the nuclear envelope. *J Biol Chem* **271**, 23478-23486
186. Baudin, F., Bach, C., Cusack, S., and Ruigrok, R. W. (1994) Structure of influenza virus RNP. I. Influenza virus nucleoprotein melts secondary structure in panhandle RNA and exposes the bases to the solvent. *EMBO J* **13**, 3158-3165
187. Fodor, E., Pritlove, D. C., and Brownlee, G. G. (1994) The influenza virus panhandle is involved in the initiation of transcription. *J Virol* **68**, 4092-4096
188. Tiley, L. S., Hagen, M., Matthews, J. T., and Krystal, M. (1994) Sequence-specific binding of the influenza virus RNA polymerase to sequences located at the 5' ends of the viral RNAs. *J Virol* **68**, 5108-5116
189. Cianci, C., Tiley, L., and Krystal, M. (1995) Differential activation of the influenza virus polymerase via template RNA binding. *J Virol* **69**, 3995-3999
190. Klumpp, K., Ruigrok, R. W., and Baudin, F. (1997) Roles of the influenza virus polymerase and nucleoprotein in forming a functional RNP structure. *EMBO J* **16**, 1248-1257

191. Desselberger, U., Racaniello, V. R., Zazra, J. J., and Palese, P. (1980) The 3' and 5'-terminal sequences of influenza A, B and C virus RNA segments are highly conserved and show partial inverted complementarity. *Gene* **8**, 315-328
192. Pflug, A., Guilligay, D., Reich, S., and Cusack, S. (2014) Structure of influenza A polymerase bound to the viral RNA promoter. *Nature*
193. Reich, S., Guilligay, D., Pflug, A., Malet, H., Berger, I., Crepin, T., Hart, D., Lunardi, T., Nanao, M., Ruigrok, R. W., and Cusack, S. (2014) Structural insight into cap-snatching and RNA synthesis by influenza polymerase. *Nature*
194. Tarus, B., Bakowiez, O., Chenavas, S., Duchemin, L., Estrozi, L. F., Bourdieu, C., Lejal, N., Bernard, J., Moudjou, M., Chevalier, C., Delmas, B., Ruigrok, R. W., Di Primo, C., and Slama-Schwok, A. (2012) Oligomerization paths of the nucleoprotein of influenza A virus. *Biochimie* **94**, 776-785
195. Hope, H. (1988) Cryocrystallography of biological macromolecules: a generally applicable method. *Acta crystallographica. Section B, Structural science* **44 (Pt 1)**, 22-26
196. Cole, C., Barber, J. D., and Barton, G. J. (2008) The Jpred 3 secondary structure prediction server. *Nucleic Acids Res* **36**, W197-201
197. Weber, F., Kochs, G., Gruber, S., and Haller, O. (1998) A classical bipartite nuclear localization signal on Thogoto and influenza A virus nucleoproteins. *Virology* **250**, 9-18
198. Chan, W. H., Ng, A. K., Robb, N. C., Lam, M. K., Chan, P. K., Au, S. W., Wang, J. H., Fodor, E., and Shaw, P. C. Functional analysis of the influenza virus H5N1 nucleoprotein tail loop reveals amino acids that are crucial for oligomerization and ribonucleoprotein activities. *J Virol* **84**, 7337-7345
199. Martin-Benito, J., Area, E., Ortega, J., Llorca, O., Valpuesta, J. M., Carrascosa, J. L., and Ortin, J. (2001) Three-dimensional reconstruction of a recombinant influenza virus ribonucleoprotein particle. *EMBO Rep* **2**, 313-317
200. Coloma, R., Valpuesta, J. M., Arranz, R., Carrascosa, J. L., Ortin, J., and Martin-Benito, J. (2009) The structure of a biologically active influenza virus ribonucleoprotein complex. *PLoS Pathog* **5**, e1000491
201. Schmidt, G., Lenzen, C., Simon, I., Deuter, R., Cool, R. H., Goody, R. S., and Wittinghofer, A. (1996) Biochemical and biological consequences of changing the specificity of p21ras from guanosine to xanthosine nucleotides. *Oncogene* **12**, 87-96
202. Cool, R. H., Schmidt, G., Lenzen, C. U., Prinz, H., Vogt, D., and Wittinghofer, A. (1999) The Ras mutant D119N is both dominant negative and activated. *Mol Cell Biol* **19**, 6297-6305
203. Kochs, G., Haener, M., Aebi, U., and Haller, O. (2002) Self-assembly of human MxA GTPase into highly ordered dynamin-like oligomers. *J Biol Chem* **277**, 14172-14176
204. Steegmaier, M., Oorschot, V., Klumperman, J., and Scheller, R. H. (2000) Syntaxin 17 is abundant in steroidogenic cells and implicated in smooth endoplasmic reticulum membrane dynamics. *Molecular biology of the cell* **11**, 2719-2731
205. Tazi-Ahnini, R., di Giovine, F. S., McDonagh, A. J., Messenger, A. G., Amadou, C., Cox, A., Duff, G. W., and Cork, M. J. (2000) Structure and polymorphism of the human gene for the interferon-induced p78 protein (MX1): evidence of association with alopecia areata in the Down syndrome region. *Human genetics* **106**, 639-645
206. Everitt, A. R., Clare, S., Pertel, T., John, S. P., Wash, R. S., Smith, S. E., Chin, C. R., Feeley, E. M., Sims, J. S., Adams, D. J., Wise, H. M., Kane, L., Goulding, D., Digard, P., Anttila, V., Baillie, J. K., Walsh, T. S., Hume, D. A., Palotie, A., Xue, Y., Colonna, V., Tyler-Smith, C., Dunning, J., Gordon, S. B., Gen, I. I., Investigators, M., Smyth, R. L., Openshaw, P. J., Dougan, G., Brass, A. L., and Kellam, P. (2012) IFITM3 restricts the morbidity and mortality associated with influenza. *Nature* **484**, 519-523
207. Goujon, C. (2014) [Human MX2 is an effector of IFN-mediated resistance to HIV-1 infection]. *Medecine sciences : M/S* **30**, 233-235
208. Wang, J., Reuschel, E. L., Shackelford, J. M., Jeang, L., Shivers, D. K., Diehl, J. A., Yu, X. F., and Finkel, T. H. (2011) HIV-1 Vif promotes the G(1)- to S-phase cell-cycle transition. *Blood* **117**, 1260-1269
209. Chen, Y., Liang, W., Yang, S., Wu, N., Gao, H., Sheng, J., Yao, H., Wo, J., Fang, Q., Cui, D., Li, Y., Yao, X., Zhang, Y., Wu, H., Zheng, S., Diao, H., Xia, S., Zhang, Y., Chan, K. H., Tsoi, H. W., Teng, J. L., Song, W., Wang, P., Lau, S. Y., Zheng, M., Chan, J. F., To, K. K., Chen, H.,

Li, L., and Yuen, K. Y. (2013) Human infections with the emerging avian influenza A H7N9 virus from wet market poultry: clinical analysis and characterisation of viral genome. *Lancet* **381**, 1916-1925

210. Naffakh, N., Tomoiu, A., Rameix-Welti, M. A., and van der Werf, S. (2008) Host restriction of avian influenza viruses at the level of the ribonucleoproteins. *Annual review of microbiology* **62**, 403-424
211. Imai, M., and Kawaoka, Y. (2012) The role of receptor binding specificity in interspecies transmission of influenza viruses. *Current opinion in virology* **2**, 160-167
212. Hutchinson, E. C., and Fodor, E. (2012) Nuclear import of the influenza A virus transcriptional machinery. *Vaccine* **30**, 7353-7358
213. Riegger, D., Hai, R., Dornfeld, D., Manz, B., Leyva-Grado, V., Sanchez-Aparicio, M. T., Albrecht, R. A., Palese, P., Haller, O., Schwemmle, M., Garcia-Sastre, A., Kochs, G., and Schmolke, M. (2015) The nucleoprotein of newly emerged H7N9 influenza A virus harbors a unique motif conferring resistance to antiviral human MxA. *J Virol* **89**, 2241-2252
214. Weber, F., Haller, O., and Kochs, G. (2000) MxA GTPase blocks reporter gene expression of reconstituted Thogoto virus ribonucleoprotein complexes. *J Virol* **74**, 560-563
215. Haller, O., Frese, M., and Kochs, G. (1998) Mx proteins: mediators of innate resistance to RNA viruses. *Revue scientifique et technique* **17**, 220-230
216. Manz, B., Dornfeld, D., Gotz, V., Zell, R., Zimmermann, P., Haller, O., Kochs, G., and Schwemmle, M. Pandemic Influenza A Viruses Escape from Restriction by Human MxA through Adaptive Mutations in the Nucleoprotein. *PLoS Pathog* **9**, e1003279

Abstract

The human Mx protein family is composed of two interferon-inducible dynamin-like large GTPases named MxA and MxB which represent a potent barrier of the innate immune system against viral infections. The cytosolic MxA protein shows broad antiviral activity against several single-stranded RNA viruses, like the orthomyxovirus family, including influenza A, B, C and the closely related Thogoto virus (THOV). In contrast, the human MxB protein acts as a post entry inhibitor of the human immunodeficiency virus type 1 (HIV-1) and the simian immunodeficiency virus (SIV). The target structures of Mx may be the viral nucleoproteins (NPs), which oligomerize around the viral genome to form the so-called viral ribonucleoprotein particles (vRNPs). This vRNPs serve as a template for viral transcription and replication. However, the exact mechanism how vRNPs are inhibited by Mx proteins is not well understood.

Large GTPases are mechano-chemical enzymes, which bind and hydrolyze guanosine-5'-triphosphate (GTP) in the GTPase (G) domain to perform its biological function. It was previously demonstrated that dimerization via the G domains leads to stimulation of the GTPase activity. The formed interface between the G domains is named G interface. To clarify the role of GTP binding and the importance of the G interface formation for the catalytic and antiviral function of MxA, several G domain mutants were characterized. I showed that residues in the catalytic center and the nucleotide itself were crucial for G domain dimerization and catalytic activation. Furthermore, in pulldown experiments, it was demonstrated that binding of MxA to THOV NPs is independent of the nucleotide loading state of MxA. However, nucleotide binding and hydrolysis were essential for the antiviral activity against Thogoto, Influenza and La Cross viruses. In cell-based assays, it was demonstrated that GTP binding facilitates the formation of MxA assemblies associated to ER membranes, and GTP hydrolysis leads to dynamic redistribution to viral target sites.

In the second part of this study, I determined the crystal structure of the THOV NP in the RNA-free state, and biochemically characterized its RNA binding and oligomerization properties. The NP crystallized in a trimeric form, which was also the predominant species in solution, as shown by analytical gel filtration and right-angle light scattering analysis. The structure revealed a crescent-shaped and mainly α-helical molecule with a head and a body domain forming a positively charged RNA-binding groove. A prominent C-terminal extension, referred as to the tail loop, was inserted into the adjacent monomer, indicating its important role for oligomerization. The atomic structure of the Thogoto virus NP provides an additional model for the viral RNP formation within the orthomyxovirus family and is useful for future investigations for the clarification of the viral transcription and replication mechanism.

Zusammenfassung

Die Familie der humanen Mx Proteine besteht aus zwei interferon-induzierten dynamin-ähnlichen großen GTPasen namens MxA und MxB. Beide Proteine gehören zum angeborenen Immunsystem und bilden eine effiziente Barriere gegen eine Vielzahl von viralen Infektionen. Das im Zytosol lokalisierte MxA kennzeichnet sich durch ein breites antivirales Spektrum gegen einzelsträngige RNA Viren aus. Dies beinhaltet das Influenza Virus A, B und C sowie das Thogoto Virus (THOV). MxB hingegen zeigt antivirale Aktivität gegenüber dem humanem Immunschwäche Virus 1 (HIV-1) und dem simianem Immunschwäche Virus (SIV). Als Zielstruktur von MxA wurde das virale Nukleoprotein (NP) ausgemacht, welches sich um das virale Genom assembliert und zusammen mit der viralen Polymerase die sogenannten viralen Ribonukleopartikel (vRNPs) bildet die wiederrum essentiell für Transkription und Replikation des Virus sind. Der exakte antivirale Mechanismus der Mx Proteine ist zurzeit jedoch nicht bekannt. Um deren biologische Funktion zu erfüllen, binden und hydrolysieren große GTPasen Guanosine-5‘-Triphosphat (GTP) in ihrer GTPase (G) Domäne. Studien konnten zeigen, dass die Dimerisierung der G Domänen zur einer Stimulation der GTPase Aktivität führt. Die dabei entstehende Kontaktfläche heißt G-Domänen-Kontaktfläche.

In der vorliegenden Arbeit wurde die Rolle dieser GTP Bindung und die Bildung der G Domänen-Kontaktfläche für die katalytische und antivirale Funktion untersucht. Hierzu wurden mehrere G Domänen Mutanten generiert und biochemisch charakterisiert. Ich konnte mit diesen Mutanten zeigen, dass wichtige Aminosäuren im katalytischen Zentrum der G Domäne sowie das gebundene Nukleotid selbst von zentraler Bedeutung ist für die Dimerisierung der G-Domänen und deren katalytische Aktivierung. Weiterhin konnte in Pulldown-Experimenten gezeigt werden, dass MxA Nukleotid-unabhängig THOV NPs binden kann, wohingegen die antivirale Aktivität gegen Thogoto, Influenza und La Cross Viren eine Nukleotidbindung voraussetzt. In Zell-basierten Experimenten konnte ebenfalls gezeigt werden, dass GTP Bindung die Assemblierung von MxA an Membranen des endoplasmatischen Retikulums begünstigt und die darauffolgende GTP Hydrolyse führt zur einer dynamischen Umverteilung an die viralen Strukturen.

Im zweiten Teil der vorliegenden Doktorarbeit wurde mittels der Röntgenkristallographie die Struktur des THOV NP im RNA-freien Zustand gelöst und mit biochemischen Experimenten deren RNA Bindungs- und Oligomerisationsverhalten analysiert. Im Kristall lag das THOV NP als Trimer vor. Diese Anordnung konnte ebenfalls durch analytische Gelfiltration sowie optische Lichtstreuexperimente auch in Lösung identifiziert werden. Strukturelle Untersuchungen des NPs haben ergaben, dass das Protein ein halbmondartige vorwiegend α-helikal und globuläre Form aufweist. Weiterhin konnte ein positivgeladener RNA-Bindebereich zwischen einer Kopf- und Körperdomäne identifiziert werden. In dem kristallographischen Trimer reicht ein C-terminaler Schwanz in das

benachbarte NP. Diese Anordnung zeigt, dass diese C-terminale Region eine wichtige Funktion für die Oligomerisierung des THOV NP innehat. Die hier präsentierte atomare Struktur des THOV NP bietet ein weiteres Model für die Assemblierung der viralen RNPs innerhalb der orthomyxovirus Familie und schließt mit dem Ausblick auf weitere Aufklärung des viralen Transkriptions- und Replikationsmechanismus.

Publications

Olal, D., Dick, A., Woods, V. L., Jr., Liu, T., Li, S., Devignot, S., Weber, F., Saphire, E. O., and Daumke, O. (2014) Structural insights into RNA encapsidation and helical assembly of the Toscana virus nucleoprotein. *Nucleic Acids Res* **42**, 6025-6037

Dick, A., Graf, L., Olal, D., von der Malsburg, A., Gao, S., Kochs, G., and Daumke, O. (2015) Role of nucleotide binding and GTPase domain dimerization in dynamin-like myxovirus resistance protein A for GTPase activation and antiviral activity. *J Biol Chem* **290**, 12779-12792

Acknowledgement

Many thanks to Oliver Daumke and the whole AG Daumke group. Many thanks also to Udo Heinemann and his group. Furthermore, I want to thank Daniel Olal, Georg Kochs, Laura Graf, Song Gao, David Schwefel, Chris Fröhlich, Janko Brand, Arasu Balasubramaniyam Sivanandam, Arthur Melo, Sabine Werner, Marion Pabst, Uwe Müller and the BESSY team, the DESY team in Hamburg.

Special thanks to my parents my brother, my friends and Beatriz Casasola Rodrigues.

Erklärung

Ich versichere, dass die hier vorliegende Dissertation selbständig angefertigt, die benutzten Quellen und Hilfsmittel vollständig angegeben und die Stellen der Arbeit - einschließlich Tabellen und Abbildungen - die anderen Werken im Wortlaut oder dem Sinn nach entnommen sind, in jedem Einzelfall als Entlehnung kenntlich gemacht wurden; dass dieser Forschungsbericht noch keiner anderen Fakultät oder Universität zur Prüfung vorgelegen wurde. Die Bestimmungen der Promotionsordnung sind mir bekannt. Diese Arbeit wurde von Prof. Dr. Oliver Daumke sowie Prof. Dr. Udo Heinemann betreut.

Berlin im März 2016

Alexej Dick